JAERI-M
85-077

JAPANESE CONTRIBUTIONS TO IAEA INTOR WORKSHOP, PHASE TWO A, PART 2

CHAPTER V : TRANSIENT ELECTROMAGNETICS

July 1985

Masao KASAI[*1], Koju UEDA[*2], Setsuo NIIKURA[*1], Akihisa KAMEARI[*1], Toyoaki KIMURA, Ikuro KONDO, Yoshimi MATSUZAKI, Masahiro MORI, Seiichi TSUJIMURA[*3], Toshihide TSUNEMATSU, Masao YAMADA[*1], Hideaki YOKOMIZO, Noboru FUJISAWA, Hiromasa IIDA, Yutaka IMAMURA[*3], Masana NISHIKAWA[*1], Ryuta SAITO[*2] and Tatsuzo TONE

日 本 原 子 力 研 究 所
Japan Atomic Energy Research Institute

JAERI-M レポートは，日本原子力研究所が不定期に公刊している研究報告書です。

入手の問合わせは，日本原子力研究所技術情報部情報資料課（〒319－11茨城県那珂郡東海村）あて，お申しこしください。なお，このほかに財団法人原子力弘済会資料センター（〒319-11茨城県那珂郡東海村日本原子力研究所内）で複写による実費頒布をおこなっております。

JAERI-M reports are issued irregularly.

Inquiries about availability of the reports should be addressed to Information Division, Department of Technical Information, Japan Atomic Energy Research Institute, Tokai-mura, Naka-gun, Ibaraki-ken 319-11, Japan.

編集兼発行　日本原子力研究所
印　　刷　日立高速印刷株式会社

Japanese Contributions
to IAEA INTOR Workshop, Phase Two A, Part 2
Chapter V : Transient Electromagnetics

Masao KASAI[*1], Koju UEDA[*2], Setsuo NIIKURA[*1], Akihisa KAMEARI[*1], Toyoaki KIMURA[+1], Ikuro KONDO[+1], Yoshimi MATSUZAKI[+2]. Masahiro MORI[+2], Seiichi TSUJIMURA[*3], Toshihide TSUNEMATSU[+2], Masao YAMADA[*1], Hideaki YOKOMIZO, Noboru FUJISAWA, Hiromasa IIDA, Yutaka IMAMURA[*3], Masana NISHIKAWA[*1], Ryuta SAITO[*2] and Tatsuzo TONE

Department of Large Tokamak Research,
Naka Fusion Research Establishment, JAERI

(Received May 31, 1985)

This report corresponds to Chapter V of Japanese contribution report to IAEA INTOR Workshop, Phase Two A, Part 2. Simulation results are shown for feedback control of plasma position, electromagnetic forces at disruptions, penetration of electric and magnetic fields, and benchmark tests for transient electromagnetics. Design guide lines for feedback control system and database assessments are also reported.

Keywords: Design Guide Lines, Tokamak
Plasma Position Control, Transient Electromagnetics
INTOR, Feedback Control, Disruptions, Benchmark Test

+1 Department of JT-60 Facility
+2 Department of Thermonuclear Fusion Research
*1 Mitsubishi Atomic Power Industries, Inc.
*2 Mitsubishi Electric Corporation
*3 Mitsubishi Heavy Industries, Ltd.

IAER INTORワークショップ，フェーズⅡA，パート2報告書 第Ⅴ章：電磁過渡現象解析

日本原子力研究所那珂研究所臨界プラズマ研究部

笠井 雅夫[*1]・上田 孝寿[*2]・新倉 節夫[*1]・亀有 昭久[*1]・木村 豊秋[+1]
近藤 育朗[+1]・松崎 誼[+2]・森 雅博[+2]・辻村 誠一[*3]・常松 俊秀[+2]
山田 政男[*1]・横溝 英明・藤沢 登・飯田 浩正・今村 豊[*3]
西川 正名[*1]・斎藤 龍太[*2]・東稔 達三

（1985年5月31日受理）

この報告書はIAEA主催のINTORワークショップ，フェーズⅡA，パート2における日本の報告書の第5章に相当するものである。プラズマ位置のフィードバック制御解析，ディスラプション時の電磁力，立上げ時の電場・磁場の浸み込み，プラズマ位置制御およびディスラプション時の渦電流に関するベンチマーク解析等について記載している。また，位置制御コイルの設置場所やシェル構造等に関するデザインガイドライン，プラズマ位置形状制御に関する実験結果やデータベース，シェル材や絶縁材の照射損傷に関するデータベースについても述べられている。

+1） JT−60試験部
+2） 核融合研究部
*1） 三菱原子力工業㈱
*2） 三菱電機㈱
*3） 三菱重工業㈱

Contents

1. Introduction (M. Kasai) 1

2. Plasma Stabilization 2
2.1 Summary of Plasma Stabilization Experimental Experience 2
(H. Yokomizo)
2.2 Vertical Position Control 3
2.2.1 Plasma Model (M. Kasai, T. Tsunematsu, K. Ueda) 3
2.2.2 Parametric Studies on Vertical Position Control 4
(M. Kasai, K. Ueda, S. Niikura, A. Kameari)
2.3 Radial Position Control (M. Kasai, S. Niikura) 18
2.4 Plasma Shape Control (M. Kasai).................................. 22

3. Start-up Effects 57
3.1 Magnetic and Electrical Field Penetration (M. Kasai, S. Niikura) . 57
3.2 Components Specification (M. Kasai) 59

4. Plasma Disruption Effects 63
4.1 Plasma Model (M. Kasai, S. Niikura) 63
4.2 Induced Voltage (M. Kasai, A. Kameaari) 63
4.3 Forces (S. Niikura) 64

5. Conclusions 78
5.1 Plasma Stabilization (M. Kasai) 78
5.2 Start-up (M. Kasai) 78
5.3 Disruption (S. Niikura, M. Kasai) 79
5.4 Design Guidelines (M. Kasai, M. Yamada, H. Iida, R. Saito) 79

6. References (Section 1 to 5) 81

7. Appendix 83
7.1 Data Base Assessment 83
7.1.1 Experimental Data for the Position Control Systems 83
JT-60 Plasma Control System Pasrameters
JFT-2M Equilibrium control System Parameters
JFT-2M Fast Pulse Power Supply Technology
7.1.2 Irradiation Effects of Active Coil Insulation materials 109
7.1.3 Radiation Effects on Passive Shell Materials 123
7.2 Benchmark Tests of the Model for Transient Electromagnetics 157

目　　次

1. 序（笠井） …… 1
2. プラズマ安定化 …… 2
　2.1 プラズマ安定化実験のまとめ（横溝） …… 2
　2.2 垂直位置制御 …… 3
　　2.2.1 プラズマモデル（笠井，常松，上田） …… 3
　　2.2.2 垂直位置制御のパラメータスタディ（笠井，上田，新倉，亀有） …… 4
　2.3 水平位置制御（笠井，新倉） …… 18
　2.4 プラズマ形状制御（笠井） …… 22
3. 立上げ時効果 …… 57
　3.1 電場・磁場の浸み込み（笠井，新倉） …… 57
　3.2 コンポーネント仕様（笠井） …… 59
4. プラズマディスラプション効果 …… 63
　4.1 プラズマモデル（笠井，新倉） …… 63
　4.2 発生電圧（笠井，亀有） …… 63
　4.3 電磁力（新倉） …… 64
5. 結　論 …… 78
　5.1 プラズマ安定化（笠井） …… 78
　5.2 スタートアップ（笠井） …… 78
　5.3 ディスラプション（新倉，笠井） …… 79
　5.4 デザインガイドライン（笠井，山田，飯田，斉藤） …… 79
6. 参照文献（第5.1節から第5.5節まで） …… 81
7. 添付資料 …… 83
　7.1 データベースアセスメント …… 83
　　7.1.1 位置制御システムデータ …… 83
　　　JT−60 プラズマ制御系パラメータ
　　　JFT−2M 平衡制御系パラメータ
　　　JFT−2M 高速パルス電源技術
　　7.1.2 制御コイル絶縁材の照射損傷 …… 109
　　7.1.3 シェル材の照射損傷 …… 123
　7.2 電磁過渡解析に関するベンチマークテスト …… 157

1. Introduction

The vertically elongated plasmas are adopted in the design of the next generation machines such as Fusion Experimental Reactor at JAERI and INTOR, because of their expected high beta limit and economical use of the space inside the D-shaped toroidal field coils. Since the decay index n-value of the external equilibrium field is negative, the vertically elongated plasma is positionally unstable against the vertical movement. The growth rate of the vertical instability has to be suppressed with the conductive components surrounding the plasma so that the active feedback control with poloidal coils can stabilize the vertical instability. For this purpose, the highly conductive shells will be installed in the blanket modules in the next generation machines. However, the highly conductive shells are feared to induced too large electromagnetic forces at plasma disruption and to reduce the tritium breeding ratio in the blanket.

The location of active control coils will provide significant impacts on the design and assembling/disassembling of future tokamaks. The active coils inside radiation shield/coil vacuum chamber would make overall tokamak machine and its maintenance procedure unreliable, though they mitigate the requirement for conductive shell design. On the other hand, when the active coils are located outside the shield/coil chamber with low toroidal one turn resistance, the shielding effect of passive elements against the control magnetic field would be problem from the view point of feedback control property. Toroidal one turn resistance of radiation shield/coil vacuum chamber affects this shielding effect, since it surrounds plasma perfectly.

The discussions on these problems are described in the following sections.

2. Plasma Stabilization

2.1 Summary of Plasma Stabilization Experimental Experience

A dee-shaped plasma may have attractive properties for future tokamak reactors. Control of the plasma shape and position is one of most important techniques in these devices, because vertical elongation make the plasma subject to axisymmetric positional instability. The positional instability of elongated plasmas has been studied by many authors and has been observed in several laboratories.

This section reviews the recent progresses of the vertical stability experiment on Doublet III. Plasmas with surface elongations of up to 1.8 have been stably produced in the upper lobe of Doublet III tokamak with the use of both passive and active controls. The growth rates of vertical instability have been measured for plasmas with various elongation, triangularity, other plasma parameters. The measured growth rates are compared qualitatively with the predictions of a simplified model which is based on the relationship between the decay index of the externally applied field and the passive stabilization effect due to eddy currents, and also compared quantitatively with those obtained from numerical calculations based on a more realistic model which utilizes a linear perturbation treatment of the plasma equilibrium.

The following conclusions are obtained (see Reference [1]).

a) Stable plasmas with elongations over the entire range from 1.0 to 1.8 (aspect ratio ≅ 3.4) are produced in the upper half of Doublet III with passive and active control. The maximum value 1.8 lies well above elongations obtained in other experiments. This is due to the fact that the field-shaping coils, which are connected in parallel, are located close to the plasma surface. They play a large part in stabilizing positional instability.

b) Active feedback control fails to stabilize the positional instability of plasmas with elongations of more than 1.8. The upper limit of the elongation is determined by the strength of the passive stabilization effect (n_s) even with active feedback control. The unstable plasma oscillates in the vertical direction, and simultaneous changes occur in the plasma shape and elongation.

c) A dee-shaped plasma with a larger triangular deformation is more positionally stable than a plasma with a smaller triangular deformation because the triangular deformation of the cross-section tends to reduce the value of the decay index relative to that required for an ellipse of the same elongation.

d) The broad profile of the plasma current is beneficial in reducing the vertical instability of an elongated plasma.

e) The maximum elongation is decreased from ∿1.8 to ∿1.25 as the plasma minor radius is reduced from ∿41 cm to ∿33 cm. A low aspect ratio is beneficial for increasing the elongation and reducing vertical instability.

2.2 Vertical Position Control

2.2.1 Plasma model

The analyze transient electromagnetic effects, many different models are being used, including various models for the plasma, models for passive elements, and models for active components. This section provides a brief description of the various plasma models.

The following plasma models are being considered.

1. Rigid circular filament of constant radius and current, with zero mass and only vertical displacements allowed.

2. Same plasma model as 1, but for evaluating the mutual inductance between the plasma and other conductive circuits during plasma movement, the plasma is represented by a pair of filaments. This is called a dipole mode.

3. Plasma column with rigid vertical displacement either with or without skin currents in accordance with ideal MHD theory.

4. Plasma column with non-rigid vertical displacement either with or without current redistribution in accordance with ideal MHD theory.

5. Two-dimensional MHD equilibrium plasma flux diffusion and electromagnetics model.

The difference of analysis results on plasma stabilization effect is not large between model 1 and 2, as shown in Fig. 2.2.1. However, model 3 provides higher stabilizing effect comparing with model 2, since plasma magnetic surfaces shift outward direction and plasma current effectively approaches to outboard shell structures. So this improvement depends on shell configuration and plasma βp etc. In the case of '83 JAERI FER, model 3 provides approximately 50% lower growth rate of vertical position instability as shown in Fig. 2.2.2.

In order to examine the difference between third and fourth models, the stability of the axisymmetric modes of a tokamak plasma is analyzed for the Solov'ev equilibrium [2] by using the linear ideal MHD code ERATO-J [3,4]. The comparison with the results by using the rigid model (n-index theory) [5] and the rigid displacement model [6] is made. In the rigid displacement model the constant vertical or horizontal displacement is assumed in the equation of motion. Figures 2.2.3 shows the stability boundary in the e-δ plane for different values of the aspect ratio, A, where e and δ denote the ellipticity and triangularity of the plasma cross-section, respectively. The position of the conducting shell is infinitely far from the plasma surface. The inner region of the solid lines are the stable region obtained by using the full MHD equation. The dashed line and the dashed solid line correspond to the lines for n_i=0 and n_i=1.5, respectively. The n-index, n_i, is obtained at the magnetic axis of the Solov'ev equilibrium. The circle denotes the stability boundary against the vertical shift of the plasma (n_i=0) by using the formula [5].

$$e < e_c = 1 + \frac{1}{A^2} \cdot \left(\frac{3}{4} \cdot \ln 8A - \frac{17}{16} \right) \qquad (2.2.1)$$

The results by using the rigid model agree with the ones by using full MHD equation for $\delta \sim 0$. The stability boundaries by using the rigid displacement model are shown by the dashed lines in Fig. 2.2.4. The rigid displacement model gives the oposit dependency of the triangularity on the stability boundary. The comparison of three models shows that the analysis of the axisymmetric instability requires the full MHD calculations for large δ.

The analysis by using the full MHD equation shows that the maximum value of the ellipticity, e_c, is about 1.2 when the conducting shell is placed at infinity. The stabilizing effect of the conducting shell increases e_c up to e_c=1.8 for $a_w/a_p \sim 2.0$ [4], where a_w and a_p denote the minor radus of the conducting shell and the plasma.

2.2.2 Parametric studies on vertical position control

Fundamental conditions

To denote the positions and the directions, we use the cylindrical coordinate (R, ϕ, Z). Configurations of the plasma, the control coils and the conductive components are assumed to be symmetric to the Z=0 plane. In what follows, we shall study under the following conditions.

(a) In the equilibrium state, the axisymmetric plasma is maintained by the external equilibrium field which is mainly characterized by the vertical field at the plasma center, B_{ZO} and the decay index n-value. The n-value is define by [7]

$$n = -\frac{1}{I_p B_{zo}} \int_p \frac{\partial B_R^e}{\partial Z} j_p \, R ds, \qquad (2.2.2)$$

where, I_p is the toroidal plasma current, B_R^e is the equilibrium radial field and j_p is the distributed toroidal plasma current density. The integral is taken over the plasma cross section. It is assumed that the plasma moves rigidly in the vertical direction without the plasma current redistribution and that the plasma current and the external equilibrium field do not change during the plasma motion. In these assumptions, the Z-directional force exerted on the plasma column by the external equilibrium field is given by $2\pi n I_p B_{zo} Z_p$ where Z_p is the plasma vertical position from the equilibrium position.

(b) The active control radial field is generated by one pair of the poloidal coils to simplify the analysis. The top and bottom coils are connected in a series and current directions are inversed to each other.

(c) The conductive structures surrounding the plasma are not axisymmetric in general but are located cylically in the toroidal direction. These are approximated by the assemblies of thin conductors and the eddy currents in the conductors are expanded to the eddy current eigenmodes which are mutually decoupled and have the time constants, τ_i's as shown in Ref. [8,9]. Each eddy current mode is normalized to be a circuit with a self-inductance τ_i and a resistance of one unit.

(d) In the equilibrium state, the mutual inductances between the plasma and the control coils and between the plasma and the eddy current modes are zero because of the symmetricity for the Z=0 plane. The Z-derivatives of the mutual inductances between the plasma and the others are claculated by the dipole plasma current approximation given in Ref. [10]. The dipole currents are located at $R=R_p$ and $Z=\pm\pi a_p/4$ and the Z-derivatives of the mutual inductances are given by dividing the mutual inductances between the dipole currents and others by $\pi a_p/2$, here a_p is the minor radius of the plasma.

(e) The plasma displacement from the equilibrium state is small and the coupling between the plasma motions in the radial direction and in the vertical direction is neglected and the equations of the plasma motion in the vertical direction is linearized around the equilibrium state.

Basic equations

The interactions among the plasma vertical motion, the control coil and the eddy current modes in the conductive components are shown by the following evolution equations. The first one is the equation of the plasma motion given by,

$$M_p \ddot{Z}_p = -2\pi R_p I_p \left(-\frac{nB_{zo}}{R_p} Z_p + v_c I_c + \Sigma v_i I_i + B_d\right). \qquad (2.2.3)$$

Here, M_p and R_p are the plasma mass and the major radius of the plasma column, respectively. I_c, I_i and B_d are the control coil current, the current of the i-th eddy current mode and the disturbance radial field, respectively. ν_c and ν_i are the radial field of the unit current of the control coil and the average radial field of the unit current of the i-th eddy current mode, respectively. These are given by,

$$\nu_c = -\frac{M'_{pc}}{2\pi R_p} \text{ and } \nu_i = -\frac{M'_{pi}}{2\pi R_p} \qquad (2.2.4)$$

where M'_{pc} and M'_{pi} are the Z-derivatives of mutual inductances between the plasma and the control coil and between the plasma and the i-th eddy current mode, respectively. A dot (˙) indicates differentiation with respect to time. The summation is taken over the eddy current modes taken into consideration. The inertia term of Eq. (2.2.3) is neglected in what follows under the condition that the poloidal Alfven time scale motion is stabilized by the stabilizing effect of the conductive components.

The second equation is the circuit equation of the control coil.

$$L_c \dot{I}_c + \sum_i M_{ci} \dot{I}_i + I_p M'_{pc} \dot{Z}_p + R_c I_c = V_c , \qquad (2.2.5)$$

where L_c and R_c are the self-inductance and resistance of the control coil, respectively and V_c is the voltage applied to the control coil by the power supply. M_{ci} is the mutual inductance between the control coil and the i-th eddy current mode.

The others are the circuit equations of the eddy current modes.

$$M_{ci} \dot{I}_c + \tau_i \dot{I}_i + I_p M'_{pi} \dot{Z}_p + I_i = 0, \quad (i=1, \ldots , N_{mode}). \qquad (2.2.6)$$

Here, N_{mode} is the number of the eddy current modes taken into consideration.

By Laplace transformations of Eqs. (2.2.3), (2.2.5) and (2.2.6), the block diagram of the control object composed of the plasma, the control coil and the eddy current modes is obtained as shown in Fig. 2.2.5. Here,

$$N(s) = \sum_i \frac{n_i s\tau_i}{1+s\tau_i} , \qquad \text{where } n_i = -\frac{{M'_{pi}}^2 I_p}{2\pi B_{zo} \tau_i} , \qquad (2.2.7)$$

$$M(s) = \sum_i \frac{\mu_i s\tau_i}{1+s\tau_i} , \qquad \text{where } \mu_i = \frac{M_{ci} M'_{pi}}{M'_{pc} \tau_i} , \qquad (2.2.8)$$

and

$$K(s) = \sum_i \frac{\kappa_i s\tau_i}{1+s\tau_i} , \qquad \text{where } \kappa_i = \frac{{M_{ci}}^2}{L_c \tau_i} , \qquad (2.2.9)$$

These transfer functions represent the properties of the eddy current in the conductive components. The N-function, N(s), represents the stabilizing effect of the plasma vertical motion by the eddy current. The shielding function, M(s), represents the shielding effect to the magnetic field of the control coil. When the plasma is perfectly surrounded by the conductive components and the control coil is located outside the components, $M(\infty)=1$. The coupling function, K(s), represents the magnetic coupling effect between the control coil and the eddy current.

The overall transfer function of the control object from the coil voltage V_c to the plasma displacement Z_p is given by,

$$F(s) = \frac{\dfrac{R_p \tau_c \nu_c}{B_{zo} L_c} \cdot \dfrac{1-M(s)}{1+s\tau_c\{1-K(s)\}}}{n+N(s)+N_c(s)} , \quad (2.2.10)$$

where

$$N_c(s) = \frac{n_c s\tau_c \{1-M(s)\}^2}{1+s\tau_c \{1-K(s)\}} , \quad (2.2.11)$$

$$n_c = -\frac{M'^2_{pc} I_p}{2\pi B_{zo} L_c} \quad \text{and} \quad \tau_c = \frac{L_c}{R_c} . \quad (2.2.12)$$

The growth time γ_g of the plasma vertical motion without the feedback control is the root of the equation given by,

$$n + N(\gamma_g) + N_c(\gamma_g) = 0. \quad (2.2.13)$$

When the decay index n-value is negative, Eq. (2.2.13) has a real positive root γ_g and the plasma moves vertically in the time scale of $1/\gamma_g$.

We consider a feedback control system as shown in Fig. 2.2.5. The position detector detects the plasma vertical position with the first order time delay, T_{delay}. The PID controller generates the proportional, integral and derivative signal of the difference between the reference plasma position, Z_{ref} and the detected plasma position, Z_{det}. Here, G, T_I, T_D and T_A is the gain, the integral time, the derivative time and the first order time delay of the derivative, respectively. The voltage limiter limits the maximum and minimum voltages of the power supply to $\pm V_L$. The power supply is approximated by the thyristor with the dead time, T_{dead}.

The transfer function of the open-loop of this feedback control system is given by,

$$A(s) = G\left(\frac{1}{sT_I} + 1 \frac{sT_D}{1+sT_A}\right) \cdot \frac{1}{1+sT_{delay}} \cdot e^{-sT_{dead}} F(s) . \quad (2.2.14)$$

Since the transfer function F(s) has one real positive pole at $s=\gamma_g$ when the n-value is negative, the stability criterion of the feedback loop is represented by Nyquist criterion that the plot of the transfer function of the open-loop, A(s) in the complex plane encircles counter-clockwise the point (-1,j0) when the s vaies from $-j\infty$ to $+j\infty$, here j is an imaginery unit. Equivalently, the stability criterion is represented that the phase is greater than -180 degrees when the gain is equal to 1 in the gain-phase diagram of A(s).

Based on these formulations, the stabilizing properties of passive elements are studied for various types of shell models.

In order to see the machine dependence of control properties (such as difference of the decay index n value, shell design, etc.), we will show the parametric studies on two types of tokamak reactors, i.e. JAERI FER and INTOR.

I. Design studies on passive shells of JAERI FER '84

Main plasma parameters of the JAERI FER '84 are summerized in Table 2.2.1.

The following items should be taken into account in designing shell structures for tokamak fusion reactors.

1) The conductive shells have high enough stabilizing effect on plasma vertical position instability without making active coil design and its installation difficult.

2) They should not induce excessive electro-magnetic forces in the blanket structures at plasma disruption.

3) Their structures should be consistent with remote maintenance procedures.

4) They should not excessively reduce the tritium breeding ratio.

We first studied whether the usual reactor component, such as first wall, blanket, shield and coil vacuum chamber, can stabilize the vertical position instability of the JAERI FER plasma without installing special conductive shell structures around the plasma, since this system should be the most preferable based on the above mentioned items except the item on active coil design and installation.

Figure 2.2.6 shows N(S)-function (defined by eq. (2.2.7)) of this passive element system. Since the n-index of the FER plasma is -1.62, the growth time of plasma vertical movement is approximately 4 msec. Figure 2.2.7 shows the gain-phase diagrams of this feedback control system as a parameter of active coil location. The location (a) is inside the shield and coil vacuum chamber, the location (b) is between the coil vacuum chamber and the toroidal field coils. Only the system with active coils at location (a) can stabilize the plasma vertical position instability. The design and installation of active coils used at location (a) (inside the shield/coil vacuum chamber) should not be practical considering associated engineering problems such as remote handling, insulation, support of feeder lines, space arrangement, etc. So we gave up this kind of system and decided to install high conductive shells for stabilization of plasma positional instability.

It is well known that the toroidal one-turn conductive ring inside the blanket is the most preferable for a shell effect alone. However, this kind of structure will uselessly complicate the remote handling process and make it unreliable, since the segments of conductive ring must be connected and/or disconnected with each other by remote handling machine in the torus chamber. And the design of the remote machine itself would be difficult, because the blanket structure would not be so rigid to support the machine, and the port areas available for machine access are considered to be limited by the design requirements such as neutron/γ-ray shield around the ducts and the space for drawing coolant pipes and supporting the units. Therefore, we installed the conductive shell into each blanket module.

In this type of structure, large electro-magnetic stress and deformation may be induced at plasma disruptions especially in the inboard structure containing the conductive shell, since their support could not be sufficient because of restricted accessibility behind the inboard blanket modules. Further more, shell structures result in the reduction of tritium breeding ratio due to the increase in neutron absorbtion and the decrease in volume fraction of breeding material.

Considering these problems, we designed various types of the conductive shells, and performed parametric studies on their stabilizing characteristics and on the feedback control of plasma vertical position.

<u>Parametric study on shell effects</u>

Figures 2.2.8 (a) and (b) show our model of the conductive shell installed in the blanket module for this parametric study. In designing these configurations, the followings are considered.

(a) Each conductive shell should be separately installed in each blanket module, since it is difficult to connect and/or disconnect the conductive shells with each other by remote handling within the limited space and accessibility.

(b) The material of the conductive shell behind the first wall (front shell) serves also as neutron multiplier, since this region is the most effective zone for the tritium breeding.

(c) The copper is used as the shell material at the side wall of the blanket module, since the conductivity of this part affects the overall shell effects significantly.

Five design choices are selected for the parametric study: (1) number of conductive shell segments along the torus, (2) with or without conductive shell in the inboard blanket (inboard shell), (3) thickness of outboard front shell, (4) thickness of outboard side shell, and (5) with or without conductive shell at the rear of tritium breeding zone (end shell). The stabilizing effect of conductive shells represented by N-function is numerically calculated for ten shell models shown in Table 2.2.2. The parameters used to compare the stabilizing effect are summarized in Table 2.2.3.

(1) Number of conductive shell segments along the torus

The number of blanket modules is one of the most important design parameters with respect to assembling and disassembling the torus structure. Here, two series of survey are carried out: (a) with only outboard shell (model 10-30-80) and (b) with both inboard and outboard shell (model 20-40-90). Figures 2.2.9 and 2.2.10 show the N-functions of these two series with parameter of the number of the shell segments. As shown in these figures, the curves of N-function increase with the number of shell segments decreasing for both cases. In Figure 2.2.11, plasma instability growth times are plotted for the number of shell segments. The growth time is approximately in proportion to the reverse of the number of segments.

(2) With or without inboard conductive shell

The effect of inboard conductive shell can be understood by comparing two series of survey described above. Figure 2.2.11 shows that the inboard shell increases the growth time of positional instability by approximately 10 msec for every number of torus segmentation.

(3) Thickness of outboard front shell

Neutronics indicates that the tritium breeding ratio is sensitive to material and thickness of the outboard front shell. Here, we surveyed the effect of Pb shell thickness for the system of 28 shell segments. Two series are studied: model 30 and 31 for outboard side shell of 15 mm in thickness, and model 32 and 33 for that of 22.5 mm. The N-functions of these models are shown in Fig. 2.2.12. The sensitivities of the front shell thickness, t_{fs}, on the growth time, τ_g, are summarized as

$$\frac{\partial \tau_g}{\partial t_{fs}} = \begin{cases} 0.07 \text{ mspc/mm } P_b \text{ for 15 mm thick Cu side shell} \\ 0.11 \text{ msec/mm } P_b \text{ for 22.5 mm thick Cu side shell} \end{cases}$$

(4) Thickness of outboard side shell

Copper is used as a material of side shell, because of its high electrical conductivity. The tritium breeding ratio is also sensitive to the side shell thickness, since copper absorbs neutrons and reduce the area of breeding zone. Summarizing the results in Fig. 2.2.12, the results are represented as

$$\frac{\partial \tau_g}{\partial t_{ss}} = \begin{cases} 0.55 \text{ msec/mm for 60 mm thick } P_b \text{ front shell} \\ 0.76 \text{ msec/mm for 100 mm thick } P_b \text{ front shell} \end{cases}$$

where t_{ss} is the thickness of the conductive side shell.

(5) With or without outboard end shell

The effect of the existence of outboard end shell can be evaluated by the comparison of the N-functions for model 30 and 50. As shown in Fig. 2.2.13, the N-function is almost the same for these two models. The difference of τ_g between these models is a few milliseconds.

Evaluation of shell effect and design of the shell structure

Based on the results of parametric analyses and other design requirements, we designed two candidate shell structures including shield and vacuum chamber for superconducting coils (SC coils): (a) reference shell structure and (b) alternative shell structure. Both structures are designed so that the conductive shells (excluding non conductive components such as shield and vacuum chamber for SC coils) have the stabilizing effect of Approximately 30 msec in growth time of plasma positional instability, according to the previous year's design study. Both shell structures are shown in Figs. 2.2.14 and 2.2.15, respectively.

(1) Number of segments

Since the number of toroidal coils is fourteen, the minimum number of the blanket modules should be twenty eight from the view point of assembling and disassembling by remote handling. Consequently, the number of the conductive shell segmentation can not be less than 28, unless the conductive shells are connected with each other at some points in the toroidal direction. However, the connections between the adjacent conductive shells are prohibited by the specifications of FY '83 FER design, since the remote handling in the torus with narrow access ports would not be reliable. Therefore, we chose the shell segmentation of 28 to maximize the stabilizing effect within our design restrictions.

(2) Inboard shell

The inboard conductive shell is effective to stabilize the plasma positional instability. However, the electro-magnetic forces at plasma disruption would induce large stresses and deformations in the inboard blanket structures, when the conductive shells are set up in the inboard blankets. Figs. 2.2.16 and 2.2.17 show deformations of the blanket structures designed in the previous year, i.e. FY '82 with and without the conductive shells in the inboard blanket modules, respectively. The maximum deformations are 27.24 mm for the blanket module with inboard conductive shell (case 1), and 9.66 mm for that without inboard shell (case 2), respectively. The maximum electro-magnetic force of $\sim$60 kgf/cm^2 in case 1 inboard module is six times as large as that of 10 kgf/cm in case 2. The maximum stress intensities of case 1 inboard module are 62.6 kgf/mm^2, 113.3 kgf/mm^2 and 115.1 kgf/mm^2 in the membrane, bending and membrane plus bending stresses, respectively. On the other hand, those of case 2 are 19.3 kgf/mm^2, 16.2 kgf/mm^2 and 30.6 kgf/mm^2. From these results, we gave up to install the inboard shell in spite of its desirable stabilizing effect.

(3) Front shell

The material of the front shell are designed to serve as both conductive shell and neutron multiplier. The typical neutron multipliers, i.e. Pb and Be are chosen for this purpose. Since the electrical conductivity of Be is higher than that of Pb, Be is primarily selected as the front shell material. However, the parametric studies on neutronics indicate that the tritium breeding ratio is higher with Pb front shell than with Be one. So the Be front shell is locally replaced by Pb shell st the portion being relatively less effective for plasma stabilization (i.e. around the mid-plane) in the reference shell structure. In the alternative design, to reduce the electro-magnetic forces at plasma disruption, this portion of Pb is designed to serve only as the neutron multiplier by cutting the Pb shell into small blocks and coating their surface with ceramics, for example. In this case, the Pb shell is electrically replaced by the stainless steel blanket wall.

The thickness of Be/Pb shell is set to be 60 mm from the following reasons: (a) the Be/Pb shell of 60 mm thick is considered to be reasonable, based on the parametric study in section 2, (b) the sensitivity of Be/Pb thickness on the tritium breeding ratio is relatively weak at the thickness of about 60 $\sim$ 100 mm, since the thick Pb/Be shell needs to be cooled, which results in decrease in the tritium breeding ratio due to the neutron absorption by the coolant pipe and (c) difficulty of fabrication increases with the Pb/Be shell thickness.

(4) Side shell

In both reference and alternative shell designs, the thickness of Cu side shell is set to be 30 mm thicker than that used in parametric study to compensate the deterioration of shell property caused by the removal of inboard conductive shell.

(5) End shell

In the alternative model, the end shell of 30 mm thick is placed to moderate the shell effect reduction due to the removal of Pb shell effect.

The N-functions of these two shell designs are shown in Figures 2.2.18 and 2.2.19. The growth times of plasma positional instability are 44 msec and 32 msec for the reference and alternative models, respectively. The increases in the growth time due to the shield and the vacuum chamber for SC coils are approximately 10 msec for reference model and 5 msec for alternative model. Figures 2.2.20 and 2.2.21 show the shielding and coupling functions with the control coil-A and -B (see the following paragraphs) for both shell models.

Active control

In this paragraph, we show the results of parametric studies and simulations on the feedback control of plasma positional instability for two shell structures selected in previous paragraph.

(1) Position of feedback control coil

One pair of poloidal coils is considered to generate the radial magnetic field for simplicity of the analysis. The top and bottom coils are connected in series so that the current directions are inverse to each other. These coils are located outside the toroidal field coils to avoid the remote assembling and disassembling of control coils. Two locations are considered as the candidate. One is at 3.5 m and ±6.15 m in the radial and vertical directions, respectively (control coil-A). The other is at 5.7 m and ±6.5 m (control coil-B). Figures 2.2.22 (a) and (b) show the magnetic field configurations produced in plasma region by control coil-A and -B, respectively. The control coil-A produces fairly good radial field. However, the mutual inductance of 6.2×10^{-7} H/m between the coil-A and plasma vertical movement is lower than that of 1.8×10^{-6} H/m between the control coil-B and plasma vertical movement. So we chose the control coil-B as a reference.

(2) Gain-phase diagram of feedback control system

Figures 2.2.23 (a) and (b) show the gain-phase diagrams of open loop transfer functions for the P and PID feedback control system composed of the reference shell structure and the control coil-B. In these diagrams, both T_{dead} and T_{delay} are assumed to be 1 msec. And T_A is given by $T_A = T_D/10$ in Fig. 2.2.23 (b). There are stable regions where the phase is larger than -180 degree in both diagrams. However, the PID controller increases the phase margin as compared with the P controller. This is essentially due to the derivative action.

(3) Parametric studies on the feedback control

Figures 2.2.24 (a) ∿ (d) show the typical simulation results of the plasma vertical position control. The disturbance field is assumed to rise as

$$B_d = B_{do}\ (1 - e^{-t/\tau_{Bd}}),\ B_{do} = 10 \text{ Gauss},\ \tau_{Bd} = 1 \text{ msec.}$$

The maximum voltage of the control coils is limited to be ±500 V in these simulations. The PID feedback control (essentially PD control) reduces the maximum plasma displacement, Z_{pMax}, and the power supply capacity (Max. voltage x Max. current) of the control coils, P_{PSC}, in comparison with the P feedback control. From Figures 2.2.24(a) and (b), the Z_{pMax} and the P_{PSC} can be estimated to be approximately 1.7 ∿ 1.9 mm and 50 ∿ 70 MVA, respectively for the control system with the reference shell structure and the control coil-B. This power of 50 ∿ 70 MVA is relatively small compared with that for equilibrium field and ohmic heating field poloidal coils. However, if we would superpose the active control field component on the equilibrium field component, the plasma vertical position control will increase the requirement for the overall poloidal power supply capacity to the intolerable level, sence the maximum coil voltage comes from the requirement by the positional control, and the maximum coil current comes from that by plasma equilibrium. In our FER design, the maximum coil voltage for positional control is approximately 10 times as high as that for plasma start up, and the maximum coil current for plasma equilibrium is approximately 10 to 100 times as large as that for positional control. Consequently, we install the active control coils separately from the equilibrium field coils. In case of the control coil-A, the P_{PSC} is approximately 1.5 times as large as that in case of the control coil-B for the reference shell structure, though the Z_{pMax} is almost the same. On the other hand, the Z_{pMax} in case of the alternative shell structure is approximately 1.5 times as large as that in case of the reference one, though the P_{PSC} is almost the same.

Table 2.2.4 summarizes the sensitivity studies of P feedback control for the parameters of uncertainty of position detector, Z_{qnt}, rise time constant of disturbance field, τ_{Bd}, delay time of position detector, T_{delay}, dead time of the thyrister, T_{dead}, and coil voltage limiter, V_l. In these studies, the quantitizer is put into the block diagram to estimate the effect of accuracy of position detection. The quantitizer generates a signal of $k \cdot Z_{qnt}$ for the value from $(k-\frac{1}{2})Z_{qnt}$. Here, k is integer, and the infinitely accurate detector is represented by $Z_{qnt}=0$. The sensitivity of these parameters on the Z_{pMax} and the power supply capacity is fairly weak except τ_{Bd} and V_L. The voltage limiter makes the sensitivity of these parameters weak furthermore. From this table and Fig. 2.2.24 (a), it can be noticed that the power supply capacity is approximately proportional to the maximum voltage, though the excessively low voltage limitation makes the control quality poor as shown in Fig. 2.2.25.

Summary

We designed two candidate shell structures based on the sensitivity analyses of the conductive shell effects on plasma vertical position instability. And we performed the simulation studies on the feedback control of plasma vertical movement for the disturbance radial field of 10 Gauss with a rise time of 1 msec. The main conclusions of this work are as follows.

(1) The growth time of plasma vertical position instability, is roughly proportional to the inverse of the number of the conductive shell segments in the toroidal direction. From the constraint on remote maintenance, the conductive shell is installed in each blanket of twenty eight modules, minimizing the number of the shell segments consistent with remote maintenance.

(2) Though the conductive shells in the inboard blanket modules are effective to suppress the growth rate of plasma vertical position instability, they would enlarge the electro-magnetic forces induced at plasma disruption in the inboard blanket structures. Because of the restriction on accessibility behind the inboard blanket modules, the supports of the modules would not be so rigid that the inboard blanket structures could withstand the induced forces. So it is desirable to design the shell structure so that the plasma vertical position instability can be suppressed only by the conductive shells in the outboard blanket modules.

(3) The thickness of Cu side shell and Be/Pb front shell are set to be 30 mm and 60 mm in our FER design, respectively, so that the enough stabilizing effect can be obtained only by the conductive shells in the outboard blanket modules. The Pb/Be front shells serve also as the neutron multiplier. If the Pb/Be front shells are not desired, we can replace them by Cu plane of approximately 4.5 mm thick, for example.

(4) The PID controller (essencially PD controller) increases the stable region in gain-phase diagram and improves the quality of the feedback control system, as compared with the P controller.

(5) The power supply capacity does not strongly depend on the shell structure but on the control coil position. On the other hand, the maximum plasma displacement depends mainly on the shell structure.

(6) The maximum plasma displacement and the power supply capacity do not largely depend on the parameters such as the thyristor dead time, the position detector delay time and the accuracy of plasma position detection. Since the voltage limitation of the control coils does not affect so much the maximum coil current, the power supply capacity is roughly proportional to the maximum coil voltage, though the maximum plasma displacement does not largely depend on it.

II. INTOR

In the INTOR, it is tried to obtain stable high-ß plasma with a non-circular cross-section of comparatively large elongation and also both of suppression and control of the vertical position instability are necessary. We had already reported a shell structure producing the shell effect through which short instability growth time could be suppressed by much the same as a few tens of milliseconds, and there was shown a brief description about the feedback control of its instability [11].

Here, parametric calculations using the INTOR plasma parameters as shown on Table 2.2.5 are carried out for both structures of Figures, 2.2.26 and 2.2.27.

Fig. 2.2.26 shows three kinds of the INTOR shell structures, which have already set as one of obligations on the INTOR Workshop, January 1984, and also the numerical values with their parameters of structures have been determined and shown in the Appendix 2 of January session summary.

Fig. 2.2.27 shows the case that the shell structure shown in Fig. 2.2.26(c) is temporarily installed in the INTOR reactor shown in Fig. 2.2.28. This reactor is divided into 24 sectors along the toroidal direction. In Fig. 2.2.27 is shown the thin plate structure of the reactor (a half of the upper part of one sector). The overall structure is shown in Fig. 2.2.27(c). Its structure of the shell-I (corresponding to Fig. 2.2.26(c), which plays an important role in producing shell effect, and the structure of the shell-(I+II) are especially magnified as shown in Figs. 2.2.27, (a) and (b), respectively.

Although the thickness of each part of the shell-I and shell-II is shown in copper, this does not mean that copper is only a material available for the purpose. It was selected merely as an example. Both dimensions of the shell-I and shell-II are shown in reference [11].

Each thickness of the shields and the blanket is shown as follows:

Shield-1 (Inboard Side)	40 cm (SUS)
Shield-2 (Inboard Side)	40 cm (SUS)
Shield-I (Outboard Side)	30 cm (SUS)
Shield-II (Outboard Side)	40 cm (SUS)
Shield-III (Outboard Side)	30 cm (SUS)
Blanket	5 cm (SUS)

The candidate positions of control coils and their cross-section of the simplified reactor structure are shown in Figure 2.2.28. The positions and dimensions of the above mentioned radiation shields and blanket are determined referring to this structure.

n_s values obtained from three cases in Figs. 2.2.26 (a), (b) and (c) had been already given in Reference [11] and found to be about 0.73, 0.64 and 1.52, restectively. In this case, the dipole model was used for representation of the INTOR plasma column, and the radial position of dipole was selected the INTOR plasma major radius, 5.3m. Field index, n with the INTOR high-ß plasma is about -1.3 and therefore useful shell effect can be not obtained from both of (a) and (b) in Fig. 2.2.26, if based on the dipole model. Only the shell structure, (c) is found to give a useful shell effect.

Figure 2.2.29 shows n_s values obtained from the filamentary model and there, both of (a) (called Plate type) and (c) (called Rectangular type) are given together on selecting the radial position as a variable. Solid lines indicate the sum, $\Sigma\, n_i$ (more in n_i-value than ($x10^{-3}$) and dotted lines are given for the maximum n_s. It is found from the figure that n_s value obtain from the filamentary model is larger than one from the dipole model but more n_s value in $\Sigma\, n_i$ (the maximum n_s) than 1.0 can be not obtained before more major radius than 5.4m (5.5m) is selected. Judging from these results, the above shell of the plate type, (c) in Fig. 2.2.26 may be used for the INTOR high-ß pump limiter plasma.

In Figure 2.2.30 is shown the time dependence of the displacement of the plasma column z_p, along the axis (in case of being not controlled), when the external disturbance, $B_d = B_o\,[1-\exp(-t/\tau_d)]$, is imposed with B_o being fixed at 10 Gauss and τ_d being varied from 0.1 ms to 1 ms, in the case of Fig. 2.2.27. It is found from the value of z_p after 1 ms that the time evolutions is z_p from different τ_d show almost the same growth time, about 40 ms. It is also shown that z_p can be kept less than or nearly equal to 2 cm due to the shell effect at the time of several ms after the external disturbance was imposed.

Figure 2.2.31 is obtained from the case that the decay index is -1.3 and that the torus is toroidally divided into 24 sectors. In Fig. 2.2.31 is shown the time dependence of z_p when an external disturbance, of which τ_d = 1.0 ms and B_d = 10 Gauss, is imposed, where the number of toroidally divided sectors is given as a parameter. The plasma column growth time, γ_g is approximately 50 ms, 40 ms and 30 ms, when the number of sectors is 14, 24 and 34, respectively.

In Figure 2.2.32 is shown the plasma column growth time, γ_g^{-1}, expected in the reactor structure given as a function of the thickness of a pair of plates placed along the toroidal direction at the upper and lower part of shell-I. In this case the number of sectors is set to be 24.

The shell-I gives the shell effect caused only by the structure shown in Fig. 2.2.26 (a), and the shell-(I+II) gives the shell effect caused only by the structure shown in Fig. 2.2.26 (b). Comparison of these two cases shows that the structure of the shell-II can be expected to give more shell effect than in case of only the shell-I.
The upper two cases in Fig. 2.2.32 correspond to the case shown in Fig. 2.2.27 (c). The case that the structure of the shell-II is removed from the structure shown in Fig. 2.2.27 (c), has more shell effect than in Fig. 2.2.27 (b) but less shell effect than in Fig. 2.2.27 (c). These show that substantial shell effect due to the shell-II can be expected, too.

The open loop transfer function, A(s) is examined first before the vertical position control is studied. In this discussion, the reactor structure with 24 sectors is selected, and the thickness of the shell structure is set to be equal to the value shown in Fig. 2.2.27 (a) and (b).

The Bode diagram are shown in Figure 2.2.33 for the case of PI control. The delay time at the detector, T_{delay}, and the dead time for the power supply, T_{dead}, are taken as parameters. It can be seen that PI control can give a stable system if $T_{delay} = T_{dead} = 0$, but that it does not give a stable system if $T_{delay} \neq 0$, as the phase is shifted less than -180° for $\omega \geq 10^3$ (1/sec.).

The Bode diagram is shown in Figure 2.2.34 for the case of PID control. It can be seen that the phase is shifted less than -180° for $\omega \cong 10^3$ (1/sec) if T_{delay} = 5 ms, but that stable control is possible if T_{delay} = 4 ms, as more phase margin than 30° is given.

The typical control results for the case $T_{dead} = T_{delay}$ = 2 ms are given in Figure 2.2.34. The PID control is started at t=1ms. The value of z_p reaches the maximum at about 3 ms, and then it fluctuates slightly to be attenuated and stabilized. The coil voltage is started to increase rapidly at 3 ms and reaches the maximum value of 2.0 KV at about 4.7 ms, and then it fluctuates to be attenuated. The coil current is slightly flowed prior to the time at 3 ms, increase to reach the first peak at about 6 ms, gets the maximum of approximately 0.14 MA at about 20 ms, and then is stabilized. In this case, the power supply of approximately 300MVA is required for suppression and control of the vertical instability.

In Figure 2.2.35, the time dependence of z_p is shown, where T_{delay} is fixed at 2 ms and T_{dead} is varied as a parameter. Three cases in T_{dead}, -1.0, 2.0 and 4 ms are shown there. As T_{dead} decreases, the maximum value of z_p decreases and the fluctuation is moderated, attaining more stable control. The current required for the control coils in three cases is not much varied, and the voltage required decreases as T_{dead} decreases. The required power supply is approximately 230 MVA when T_{dead} = 1.0 ms.

The survey of T_{delay} is also considered to be required. The installation position of the detector should be fully examined in the future, because it can be seen from Fig. 2.2.34 and Fig. 2.2.35 that the choice of the installation position is a critical factor.

As shown in the above, parametric calculations are carried out for the case that the shell structure described in the previous report (11) is actually installed in the simplified reactor structure. One of the aims in these analyses is to know if expected shell effects can be realized in the reactor structure. As a result, it is found that such a reactor structure as in Fig. 2.2.27 (c) can have the instability growth time. about 40 ms as much as in shell-(I+II) of previous report, but only the shell-(I+II) in Fig. 2.2.27 (b) can have about 20 ms in the growth time. This difference is thought to come from that, in this report, the shell effect is evaluated taking various modes of the eddy current into consideration but, in the previous [11], it is evaluated in consideration of only one mode with the maximum time constant. Also it is confirmed that the shell effect increases with increasing toroidal bar thickness of the shell-I, and, therefore, its thickness and material should be selected on trade-off with the breeding ratio of tritium in blankets. Dependence of the shell effect upon the number of toroidally divided sectors shows that three cases, 14, 24 and 34 sectors result in about 47, 36 and 28 ms, respectively.

In the above mentioned reactor, some control characteristics are studied under the disturbance field : B_o = 10 Gauss and τ_d = 1 msec, whose field is found to produce the maximum axial displacement, about 2 cm. Although the capacity of power supply required for suppression and control of the vertical instability is dependent upon the dead time of the power supply, the delay time of position detector, etc., it is found to be about 230 MVA if typically selected on T_{delay} = 2 ms and T_{dead} = 1.0 ms.

2.3 Radial Position Control

Formations

The kinetic equation of plasma radial movement is simply expressed as eq. 2.3.1 by using the Shafranov formula [12].

$$M_p \ddot{R}_p = \frac{\mu_0 I_p^2}{2} \left(\ell n \frac{8R_p}{A_p} + \beta_p + \frac{\ell_i - 3}{2} \right) + 2\pi R_p I_p B_z \qquad (2.3.1)$$

where, M_p : plasma mass
R_p : plasma major radius
A_p : plasma minor radius
I_p : plasma current
β_p : poloidal bets
ℓ_i : normalized internal inductance
B_z : vertical field
μ_0 : permeability

Circuit equations of plasma current, active coils and eddy currents are represented as follows.

$$(L_p \dot{I}_p) + \sum_i (M_{pi} \dot{I}_i) + \sum_k (M_{pk} \dot{I}_k) + \eta_p I_p = 0 \qquad (2.3.2)$$

$$L_i \dot{I}_i + (M_{pi} \dot{I}_p) + \sum_j M_{ij} \dot{I}_j + \sum_k M_{ik} \dot{I}_k + \eta_i I_i = V_i \qquad (2.3.3)$$

$$\tau_k \dot{I}_k + (M_{pk} \dot{I}_p) + \sum_i M_{ik} \dot{I}_i + I_k = 0 \qquad (2.3.4)$$

where, L_p : plasma self inductance
η_p : plasma resistance
M_{pi}: mutual inductance between plasma and i th coil
M_{pk}: mutual inductance between plasma and k th eddy current mode
L_i : self inductance of i-th coil
M_{ij}: mutual inductance between i-th coil and j-th coil
M_{ik}: mutual inductance between i-th coil and k-th eddy current mode
η_i : resistance of i-th coil
I_i : i-th coil current
I_j : k-th coil current
τ_k : time constant of k-th eddy current mode
I_k : eddy current of k-th mode

Linearlizing eqs. (2.3.1) $\sim$ (2.3.4), the following equations are obtained.

$$2\pi I_p B_v \left(1 - \frac{1}{\Lambda_0} - n\right)\delta R_p - \frac{\mu_0 I_p^{\,2}}{2a_p}\,\delta a_p - 2\pi R_p B_v \delta I_p$$

$$+ \frac{\mu_0 I_p^{\,2}}{2}\,\delta \beta_p + \frac{\mu_0 I_p^{\,2}}{4}\,\delta \ell_i + I_p\left(\sum_i \frac{\partial M_{pi}}{\partial R}\,\delta I_i + \sum_k \frac{\partial M_{pk}}{\partial R}\,\delta I_k\right) = 0 \quad (2.3.5)$$

$$\left(I_p \frac{\partial L_p}{\partial R_p} + \sum_i I_i \frac{\partial M_{pi}}{\partial R_p} + \sum_k I_k \frac{\partial M_{pk}}{\partial R_p}\right)\delta \dot{R}_p + I_p \frac{\partial L_p}{\partial a_p}\,\delta \dot{a}_p + L_p \delta \dot{I}_p$$

$$+ I_p \frac{\partial L_p}{\partial \ell_i}\,\delta \dot{\ell}_i + \sum_i M_{pi}\delta \dot{I}_i + \sum_k M_{pk}\dot{I}_k + \eta_p \delta I_p = 0 \quad (2.3.6)$$

$$I_p \frac{\partial M_{pi}}{\partial R_p}\,\delta \dot{R}_p + M_{pi}\delta \dot{I}_p + L_i \delta \dot{I}_i + \sum_k M_{ik}\delta \dot{I}_k + \eta_i \delta I_i = \delta V_i \quad (2.3.7)$$

$$I_p \frac{\partial M_{pk}}{\partial R_p}\,\delta \dot{R}_p + M_{pk}\delta \dot{I}_p + \sum_i M_{ik}\delta \dot{I}_i + \tau_k \delta \dot{I}_k + \delta I_k = 0 \quad (2.3.8)$$

where, $\Lambda_0 = \ln(8R_p/a_p) + \beta_p + (\ell_i - 3)/2$ and
$B_v = -\mu_0 I_p \Lambda_0/(4\pi R_p)$.

By Laplace transformations of eqs. (2.3.5) $\sim$ (2.3.8), six transfer functions are obtained as follows [13,14].

$$N(s) = \sum_k \frac{s\tau_k}{1+s\tau_k}\,n_k, \quad n_k = -\frac{I_p M_{p\ell}^{\prime\,2}}{2\pi B_v \tau_k} \quad (2.3.9)$$

$$M(s) = \sum_k \frac{s\tau_k}{1+s\tau_k}\,m_k, \quad m_k = \frac{M'_{pk} M_{ik}}{M'_{pi}\tau_k} \quad (2.3.10)$$

$$K_i(s) = \frac{s\tau_i}{1+s\tau_i} \sum_k \frac{s\tau_k}{1+s\tau_k}\,k_{ck}, \quad k_{ck} = \frac{M_{ik}^{\,2}}{L_i \tau_k} \quad (2.3.11)$$

$$K_p(s) = \frac{s\tau_p}{1+s\tau_p} \sum_k \frac{s\tau_k}{1+s\tau_k} k_{pk}, \quad k_{pk} = \frac{M_{pk}^{\prime 2}}{L_p \tau_k} \qquad (2.3.12)$$

$$V(s) = \sum_k \frac{s\tau_k}{1+s\tau_k} v_k, \quad v_k = \frac{M_{pk}^{\prime} M_{ik}}{M_{pi}^{\prime} \tau_k} \qquad (2.3.13)$$

$$B(s) = \sum_k \frac{s\tau_k}{1+s\tau_k} b_k, \quad b_k = \frac{I_p M_{pk}^{\prime} M_{pk}}{2\pi R_p B_v \tau_k} \qquad (2.3.14)$$

The N(s) represents the stabilizing effect of eddy currents on plasma radial movement. The M(s) represents the shielding effect to radial magnetic field of control coils. The $K_i(s)$ and $K_p(s)$ represent the effective reductions of control coil and plasma impedances due to eddy currents, respectively. The V(s) represents the effective reduction of mutual inductance between plasma and coil. The B(s) represents the vertical magnetic field reduction due to eddy currents induced by plasma current change. M' means radial derivative of mutual inductance in eqs. (2.3.9)∿(2.3.14).

Simulation results

Figures 2.3.1 and 2.3.2 show the time evolutions of plasma radial position, R_p, and plasma current, I_p, for the JAERI FER with and without high conductive shell structures, respectively. In these simulations, the active feedback control of plasma radial position is assumed to be out of operation. Poloidal beta β_p, and normalized internal inductance, li, decrease with the time scale of 5 msec by 40%, and plasma are assumed to be compressed so as to conserve troidal magnetic flex in the plasma. The high conductive shells increase the time scale of plasma movement. So the presence of good conductors near the plasma would be effective to lead to long current decay times [15].

Figure 2.2.3 represents the simulation result of the feedback control of plasma radial movement in case of high conductive shell installed. The shell model and the locations and current weight of active coils are summarized in Fig. 2.3.4. Though plasma radial position can be recovered, the maximum coil voltage is quite high (approximately 4400 V) and the power supply capacity of active coil system is required to be approximately 2000 MVA which is impractical.

Figure 2.3.5 shows the simulation result of more practical case. In this case, maximum coil current and power supply capacity are approximately 1000 V, 110 KA and 110 MVA, respectively. Though plasma position can not be recovered, the time scale of plasma movement can be approximately doubled, comparing with uncontrolled case, if the initial gap of 20 m between inboard first wall and plasma surface can be held.

Concluding remarks

i) The presence of high conductive shells around the plasma would be effective to increase current decay time at plasma disruption.

ii) The impractically large power supply capacity and high coil voltage are required to recover the plasma radial position at disruption.

iii) Within the practical power supply capacity and coil voltage, the time scale of plasma radial movement may be increased by approximately factor 2, provided the gap of $\sim$25 cm between inboard first wall and plasma surface can be initially held.

2.4 Plasma Shape Control

Considering the control of plasma shape, it may be helpful to classify the problems into the following two categories.

a. The problems related to the operation scenario such as how to evolve plasma configuration and make high beta configuration with suppressing peak power and capacity of poloidal coil power supply system.

b. The problems related to the unexpected perturbations such as how to fix null points and/or separatrix lines at plasma position movements.

The problems of the category a are dealt with preprograming and/or feedforward control. One of the problems in category a is how to obtain and keep favorable plasma current profile and plasma shape for high beta plasma. Another problem is how to reduce the absolute value of the decay index n-value to mitigate the requirements for plasma vertical position control. It would be desirable to adopt limiter configurations at early start up phase, since it is difficult to suppress the increase in the absolute n-index value at low beta phase if divertor configurations are adopted at that time. Another way to ease plasma vertical position control is to decrease plasma aspect ratio and increase triangularity, since low plasma aspect ratio and high plasma triangularity would reduce the absolute n-index value as well known.

The problems of the category b are dealt with feedback control. It is important problem in this category to control null points and separatrix lines when plasmas move in the radial and/or vertical directions. If we control plasma position, shape, null points and separatrix lines independently, unavoidable interaction will be induced among the control objects mentioned above. Noninteracting control method is developed in JT-60 [16] to avoid this kind of interaction. It would be also necessary to adopt this method in the next generation tokamak reactors.

Table. 2.2.1 Main plasma parameters

Parameters	Values
Major Radius (m)	5.5
Minor Radius (m)	1.1
Aspect Ratio	5.0
Ellipticity (target)	1.5
Triangularity	0.2
First wall minor radius (m)	1.25
Averaged ion temperature (keV)	10
Averaged ion density (m^{-3})	1.36×10^{20}
Averaged effective charge	1.5
Plasma current (MA)	5.3
Safety factor at plasma (effective)	2.5
Toroidal beta (%)	4.0
Poloidal beta	2.3
Initial loop voltage (V)	50 (0.1s)
Error field (inside the plasma) (G)	50

Table. 2.2.2 Summary of conductive shell models used in parametric studies on shell effects.

<table>
<tr><th rowspan="2">MODEL NO.</th><th rowspan="2">NO. OF DIVISION</th><th colspan="2">INBOARD</th><th colspan="3">OUTBOARD</th><th rowspan="2">GROWTH TIME: τ_G (ms)</th></tr>
<tr><th>F/W</th><th>S/W</th><th>F/W</th><th>S/W</th><th>E/W</th></tr>
<tr><td>10</td><td rowspan="2">14</td><td>SS (10)</td><td>SS (20)</td><td rowspan="3">Pb (60)</td><td rowspan="4">Cu (15)</td><td rowspan="7">NONE</td><td>32.21</td></tr>
<tr><td>20</td><td>Pb (60)</td><td>Cu (15)</td><td>41.04</td></tr>
<tr><td>30</td><td rowspan="6">28</td><td rowspan="4">SS (10)</td><td rowspan="4">SS (20)</td><td>17.74</td></tr>
<tr><td>31</td><td>Pb (100)</td><td>20.62</td></tr>
<tr><td>32</td><td>Pb (60)</td><td rowspan="2">Cu (22.5)</td><td>21.90</td></tr>
<tr><td>33</td><td>Pb (100)</td><td>26.29</td></tr>
<tr><td>40</td><td>Pb (60)</td><td>Cu (15)</td><td rowspan="4">Pb (60)</td><td rowspan="4">Cu (15)</td><td>27.62</td></tr>
<tr><td>50</td><td>SS (10)</td><td>SS (20)</td><td>Cu (15)</td><td>19.73</td></tr>
<tr><td>80</td><td rowspan="2">42</td><td>SS (10)</td><td>SS (20)</td><td rowspan="2">NONE</td><td>9.27</td></tr>
<tr><td>90</td><td>Pb (60)</td><td>Cu (15)</td><td>17.07</td></tr>
</table>

F/W: FRONT WALL S/W: SIDE WALL E/W: END WALL

FIGURES IN ( ) IS THICKNESS; mm

Table. 2.2.3 Parameters used in parametic studies

1. Number of Conductive Shell Segments
   14, 28, 42
2. Inboard Conductive Shells
   Existence (Pb, 60mm & Cu, 15mm) / None
3. Thickness of Outboard Front Shell
   Pb (100mm) / Pb (60mm)
4. Thickness of Outdoard Side Shell
   Cu (22.5mm) / Cu(15mm)
5. Outboard End Shell
   Existence Cu (15mm) / None

Table. 2.2.4 Prametric studies on plasma position control (Reference design, Control coil-B)

			MAX. VOLT (V)	MAX. CURRENT (kA)	P/S CAPACITY (MVA)	MAX. DIS-PLACEMENT (mm)
$V_L = \infty$	Z_{gnt} (mm)	0.0	612	118.5	72.57	−18.27
		2.0	630	118.5	74.67	−18.24
		5.0	700	120.7	84.50	−18.32
	τ_{Bd} (msec)	1.0	612	118.5	72.57	−18.27
		2.5	534	117.1	62.50	−15.59
		5.0	438	112.5	49.21	−12.64
	T_{delay} (msec)	0.5	615	115.2	70.87	−17.83
		1.0	612	118.5	72.57	−18.27
		2.0	592	125.9	74.49	−18.92
	T_{dead} (msec)	0.5	588	115.3	67.80	−17.62
		1.0	612	118.5	72.57	−18.27
		2.0	661	126.5	83.69	−19.56
$V_L = 250$ V	Z_{gnt} (mm)	0.0	250	132.4	33.09	−19.08
		2.0	250	132.0	33.01	−19.05
		5.0	250	133.1	33.28	−19.17
	τ_{Bd} (msec)	1.0	250	132.4	33.09	−19.08
		2.5	250	128.3	32.08	−17.47
		5.0	250	121.4	30.35	−14.62
	T_{delay} (msec)	0.5	250	130.4	32.60	−18.90
		1.0	250	132.4	33.09	−19.08
		2.0	250	135.8	33.95	−19.35
	T_{dead} (msec)	0.5	250	129.2	32.30	−18.66
		1.0	250	132.4	33.09	−19.08
		2.0	250	138.6	34.66	−19.90

Table 2.2. 5 Major Parameters of the INTOR

Major Radius , R_p (m)	5.3
Minor Radius , a_p (m)	1.2
Plasma Current , (MA)	6.4
Divertor Plasma	
Elongation , K	1.6
Shafranof's Field , B_0 (T)	- 0.50
Decay Index , n	- 1.30
Pump Limiter	
Elongation , K	1.50
Shafranof's Field , B_0	- 0.52
Decay Index , n	- 1.0

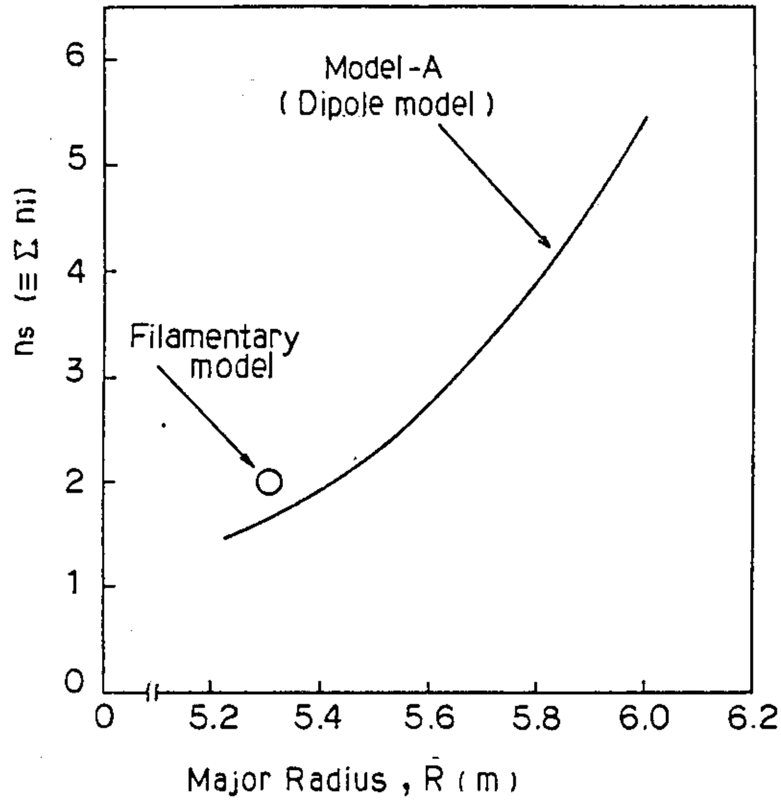

Fig. 2.2.1 Comparison of stabilizing property between filamentary model and dipole current model.

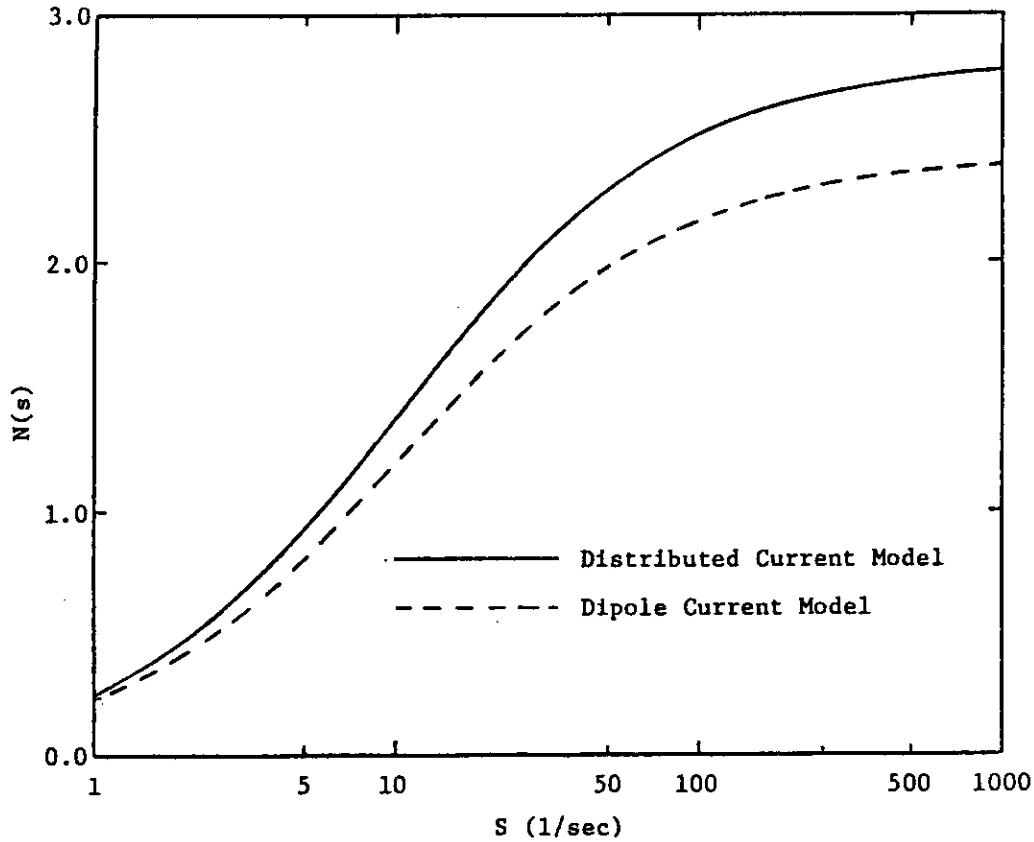

Fig. 2.2.2 Comparison of stabilizing property between distributed current model and dipole current model.

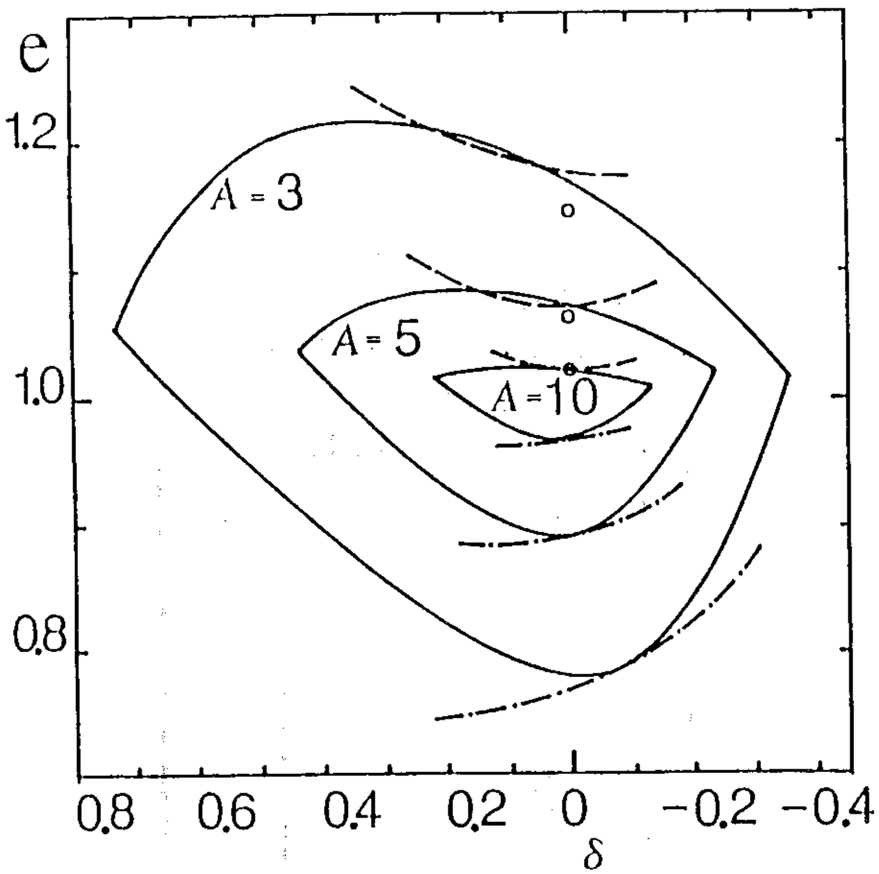

Fig. 2.2.3 The stability diagram of the Solov'ev equilibrium in $e-\delta$ plane for different values of A. The safety factor at the magnetic axis, q_0, is unity. The dashed line and the dashed solid line correspond to ones for $n_i=0$ and $n_i=1.5$, respectively.

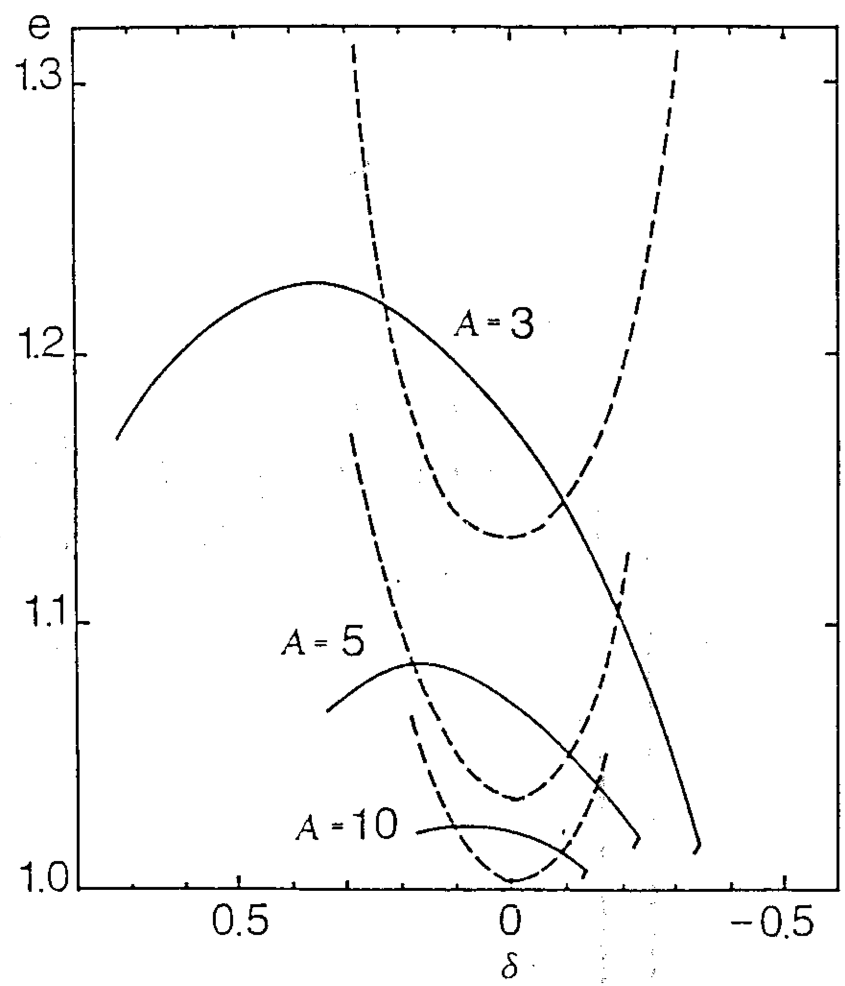

Fig. 2.2.4 The stability diagram for the full MHD model(solid lines) and the rigid displacement model(dahed lines).

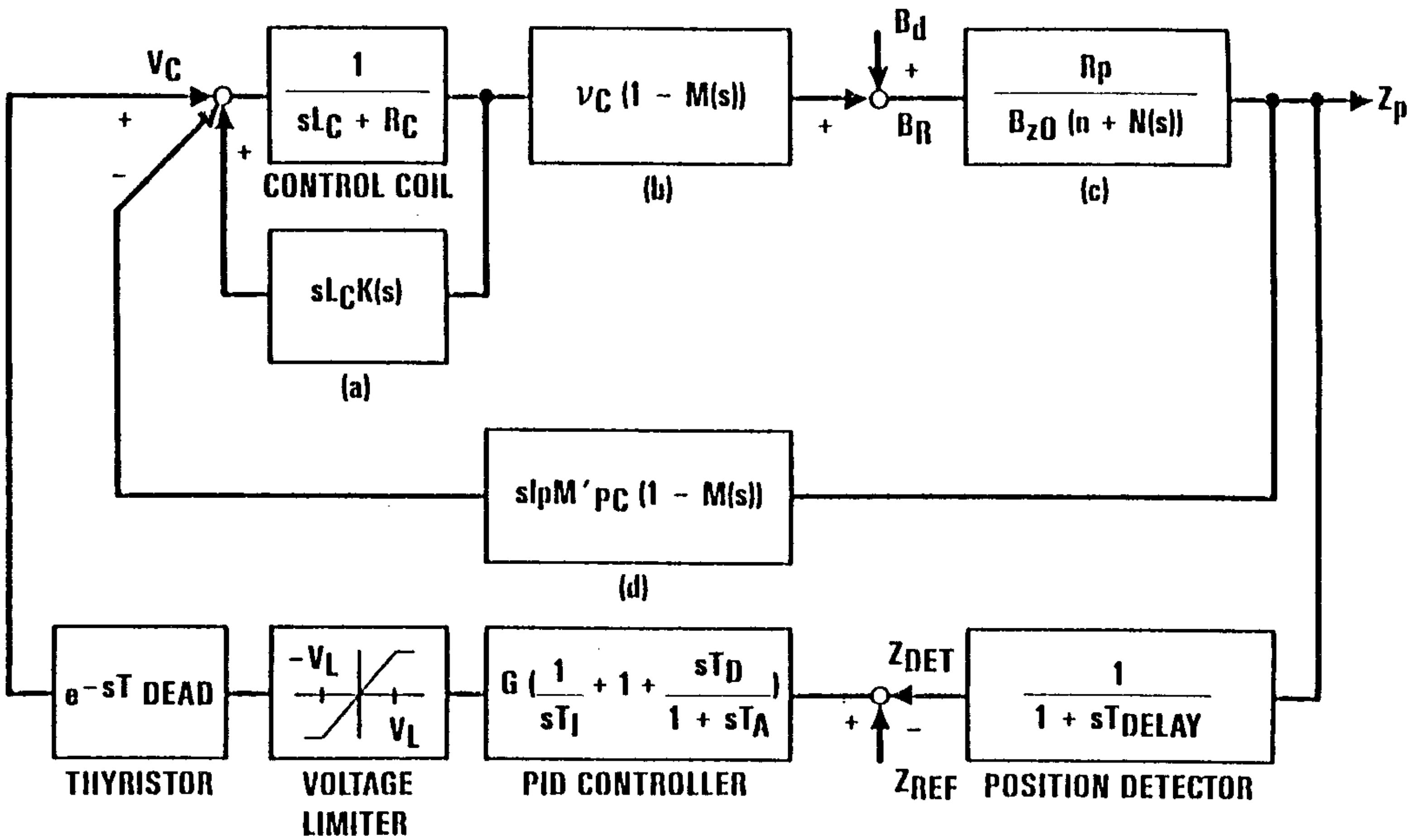

Fig. 2.2.5 Block diagram of the feedback control system of the plasma vertical position.

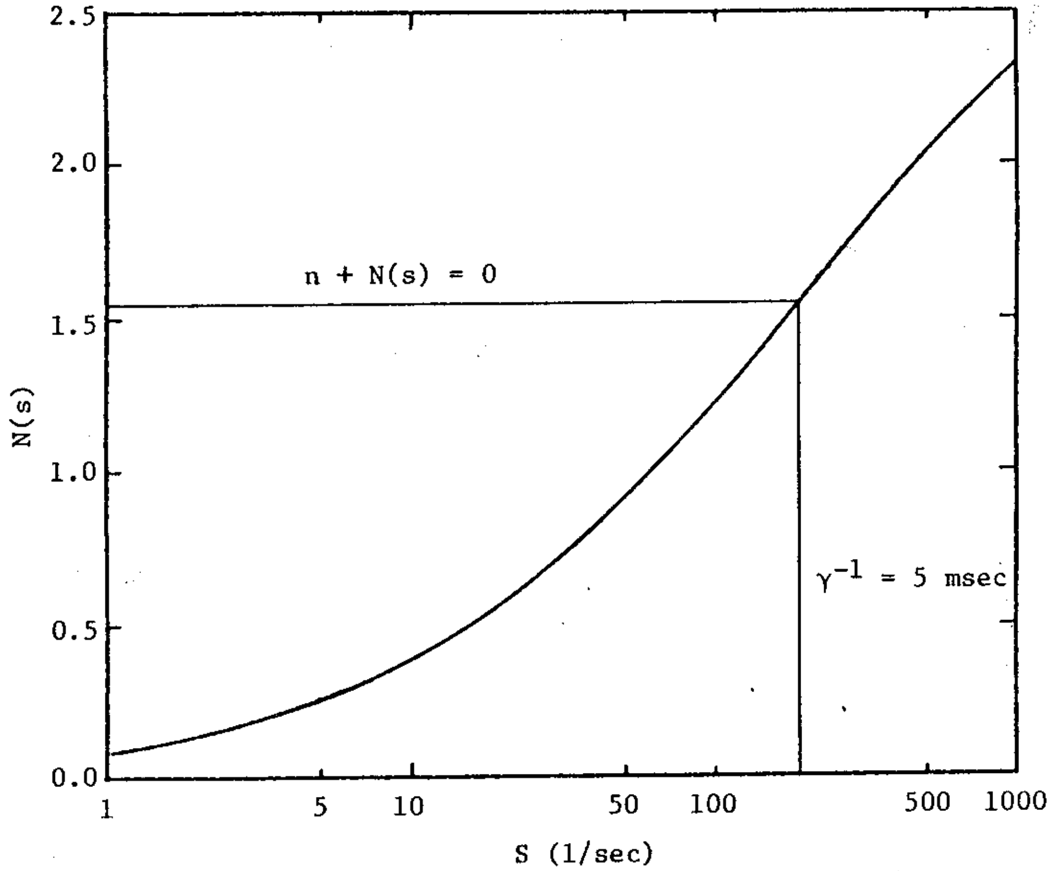

Fig. 2.2.6 N(s)-function of FWBS without high conductive shells

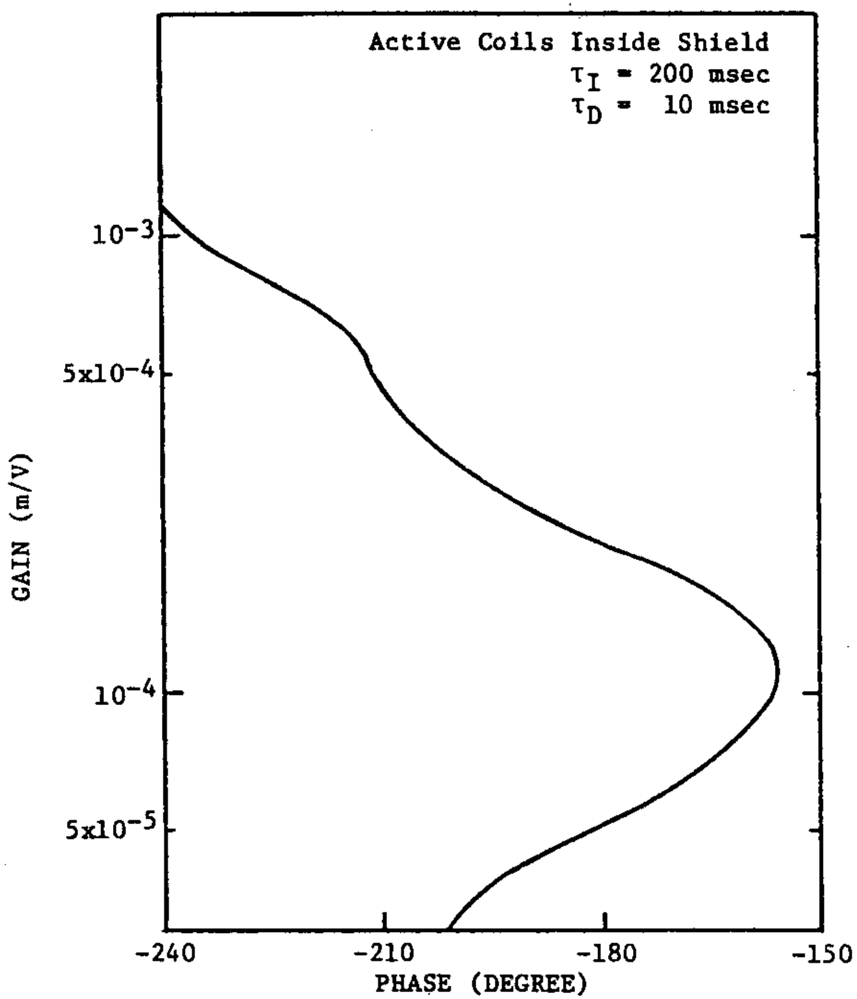

Fig. 2.2.7(a) Gain-phase diagram of open loop transfer function for PID control system without conductive shells. Active coils are located inside shield. Delay time of position detector and dead time of thyristor are assumed to be 1 msec. Integral time constant and derivative time constant are 200 msec and 10 msec, respectively.

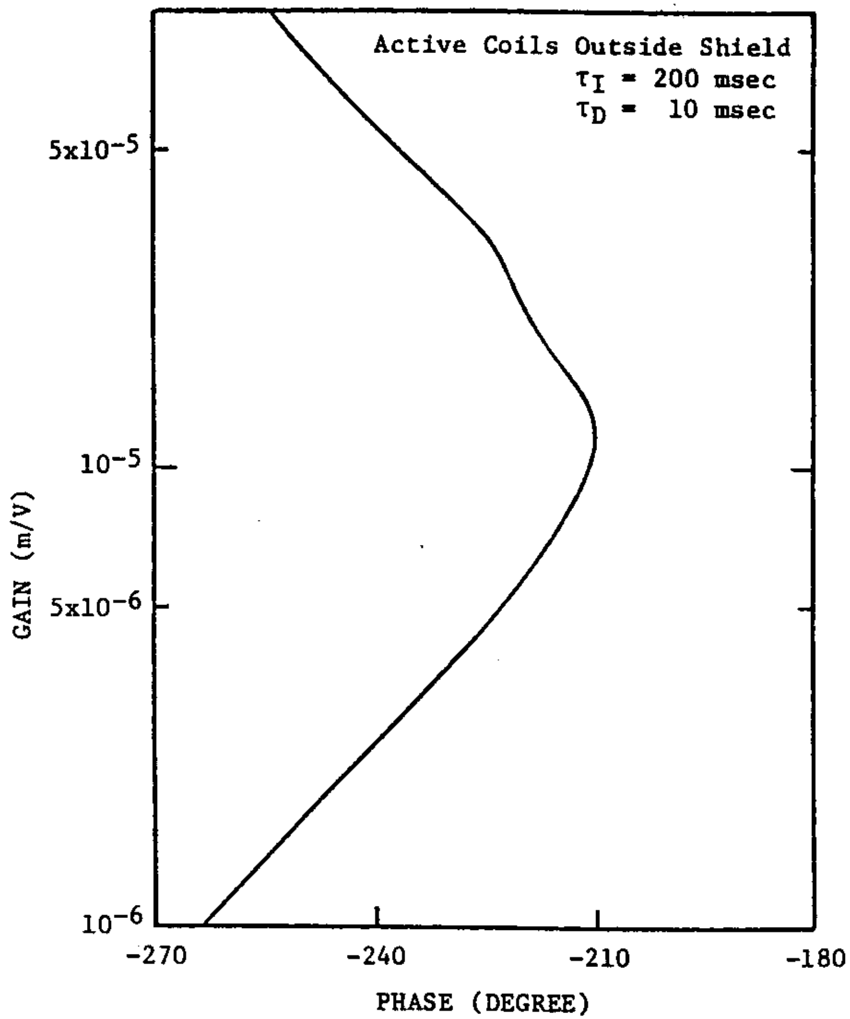

Fig. 2.2.7(b) Gain-phase diagram of open loop transfer function for PID control system without conductive shells. Active coils are located outside shield. Delay time of position detector and dead time of thyristor are assumed to be 1 msec. Integral time constant and derivative time constant are 200 msec and 10 msec, respectively.

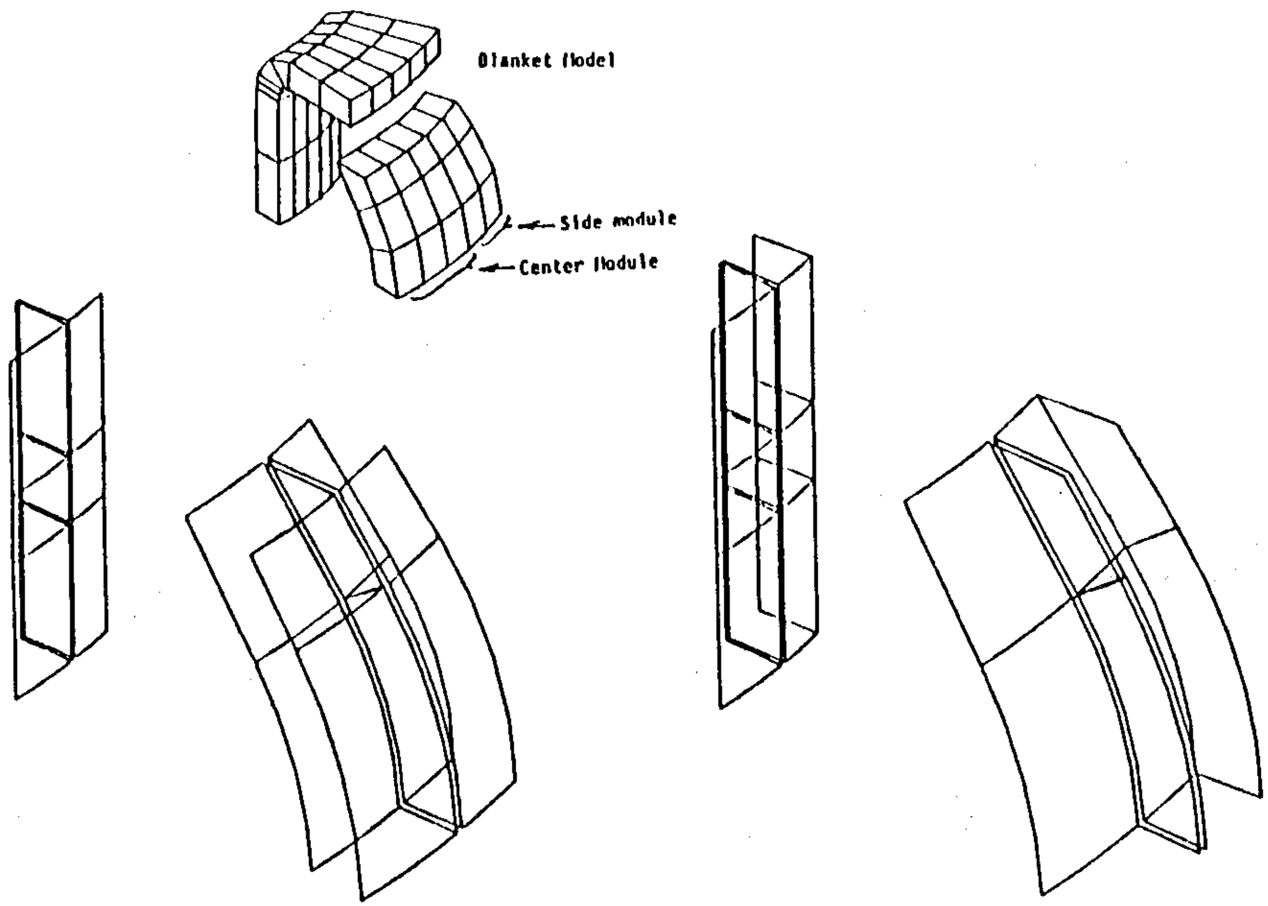

(a) Model-50

(b) Model-80,-90

Fig. 2.2.8 Conductive shell structures used in parametric studies on shell effects.

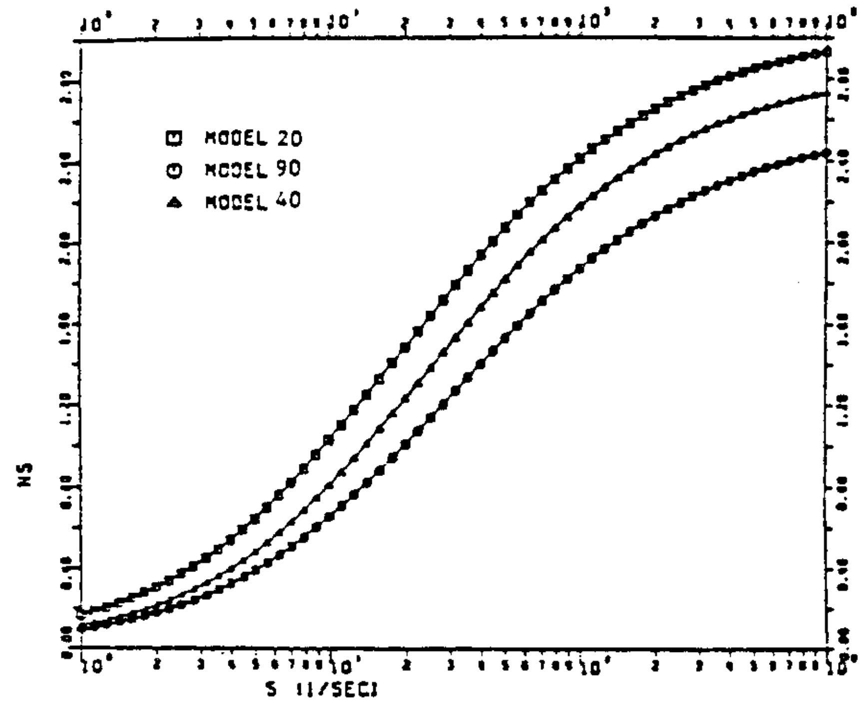

Fig.2.2.9 N-function of conductive shell in both inboard and outboard blanket module with parameter of the number of shell segments. Model 20, 90, 40, : 14, 28, 42 segments

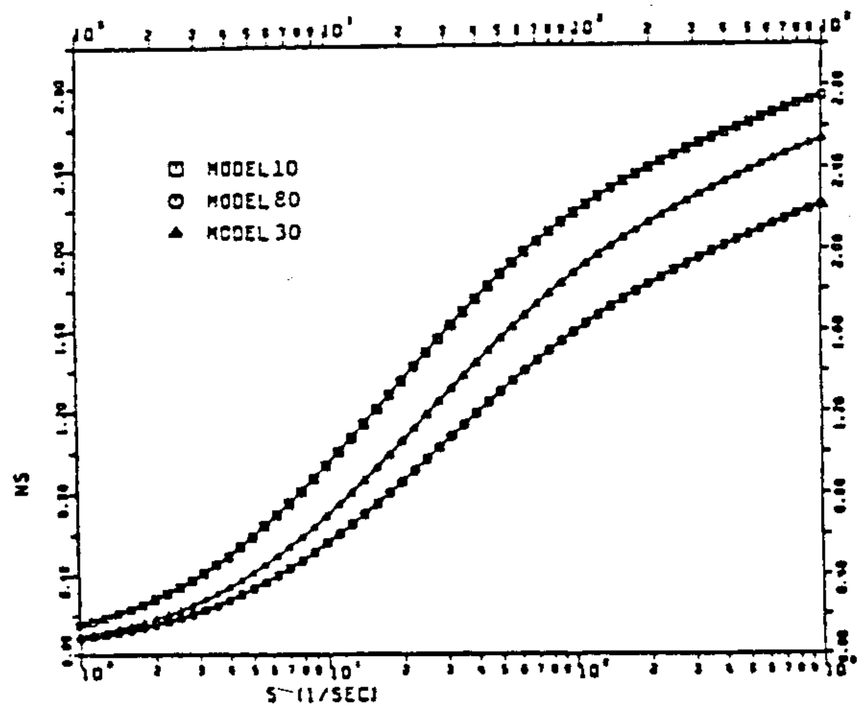

Fig. 2.2.10 N-function of conductive shell in only outboard blamket module sith parameter of the number of shell segments. Model 10, 80, 30 : 14, 28, 42 segments

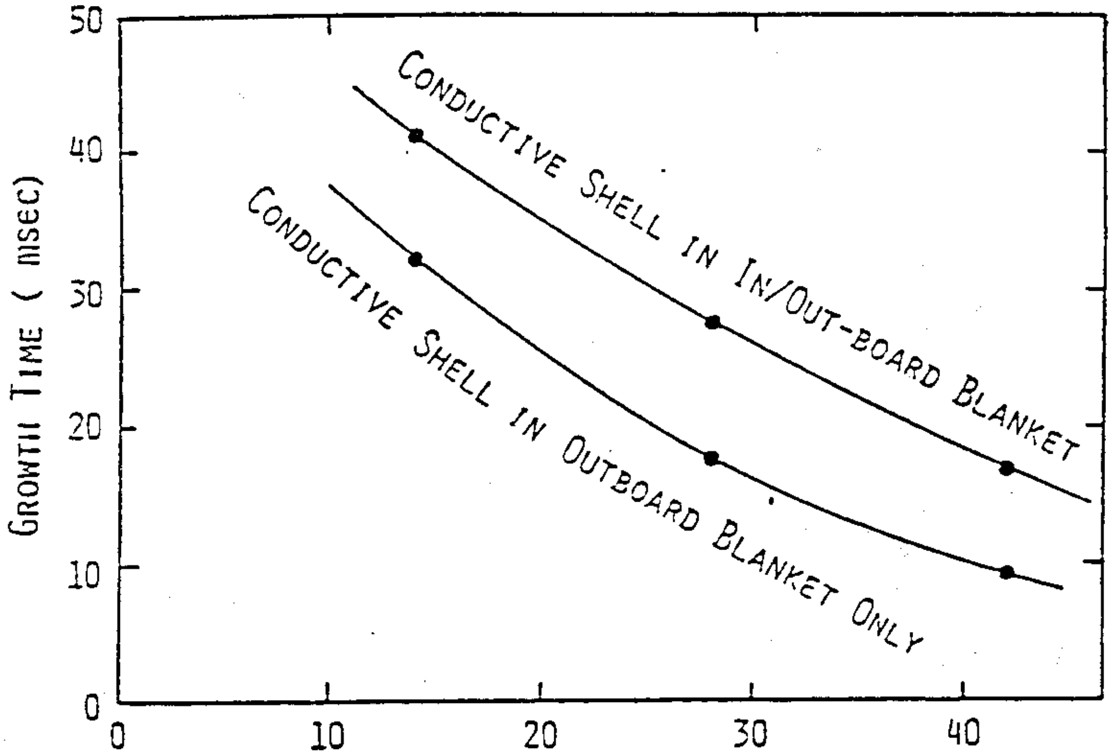

Fig. 2.2.11 Growth time vs. the number of shell segments.

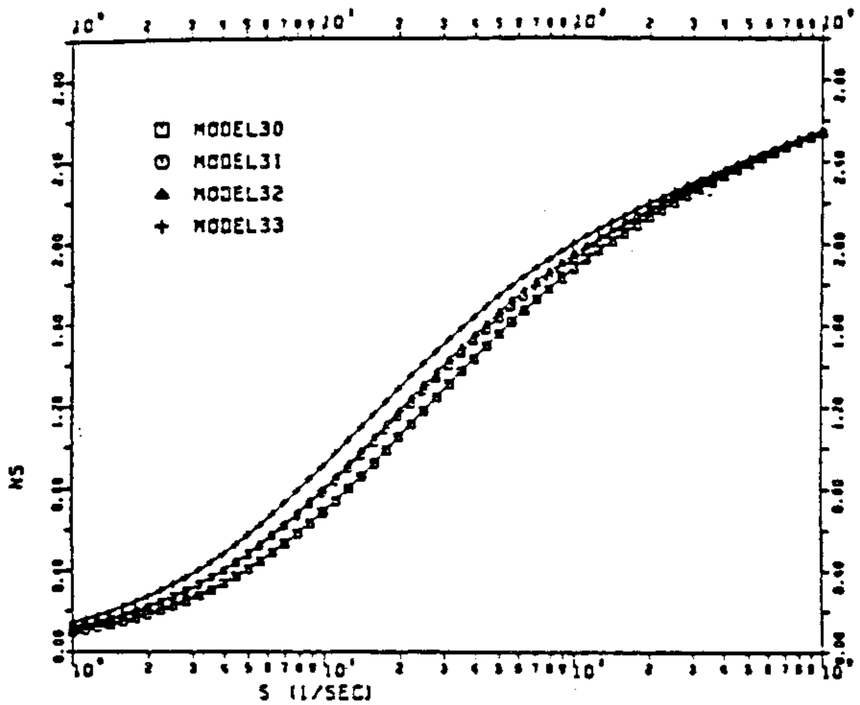

Fig. 2.2.12 N-function of conductive shell with parameter of shell thickness. Model 30, 31, 32, 33 : Pb(60mm), Cu(15mm)/ Pb(100mm), Cu(15mm)/ Pb(60mm), Cu(22.5mm)/ Pb(100mm), Cu(22.5mm)

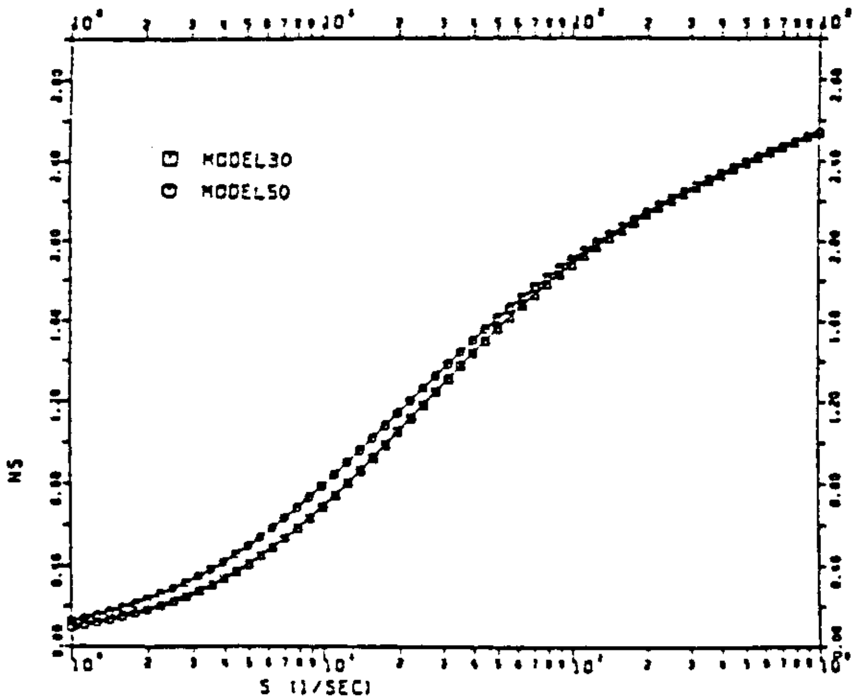

Fig. 2.2.13 Comparison of the N-function between the conductive shell with and without end shell.
Model 30, 50 : with end shell, without end shell

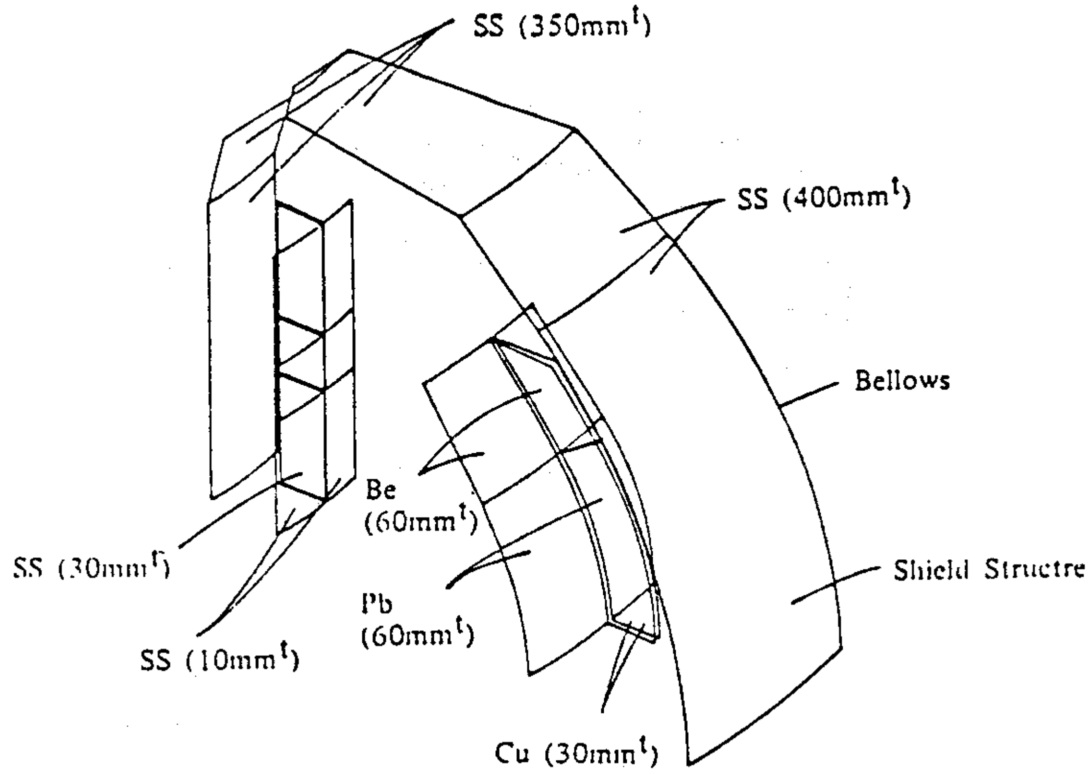

Fig. 2.2.14 Reference shell structure

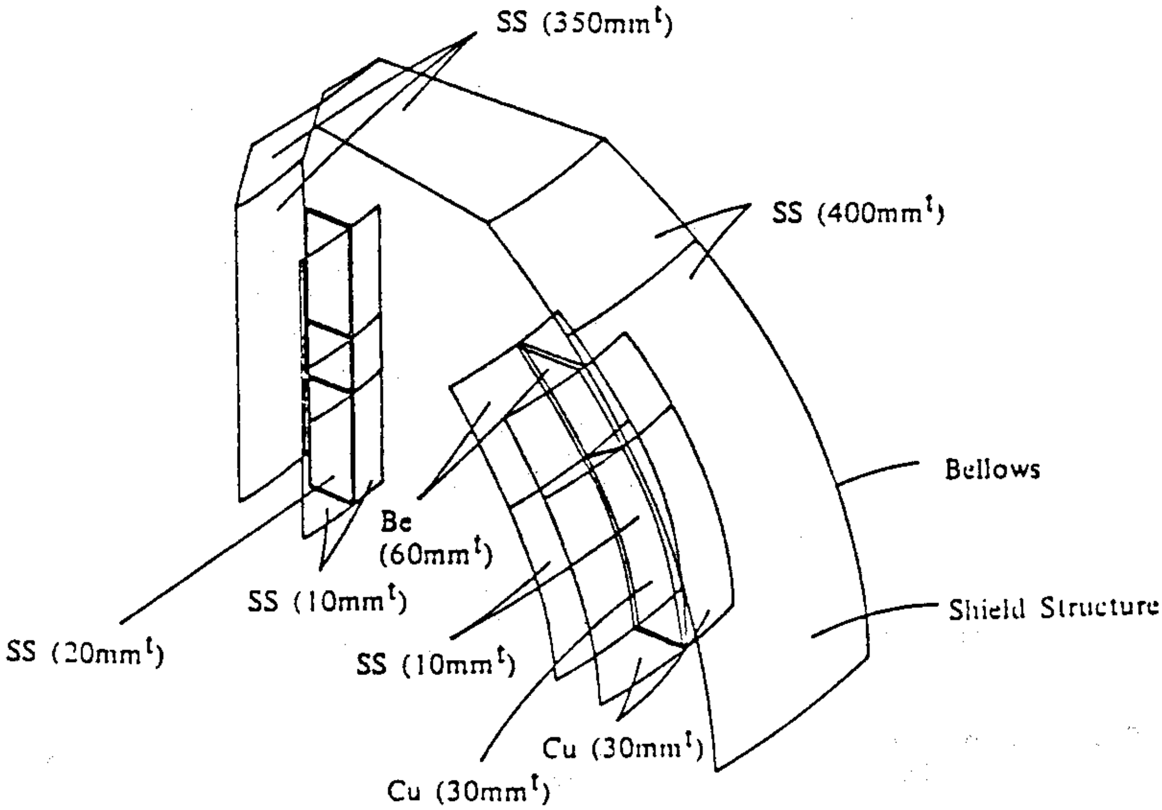

Fig. 2.2.15 Alternative shell structure

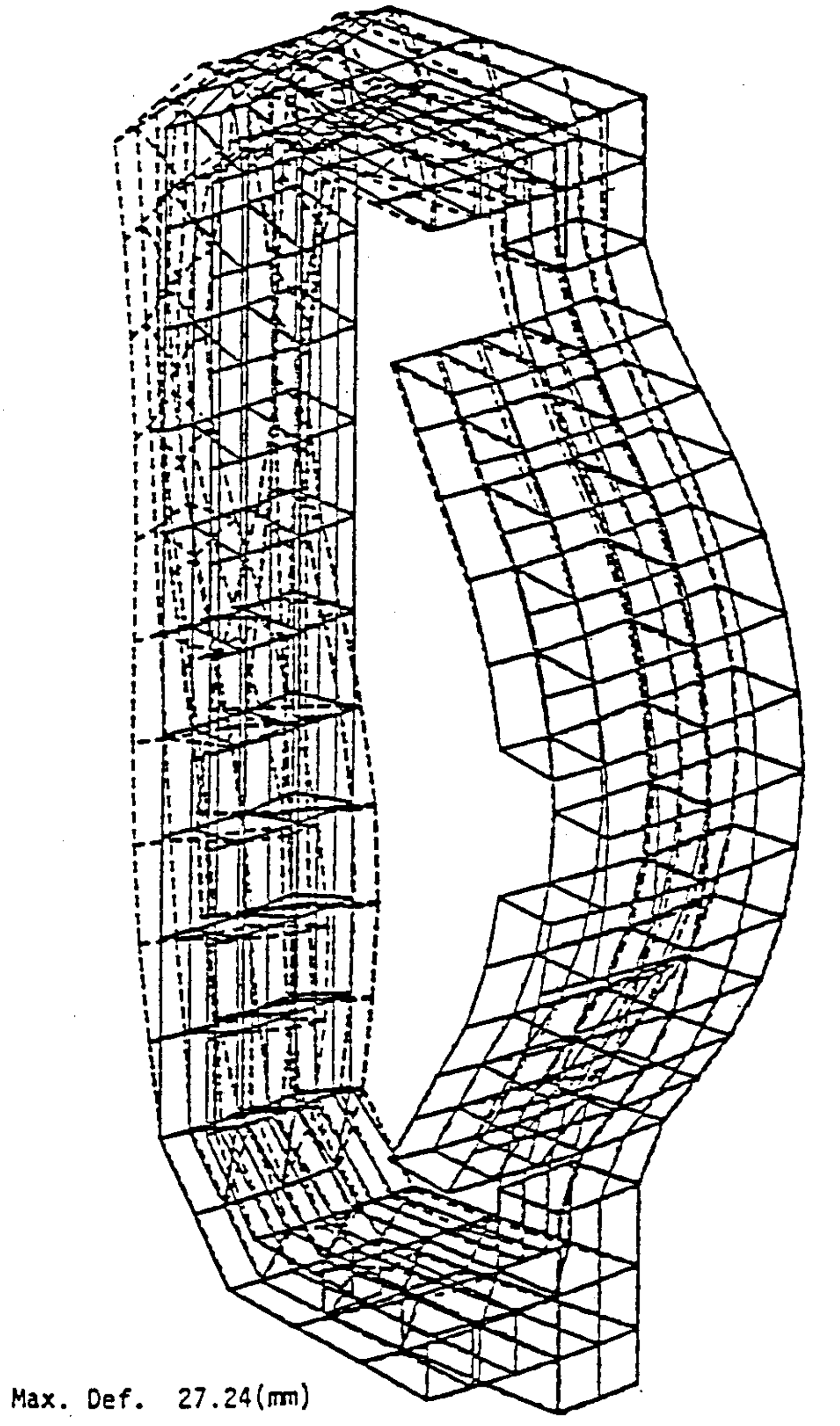

Fig. 2.2.16 Deformation of blanket structure with inboard conductive shell, designed in previous year (FY' 82).

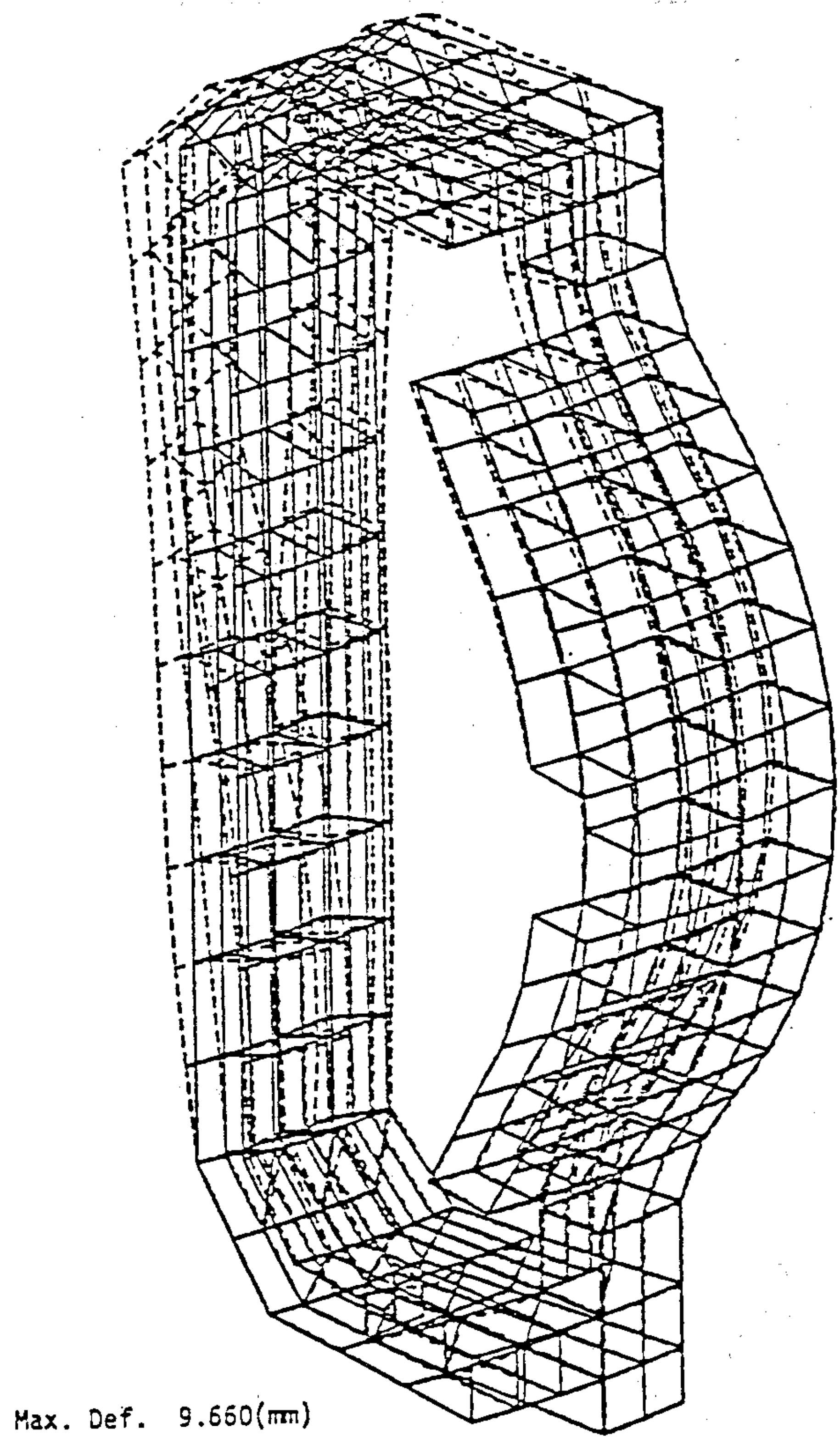

Fig. 2.2.17 Deformation of blanket structure without inboard conductive shell, designed in previous year (FY'82).

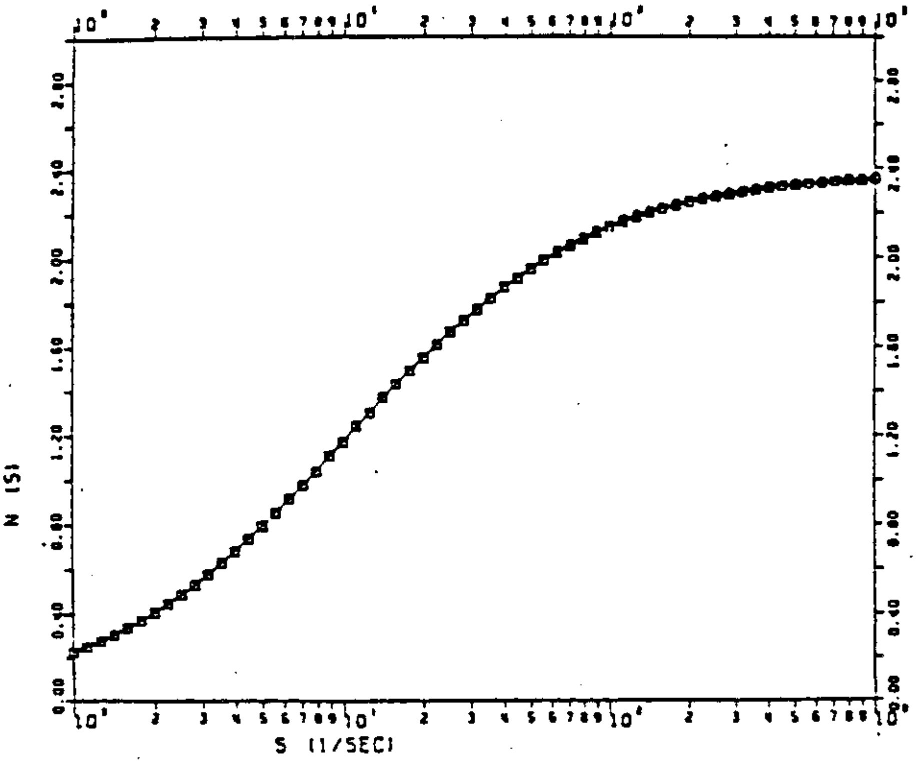

Fig. 2.2.18 N-function of reference shell structure.

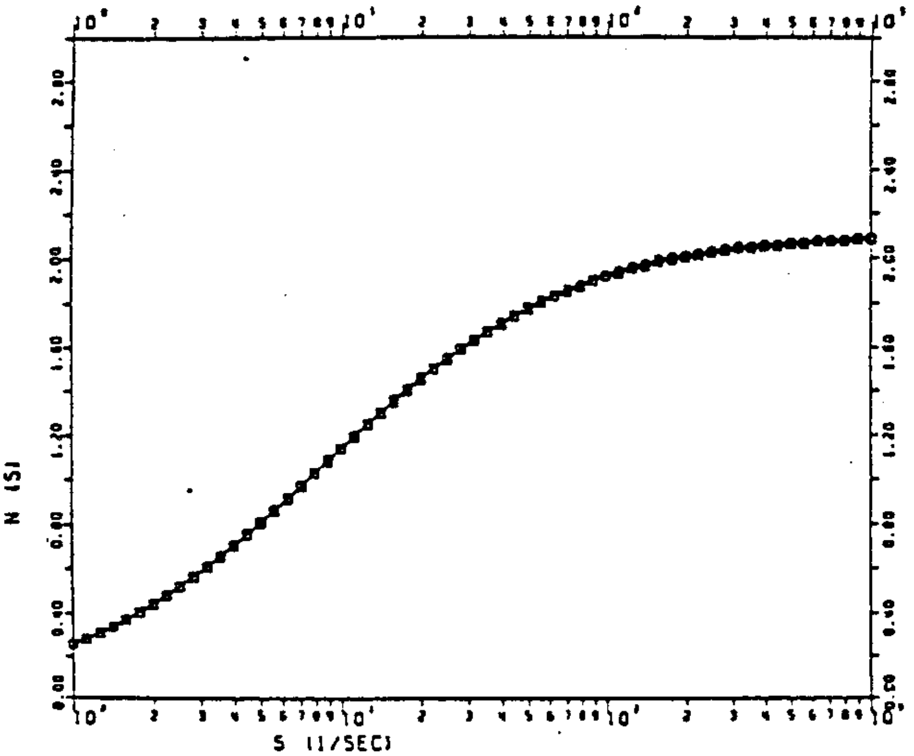

Fig. 2.2.19 N-function of alternative shell shellstructure.

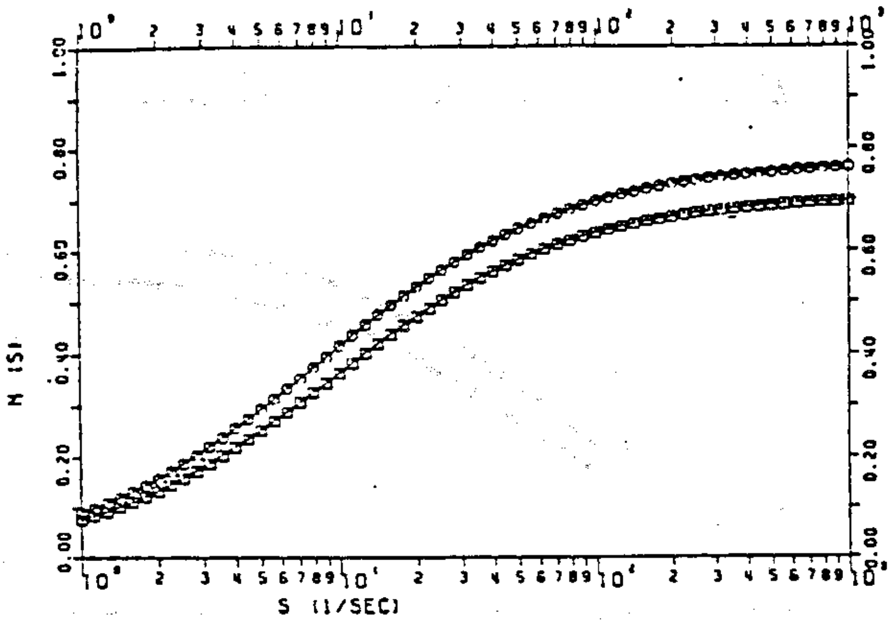

Fig. 2.2.20(a) Shielding function of reference shell structure.

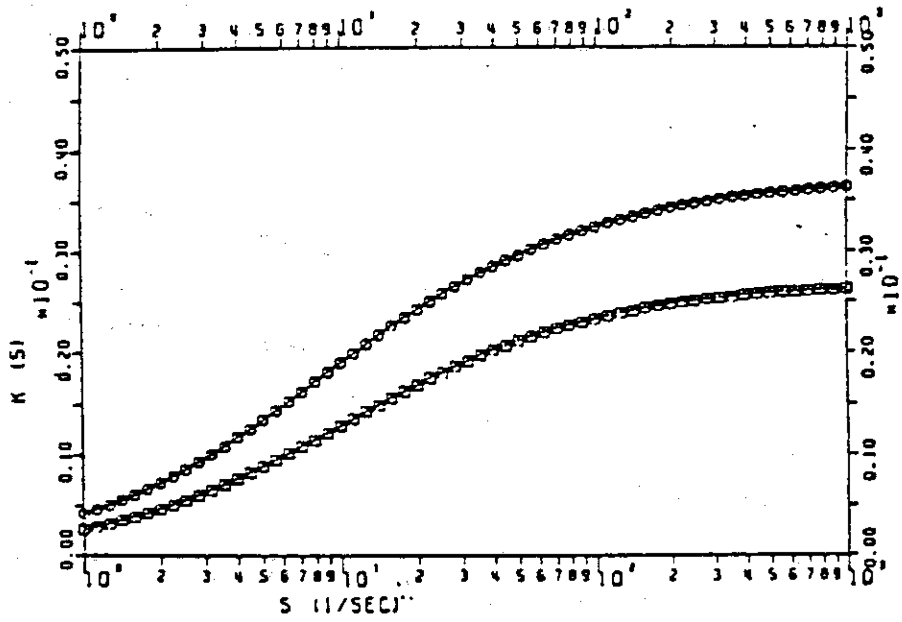

Fig. 2.2.20(b) Coupling function of reference shell structure.

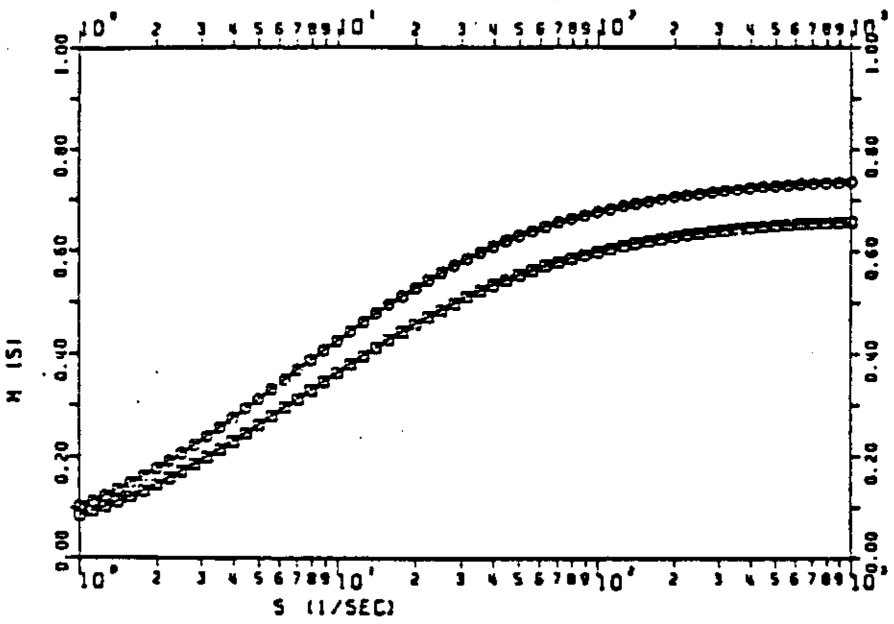

Fig. 2.2.21(a) Shielding function of alternative shell structure.

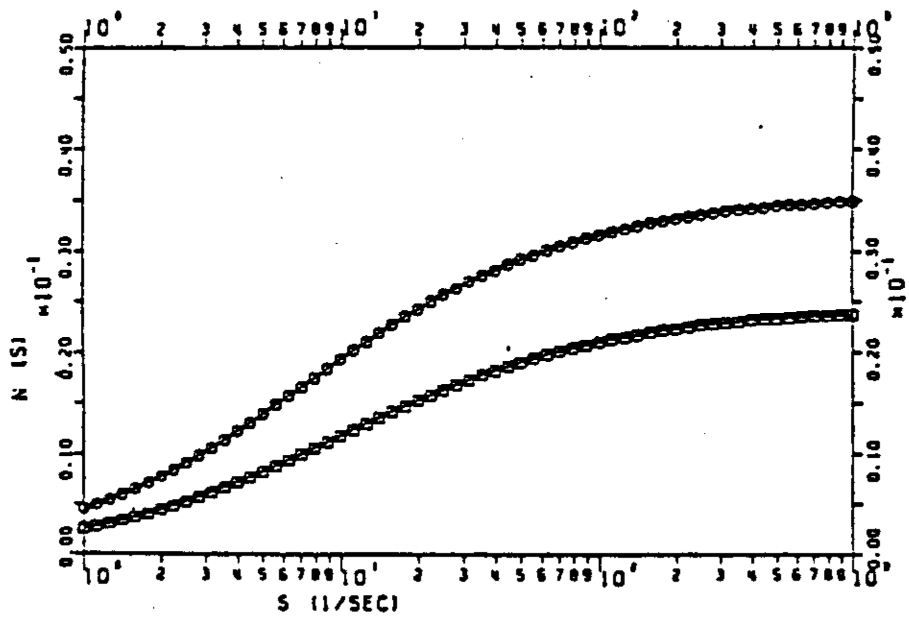

Fig. 2.2.21(b) Coupling function of alternative shell structure.

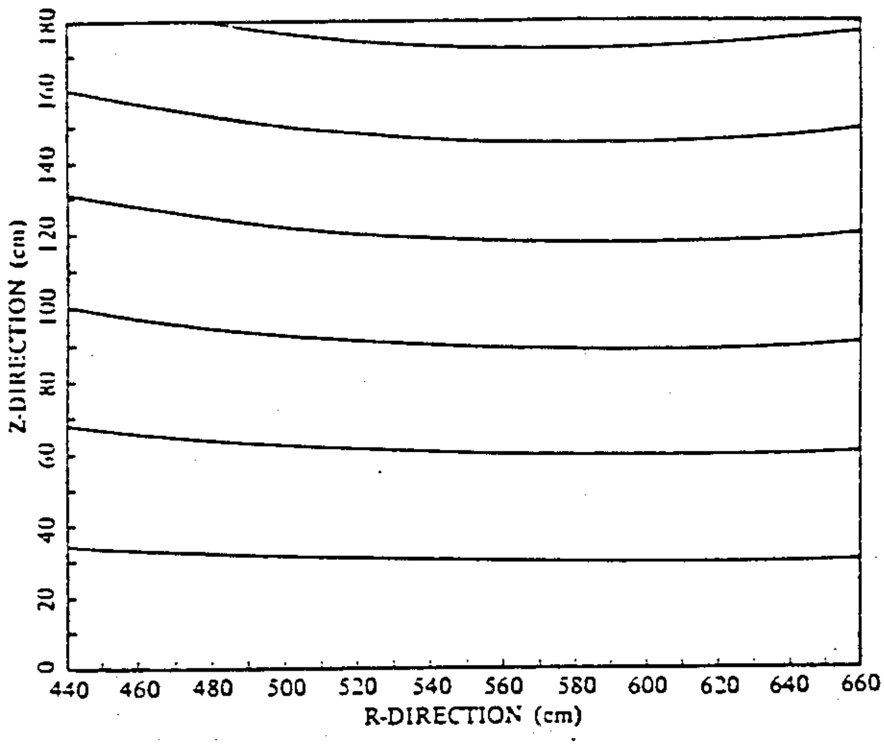

Fig. 2.2.22(a) Magnetic field configuration by control coil-A located at 3.5 m and ±6.15 m in the radial and vertical direction.

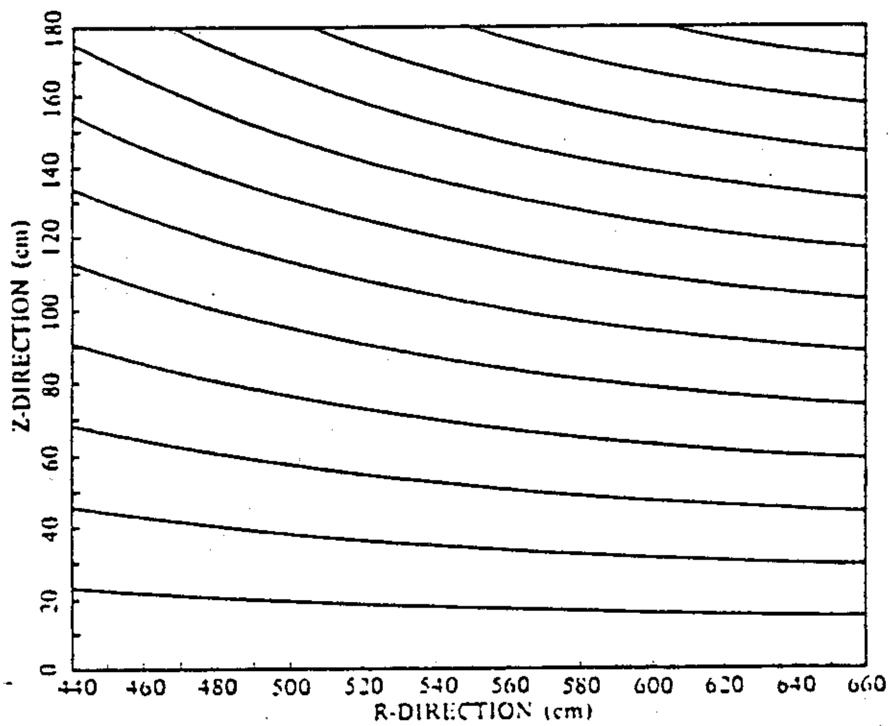

Fig. 2.2.22(b) Magnetic field configuration by control coil-B located at 5.7 m and ±6.5 m in the radial and vertical direction.

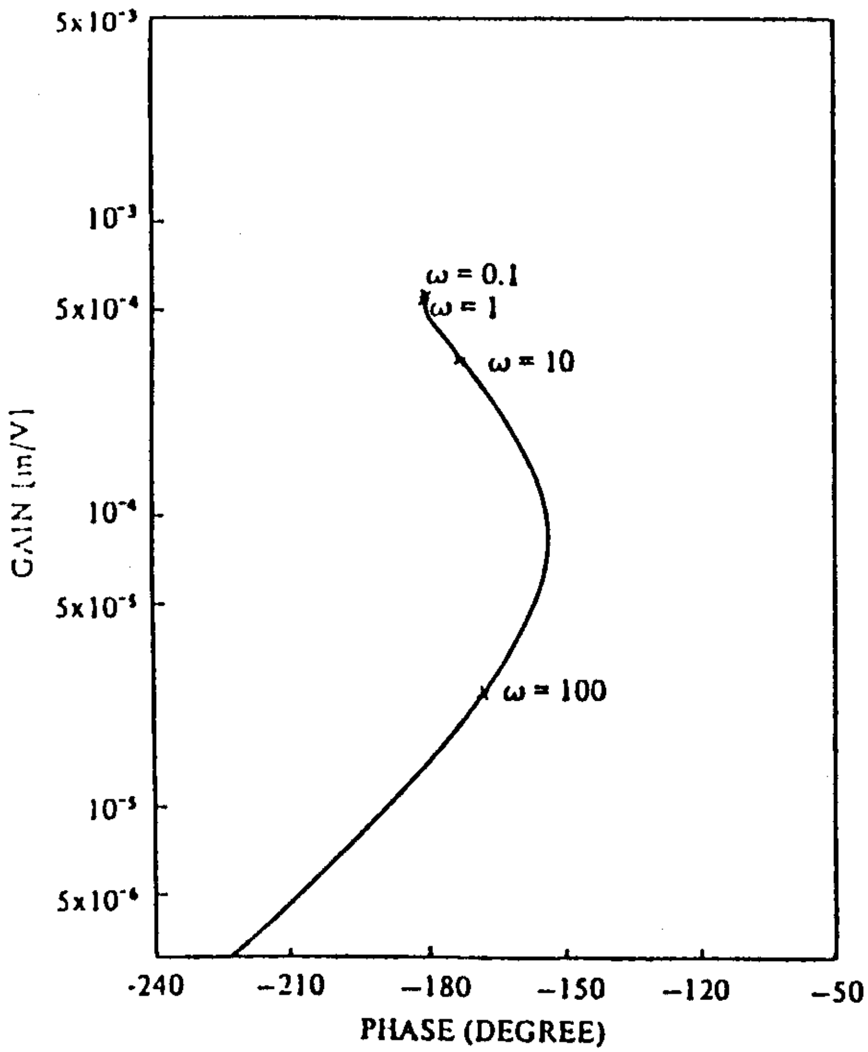

Fig. 2.2.23(a) Gain-phase diagram of open loop transfer function for P feedback control system with the reference shell structure and control coil-B.

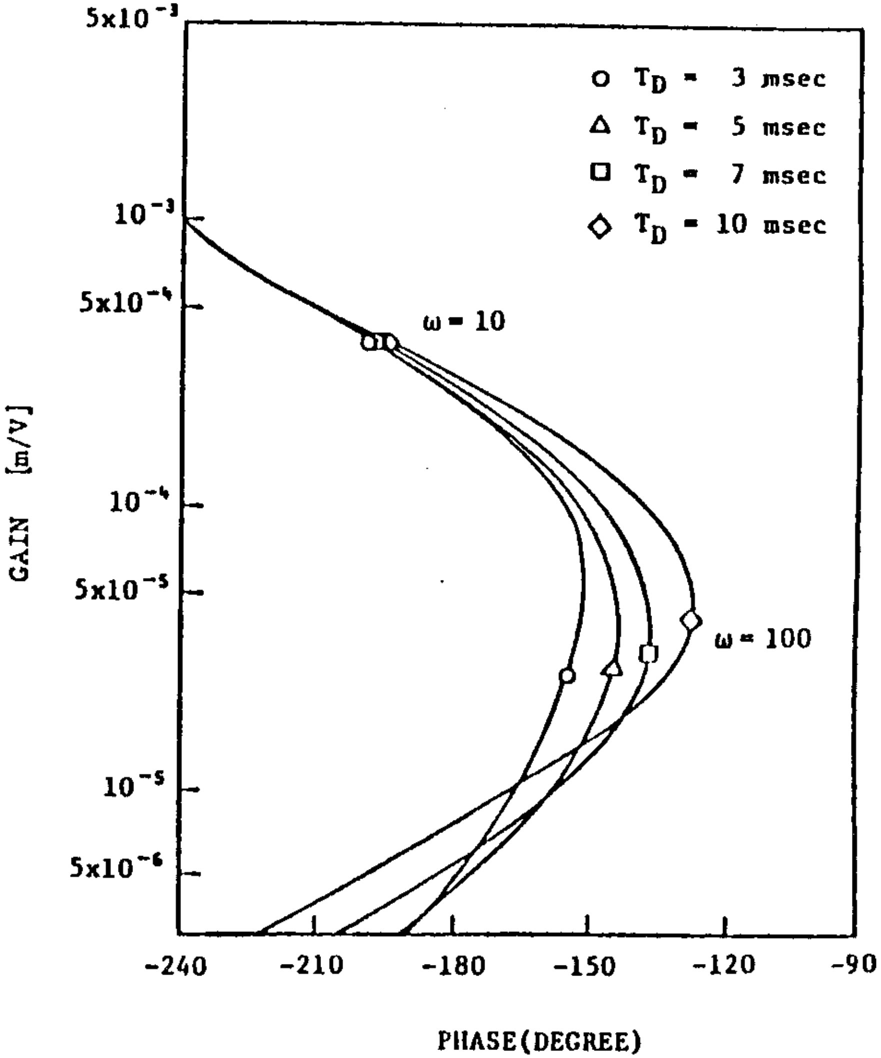

Fig. 2.2.23(b) Gain-phase diagram of open loop transfer function for PID feedback control system with the alternative shell structure and control coil-B.

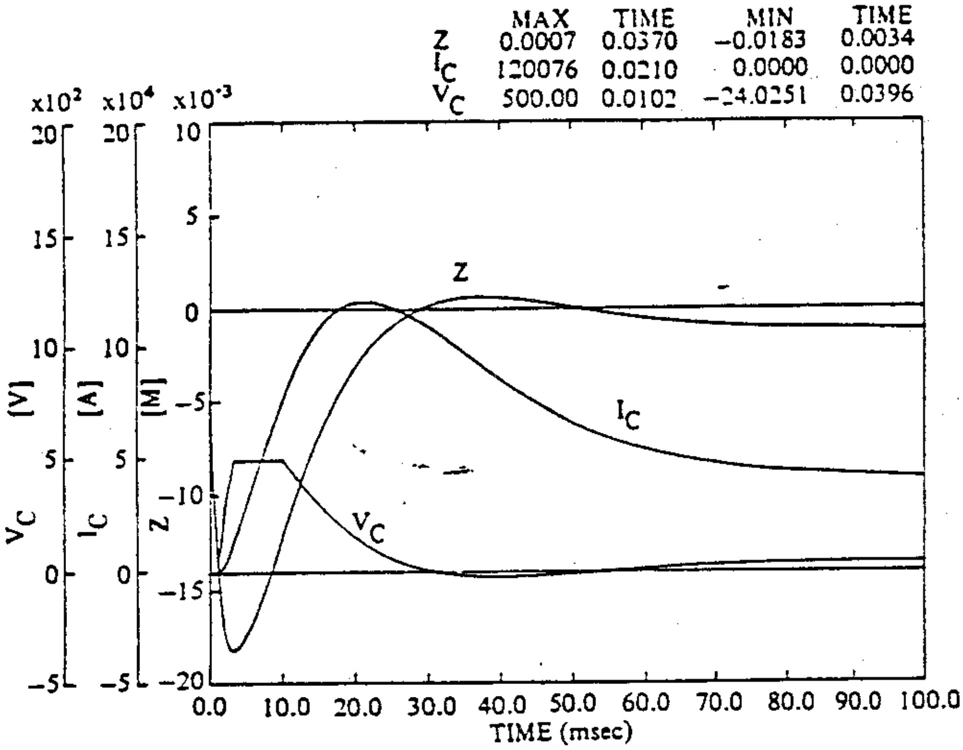

Fig. 2.2.24(a) Simuration result of plasma position control by P action with reference shell and control coil-B. G = 35000, V_L = ±500V, Power Supply Capacity : 60 MVA.

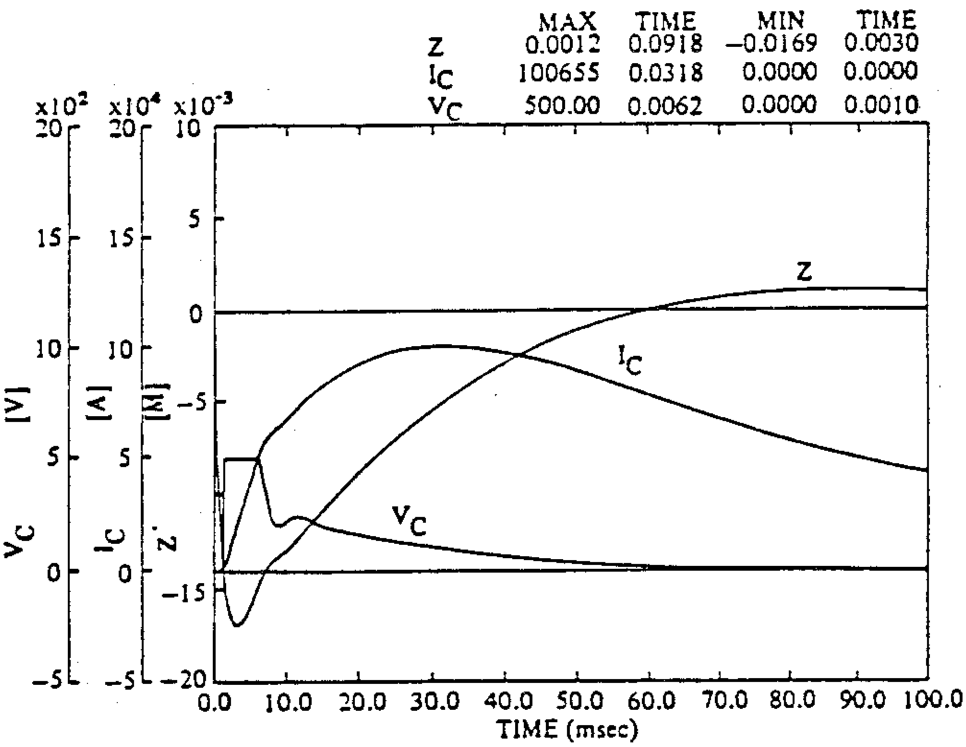

Fig. 2.2.24(b) Simuration result of plasma positon control by PID action with reference shell and control coil-B. G = 25000, T_I = 200 mesc, T_D = 10 mesc, V_L = ±500 V, Power Supply capacity : 50 MVA.

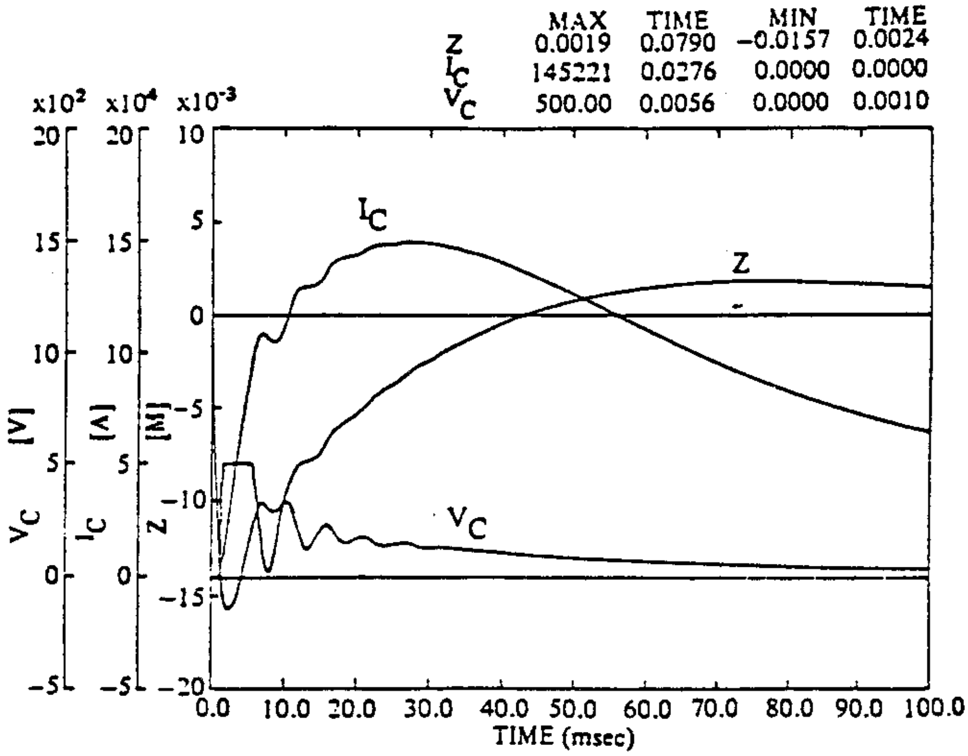

Fig. 2.2.24(c) Simulation result of plasma position control by PID action with reference shell and control coil-A. G = 30000, T_I = 50 msec, T_D = 10 msec, V_L = ±500 V, Power Supply Capacity : 75 MVA

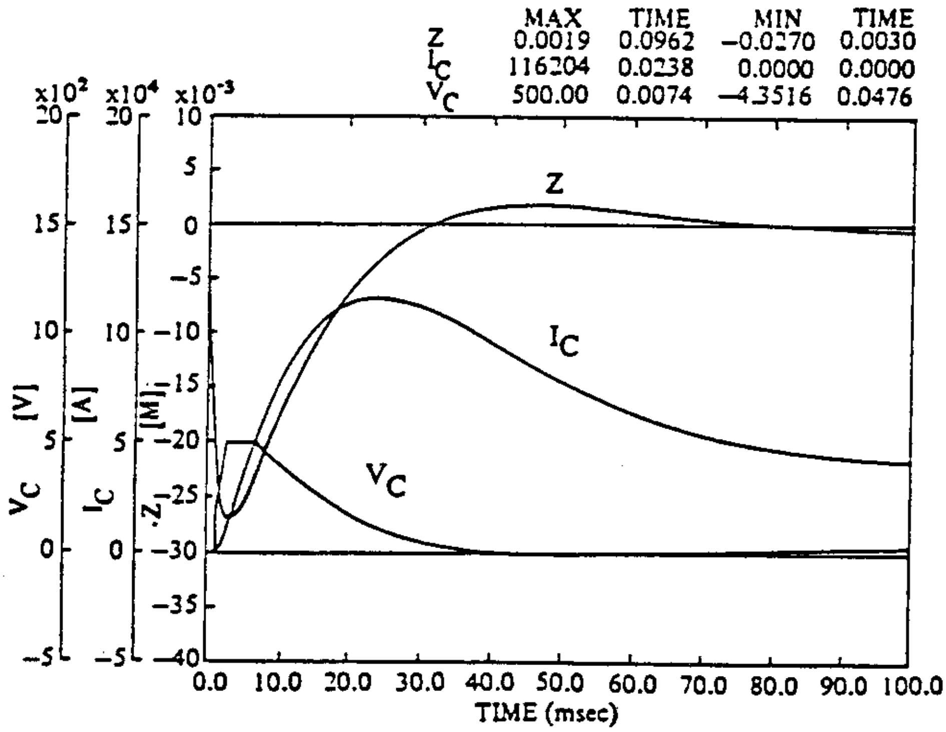

Fig. 2.2.24(d) Simuration result of plasma position control by PID action with alternative shell and control coil-B. G = 20000, T_I = 200 msec, T_D = 10 msec, V_L = ±500 V, Power Supply Capacity : 58 MVA.

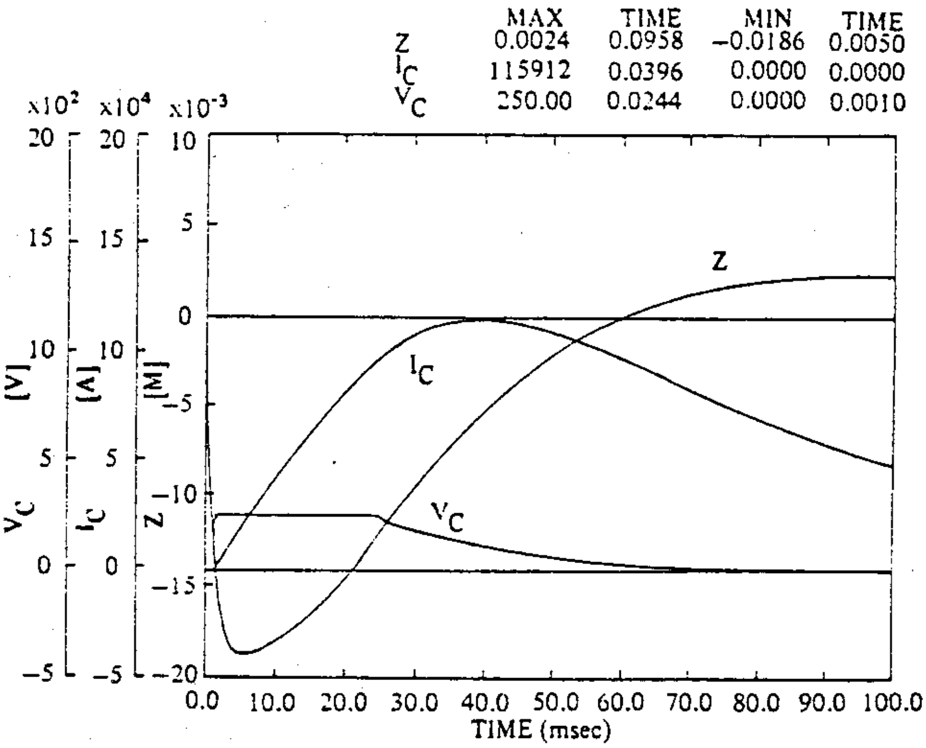

Fig. 2.2.25 Simuration result of plasma position control by PID action with reference shell and control coil-B. G =25000, T_I =200msec. T_D =10msec, V_L =±250V, Power Supply Capacity : 29 MVA.

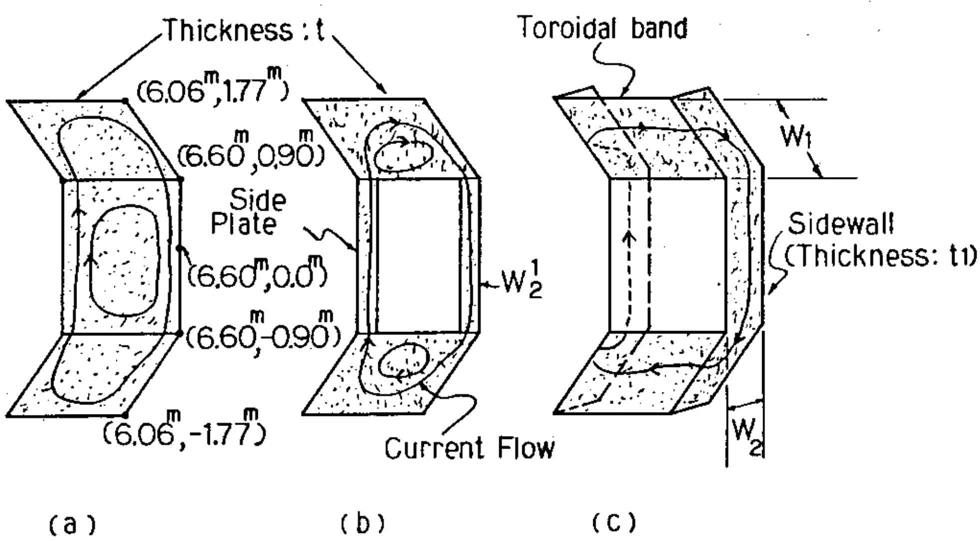

Fig. 2.2.26 Three kinds of shell structures

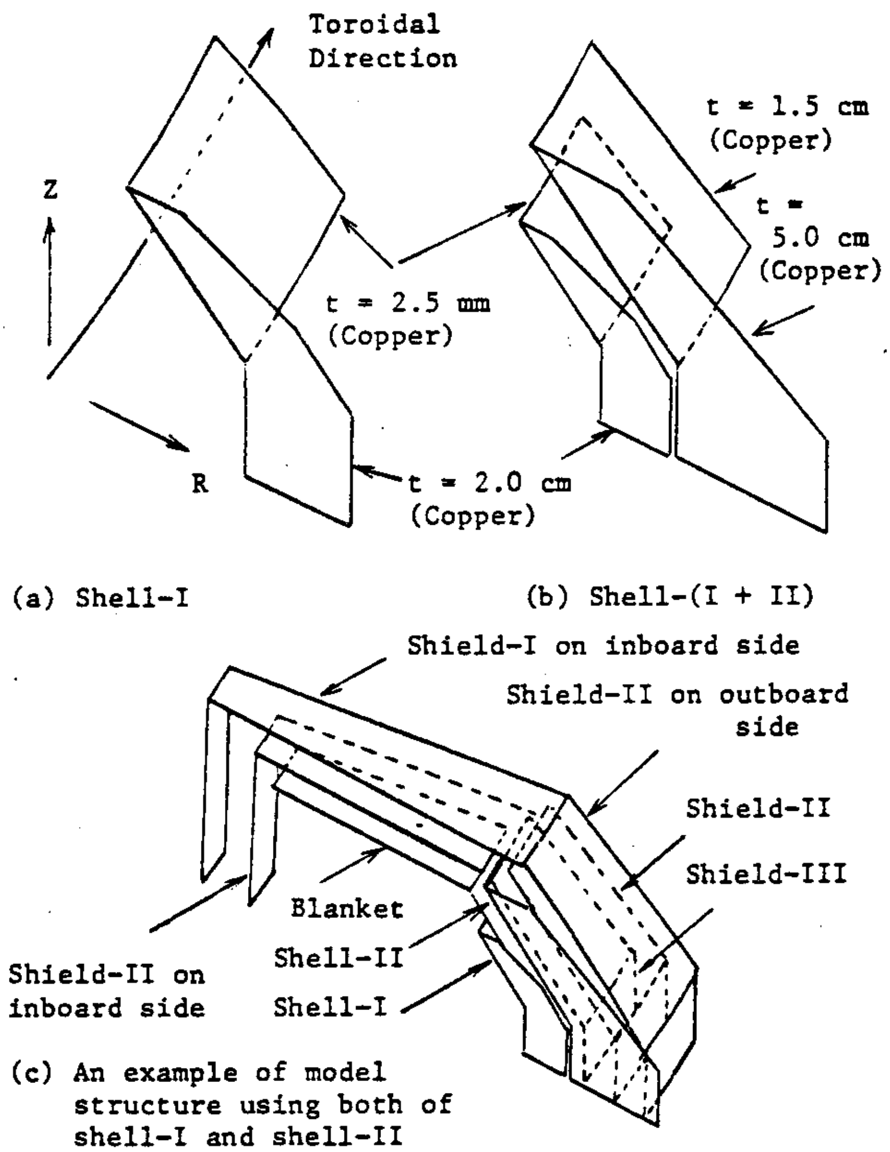

(a) Shell-I

(b) Shell-(I + II)

(c) An example of model structure using both of shell-I and shell-II

Fig. 2.2.27 A simplified model of the INTOR

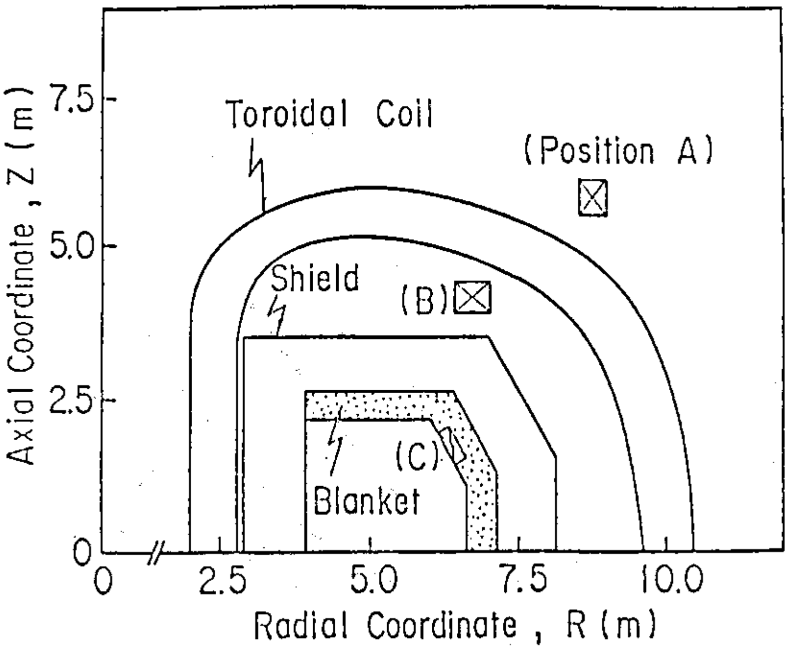

Fig. 2.2.28 Three candidates for the coil location of vertical position control

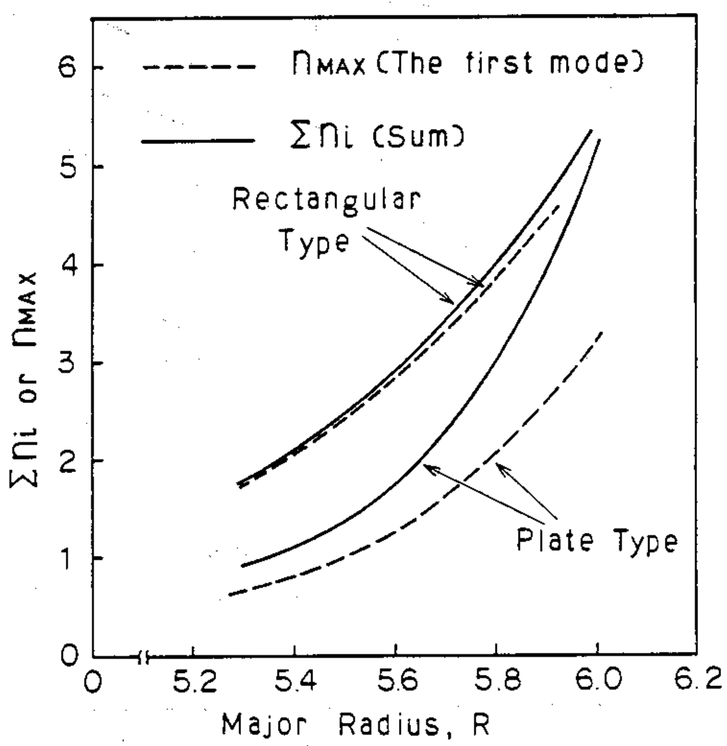

Fig. 2.2.29 Σn_i and n_{MAX} as a function of the radius position (Major Radius : R) of the filament of the filamentary model on both cases of (a) and (c) in Fig.2.2.26

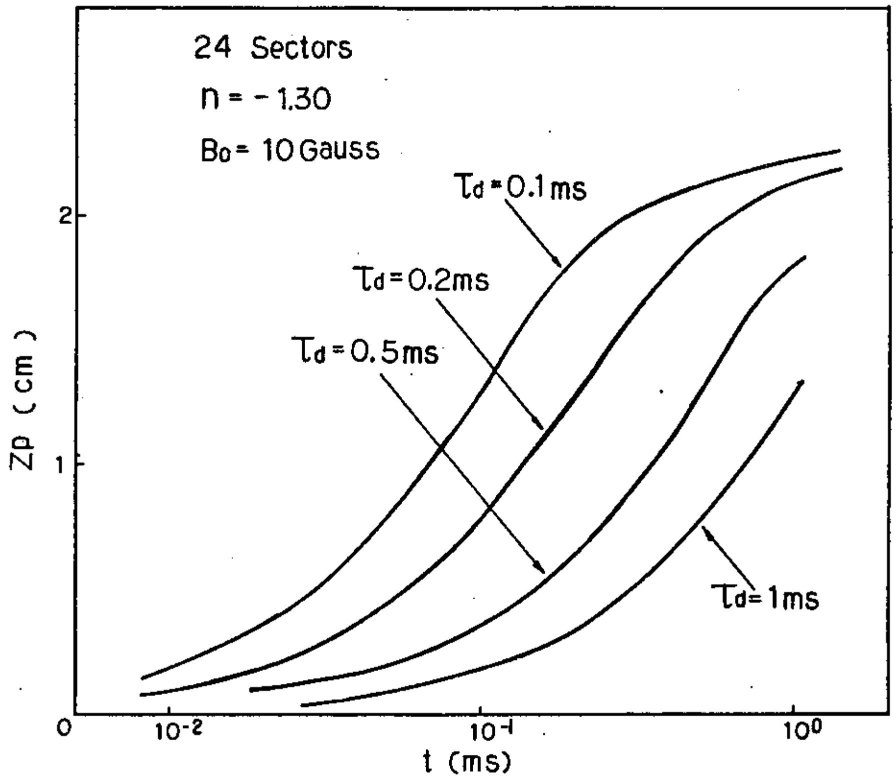

Fig. 2.2.30 Z_p as a function of τ_d with the disturbance field

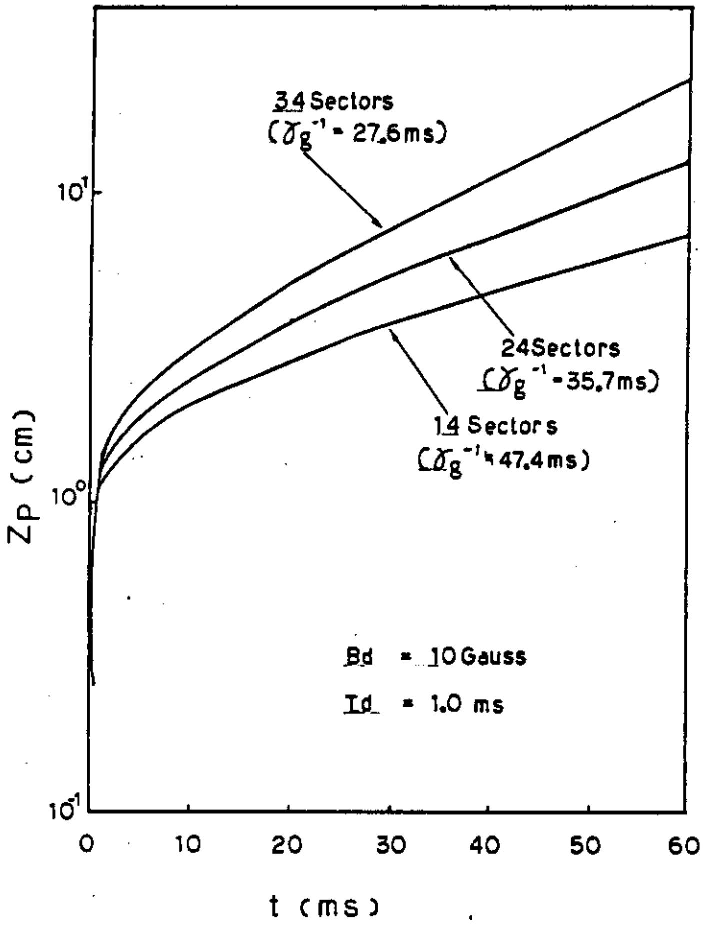

Fig. 2.2.31 Shell effect as a function of the number of toroidally divided sectors

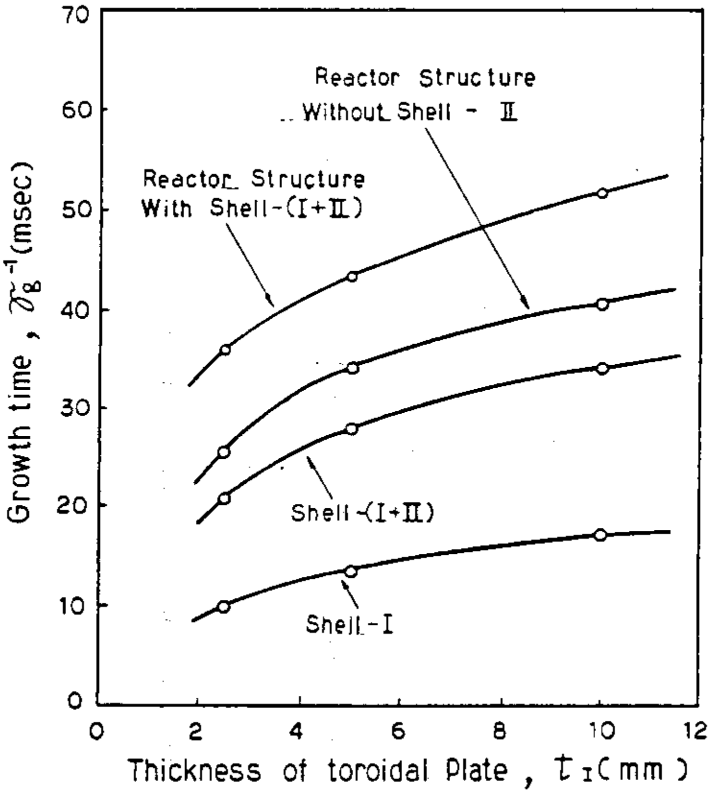

Fig. 2.2.32 Instability growth time as a funtion of the thickness of toroidal plate with the shell-I

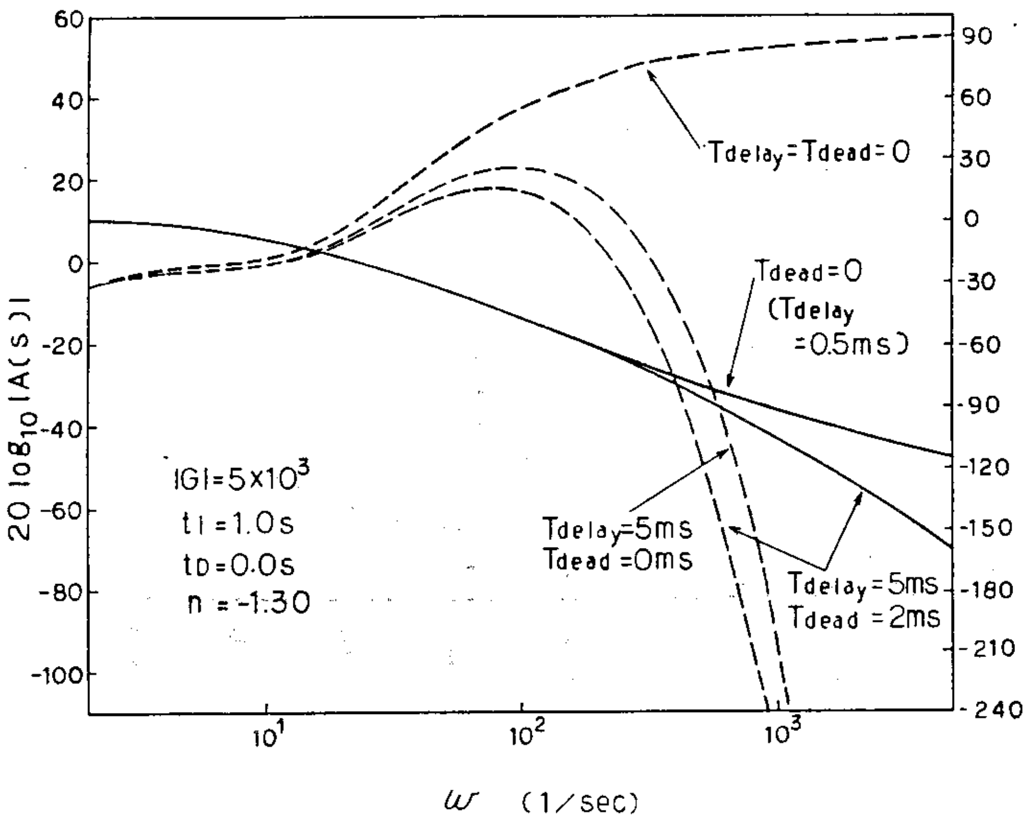

Fig. 2.2.33 Bode diagram with the PI controller

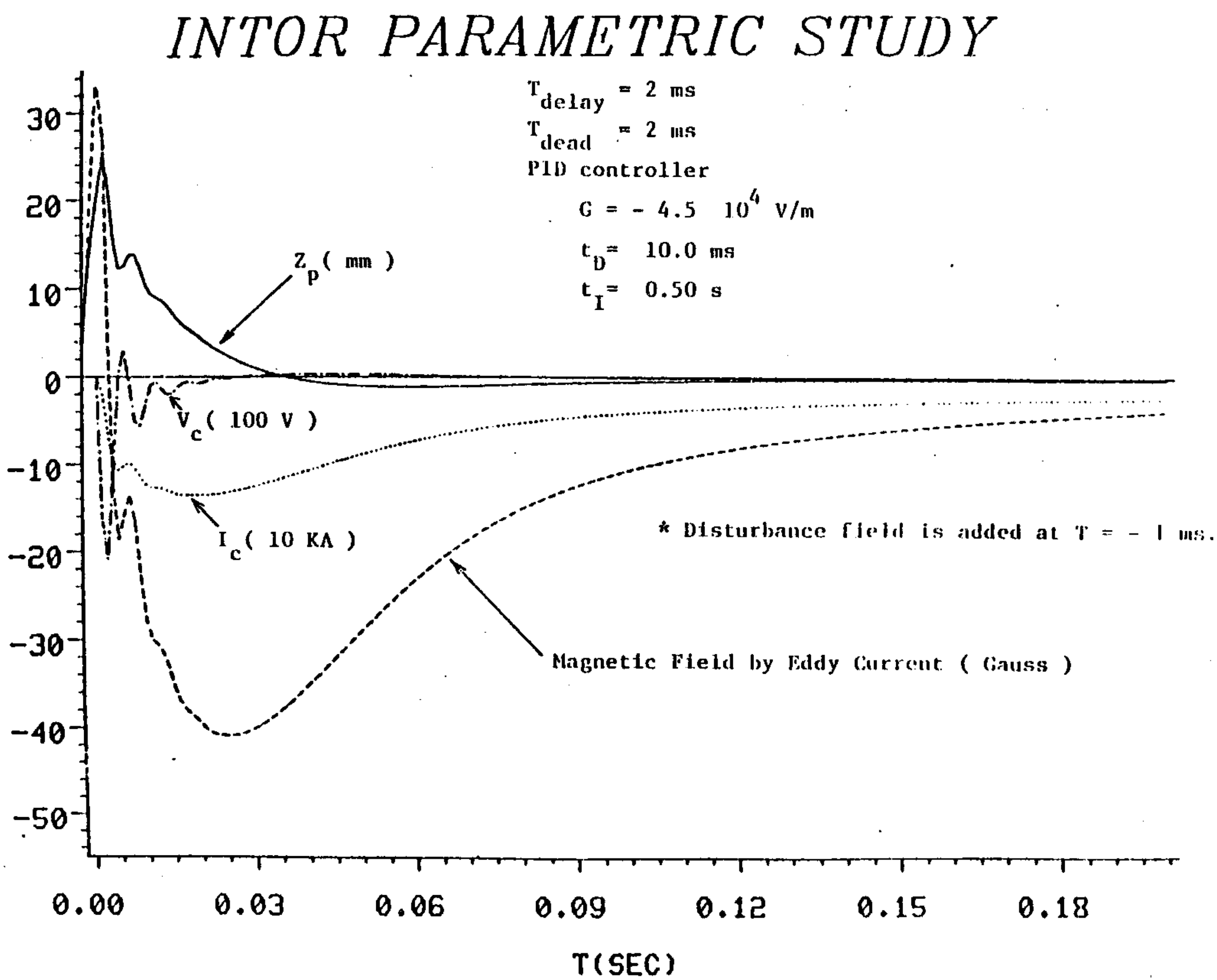

Fig. 2.2.34 A typical example of the vertical position control

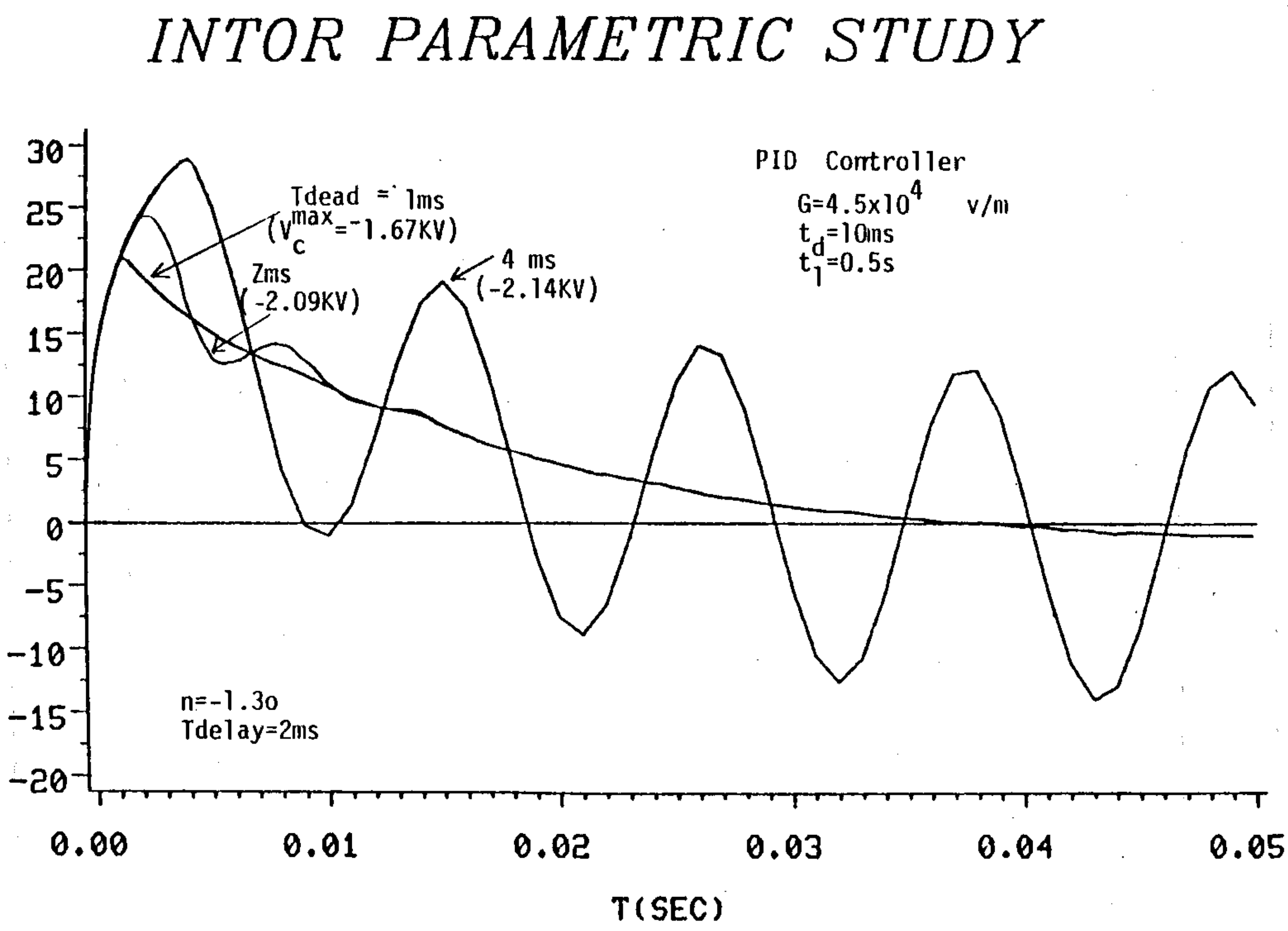

Fig. 2.2.35 Dependence of the position control characteristics upon the dead time of power supply

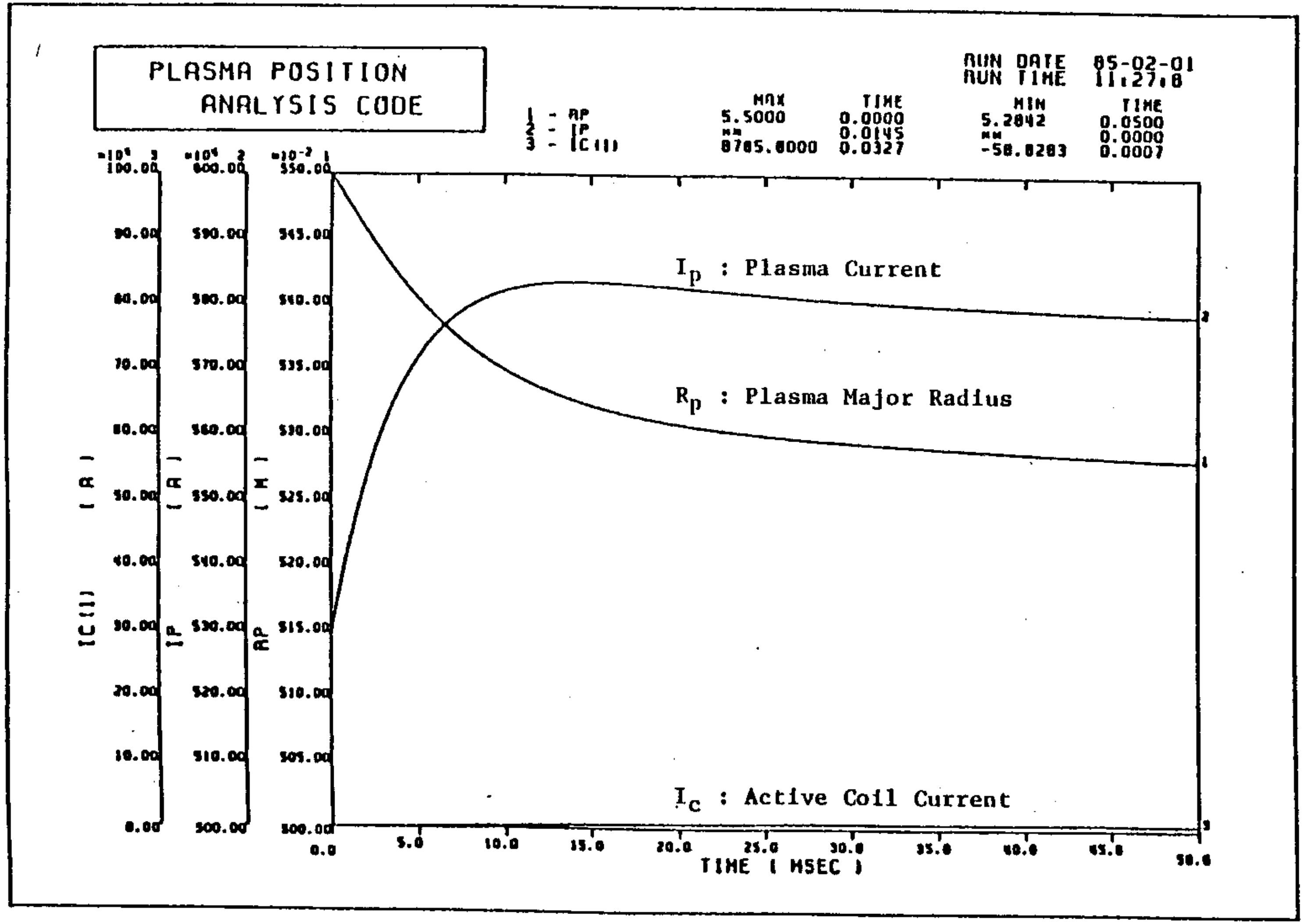

Fig. 2.3.1 Simulation result of plasma radial movement without feedback control. High conductive shells are installed in blanket modules for plasma vertical position control. β_p and ℓ_i are reduced by 40 % with a time constant of 5 msec.

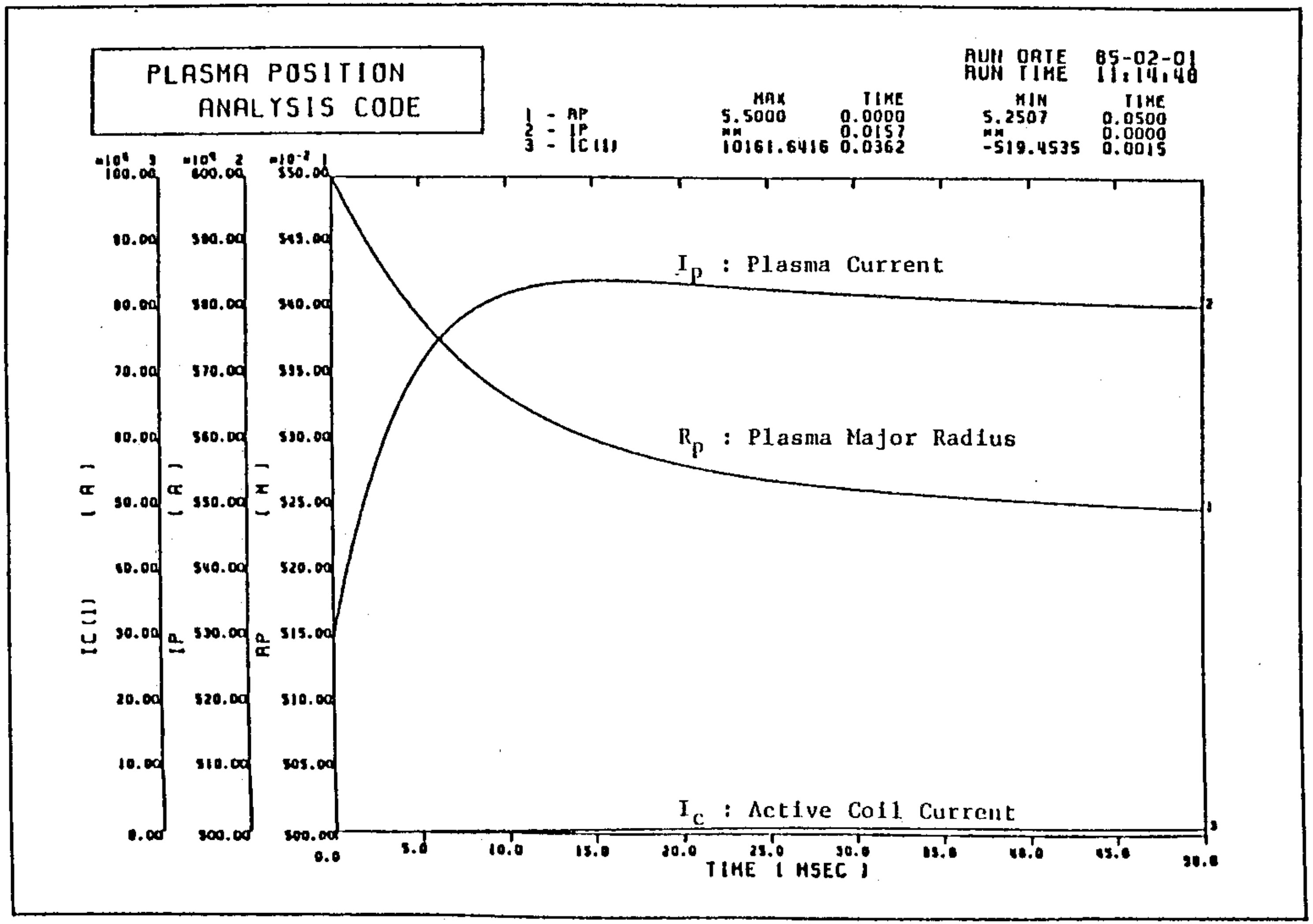

Fig. 2.3.2 Simulation result of plasma radial movement without feedback control. Conductive shells are not installed in blanket modules. Perturbation conditions are the same as those in figure 2.3.1 .

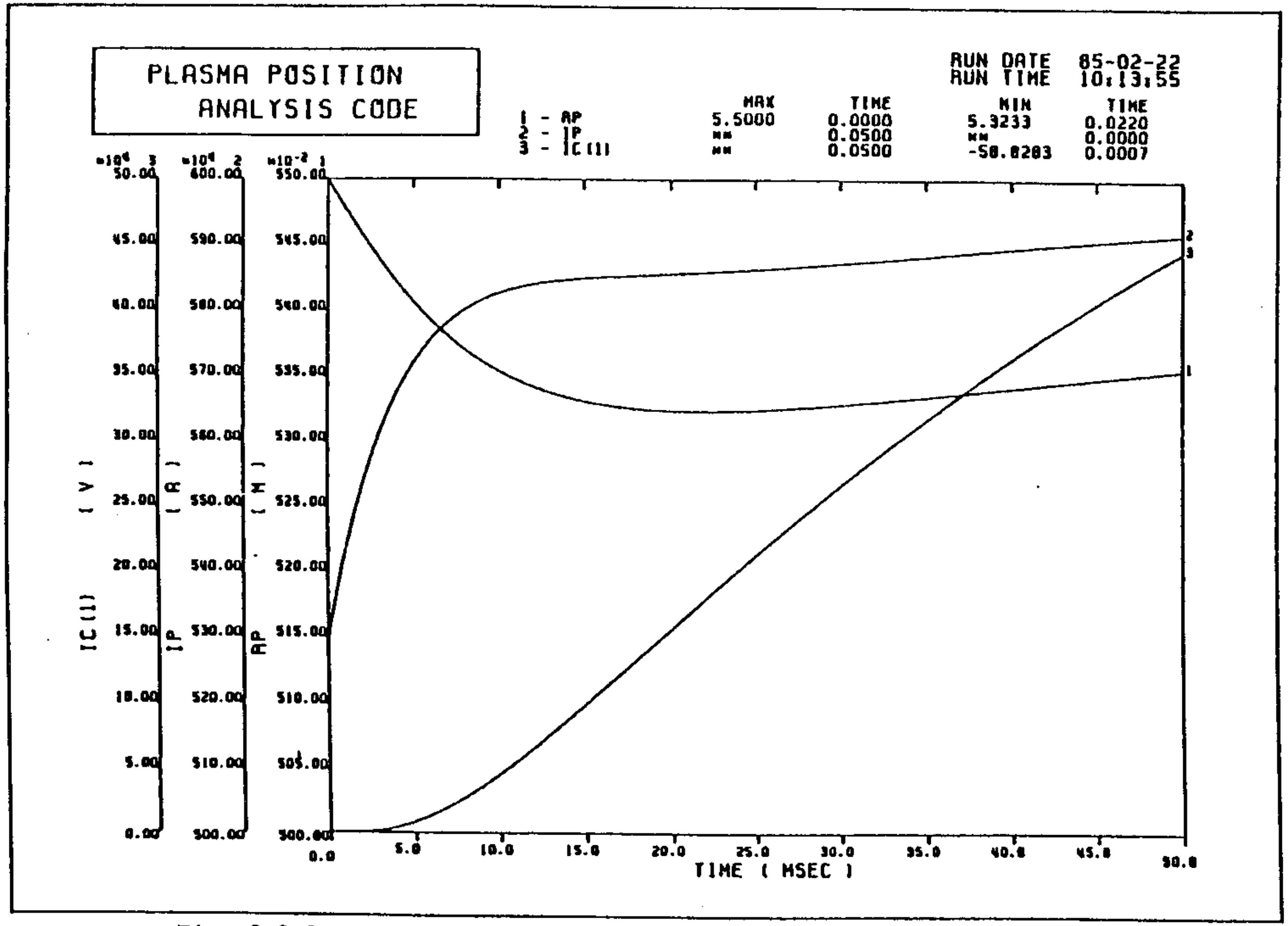

Fig. 2.3.3 Simulation result of plasma radial position control by P action. High conductive shells are installed in blanket modules for plasma vertical position control. Perturbation conditions are the same as those in figure 2.3.1.
Max. Coil Voltage: 4400 V, Max. Coil Current: 450 kA,
Max. Power: 2000 MVA.

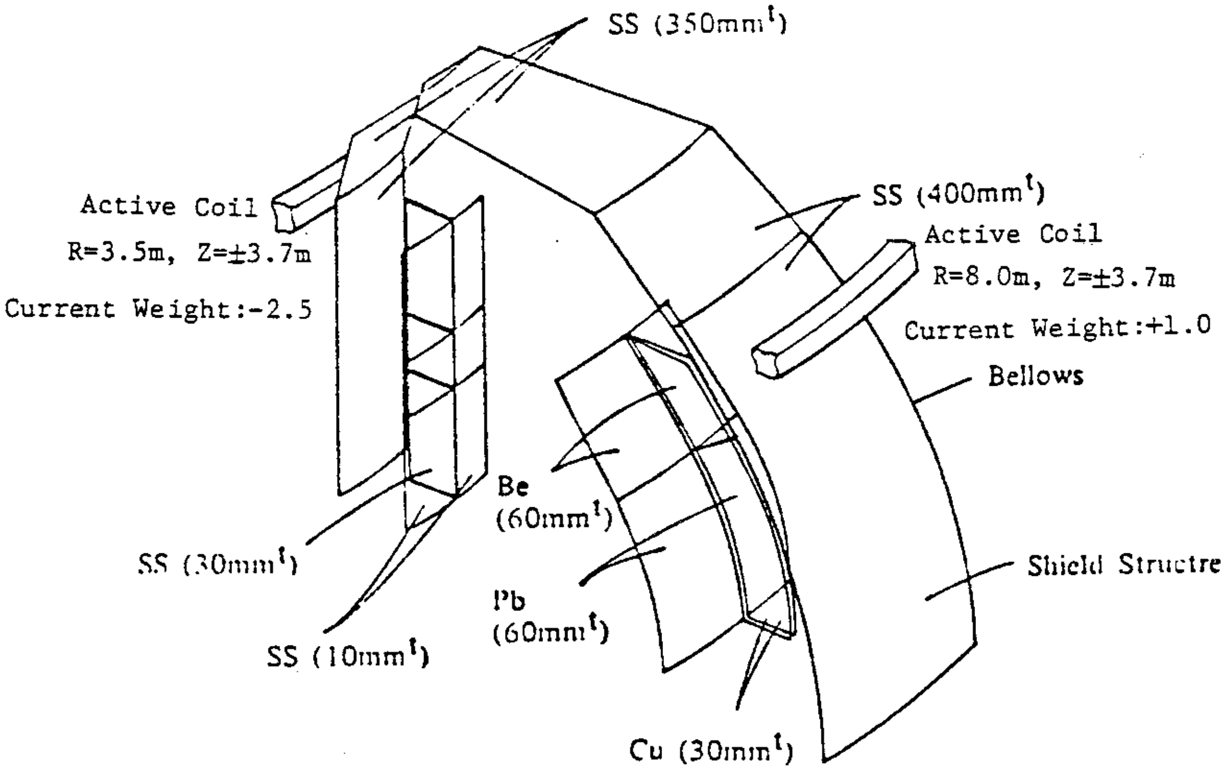

Fig. 2.3.4 Model of feedback control system for plasma radial position.

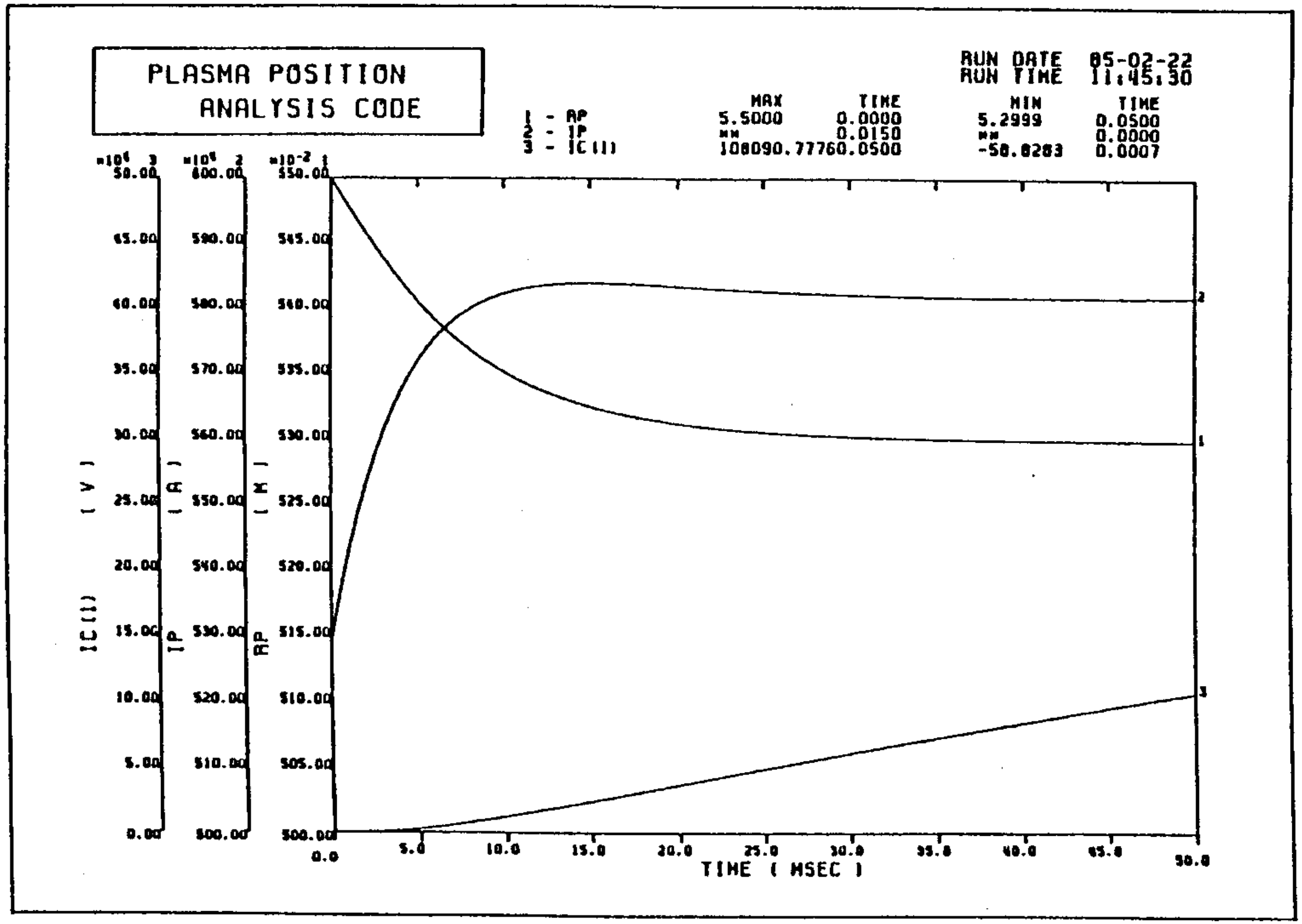

Fig. 2.3.5 Simulation result of plasma radial position control by P action. High conductive shells are installed in blanket modules for plasma vertical position control. Perturbation conditions are the same as those in figure 2.3.1.
Max. Coil Voltage: 1000 V, Max. Coil Current: 110 kA,
Max. Power: 110 MVA.

3. Start-up Effects

3.1 Magnetic and Electrical Field Penetration

In future tokamak reactors, plasmas are surrounded by mutiple layers such as first wall, blanket, shield, coil vacuum chamber and toroidal field magent including shear panels. This multilayer structure will prevent fast penetration of magnetic and electrical field at start-up phase.

The magnetic field and loop voltage applied to plasma are reduced by eddy currents and represented by eqs. (3.1.1) and (3.1.2), respectively, using Laplace transform as described in section 2.3.

$$B_v(s) = \frac{M'_{pc} I_c}{2\pi R_p} \{1 - M(s)\} \qquad (3.1.1)$$

$$V_p(s) = -M_{pOH} s I_{OH} \{1 - V(s)\} \qquad (3.1.2)$$

$$M(s) = \sum_k \frac{s\tau_k}{1+s\tau_k} m_k, \quad m_k = \frac{M'_{pk} M_{ck}}{M'_{pc} \tau_k}$$

$$V(s) = \sum_k \frac{s\tau_k}{1+s\tau_k} v_k, \quad v_k = \frac{M_{pk} M_{OHK}}{M_{pOH} \tau_k}$$

where, M_{pk} : mutual inductance between plasma and k-th eddy current mode

M_{ck} : mutual inductance between magnetic field coil and k-th eddy current mode

M_{pOH}: mutual inductance between plasma and OH coil

M_{OHk}: mutual inductance between OH coil and k-th eddy current mode

τ_k : time constant of k th eddy current mode

M' : derivative of mutual inductance

I_c : Laplace transform of magnetic field coil current

I_{OH} : Laplace transform of ohmic coil current decay rate

When plasma is perfectly surrounded by conductive structures and coils are located outside the structures, $M(s\to\infty)$ and $V(s\to\infty)$ are equal to one. So the fields are completely shielded at t = 0.

Magnetic field penetration

Figures 3.1.1 and 3.1.2 show M(s) of JAERI FER system. The comparison between the cases with and without high conductive shells is represented in Fig. 3.1.1, and the effect of one turn resistance is shown in Fig. 3.1.2. The configuration of passive elements is shown in Fig. 3.1.3. The presence of high conductive shells does not largely affect the shielding effect, M(s), since the high conductive shells does not perfectly enclose the plasma. On the other hand, the M(s) depends strongly on one turn resistance of radiation shield/coil vacuum chamber. This result suggests that the radial magnetic field for plasma vertical position control will be shielded by radiation shield/coil vacuum chamber, and the control property will be deteriorated, if the active coils are located outside the toroidal field coils, and toroidal one turn resistance will not be required because of plasma current ramp up by LHRF current drive. On the other hand, low one turn resistance of radiation shield/coil vacuum chamber will improve the property of stabilizing plasma vertical position instability, whether the control property of feedback system will be improved or not depends on which property (shielding property or stabilizing property) is effective to the overall control property. Figure 3.1.4 shows the gain-phase diagrams of the feedback control system of the JAERI FER. The curve (s) is the diagram for the standard case that one turn toroidal resistance is 0.2 mΩ. In curves (b) and (c), the shield/coil chamber has no bellows and toroidal high electric conductance. The effective thickness of the shield/coil chamber is 35 ∿ 40 cm in curves (a) and (b). In order to analyze the case that the active coils are located between shield/coil chamber and toroidal field coils, the effective thickness is set at 10 cm. A large gain value is required for feedback control when the shield/coil chamber has high electric conductance in the toroidal direction, though low one turn resistance expands the stable range of feedback controller where the phase is larger than -180 degrees when the gain in diagram is equal to one. This result suggests that the required power supply capacity of the active coils will be too large unless the active coils are located inside the shield/coil chamber. The toroidal one turn resistance of the order of 0.2 mΩ will be needed to avoid the difficulties to make the concept of active coils inside the shield compatible with other engineering problems such as remote maintenance, coil insulations, installations, space arrangements, etc.

Electrical field penetration

Assuming that plasma current is absent and ohmic heating coil current is linearly decreased, the loop voltage can be derived from eq. (3.1.2) as

$$V_p = -M_{pOH}\dot{I}_{OH}\,\{1 - \sum_k \frac{M_{pk}M_{OHK}}{M_{pOH}\tau_k}\, e^{-\frac{t}{\tau_k}}\} \qquad (3.1.3)$$

$$V_p^{Norm} = 1 - \sum_k \frac{M_{pk}M_{OHk}}{M_{pOH}\tau_k}\, e^{-\frac{t}{\tau_k}}$$

Figure 3.1.5 shows the normalized loop voltage, V_p^{Norm}, as a parameter of one turn bellow resistance. The penetration of loop voltage is largely delayed, when one turn bellow resistance is lower than approximately 0.1-0.2 mΩ.

Summarizing the magnetic and electrical field penetration, one turn resistance of approximately 0.2 mΩ is reasonable, when active coils are located outside the shield or plasma current is inductively ramped up by ohmic heating coils.

3.2 Components Specification

Components specification on one turn resistance in the toroidal direction, R_{loop} depends on the basic concept and design choice such as the scenario of plasma current ramp up and the selection of active coil locations. One turn toroidal resistance of approximately 0.2mΩ will be required unless plasma current is ramped up by non inductive method such as LHRF current drive for all operation phases including early stage operations, or if active control coils are located outside radiation shield/coil vacuum chamber. Summerizing components specification, two choices can be considered from the view point of field penetration as shown in Table 3.2.1.

Table 3.2.1 Components Specification

	Inductive I_p Rise	Noninductive I_p Rise
One-turn Resistance	∿ 0.2mΩ	no specification
Active Coil Location	no specification	inside radiation shield (if R_{loop} <<0.1mΩ)

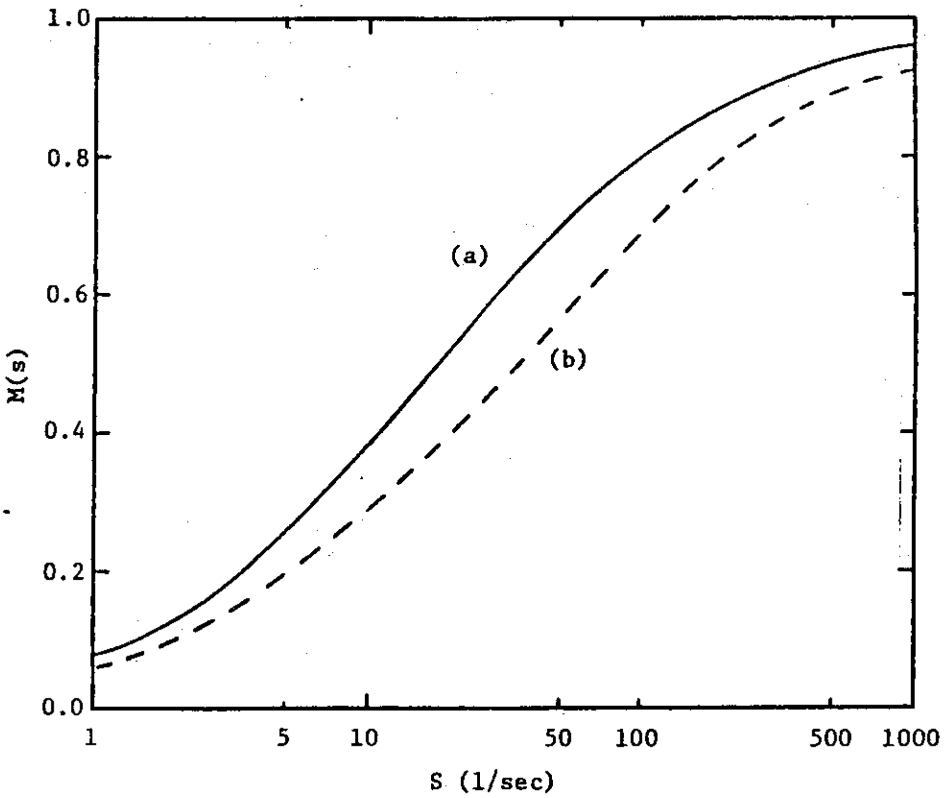

Fig. 3.1.1 Effects of magnetic field shielding as a function of conductive shell thickness.
(a) Standard shells, (b) Half of standard shell thickness.

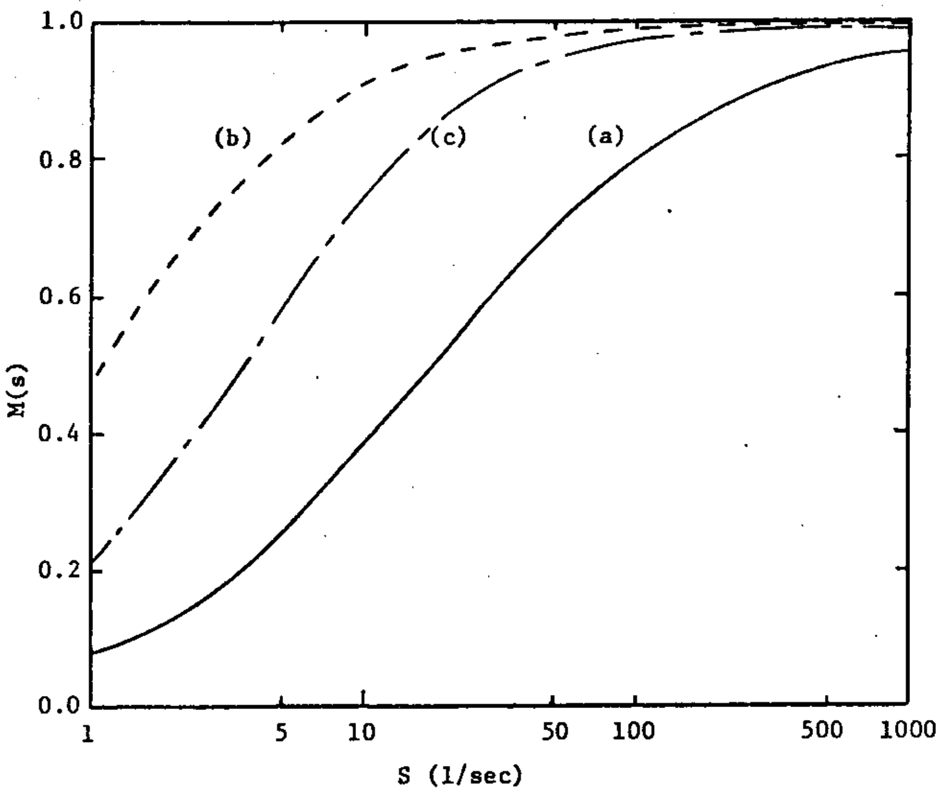

Fig. 3.1.2 Effects of magnetic field shielding as a function of toroidal one turn resistance and effective electrical thickness of shield.
(a) 0.2 mΩ of bellows resistance and 35-40 cm of effective shield thickness.
(b) 0 mΩ of bellows resistance and 35-40 cm of effective shield thickness.
(c) 0 mΩ of bellows resistance and 10 cm of effective shield thickness.

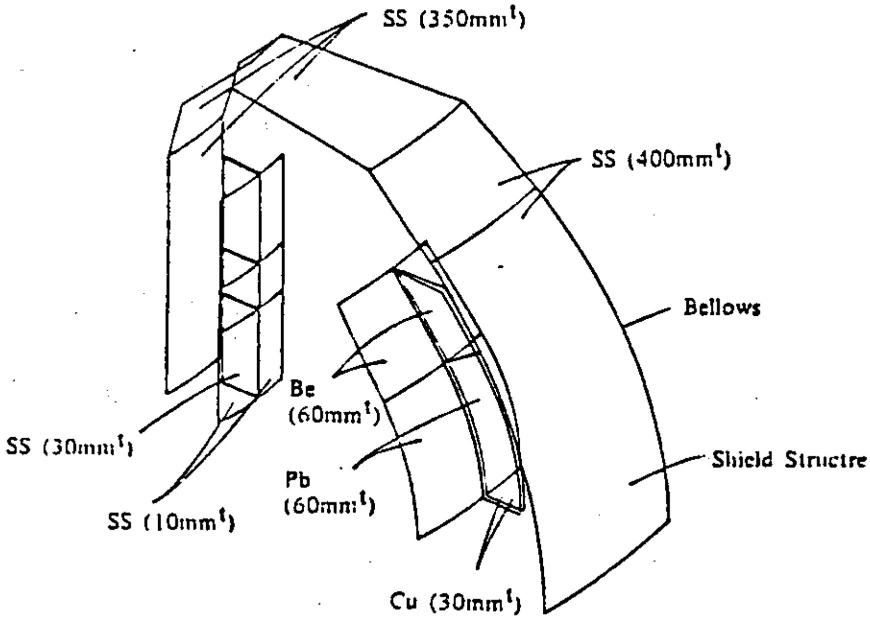

Fig. 3.1.3 Analysis model of passive elements

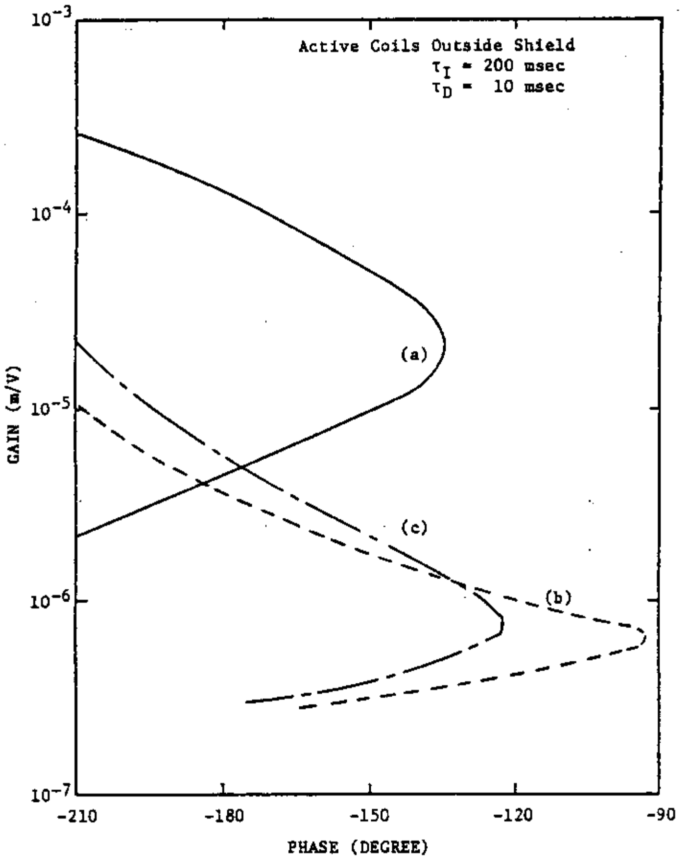

Fig. 3.1.4 Gain-phase diagrams of open. loop transfer functions for PID control systems.

(a) 0.2 mΩ of bellows resistance, 35-40 cm of effective shield thickness.

(b) 0 mΩ of bellows resistance, 35-40 cm of effective shield thickness.

(c) 0 mΩ of bellows resistance, 10 cm of effective shield thickness.

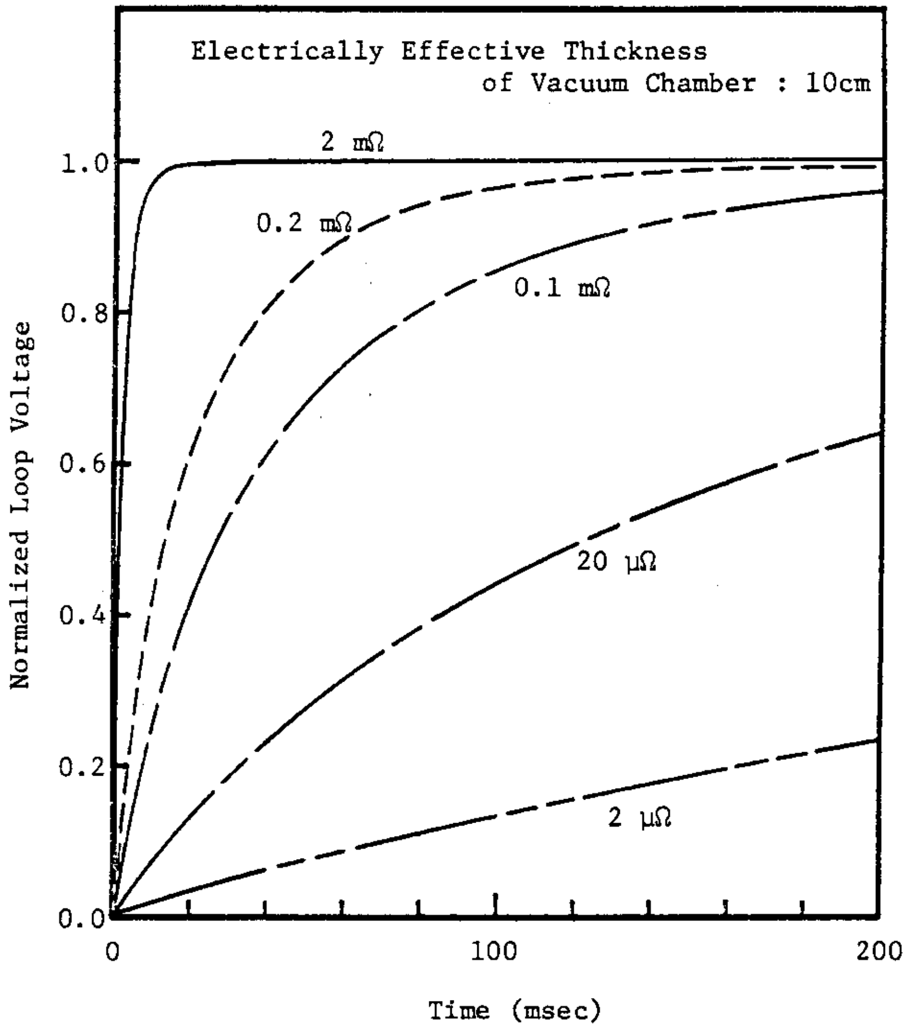

Fig. 3.1.5 Time evolution of normalized plasma loop voltage as a function of bellows resistance.

4. Plasma Disruption Effects

4.1 Plasma Models

The disruption effects such as electromagnetic forces depend on plasma models. In this section, we restrict our discussions to the models which deal with plasmas as a electric circuit.

Two models can be considered from the view point of plasma toroidal current distribution as

i) Single filament model which represents plasma as a filament ring coil.

ii) distributed current model in accordance with MHD plasma equilibrium.

Model i) provides higher maximum electromagnetic force in FER blankets than model ii) by approximately 10 $\sim$ 30%, if plasma position does not change at disruption.

The following models on the decaying pattern of plasma current can be cited as tipical examples.

a. Without plasma movement.

a-1. Current decay with a constant rate, I_p/τ_d.

a-2. Exponential decay with a time constant of τ_d.

b. Current decay with plasma movement.

Here, I_p is plasma current before disruption, and τ_d is disruption time.

The electromagnetic forces of FER blankets calculated with model a-1 are larger than those with model a-2 by approximately 50% as shown in section 4.3. In order to analize disruption effects with model b, the disruption scenario such as moving speed and direction, disruption time should be determined consistently with shell properties of passive elements, clearance around plasma, etc. The disruption analyses by model b are important future works, since our preliminary results suggest that model b brings significant changes in forces and its distribution.

4.2 Induced Voltage

During plasma disruptions, a high voltage would be induced in the components surrounding plasmas. This high voltage may produce arcing betweeen the adjacent modules of blanket and divertor plate, etc., unless the components are properly insulated. For the design specification, it does not necessarily need to evaluate accurate voltages, but enough to estimate the order of values. So we roughly estimate the voltage value induced between the adjacent blanket modules.

The current decay rate is approximately 4×10^8 A/S, since plasma current is 6 MA, and current decay time is ∿15 msec. On the approximation that plasma and blanket have concentric circular crossectional shapes, the mutual inductance between plasma and blanket, M_{pB}, is estimated as

$$M_{pB} \doteqdot \mu_0 R_p (\ell n \frac{8R_p}{a_B} - 2) = 10\ \mu H,$$

where, R_p is a plasma major radius (5.3 m), and a_B is a minor radius of the first wall (1.25 m).

Therefore, the one turn voltage induced at blanket, V_B, is evaluated as

$$V = M_{pB} |\dot{I}_p| \doteqdot 4000\ V$$

If the number of blanket modules is twenty four, the induced voltage between adjacent modules is approximately 170 V.

On the other hand, assuming that the radiation shield/coil vacuum chamber can be considered as perfect conductor, the induced voltage will be reduced. In this case, the one turn induced voltage can be approximately expressed as'

$$V_B = \mu_0 R_p |\dot{I}_p| \ell n \frac{a_s}{a_B} \sim 1850\ V$$

where, a_s is a minor radius of the shield/coil vacuum chamber, and $a_s/a_B = 2$ is assumed. In the case of 24 blanket modules, the induced voltage between adjacent modules is estimated as ∿75 Volts.

From above estimations, we specify the one turn induced voltage at disruptions as 3600 Volts: 24 modules x 75 Volts x factor 2 of safety margin.

4.3 Forces

The analyses of eddy currents and associated electromagnetic forces at plasma disruptions were performed by the EDDYTRAN program [17]. The eddy currents and electromagnetic forces were calculated for the blanket of the Fusion Experimental reactor (FER). We considered two kinds of type models, the reference and the alternative shell designs [18,19], for two kinds of the plasma current decay scenarios. The plasma of FER has double null points for divertor operation and its major and minor radii are 5.5 m and 1.1 m with elongation 1.5, respectively. The plasma current, toroidal field on the axis and thermal fusion power are 5.3 MA, 5.7 T and 440 MW, respectively.

For the reference shell design, the eddy currents on the outboard front wall detour around the ducts. So the electromagnetic forces on the outboard front wall near the ducts are larger than those for the alternative shell design. The electromagnetic forces decaying linearly between 0 sec and 15 msec are one and half times as large as those decaying exponentially with a time constant of 15 msec.

Analytical Model

In the FER design, the first wall is integrated into the blanket for better tritium breeding ratio and easy remote maintenance. Considering plasma vertical stabilization, the blanket assembly is divided into 28 modules along the torus and highly conductive shells are installed on the outboard blanket modules, as described in section 2.2.2. The blanket assembly is composed 14 center modules and 14 side modules. Each blanket module has a stainless steel can-structure filled with Li_2O pellets and water cooling tubes. The highly conductive shell is installed on the stainless steel wall.

Fig. 4.3.1 shows the analytical model. This analysis is based on pertial model between 0 and $\pi/14$ in toroidal angle, due to symmetry of electrical conditions and blanket configuration. As the boundary conditions, current potential is assumed to be plane-symmetry in the toroidal direction across the 0 and $\pi/14$ planes and antisymmetry in the Z-direction across the plasma mid-plane. EDDYTRAN program [11] prepares a whole torus model by rotating the above partial model. Eddy current and electromagnetic force analyses have been performed for two models, the reference shell design and the alternative shell design [16]. Fig. 4.3.2 shows electrical properties for each model. The plasma current of 5.3 MA is assumed to be multi-filamentary according to plasma equilibrium analysis (Table 4.3.1) and decay as described in the following two cases. As case 1, the plasma current decays exponentially with a time constant of 15 msec. As case 2, the plasma current decays linearly between 0 sec and 15 msec. The other components such as shield, cryostat vacuum chamber and others are neglected.

Eddy Currents and Electromagnetic Forces

The eddy current distribution for the reference shell design with the conditions of case 1 at 20 msec after a plasma disruption is shown in Fig. 4.3.3. The principal eddy currents are induced on the outboard front wall near the plasma mid-plane in the plasma current direction. These currents flow through the side wall and return on the outboard end wall and the beryllium part of the outboard front wall. The eddy current on the lead part of the outboard front wall detour around the duct part. The other remarkable eddy currents occur on the inboard end wall. The eddy current distribution for the alternative shell design is shown in Fig. 4.3.4. This eddy currents are with the condition of case 1 at 20 msec after a plasma disruption. The eddy currents on the outboard front wall near the plasma mid-plane are smaller in comparison with the reference shell design. However the eddy currents on the outboard end wall near the plasma mid-plane are rather larger. The other eddy current modes are similar to those for the reference shell design.

Fig. 4.3.5 shows the joule loss distribution due to the eddy currents for the reference shell design with the condition of case 1 at 20 msec after a plasma disruption. The major joul heat appears on the lead part of the outboard front wall near the plasma mid-plane due to the high current density and the high resistivity of lead. Fig. 4.3.6 shows the joul loss distribution for the alternative shell design with the same condition as for the reference shell design. In this case, the joule heat on the lead part is reduced.

The electromagnetic force distribution, due to interaction with the toroidal field, shown in Fig. 4.3.7 is for the reference shell design with the condition of case 1 at 20 msec after a plasma disruption. The toroidal field is assumed to be 5.7 T at R=5.5 m and dependent on 1/R (R is the coordinate in the major radius direction). R-direction components of these electromagnetic forces are reversed across the plasma mid-plane. The R-direction and Z-direction components are also reversed across 0 and $\pi/14$ planes in the toroidal direction. Large electromagnetic forces are observed on the outboard side wall, the outboard front wall near the duct and the inboard end wall. The force on the outboard side wall, due to saddle-like currents, is about 30 kgf/cm^2, in-plane force. The force on the outboard front wall, due to detouring currents around the duct, is about 14 kgf/cm^2, out-of-plane force. That on the inboard end wall is about 29 kgf/cm^2, out-of-plane force. The similar electromagnetic force distribution for the alternative shell design is shown in Fig. 4.3.8. On the outboard front wall, the electromagnetic force is smaller in comparison with the reference shell design while it is larger on the outboard end wall. The other electromagnetic forces are similar to those of the reference shell design. If importance should be given to the fact that the stiffness of the first wall is smaller than that of the end wall, the alternative shell design could prefered than the reference shell design.

The time dependencies of electromagnetic forces due to the eddy currents and the toroidal field are shown in Fig. 4.3.9 and Fig. 4.3.10 for the condition of case 1 and case 2, respectively. In case 1, the maximum electromagnetic forces on the inboard front wall and the inboard side wall appear at 5 msec. On the outboard front wall and the inboard end wall, they appear at 20 msec. At the outboard end wall, it appears at 30 msec. The electromagnetic forces on the outboard end wall decay with larger time constants compared with those on the other walls. In case 2, most of the electromagnetic forces reach the maximum earlier and decay with shorter time constants than for case 1. The electromagnetic forces on most of the walls reach the maximum at 15 msec and one and a half times as large as in case 1.

Concluding Remarks

We performed eddy current and electromagnetic analyses for two candidate shell designs [18] with two kinds of the plasma current decay scenarios. The major conclusions are as follows.

1. The eddy currents and joule heat on the outboard front wall near the plasma mid-plane for the reference shell design are larger than those for the alternative shell design.

2. The electromagnetic forces on the outboard front wall near the duct for the reference shell design are larger than those for the alternative shell design.

3. The maximum electromagnetic force for the reference design is about 30 kgf/cm^2 which appears on the outboard side wall (in-plane force) and the inboard end wall (out-of-plane force).

4. The electromagnetic forces decaying linearly between 0 sec and 15 msec are one and half times as large as those decaying exponentially with a time constant of 15 msec. The former increase and decay with shorter time constants than the latter.

Table 4.3.1 Plasma Current Distribution

ip (A)	9.55709×10^{2}	2.27255×10^{4}	7.46850×10^{3}		
R (m)	4.70000	5.01703	5.35943		
Z (m)	1.83367	1.87327	1.81705		
ip (A)	9.62207×10^{3}	9.20978×10^{4}	1.40868×10^{5}	3.78005×10^{4}	
R (m)	4.67341	5.03898	5.49459	5.86714	
Z (m)	1.44778	1.47487	1.45326	1.35840	
ip (A)	2.21881×10^{4}	1.40597×10^{5}	2.59948×10^{5}	2.51907×10^{5}	2.20546×10^{4}
R (m)	4.64461	5.03843	5.51377	5.97538	6.31767
Z (m)	0.97662	0.98883	0.98668	0.96685	0.85532
ip (A)	3.12003×10^{4}	1.70315×10^{5}	3.23987×10^{5}	3.88272×10^{5}	1.36859×10^{5}
R (m)	4.63274	5.03774	5.51653	5.99685	6.36971
Z (m)	0.49251	0.49530	0.49480	0.49164	0.46669
ip (A)	3.49432×10^{4}	1.80360×10^{5}	3.45022×10^{5}	4.28295×10^{5}	1.93643×10^{5}
R (m)	4.62508	5.03751	5.51713	5.99960	6.38947
Z (m)	0.0	0.0	0.0	0.0	0.0

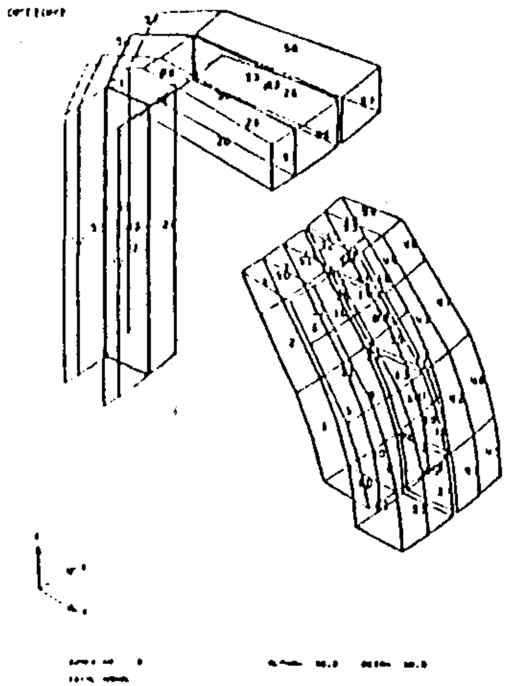

WALL AND PLATE NAME	PART NUMBER	REFERENCE MATERIAL (THICKNESS[mm])	ALTERNATIVE MATERIAL (THICKNESS[mm])
FRONT WALL OF OUTBOARD CENTER MODURE	1, 4, 5, 8, 9 2, 3, 6, 7, 10, 11	Pb(60.0) Be(60.0)	S.S.(10.0) Be(60.0)
FRONT WALL OF OUTBOARD SIDE MODURE	12,13,16,17 14,15,18,19	Pb(60.0) Be(60.0)	S.S.(10.0) Be(60.0)
FRONT WALL OF INBOARD CENTER MODURE	20 ~ 25	S.S.(10.0)	S.S.(10.0)
FRONT WALL OF INBOARD SIDE MODURE	26 ~ 28	S.S.(10.0)	S.S.(10.0)
END WALL OF OUTBOARD CENTER MODURE	30 ~ 40	S.S.(100.0)	Cu(30.0)
END WALL OF ONTBOARD SIDE MODURE	41 ~ 48	S.S.(100.0)	Cu(30.0)
END WALL OF INBOARD CENTER MODURE	{ 50,51,53,54 52,55	S.S.(130.0) S.S.(180.0)	S.S.(130.0) S.S.(160.0)
END WALL OF INBOARD SIDE MODURE	{ 56,57 58	S.S.(130.0) S.S.(180.0)	S.S.(130.0) S.S.(180.0)
SIDE WALL OF OUTBOARD CENTER MODURE	65 ~ 68	Cu(30.0)	Cu(30.0)
SIDE WALL OF OUTBOARD SIDE MODURE	69 ~ 72	Cu(30.0)	Cu(30.0)
SIDE WALL OF INBOARD CENTER MODURE	80 ~ 82	S.S.(10.0)	S.S.(10.0)
SIDE WALL OF INBOARD SIDE MODURE	83 ~ 85	S.S.(10.0)	S.S.(10.0)
SIDE WALL AT DUCT	61	S.S.(10.0)	S.S.(10.0)
UPPER PLATE AT DUCT	60	S.S.(10.0)	S.S.(10.0)
END PLATE OF OUTBOARD CENTER MODURE	90 ~ 92	S.S.(10.0)	S.S.(10.0)
END PLATE OF OUTBOARD SIDE MODURE	93 ~ 94	S.S.(10.0)	S.S.(10.0)
END PLATE OF INBOARD CENTER MODURE	95 ~ 96	S.S.(10.0)	S.S.(10.0)
END PLATE OF INBOARD SIDE MODURE	97	S.S.(10.0)	S.S.(10.0)

Fig. 4.3.1 Model and Electrical property of Blanket for Structural Analysis

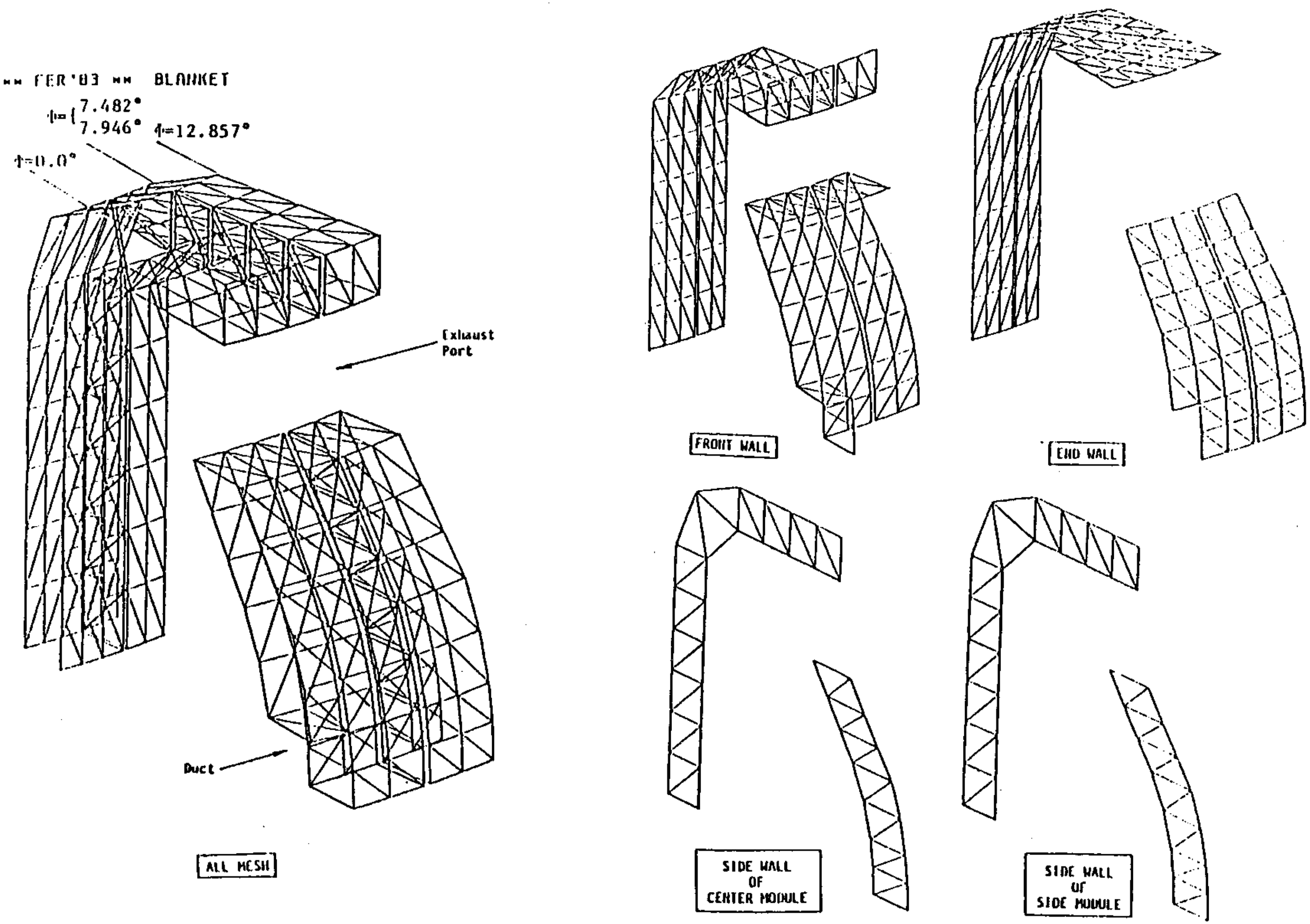

Fig. 4.3.2. Mesh of Blanket for Eddy Curent and Electromagnetic Force

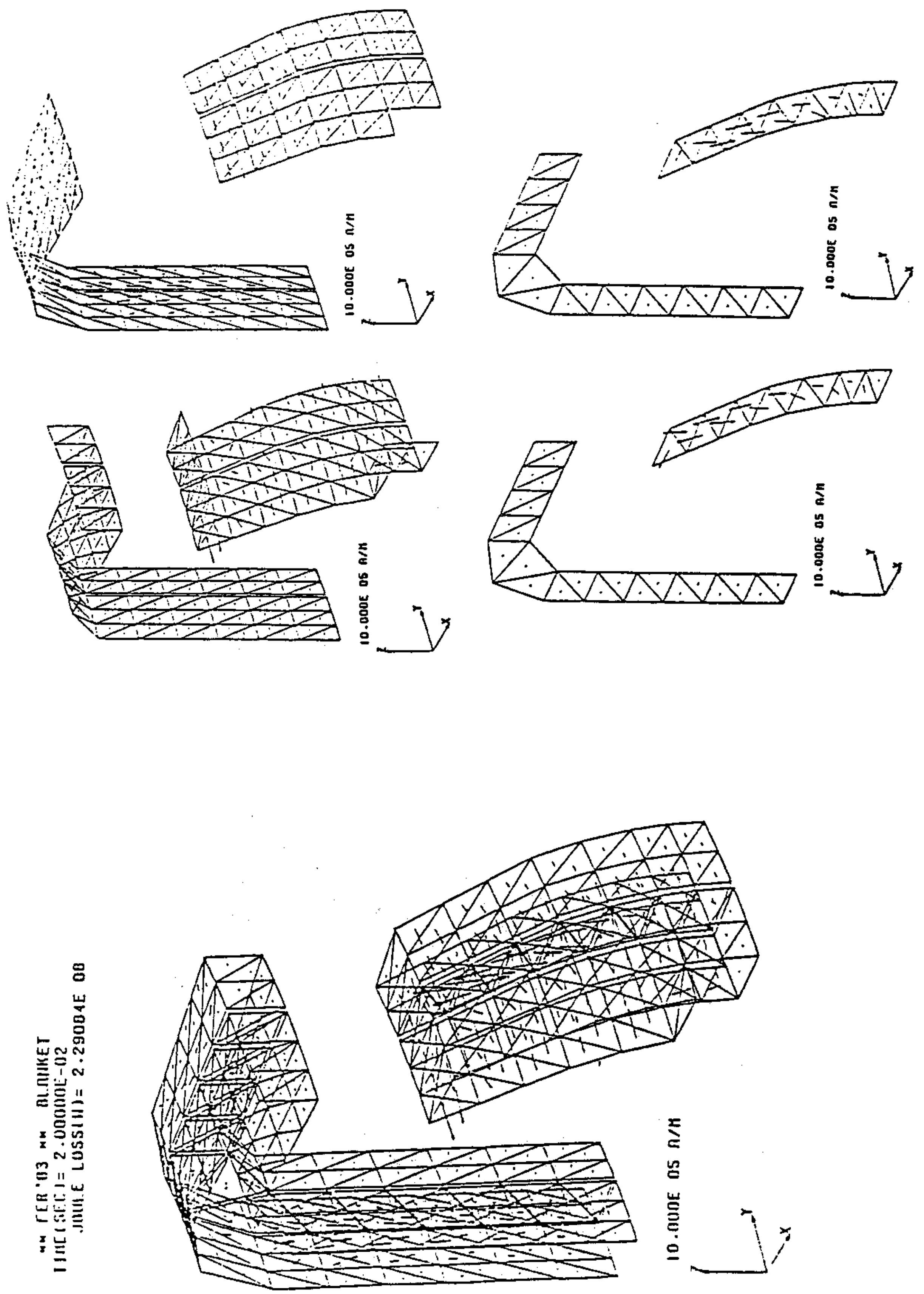

Fig. 4.3.3 Eddy Curent Distribtion During Plasma Disruption
(Reference) (Time:20msec) (Case 1)

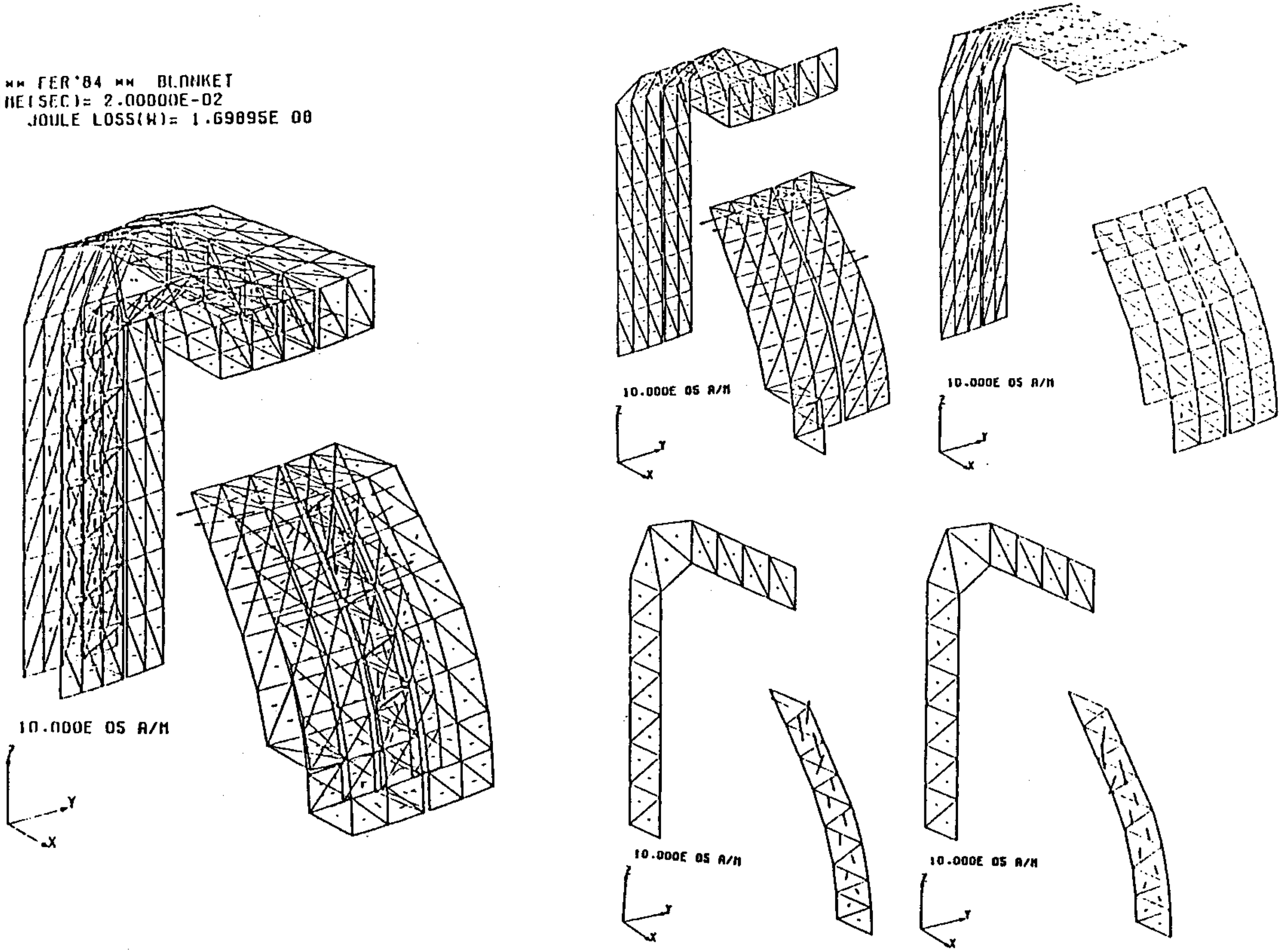

Fig. 4.3.4 Eddy Curent Distribution During Plasma Disruption (Alternative) (Time:20msec) (Case 1)

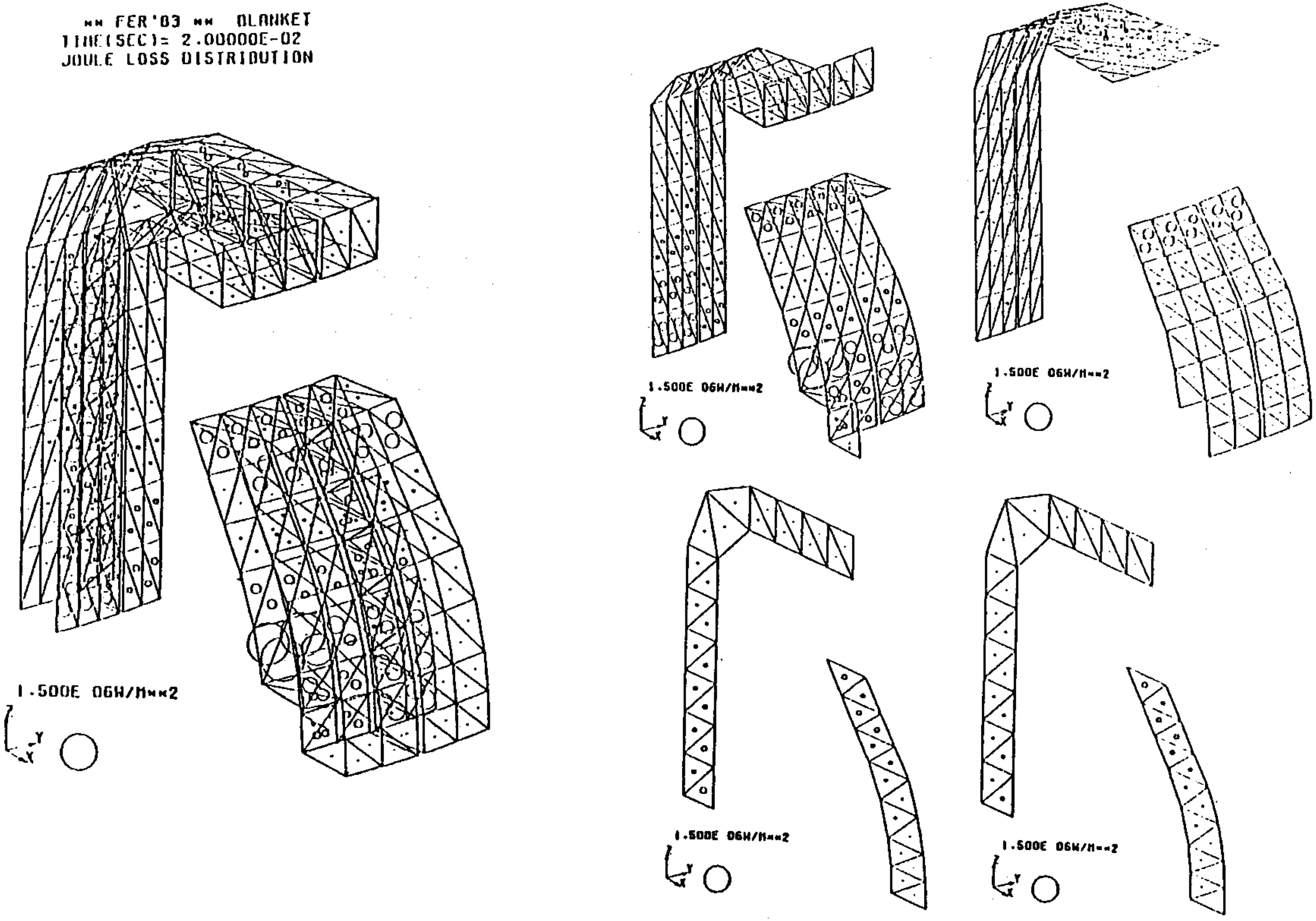

Fig. 4.3.5 Jouile Loss Distribution Duriong Plasma Diruption
(Reference) (Time;20msec) (Case 1)

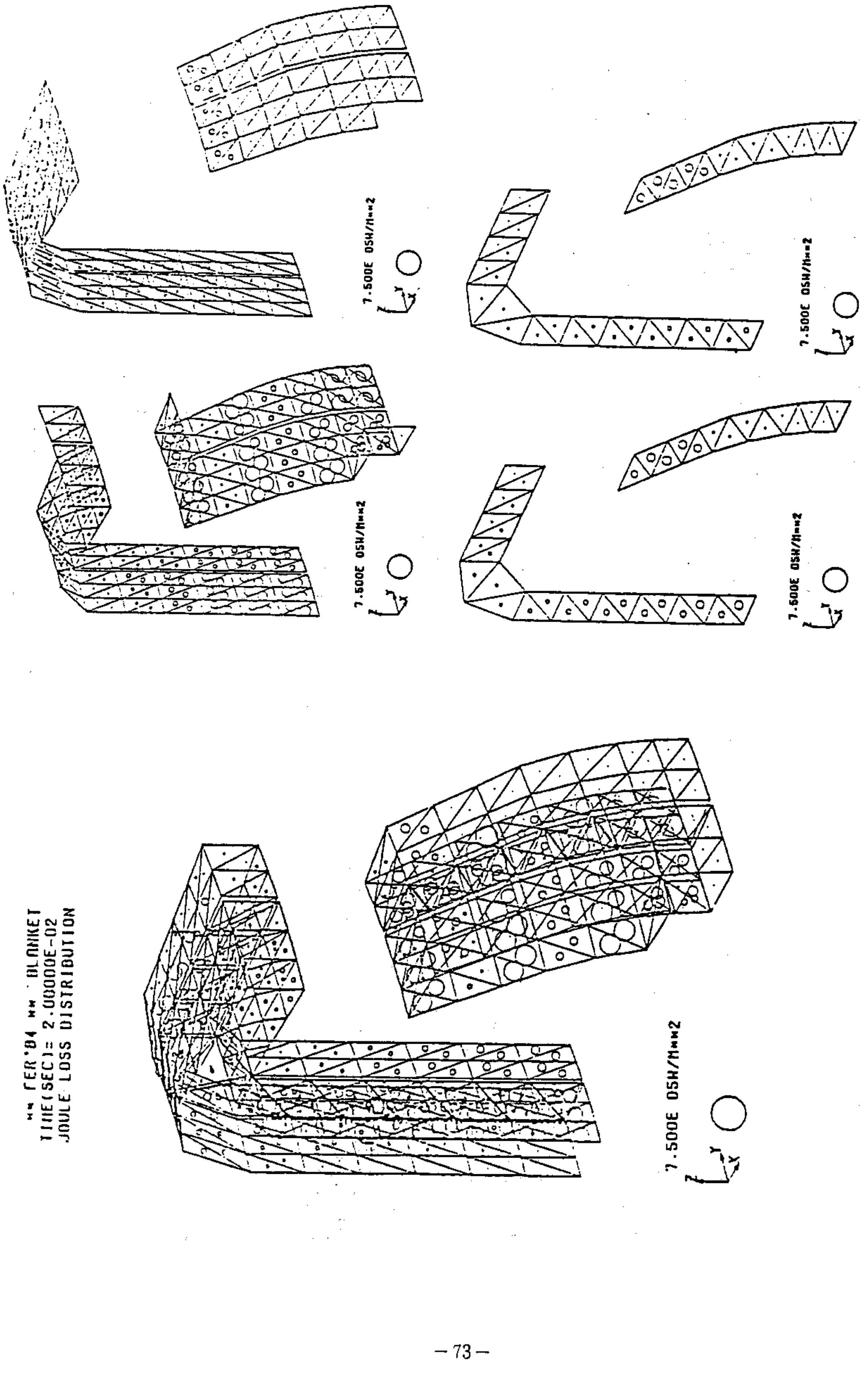

Fig. 4.3.6 Joule Loss Distribution During Plasma Disruption (Alternative) (Time:20msec) (Case 1)

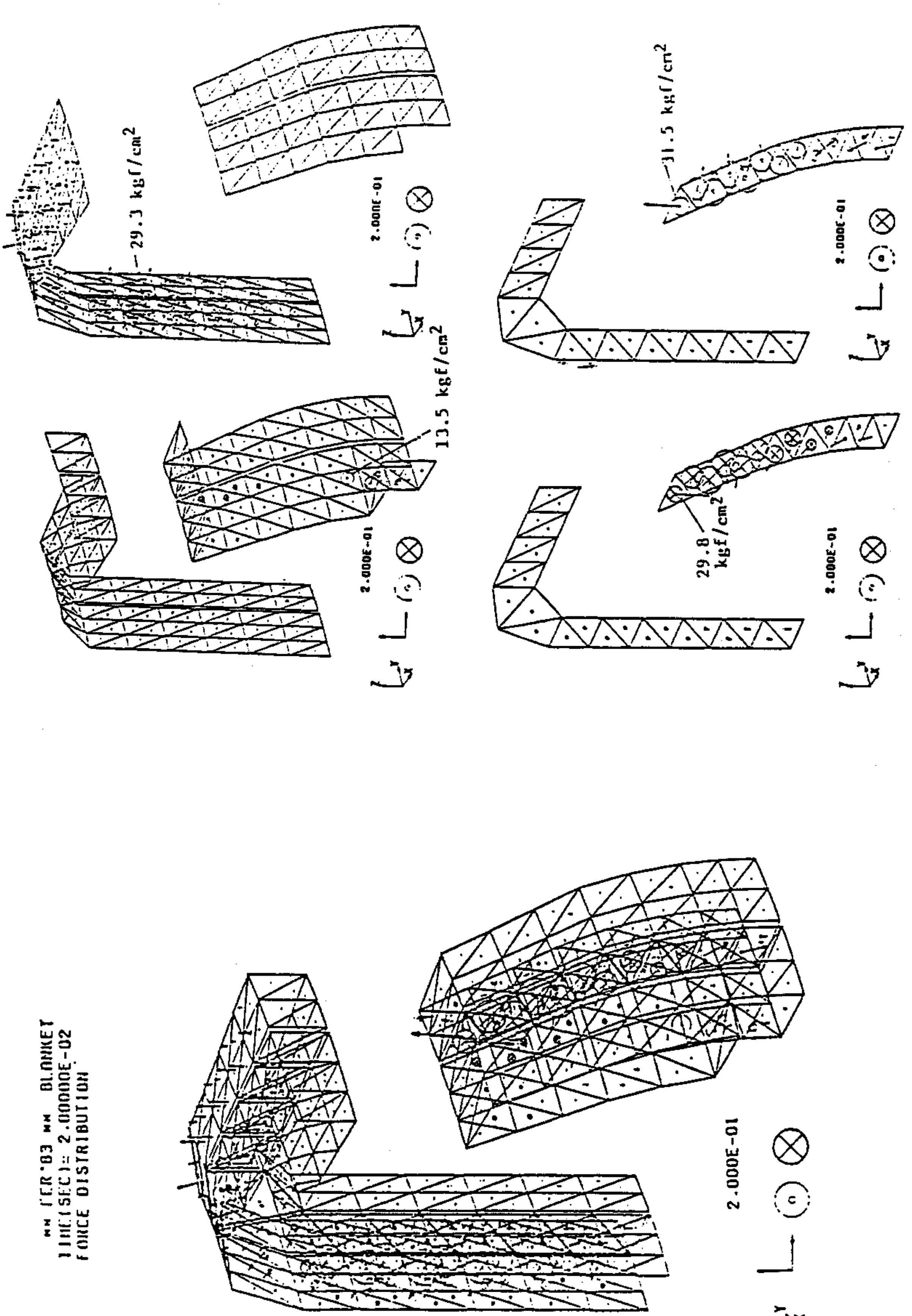

Fig. 4.3.7 Electromagnetic Force Due to Toroidal Magnetic Field (Reference) (Time:20msec) (Case 1)

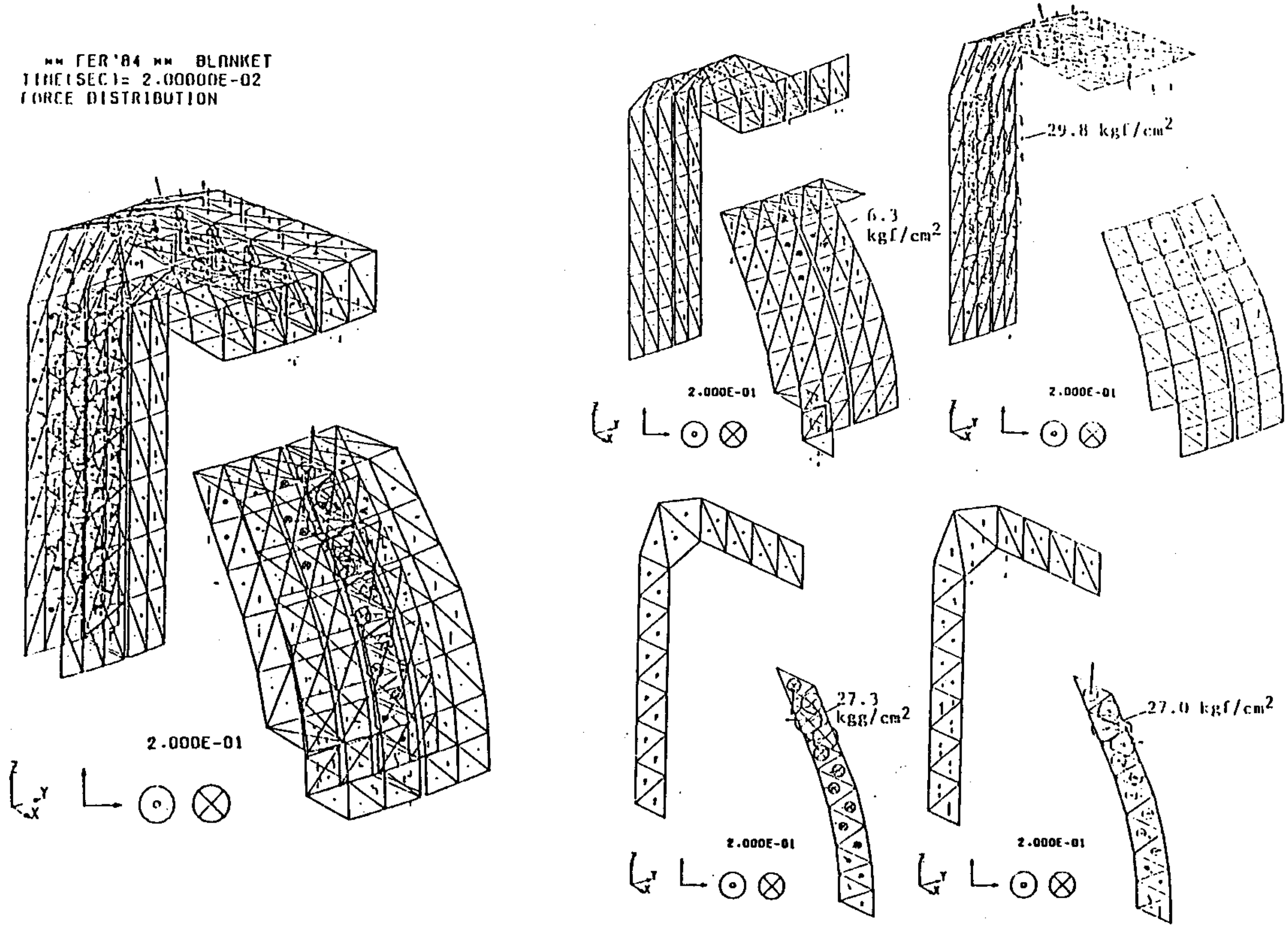

Fig. 4.3.8 Electromagnetic Force Due to Toroidal Magnetic Field (Alternative) (Time:20msec) (Case 1)

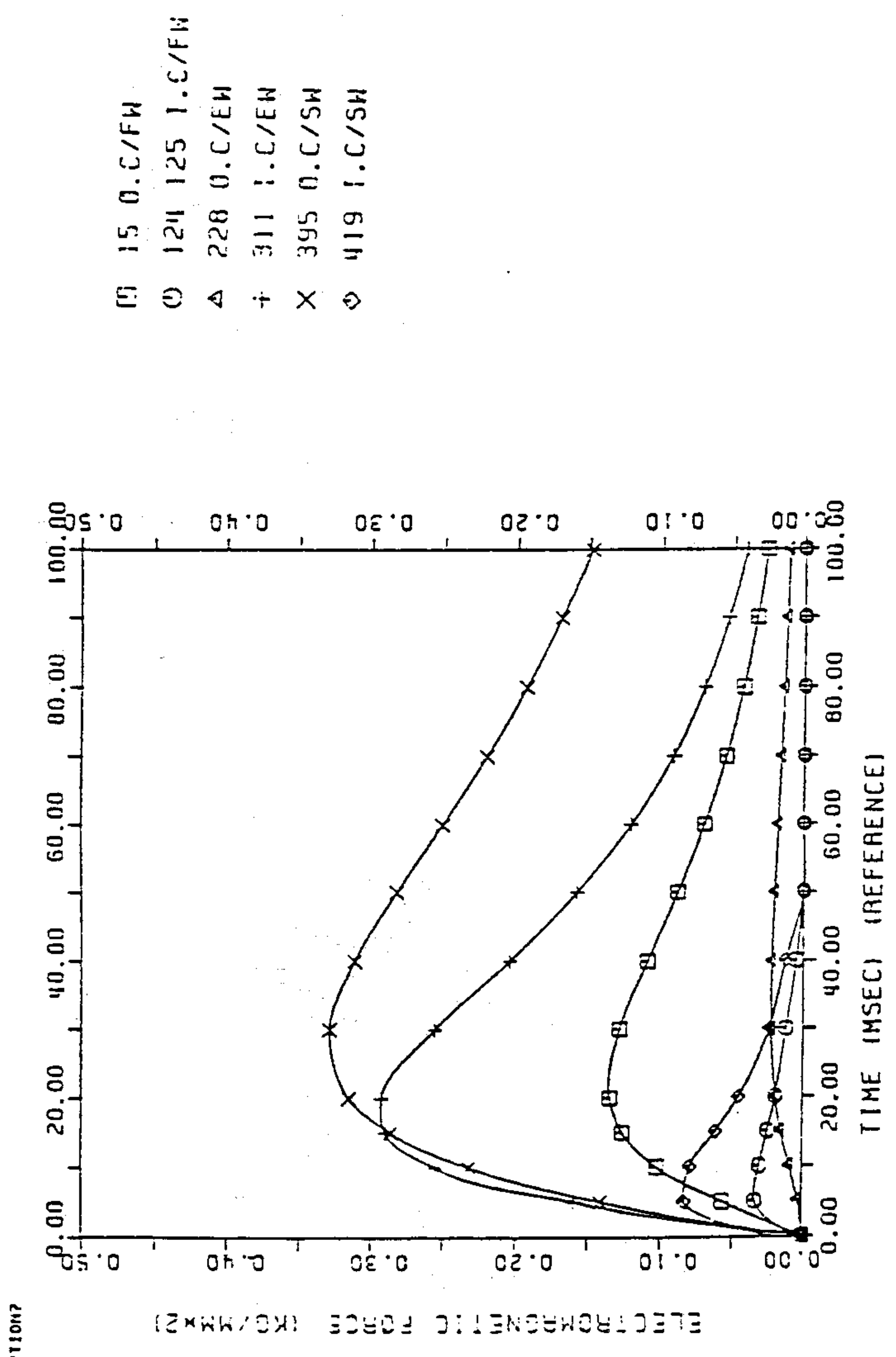

Fig. 4.3.9 Time Dependence of Electromagnetic Force Due to Toroidal Magnetic Field During Plasma Disruption (Reference) (Case 1)

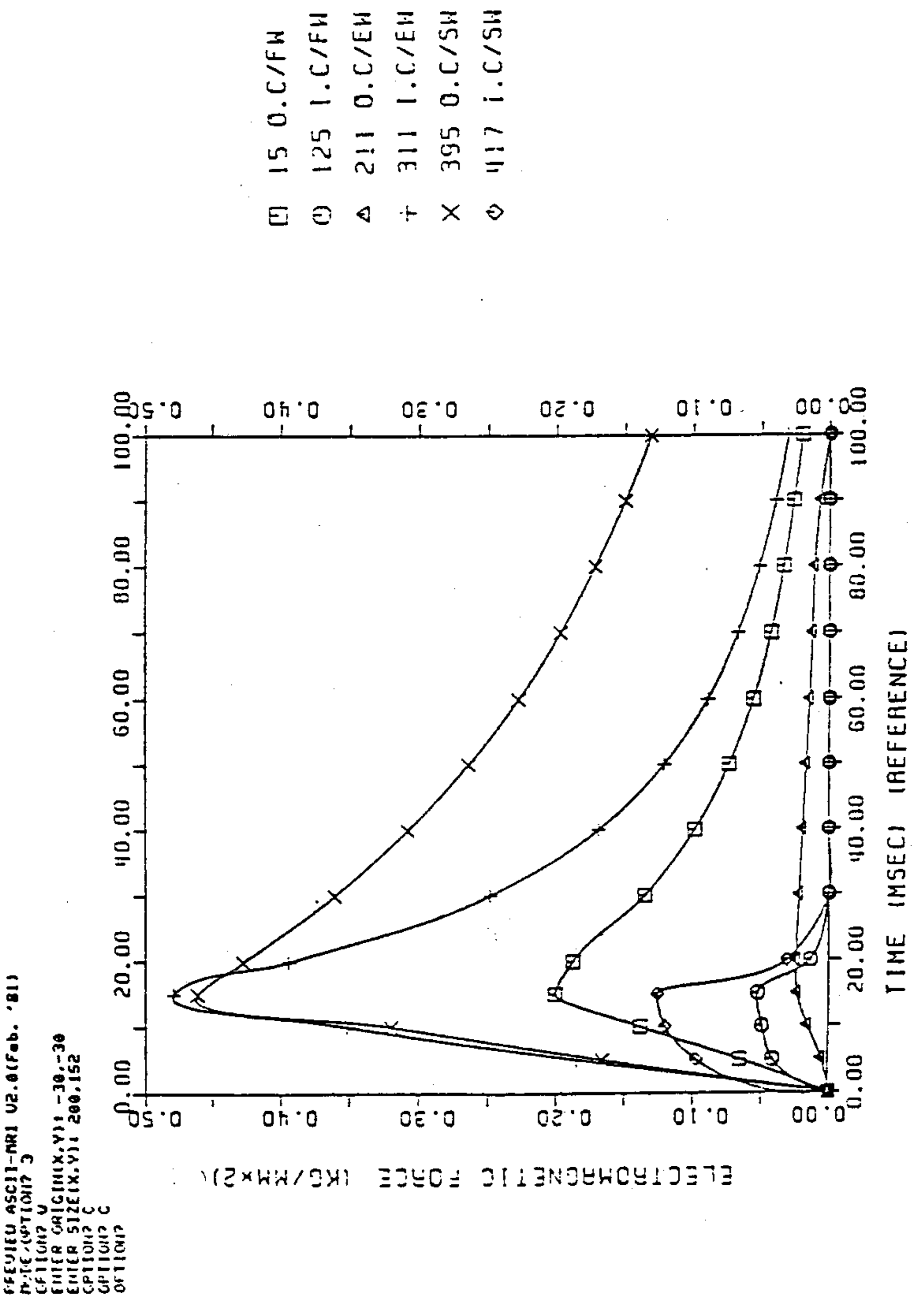

Fig. 4.3.10 Time Dependence of Electromagnetic Force Due to Toroidal Magnetic Field During Plasma Diruption (Reference) (Case 1)

5. Conclusions

5.1 Plasma Stabilization

Since the small number of conductive shell segmentation is preferable for stabilizing plasma vertical instability, the electrical connections between the adjacent conductive shells significantly improve the stabilizing property of passive shells. However, this kind of connection by remote handling makes remote maintenance procedure complicate and unreliable.

The conductive shells installed in inboard blanket modules is effective to stabilize the positional instability. However, the electromagnetic forces at plasma disruption would induce large stresses and deformations in the inboard blanket structures containing conductive shells, since their support could not be sufficient because of restricted accessibility behind the inboard blanket modules. Therefore, it should be better not to set up the inboard shells.

Saddle shape shells installed only in outboard blanket modules has been analytically found to stabilize vertical position instability of the JAERI FER, even when the active control coils are located outside the toroidal coils. This kind of vertical control system will provide the least impacts on overall tokamak reactor design.

5.2 Start-up

Magnetic and electrical field will be prevented by eddy currents to penetrate the radiation shield/coil vacuum chamber which surrounds plasma perfectly.

Since toroidal one turn resistance of larger than 0.2mΩ is not effective to penetrate plasma loop voltage as shown in section 3.1, it is adequate to set it at approximately 0.2mΩ if plasma current is inductively ramped up by Ohmic heating coils.

A large power supply capacity would be required for feedback control of plasma position when the radiation shield/coil vacuum chamber has high electrical conductance in the toroidal direction and the active control coils are located outside it, since a large gain value is needed to apply control magnetic field in plasma due to the magnetic shielding effect.

Toroidal one turn resistance of $\sim$ 0.2mΩ would also be necessary in order to prevent the excessive increase in power supply capacity of active control coils if they are installed outside the shield/coil chamber.

Summerizing the requirement on toroidal one turn resistance, approximately 0.2mΩ would be required if plasma current is ramped up inductively or active coils are located outside radiation shield/coil chamber to make active coil design and installation easy.

5.3 Disruption

Plasma disruptions induce high voltage and large electromagnetic forces in the components surrounding plasma. Rough estimation of induced loop voltage at blanket module would be less than ~2,000V which is equivalent to the voltage of 75V between adjacent blanket modules in the case of 24 blanket modules. However, it is desirable to take a safety margin of a few factor in order to specify the induced voltage at plasma disruptions.

The high conductive shells installed in blanket modules produce large electromagnetic forces at disruptions if the decay time of plasma current does not depend on shell properties of passive elements. Especially in the inboard blanket modules, the large induced force would generate excessive stresses and deformations in the blanket structures when they contain high conductive shells. Since the electromagnetic forces at disruptions depend on plasma models and current decay time and are generally too large in the next generation machine, it is necessary to specify the realistic disruption scenario in order to avoid their over estimation. And it will be fruitful to develop the control methods to increase plasma current decay time.

5.4 Design Guidelines

For plasma vertical movement stability, installation of active control coils located outside the toroidal field coils along with high-conductive shells in the FWBS is recommended based on the following considerations.

<u>A. Design Guidelines for Active Control Coils</u>

1. From the view-point of plasma vertical movement stabilization, preferably active control coils should be located as close to plasma as possible. When active control coils are to be installed inside the shield, passive shells are not necessarily required. However, such active control coils, being saddle-shaped modular type, could not be reliable systems because of the reasons mentioned below, and would bring in substantial risk into the reactor design. The problems associated with the internal active control coils include the following items;

    1) Insufficiency of data and practices for the inorganic insulator to be applied in the plasma vacuum region.

    2) Integrity of the coil structures including feeders against large electromagnetic forces.

    3) Connection/disconnection operations (including insulation work) of many feeders on assemblying/disassemblying of the FWBS modules for maintenance.

2. On the other hand, active control coils located outside the toroidal field coils require high-conductive shells installed in the FWBS to be able to increase the time scale of plasma

movement, γ^{-1}, to approximately 35 msec. The external active control coils, being designed with relaxed environmental conditions and not affected by the construction and maintenance of the FWBS modules, can be of high reliability, and the expected control power is about 35 MVA which is seemingly permissible.

B. Design Guidelines for Passive Shells

1. The most effective way for passive shell installation is to build saddle-shaped shell modules made of a high-conducting material in blanket modules, considering remote assembling and disassembling of torus structures.

2. It is not necessarily required to connect adjacent shell modules electrically. However, when assembly and maintenance procedures permit electrical connections between shell modules, the connections should be located just behind the blanket modules since those made at the outside of the shield would not contribute to improvement of shell effects so much.

3. It should be better not to install high conductive shells in inboard blanket modules, since the electromagnetic forces at disruptions would induce large stresses and deformations in the inboard blanket structures if they contain high conductive shells.

6. References (Section 1 to 5)

[1] H. Yokomizo, "Positional Stability Experiment and Analysis of Elongated Plasmas in Doublet III", JAERI-M84-077, April, 1984.

[2] L.S. Solov'ev, Sov. Phys. JETP 26 (1968) 400.

[3] S. Tokuda et al., "Stability Analysis by Using Revised Version of ERATO-J", JAERI-M9899 (1982)

[4] M. Kumagai et al., "Positional Instability Analysis of Tokamak Plasmas", JAERI-M83-085 (1983).

[5] L.E. Zakharov, Sov. Phys. Tech. Phys. 16 (1971) 645.

[6] E. Rebhan, Nucl. Fusion 15 (1975) 277.

[7] A. Kameari, "Control of Plasma Vertical Position in Tokamak Reactors", Nuclear Engineering and Design/Fusion, to be published.

[8] A. Kameari, "Transient Eddy Current Analysis on Thin Conductors with Arbitrary Connection and Shapes", J. Comput. Phys., 42 (1981) 124.

[9] H. Yokomizo et al., JAERI-M6693 (1973)

[10] H. Takahashi et al., Nucl. Fusion 22 (1982) 1597.

[11] K. Ueda, S. Nishio, N. Fujisawa, M. Sugihara, S. Saito and K. Miyamoto, "Vertical Position Control of the Elongated INTOR Plasma", JAERI-M82-213 (1983).

[12] V.S. Mukovatov and V.D. Shafranov, Nucl. Fusion 11 (1971) 605.

[13] S. Seki, H. Ninomiya and H. Yoshida, "Stabilizing Effect of Passive Conductors with Arbitrary Shape for Positional Instabilities", JAERI-M83-165 (1983).

[14] H. Ninomiya, T. Ozeki, H. Yoshida and S. Seki, "Selecting Method of the Dominant Eigenmodes of Eddy Currents for Plasma Control Study", JAERI-M84-028 (1984).

[15] D.J. Strickler, Y-K.M. Peng, J.A. Holmes, J.B. Miller and K.E. Rothe, "Numerical Simulation of the Plasma Current Quench Following a Disruptive Energy Loss", ORNL/FEDC-83/2 (1983).

[16] R. Yoshino, H. Ninomiya, S. Seki, M. Kikuchi, H. Yoshida, N. Hosogane and S. Tsuji, "Noninteracting Control of JT-60 Equilibrium Configuration", JAERI-M84-120 (1984).

[17] A. Kameari and S. Niikura, "EDDYTRAN Program System for Eddy Current, Electromagnetic Force and Structural Analysis", 10the Symposium on Fusion Engineering, 1983.

[18] M. Kasai, S. Niikura et al., "Design Studies on Conductive Shells and Feedback Control of Plasma Positional Instability in the Vertical Direction", INTOR Workshop, Phase II-A, Part 2, 21 May - June, 1984.

[19] M. Kasai, S. Niikura et al., "Design of the Conductive Shell Structures in the Blanket", INTOR Workshop, Phase II-A, Part 2, 27 January, 1984.

7. Appendix

7.1 Data Base Assessment

7.1.1 Experimental Data for the Position Control Systems

JT-60 Plasma Control System Parameters
JFT-2M Equilibrium Control System Parameters

JT-60 Plasma Control System Parameters

T. Kimura
I. Kondo

I. Major parameters of JT-60

Table I Major parameters of JT-60

Major plasma radius	R_p	3.0(3.2)	m
Minor plasma radius	a_p	0.93(0.90)	m
Plasma current	I_p	2.7(2.1)	MA
Volt second	Φ	28.5	Vs
Toroidal magnetic field	B_t	4.5	T
NBI heating			
power into torus	P_{NB}	20	MW
accelerating voltage	E_{NB}	75-100	keV
pulse length	T_{NB}	10	s
LH heating			
power into torus	P_{LH}	18	MW
frequency	f_{LH}	1.7-2.3	GHz
pulse length	T_{LH}	10	s
ICRF heating			
power into torus	P_{IC}	5	MW
frequency	f_{IC}	0.11-0.13	GHz
pulse length	T_{IC}	10	s
Control magnetic field			
Vertical field	B_v	0.41(0.32)	T
coil current	mI_v	32 turns×57.5	kA
Quadrupole field at $r = a_p$	B_Q	0.037	T
coil current	mI_Q	9 turns × 25	kA
Main divertor coil current	mI_M	8 turns × 120	kA
Maximum poloidal beta at maximum plasma current	β_p	2.5	
Maximum mean plasma pressure at maximum plasma current	$\Sigma_k \overline{n_k T_k}$	$2\times10^{21}(1.3\times10^{21})$	keV/m^3
Elongation		none	
Equilibrium parameter	$\beta_p+\ell_i/2$	0.5 - 2.5	
Normalized vertical field	$B_v/(\mu_0 I_p/R)$	0.36(0.39)	
Plasma inductance	Lp	6.8	μH

( ) = divertor operation (magnetic limiter operation)

II. Poloidal field system

Table II.1 Poloidal field system parameters (Windings)

Parameter	OH Coil	V Coil	H Coil	Q Coil	M Coil
Ampere Turns (MAT)	5.5	± 1.84	± 0.12	± 0.5	±0.755
Total Turns	60	64	12	36	16
Max. Current (KA)	91.7	57.5	20	25	94.4
L (μH)	8.3	9.9	0.44	3.2	0.88
R(mΩ)* (at 75°C)	4.6	12.1	5.0	17.4	3.2
Time Constant (sec)	1.8	0.82	0.09	0.18	0.28
$R \cdot I^2$ (MW)	38.7	40.0	2.0	10.9	28.5
$1/2 \cdot LI^2$ (MJ)	34.9	16.4	0.09	1.0	3.9
Equivalent Square Wave Pulse Length (sec)	8	6	7	7	6

* not including feeders
Material Cu (0.2°/w Ag)

OH coil (or F coil) : Ohmic heating coil

V coil : Vertical field coil

H coil : Horizontal field coil

M coil : Magnetic limiter coil (Divertor coil)

The layout of each coil is shown in Fig. 1.

Table II.2 Poloidal field system parameters (Power supply)

OH coil power supply		
Type	24-phase thyrister converter	
Rated current	± 92	kA
Rated voltage	± 2.5	kV
Peak power	280(230)	MW
V coil power supply		
Type	24-phase thyrister/diode hybrid current	
Rated current	58	kA
Rated voltage	+10 ,-5	kV
Peak power	290	MW
Current step response (total feedback loop)	2-3	msec
H coil power supply		
Type	12-phase thyrister converter	
Rated current	± 22	kA
Rated voltage	± 0.5	kV
Peak power	11	MW
Current step response	2-3	msec
Q coil power supply		
Type	12-phase thyrister converter	
Rated current	± 25	kA
Rated voltage	± 1.0	kV
Peak power	25	MW
Current step response (total feedback loop)	2-3	msec
M coil power supply		
Type	12-phase thyrister converter	
Rated current	± 120	kA
Rated voltage	± 1.0	kV
Peak power	120	MW
Current step response (total feedback loop)	2-3	msec

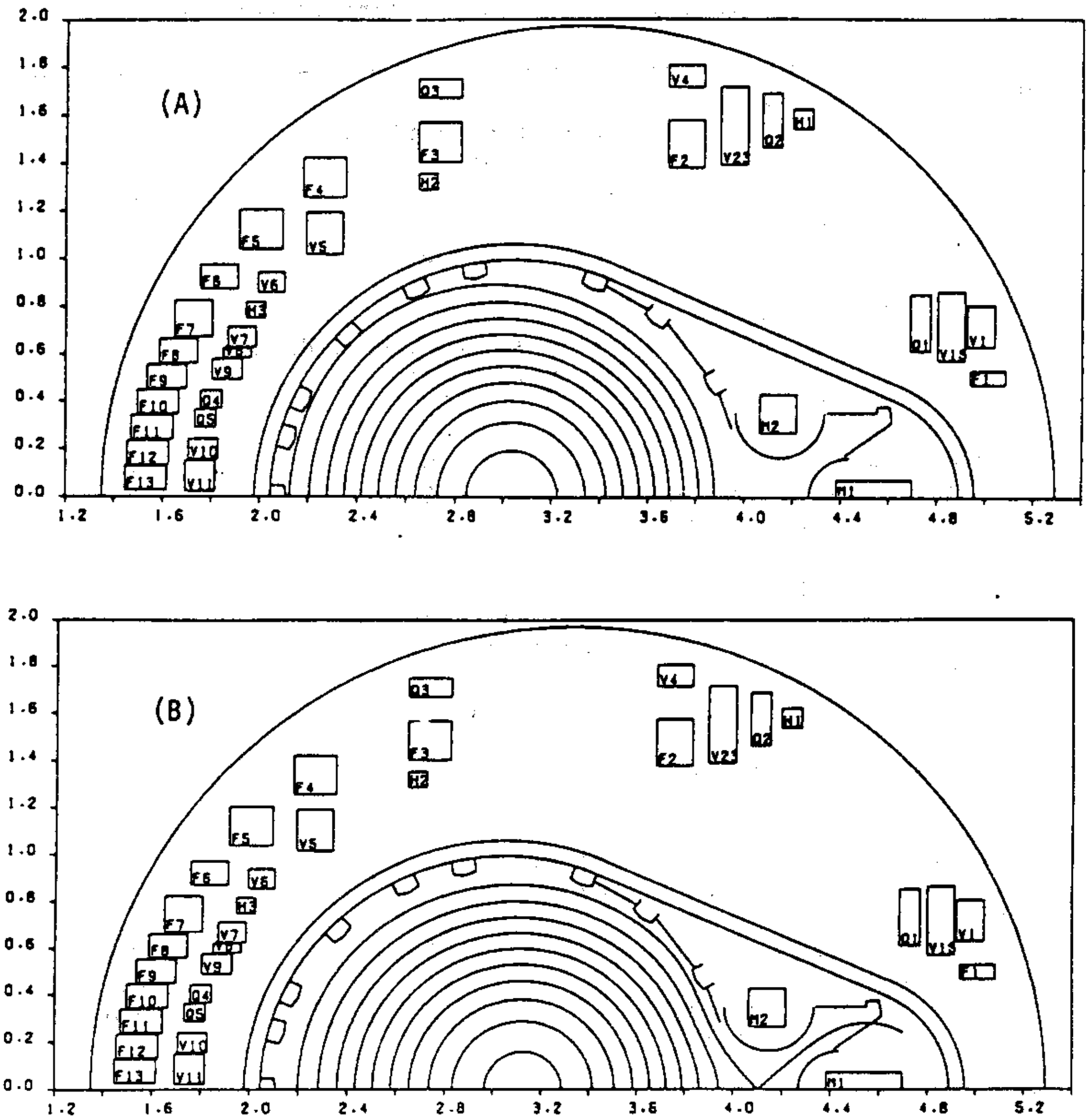

Fig. 1. Equilibrium configurations of JT-60 low β plasma.
(A) Fixed limiter operation (R_p = 3.0 m, a_p = 0.88 m, I_p = 1.5 MA, I_V = 20 kA, I_Q = 0 kA)
(B) Divertor operation (R_p = 3.15 m, a_p = 0.87 m, I_p = 1.9 MA, I_V = 21.3 kA, I_Q = 18.0 kA, I_M = 80 kA)

[From M. Kikuchi et al., JAERI-M 84-095 (1984)]

III. Real-time feedback control system

Conceptual block diagram of plasma real-time feedback control loops is shown in Fig. 2.

Main control purposes of the actuators are as follows:

i) Poloidal feed coil power supplies:

MHD equilibrium configuration

ii) NBI, RF heating systems:

Input power of additional heating

iii) Gas injection system:

Flow rate of gas injection

The real-time control computer I_b^R supervises each actuator and feedback control computer II_b with the period of 10 msec in the normal state and the period of 1 msec in the disruptive state.

The feedback control computer II_b controls the plasma MHD equilibrium configuration in conjunction with the DDC's (Derect Digital Controllers) in the poloidal field coil power supplies.

A) MHD equilibrium configuration control

1. Plasma current control

(1) Current detection — Rogowski coils

(2) Feedback control law:

$$V_F = K_F(I_{pref} - I_p)$$

where V_F : input control voltage to the power supply,

I_{pref}: reference input (preprogrammed input) for plasma current

I_p : plasma current

2. Horizontal position control

(1) R_p detection — magnetic probes

(2) VF index of curvature — $0 \leq n \leq 1.5$

$$n \equiv - \frac{R}{B_z^{ext}} \frac{\partial B_z^{ext}}{\partial R} \bigg|_{R=R_p}$$

(3) Control law: PID control

$$Y_R = K_{RP} \{\Delta X_R(i) - \Delta X_R(1)\} + \sum_{j=1}^{i} K_{RI} \Delta X_R(j)$$
$$+ K_{RD} \{\Delta X_R(i) - \Delta X_R(i-1)\} ,$$

where $\Delta X_R = R_{pref} - R_p$

ΔX_R : deviation between reference input of plasma radial position R_{pref} and measured plasma radial position R_p at the time t_i ($t_i = i \cdot \Delta t$)

K_{RP}, K_{RI} and K_{RD} denote the PID gains for radial position control. Then, the input command for the power supply is

$$V_V^{com} = V_V^{REF} + Y_R \qquad \text{(for AVR)},$$

or $I_V^{com} = I_V^{REF} + Y_R$ (for ACR),

where V_V^{REF} and I_V^{REF} are reference (or preprogrammed) input voltage and current for the power supply respectively.

3. Vertical position control

(same as horizontal position control)

(1) Z_p detection : magnetic probes

(2) Control law : PID Control

$$Y_Z = K_{ZP}\{\Delta X_Z(i) - \Delta X_R(1)\} + \sum_{j=1}^{i} K_{ZI}\Delta X_R(j)$$

$$+ K_{ZD}\{\Delta X_Z(i) - X_Z(i-1)\} ,$$

where $\Delta X_Z = Z_{pref} - Z_p$

Then,

$V_H^{com} = V_H^{REF} + Y_Z$ (for AVR)

$I_H^{com} = I_H^{REF} + Y_Z$ (for ACR)

4. Plasma shape control

(1) ΔQ_p detection : magnetic probes

$$\Delta Q \equiv \frac{1}{\mu_0 I_p} \frac{r_m^2}{2\, r_p} (\lambda_2 + \mu_2)$$

r_p : plasma minor radius,
r_m : probe position
λ_2 : 2nd harmonic parameter of B_θ
μ_2 : 2nd harmonic parameter of B_n

(2) Control law : PID control

(same as horizontal position control)

$$Y_Q = K_{QP}\{\Delta X_Q(i) - X_Q(1)\} + \sum_{j=1}^{i} K_{QI}\Delta X_Q(j)$$

$$+ K_{QD}\{\Delta X_Q(i) - \Delta X_Q(i-1)\} ,$$

where $\Delta X_Z = \Delta Q_{pref} - \Delta Q_p$,

Then,

$$V_Q^{com} = V_Q^{REF} + Y_Z \qquad \text{(for AVR)}$$

$$I_Q^{com} = I_Q^{REF} + Y_Z \qquad \text{(for ACR)}$$

5. Magnetic limiter coil current control

(1) Current detection: Rogowski coil and DCCT

(2) Control law

$$V_M^{COM} = V_M^{REF}$$

$$I_M^{COM} = I_M^{REF} \qquad (I_M^{REF} = \alpha\, I_p^{REF})$$

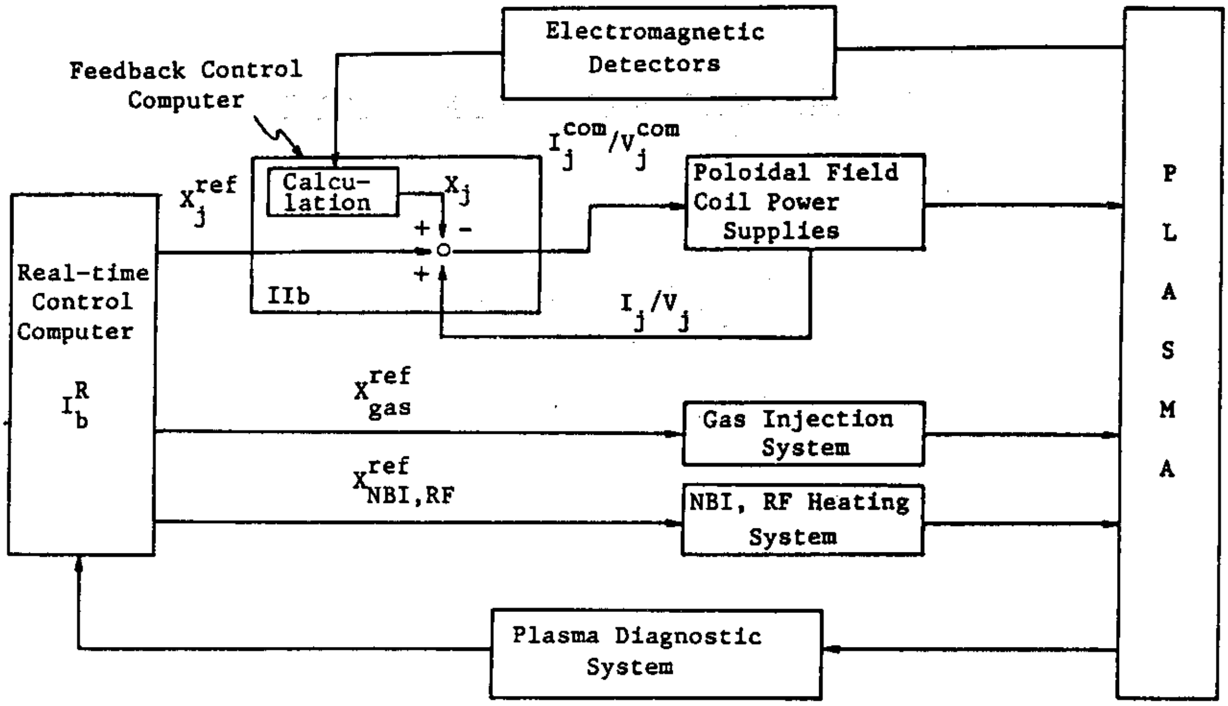

Fig. 2 Conceptual block diagram of plasma real-time feedback control system in JT-60

JFT-2M Equilibium Control System Parameters

Yoshimi Matsuzaki
Masahiro Mori

I. Plasma

A. Major radius $R_o = 1.31$ m

B. Minor radius a, b = 0.35, 0.53 m

C. Elongation $\kappa = 0.9 - 1.4$

D. Plasma current $I_p = 500$ KA

E. Poloidal beta β_p $\beta_p = 0.3 - 1.1$

F. Plasma inductance $L_p \sim 2\mu H$

II. Poloidad Field System in JFT-2M

A. Iron Core Transformer

1. maximum flux swing 2V.s

2. structure 1 core + 1 return yoke

B. Poloidal Coils

1. coil configuration Fig. 1

2. coil parameters Table 1

3. vertical field strength and configuration Table 2

C. Poloidal Power Supply

1. OH power supply

a. main load coils OH coils

b. capacitance bank for start-up

max. voltage 6 kV

max. capacitance 7.5 mF

storage energy 135 kJ

switching thyrister

c. thyrister power supply

phase 12

max. DC current 3.6 kA

max. DC voltage	0.7 kV
peak power	2.52 MW
transformer	3.712 kVA
control type	analog, ACR/AVR

2. S power supply
   a. main load coils — $S_1 - S_2 - S_{3/1}$ coils
   b. capacitance bank for start-up

max. voltage	5 kV
max. capacitance	28.8 mF
storage energy	360 kJ
switching	ignitron

   c. thyrister power supply

phase	12
max. DC current	8 kA
max. DC voltage	1.2 kV
peak power	9.6 MW
transformer	13,900 kVA
control type	analog, ACR/AVR

3. V up power supply
   a. main load coils — $V_1 - V_2 - S_{3/2}$ upside coils
   b. thyrister power supply (positive)

phase	12
max. DC current	8.25 kA
max. DC voltage	0.275 kV
peak power	2.27 MW
transformer	4,096 kVA
control type	analog, ACR/AVR

c. thysister power supply (negative)

phase	12
max. DC current	7.5 kA
max. DC voltage	0.275 kV
peak power	2.06 MW
transformer	3,725 kVA
control type	analog, ACR/AVR.

4. V low power supply

a. main load coils $V_1 - V_2 - S_{3/2}$ downside coils

b. thyrister power supply (positive)

phase	12
max. DC current	8.25 kA
max. DC voltage	0.275 kV
peak power	2.27 MW
transformer	4,096 kVA
control type	analog, ACR/AVR.

c. thyrister power supply (negative)

phase	12
max. DC current	7.5 kA
max. DC voltage	0.275 kV
peak power	2.06 MW
transformer	3,725 kVA
control type	analog, ACR/AVR.

5. Q power supply

a. main load coils $Q_{1/1} - Q_{1/2} - Q_2$ coils

b. thyrister power supply

phase	12
max. DC current	10 kA

max DC voltage	0.25 kV
peak power	2.5 MW
transformer	3,646 kVA
control type	analog, ACR/AVR.

6. H power supply

a. main load coils	H coils
b. thyrister power supply	
phase	12
max. DC current	7.5 kA
max. DC voltage	0.48 kV
peak power	3.6 MW
transformer	5,520 kVA
control type	digital, ACR/AVR.

7. B power supply

a. main load coils	B coils
b. thyrister power	
phase	6
max. DC current	0.27 kA
max. DC voltage	0.58 kV
peak power	0.16 MW
transformer	200 kVA
control type	analog, ACR.

III. Plasma Control System

A. Plasma Current Control

1. current detection : Rogowski loops

2. current control : pre-programmed currents of (S, OH, Q) coils. ACR operation of thyrister power supply.

B. Position Control

1. ΔR detection : magnitic probes and saddle loops (iso-flux method)

2. ΔZ detection : saddle loops

3. principle of control : horizontal and vertical hybrid control (Fig. 2)

4. VF index of curvature $-1.3 < n < 0$

5. feedback control law

$$Vo^{u}+\tau_{f}\dot{V}o^{u} = AIp(\Delta R+\tau_{D}^{R}\ \Delta\dot{R}) + BIp(\Delta Z+\tau_{D}^{Z}\ \Delta\dot{Z})$$

$$Vo^{L}+\tau_{f}{}^{L} = AUp(\Delta R+\tau_{D}\ \Delta\dot{R}) - BIp(\Delta Z+\tau_{D}^{Z}\ \Delta\dot{Z})$$

Vo^{U} : input control voltage to thyrister of V_{up}

Vo^{L} : input control voltage to thyrister of V_{low}

$\tau_{f} = 0.5$ ms $\tau_{D}^{R} = 30$ ms $\tau_{D}^{Z} = 15$ ms

A,B : feedback gains (variable)

Ip : plasma current

6. feedback calculation : analog circuit

C. Shape Control

preprogramed currents of (S, OH, Q) coils.

D. Passive Element

vacuum vessel time constant $\sim$7 ms

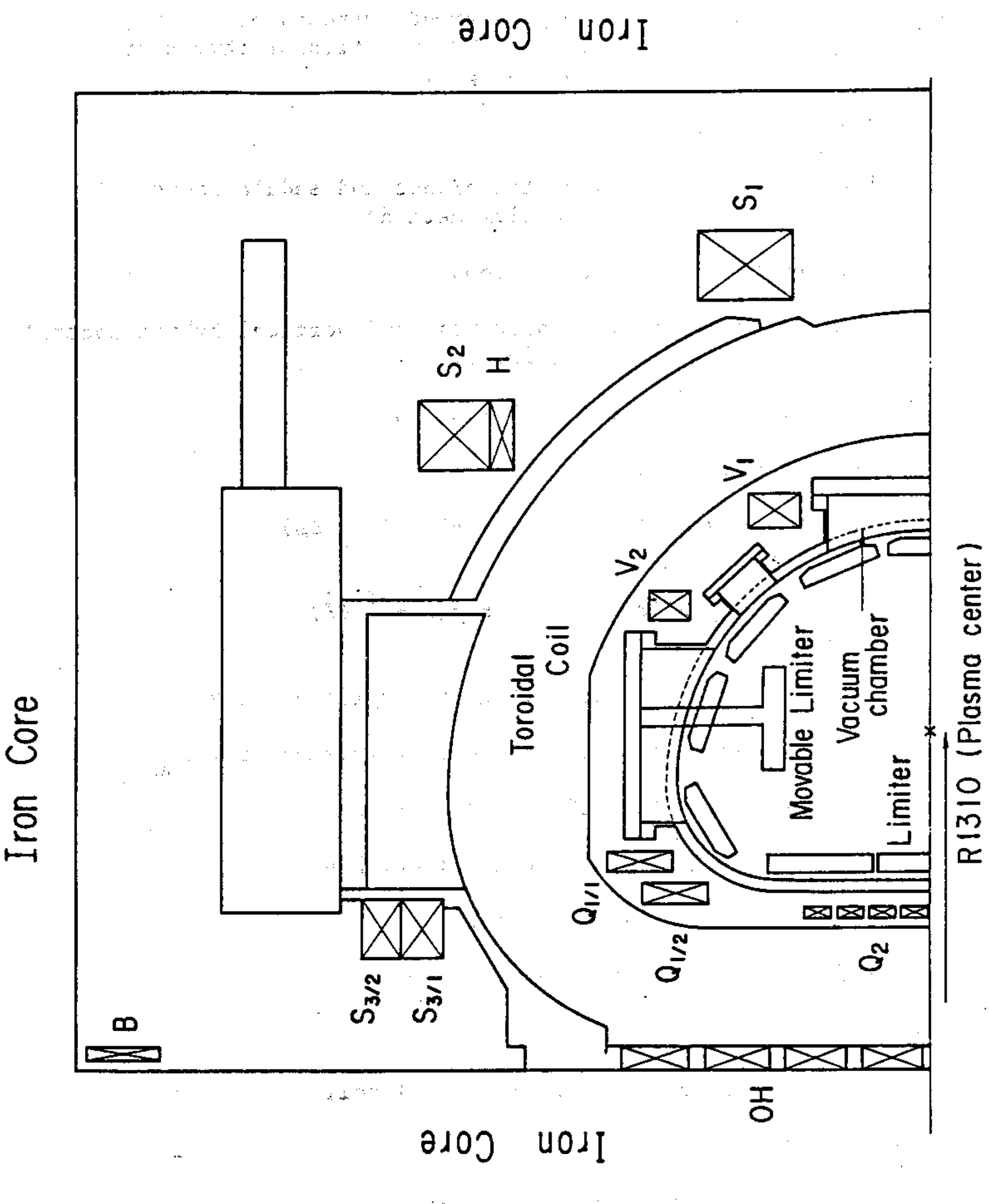

Fig. 1 Quater cross section of JFT-2M

Table 1 Poloidal coils parameters

Coils	Position of coils		Turns (upside) (changable turns)	Max. Current (kA)	Max. AT (kAT)	Resistance (mΩ)	Inductance (air core) (mH)	Cooling	Main Objects	Main Power Supply
	R (m)	Z (m)								
S_1	2.34	0.4325	56 (28, 42)	4.3	241	44.1	32.3	Water	joule plasma shaping and control	S
S_2	1.945	1.115	42 (14)	4.3	181	27.5	15.0	Water		
$S_{3/1}$	0.785	1.1905	24 (12, 18)	4.3	103	6.3	16.7	Water		
$S_{3/2}$	0.785	1.2865	14 (8, 10, 12)	7.5	105	2.0	0.41	Water	fast control of plasma position	V up & V low
V_1	1.770	0.365	10 (6, 8)	7.5	75	3.2	0.86			
V_2	1.545	0.61	6 (4)	7.5	45	1.7	0.28			
$Q_{1/1}$	0.9375	0.68	8	8.5	68	1.4	0.24		non-circularity control	Q
$Q_{1/2}$	0.8625	0.6	8	8.5	68	1.3	0.22			
Q_2	0.82	0.036 ~ 0.252	16	8.5	136	3.0	0.52	Water		
			(series connections upside and downside coils)							
OH	0.476	0 ~ 0.722	42	3.6	151	11.9		Water	V · s control	OH
H	1.945	1.005	14	4.3	60	18.3	1.88		vertical position	H
B	0.480	1.883	15	0.267	4	13.2	0.34		V · s compensation	B

Table 2 Magnetic field of poloidal field coils in JFT-2M

Coils	Radial field B_r (G)	Vertical field B_z (G)	$n^{1)} B_z$ (G)
S_1	- 105	189	- 237
S_2	- 208	57	42
$S_3/_1$	- 225	- 105	30
$S_3/_2$	- 223	- 96	32
V_1	- 257	301	- 253
V_2	- 336	100	409
$Q_1/_1$	- 258	- 162	81
$Q_1/_2$	- 238	- 196	- 32
Q_2	- 100	- 358	- 810
OH	- 125	- 259	- 370
H	- 212	74	39
B	- 206	- 62	31
Plasma	0	- 180	- 202

*) This is the value per 100 kAT and of upper coils only at the center of plasma R = 1.31 m

1) $$n = - \frac{R}{B_z} \frac{\partial B_z}{\partial R}$$

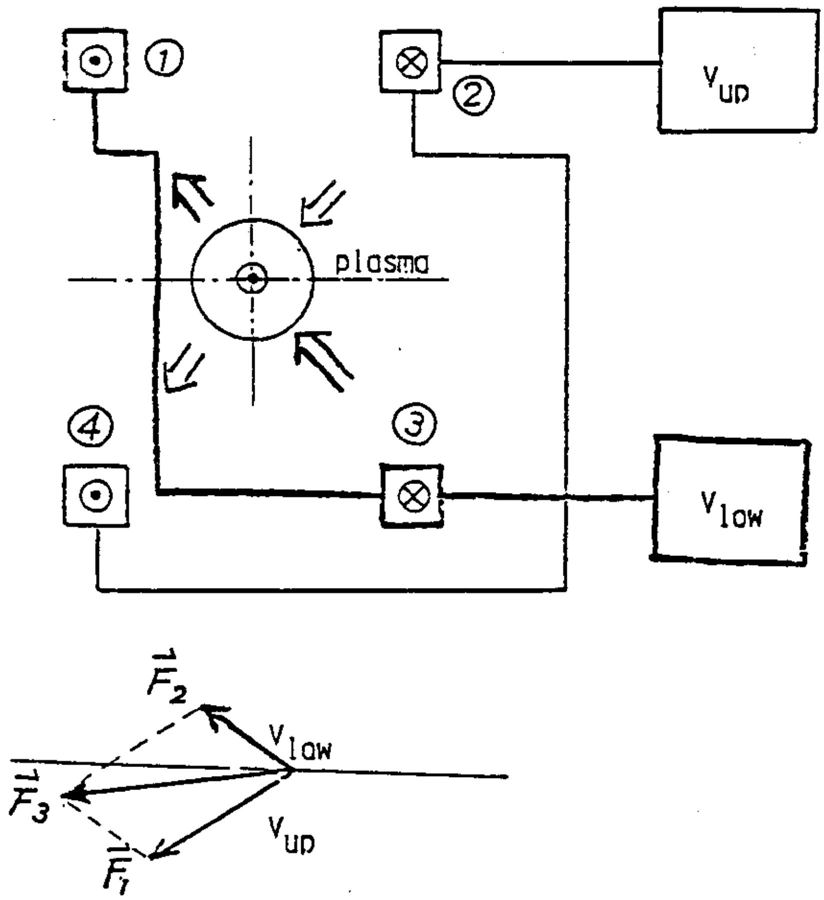

Fig. 2 Schematic diagram of horizontal and vertical hybrid control in the JFT-2M

JFT-2M Fast Pulse Power Supply Technology

K. Ueda

Table 1 Main Parameters of JFT-2M

Plasma Current (KA)	550
Major Radius (m)	1.31
Minor Radium (m)	0.35
Elongation	1 ∿ 1.6
n-Index	0.4 ∿ -2.0
Vertical Field (T)	-0.05 ∿ -0.10
Poloidal Beta	2.0
OH Flux Swing (Vs)	2.0
NBI Heating Power (MW)	2.0
ICRF " (MW)	4.5
LHRH " (MW)	1.0
ECRH " (MW)	0.2

Table 2

Name and Function of PF Coils

No.	Name of Coil Group	Member's Name	Function	Power Supply for Excitation
1	Ohmic Heating Coil	OH	Produces main magnetic flux to pass through iron core, and heats plasma.	OH Power Supply
2	Shaping Coil (S)	$S_1, S_2, S_{3/1}$	Produces main magnetic flux to pass through iron core, and produces plasma equilibration magnetic field.	S Power Supply
3	Quadruple Field Coil (Q)	$Q_{1/1}, Q_{1/2}, Q_2$	Produces equilibration magnetic field in non-circular cross-section plasma, and produces magentic limiter defining magnetic field.	Q Power Supply
4	Vertical Field Coil (V)	$V_1, V_2, S_{3/2}$	Corrects the variable component of the vertical magnetic field requir-ed for equilibrating the plasma having the tendency toward high ß being accompanied with heating pow-er input of NBI, ICRF etc. Feedback controls for locating horizontal direction of plasma.	V Power Supply
5	Horizontal Field Coil (H)	H	Feedback controls for locating ver-tical direction of plasma, and cor-rects magnetic field in horizontal direction.	H Power Supply
6	Bias Coil (B)	B	For obtaining the total magnetic flux of 2 v.s. for iron core, gives pre-excitation of -1 v.s.	B Power Supply

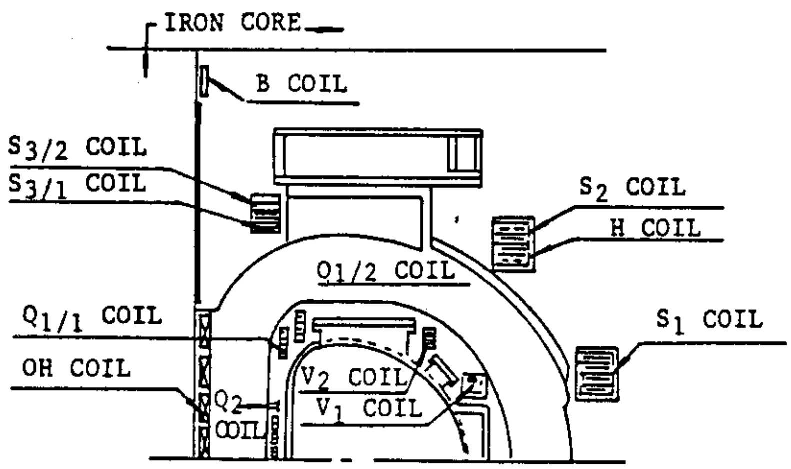

The arrangement of PF coils

Table 3 Main Parameters with PF Coils

Coil Name		Exciting current (KA)	Number of Turns	Ampere Turns (KAT)	Intermediate Taps
S	S_1	4.3	54	240.8	0, 28, 42, 56
	S_2	4.3	42	180.9	0, 14, 42
	$S_{3/1}$	4.3	24	103.2	0, 6, 12, 24
V	V_1	8.25	10	150.0	0, 6, 8, 10
	V_2	8.25	6	90.0	0, 4, 6
	$S_{3/2}$	8.25	24	198.0	0, 5, 10, 12, 14
Q	Q_1	8.25	8	136.0	0, 8
	$Q_{1/2}$	8.5	8	136.0	0, 8
	Q_2	8.5	8	136.0	-
OH		1.8	42	75.0	0, 42
N		1.1	24	26.0	0, 14

Table 4 Power Supply of PF Coils

Name of Power Supply	Power Supply for Exitation	Power Supply Bank	Power Supply	Thyristor Control System
S	Thyristor	S	480 V 7.5 KA (2420 V 4.3 KA)	P.P
	Capacitor	S_0	20 KV 50 mF	
		S	10 KV 7.2 mF or 5 KV 28.8 mF	
OH	Thyristor	OH	350 V 3.6 KA (700 V 3.6 KA)	P.P
	Capacitor	OH	6 KV 7.5 mF or 3 KV 30.0 mF	
		S-OH	10 KV 3.2 mF	
V	Thyristor (cross connection rectifier circuit)	V_{up} (+) V_{up} (-) V_{Low} (+) V_{Low} (-)	275 V 8.25 KA (-275 V 5.75 KA) 275 V 8.25 KA (-275 V 5.75 KA)	P.P - F.B
Q	Thyristor	Q	(250 V 8.5 KA)	P.P
H	Thyristor (Same as V)	M_{up} (+) M_{Low} (-)	(500 V 6.0 KA) (-530 V 6.6 KA)	P.P - F.B
B	Thyristor	B	520 V 0.27 KA	D.C

* P.P : Pre-programming, F.B : Feedback control

Table 5

ITEMS / CROSS-SECTION	TIME INTERVAL	POWER (MVA)	TURNS OF COILS			CURRENT (KA)	MAXIMUM VOLTAGE $0 < t \leq t_1$ (V)	MAXIMUM VOLTAGE $t_2 < t$ (V)
CIRCULAR	$0 - t_1$	8.3	OH -21			2.46	1,514	338
	$t_1 - t_2$	15.5	S_1	S_2	$S_{3/1}$	3.86	6,945	1,765
			-14	-42	24			
			-14	-42	12			
	$t_2 - t_3$	20.0	V_1	V_2	$S_{3/2}$	4.75	-	351
			-6	-6	12			-232
ELLIPSE	$0 - t_1$	6.6	OH -47			2.5	2,881	626
	$t_1 - t_2$	14.9	S_1	S_2	$S_{3/1}$	3.42	9,089	2,236
			-56	21				
			-56	21	-21			
	$t_2 - t_3$		V_1	$S_{3/2}$		4.5	-	317
			-10	10				-204
D SHAPE	$0 - t_1$		OH -42			3.48	2,724	626
	$t_1 - t_2$	19.4	S_1	S_2	$S_{3/1}$	3.2	8,350	2,140
			-56	-21	18			
			-56	-	6			
			-56	-21	24			
	$t_2 - t_3$	24.3	V_1	V_2	$V_{3/2}$	5.48	-	355
			-10		10			-236
			$Q_{1/1}$	$Q_{1/2}$	Q_2	7.5	216	216
			8	8	-4			
			0	8	8			

CALCULATION CONDITION

PLASMA CURRENT BUILD-UP TIME

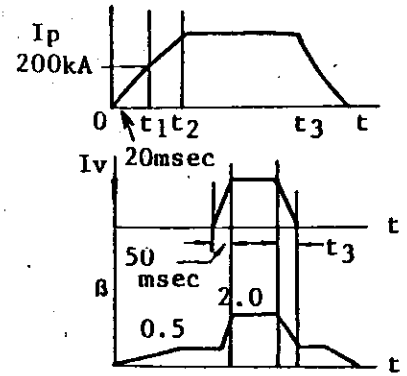

CIRCULAR
t_1 = 20 msec
t_2 = 100 msec
Ip = 200 KA AT t_1
350 KA AT t_2

ELLIPSE
t_1 = 20 msec
t_2 = 150 msec
Ip = 200 KA AT t_1
450 KA AT t_2

D SHAPE
t_1 = 20 msec
t_2 = 200 msec
Ip = 200 KA AT t_1
550 KA AT t_2

7.1.2 Irradiation Effects of Active Coil Insulation Materials

S. Tsujimura*, H. Iida and T. Tone

Japan Atomic Energy Research Institute
801-1 Naka-machi, Naka-gun, Ibaraki, Japan

* On leave from Mitsubishi Heavy Industries, Ltd.,
Tokyo, Japan

1. Introduction

Insulators is necessary to prevent conducting between adjacent conducting wires, turns, and layers in active control coils and to reduce AC loss while magnetic field is changing.

The two classes of materials which can be selected for electrical insulation in fusion reactor magnets are inorganic ceramics and organic polymers. In contrast to inorganic ceramics, organic polymers are superior in fabricability and cost. Organic polymers, however, are much less resistant to radiation damage than inorganic ceramics [1-6]. Leading candidates for magnet insulators are organic polymers.

It is desirable that active coils will be near plasma. But active coils with superconductors will be positioned outside of TF coils while that with normal conductors will be positioned between blankets and TF coils.

The materials data base for mechanical and electrical properties of organic polymers is presented.

2. Organic insulation materials

The organic insulators for fusion magnets are required to have good radiation resistance.

Fig.2.1. gives a survey of the radiation resistance of several organic materails at 77K [7]. This survey is based on mechanical properties. According to this survey, epoxies, polyimides, and polysterenes are possible candidates. Almost all magnet designs for fusion applications incorporate epoxy-fiberglass laminates [1]. Bur recent data shows that unfilled and glass-filled polyimides have a factor of 5-10 more radiation resistance than the glass-filled epoxies [8].

Candidate organic insulators for fusion magnets are listed in Table 2.1. [8-13].

3. Mechanical properties

The irradiation effects on tensile strength, compression strength, and flexure strength of epoxies and polyimides are shown in Fig.3.1.-Fig.3.6. [9, 10, 12-17]. Irradiation sources are neutron and gamma ray. Irradiation temperatures are all liquide helium temperature. Test temperatures are liquid temperature, liquid nitrogen temperature, and room temperature. Dose for insulators are generally reported in Gy (or rad), which is the unit of absorbed dose.

The G-10CR and the G-11CR after irradiation at 4.9K and warm-up to 307K and tested at 77K showed severe decrease in compression strength and flexure strength after a gamma dose of 5.5MGy [15].

The Vessel of a pure polyimide retained initial strength in compression and flexure after a gamma dose of 100MGy [13, 17].

The Norplex and Spaulrad of glass-fabric-filled polyimides showed decrease in compression strength and flexure strength after a gamma dose of 50MGy [17]. These materials remained a half of initial strength in compression and flexure after dose of 100MGy [13, 17].

The comparison of epoxies and polyimides in flexure strength is shown in Fig.3.7. [9, 15, 17].

Radiation effects in several polymers at room temperature is shown in Fig.3.8. [18, 19]. At room temperature, polyimides, epoxies, and polysterenes are possible candidates for fusion magnet insulators with lifetime dose of a few 10MGy.

Tensile fatigue curves of unirradiated and irradiated G-11CR are shown in Fig.3.9. [20]. The samples were irradiated to gamma dose of 1MGy at 295K and the fatigue testing was performed at 295K and 77K. At both temperatures, the fatigue resistance of the G-11CR was increased below 3000 cycles and decreased above 3000 cycles.

4. Electrical properties

DC resistivity of various insulators after irradiation at liquid helium temperature is shown in Fig.4.1. [11, 12]. Resistivity measurements are made at liquid nitrogen temperature and room temperature.

The G-10CR and the G-11CR decreased a tenth of their initial resistivity after a gamma dose of 10MGy.

The Kapton (pure polyimide) retained initial resistivity after 100MGy.

Electrical breakdown of various insulators after irradiation at liquid helium temperature is shown in Fig.4.2. [11, 12]. The voltage-breakdown tests performed at room temperature.

The G-10CR, G-11CR, and stycast showed a significant drops in the breakdown voltage after a dose of 100MGy.

5. Material evaluation and future work needed

As shown in section 3 and 4, irradiation data base of organic insulation materials is unsufficient to design fusion magnet.

It is difficult to evaluate sufficiently insulators for fusion magnet from existing data base of mechanical and electrical properties.

The glass-fabric-filled epoxies are little damaged by doses of less than 5MGy. There are some concern in using these materials for insulators of magnets over the doses of 20MGy. More stadies of irradiation effect on properties, especially mechanical properties, of epoxies for the dose of 20MGy are necessary.

The pure polyimide is unaffected by doses of 100MGy.

The glass-fabric-filled polyimides are not seriously damaged by doses of less than 50MGy. These materials are possible candidates for insulators in fusion magnets for the doses of less than 100MGy at least. The data accumulation of irradiation effects on properties of polyimides for the doses more than 100MGy is necessary.

It is necessary to study radiation response of candidate materials as a function of dose, dose rate, irradiation spectrum, thermal history, atmosphère, and stress condition [21].

And it is necessary to consider gass processing, fabricability, and cost as well as mechanical and electrical properties of organic insulators in selecting insulators for fusion magnets.

Table 2.1. Composition of candidate organic insulators

Materials	Matrix Resines & (Hardener)	Reinforcements	Reinforcements Weight Contents
G-10CR	Bisphenol A (heat activated amine-catalyzed)	E-glass cloth	67wt%
G-11CR	Bisphenol A (aromatic amine)	E-glass cloth	70wt%
Epikote 828 G-20	Bisphenol A (aliphatic amine)	E-glass fiber	72wt%
Epikote 828 G-22	Bisphenol A (aromatic amine)	E-glass fiber	75wt%
GFRP A	Bisphenol A (acid anhydride)	E-glass fiber	74wt%
GFRP B	Bisphenol A (aliphatic amine)	E-glass fiber	75wt%
Stycast 2850FT	Epoxy ;7% 24LV	Inorganically filled	?
Epon 828	Epoxy ;0.5% Z6020 Silane couplant	400-mesh SiO_2	40wt%

Table 2.1. Composition of candidate organic insulators (continue)

Materials	Matrix Resines & (Hardener)	Reinforcements	Reinforcements Weight Contents
Vespel(Kapton)	Unfilled polyimide	-	-
Norplex(Kerimide)	Bismaleimide (aromatic diamine)	E-glass cloth	40~60wt%
TIL-G1000	Polyimide	E-glass cloth	65wt%
Spaulrad(Spauldite)	Aromatic polyimide	E-glass cloth	70~71wt%
Nomex	Aromatic nylon paper	-	-

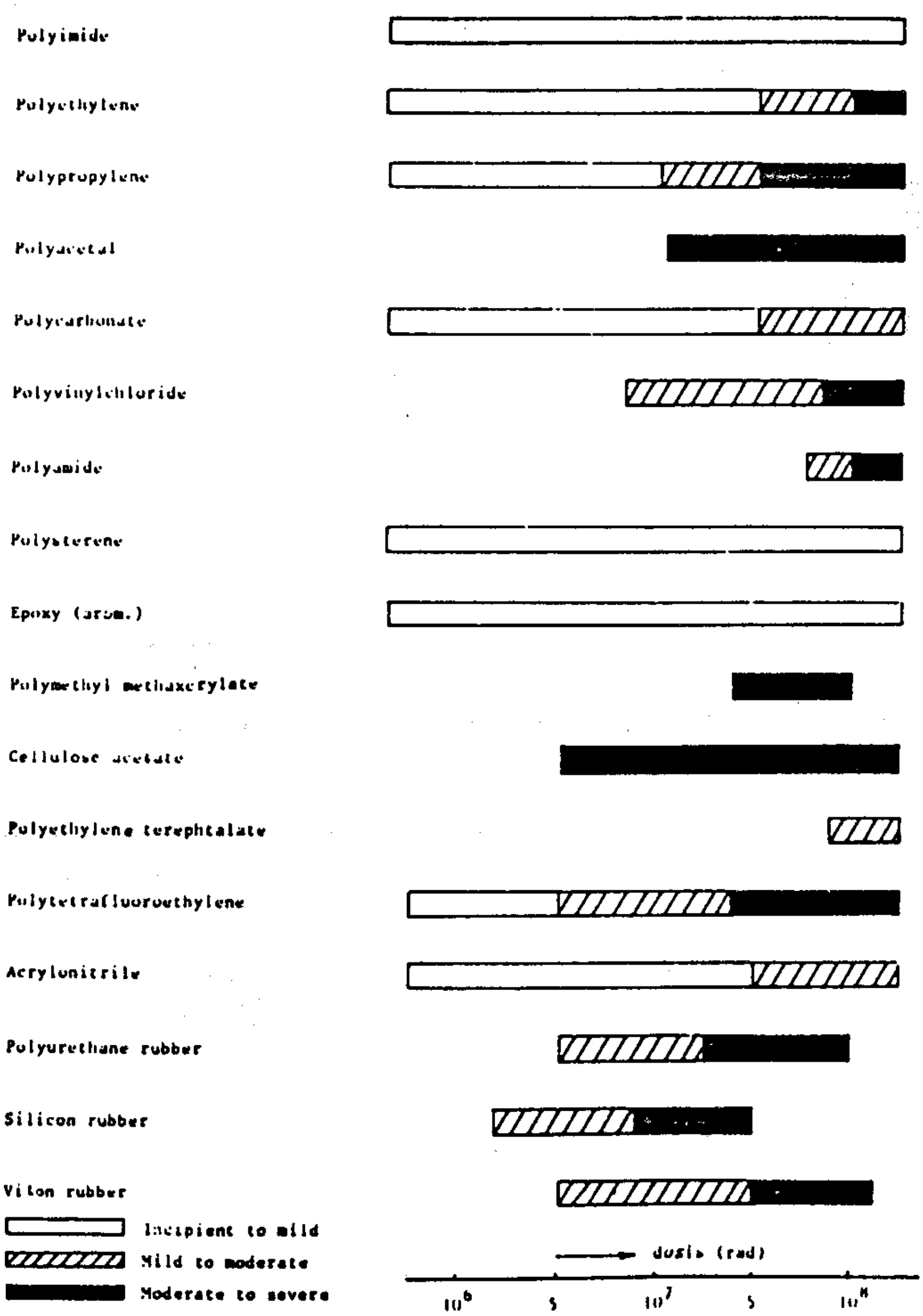

Fig.2.1. Radiation effects in several polymers at 77K.

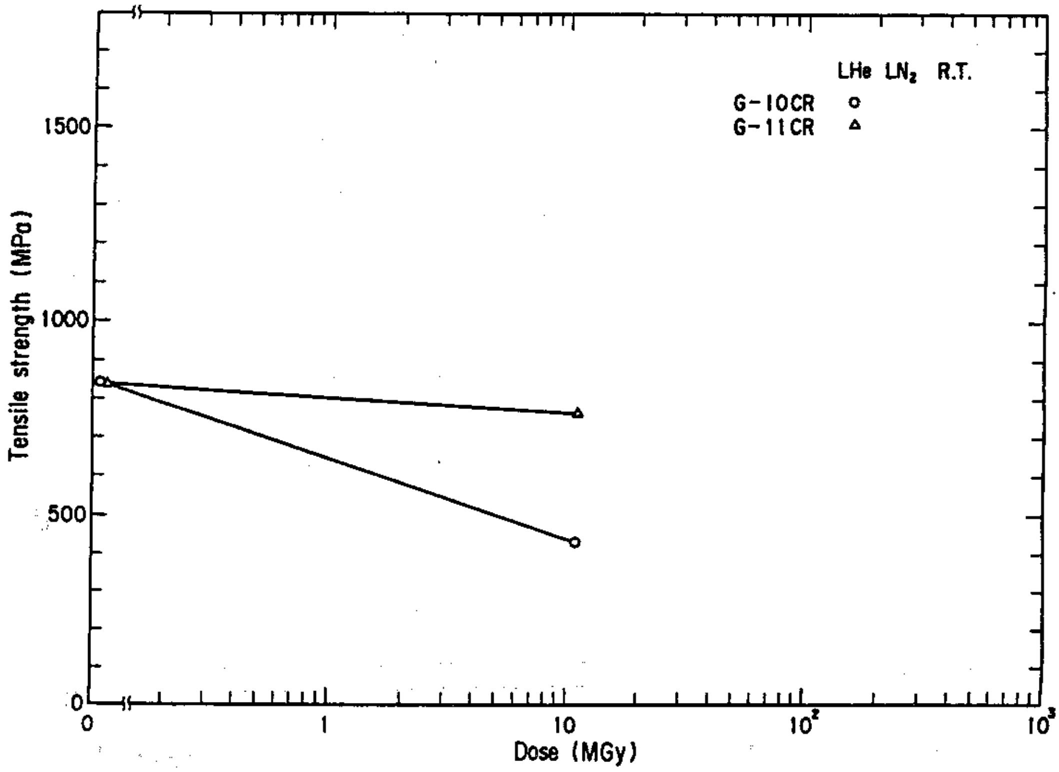

Fig.3.1 Irradiation effect on tensile strength of glass-fabric-filled epoxies.

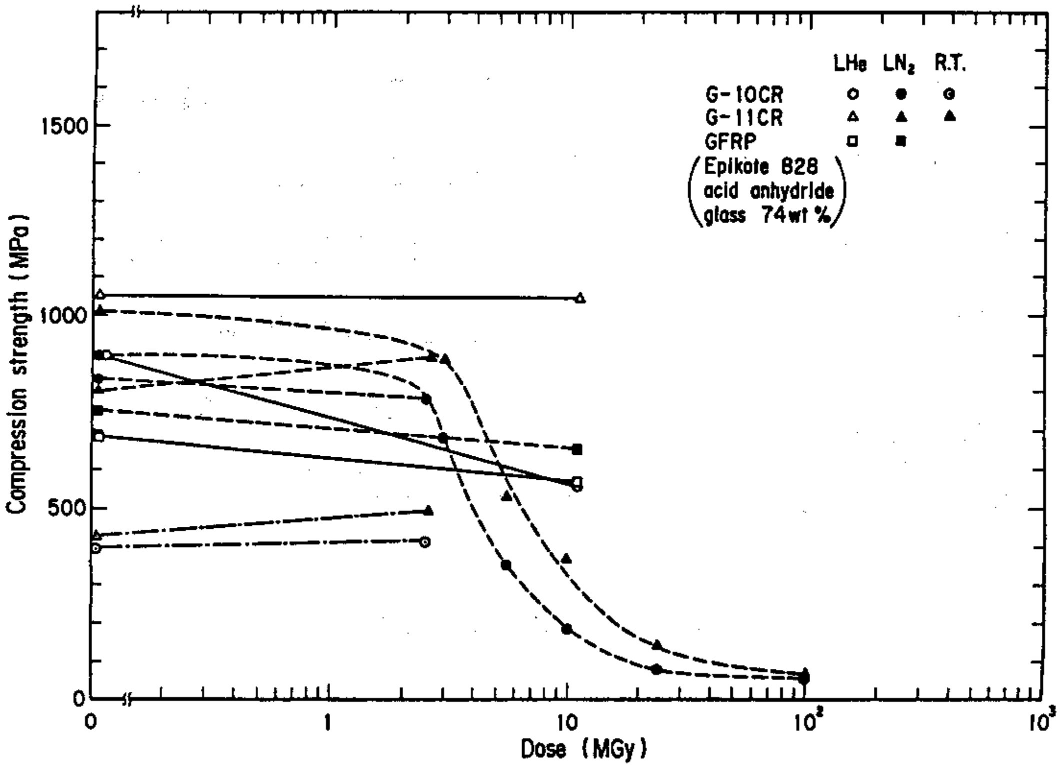

Fig.3.2 Irradiation effect on compression strength of glass-fabric-filled epoxies.

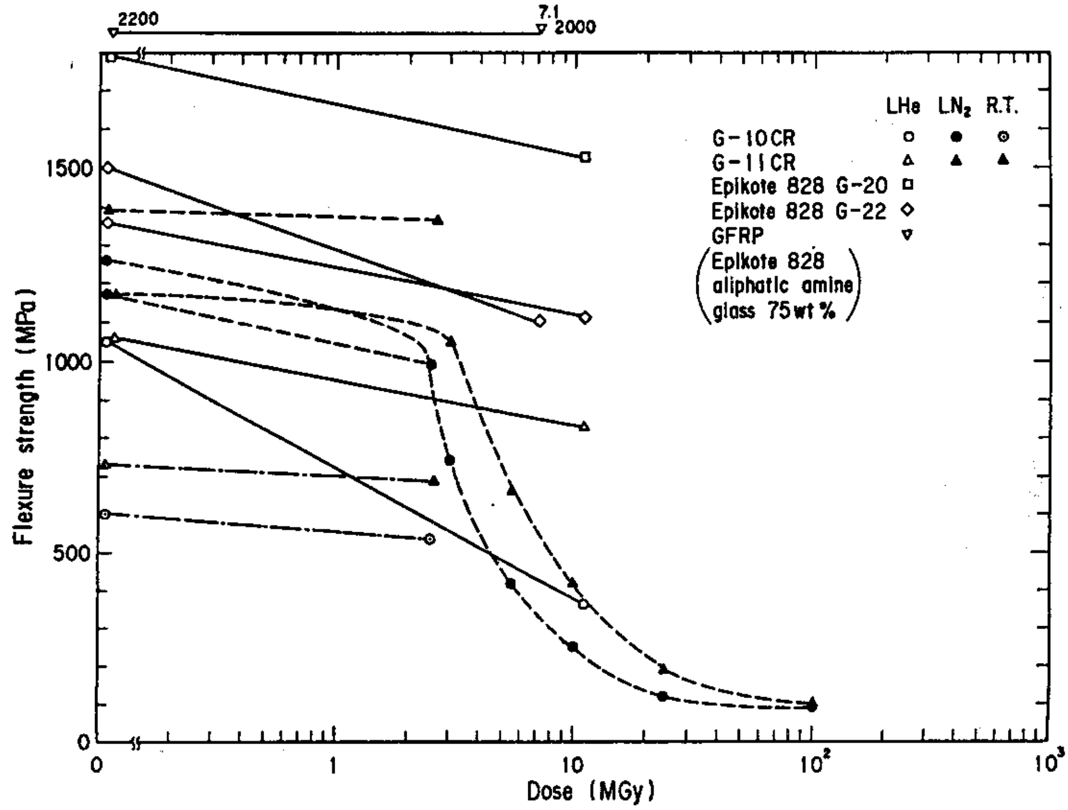

Fig.3.3 Irradiation effect on flexure strength of glass-fabric-filled epoxies.

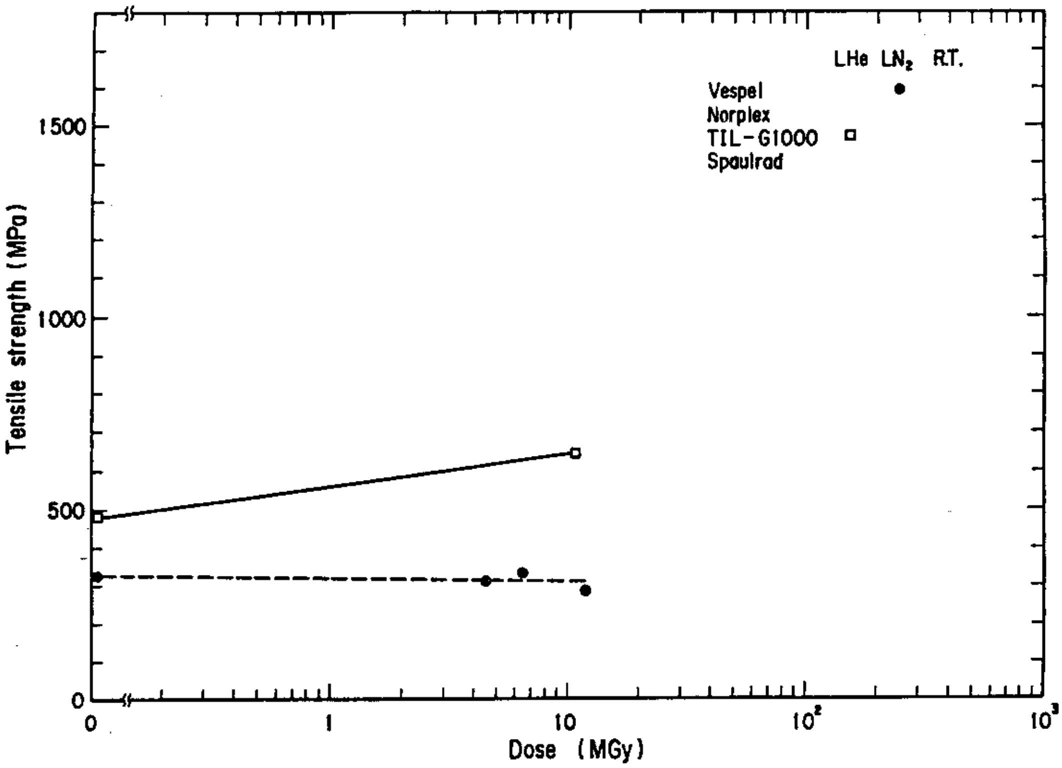

Fig.3.4 Irradiation effect on tensile strength of pure and glass-fabric-filled polyimides.

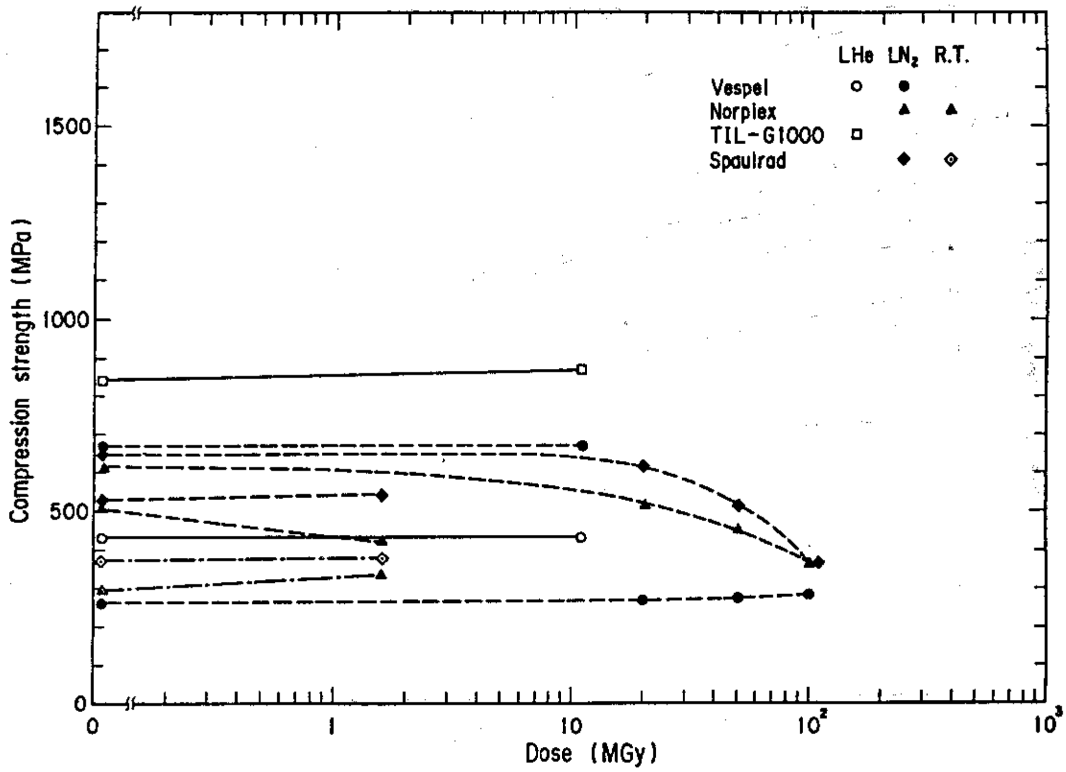

Fig. 3.5 Irradiation effect on compression strength of pure and glass-fabric-filled polyimides.

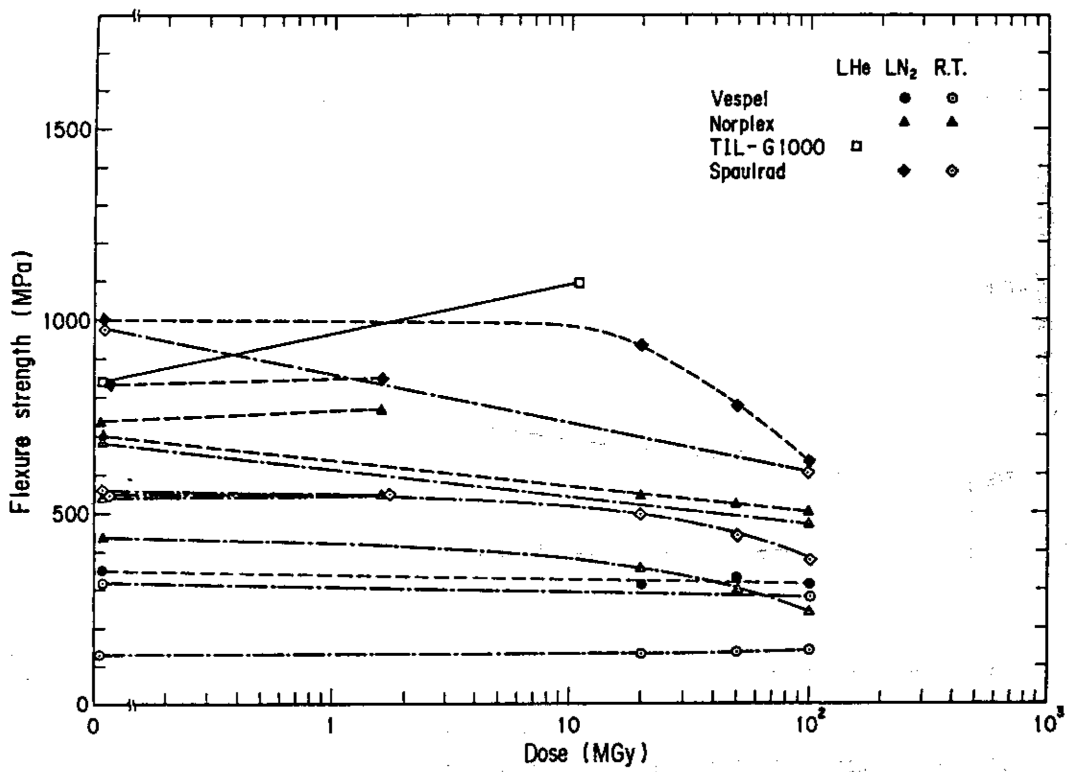

Fig. 3.6 Irradiation effect on flexure strength of pure and glass-fabric-filled polyimides.

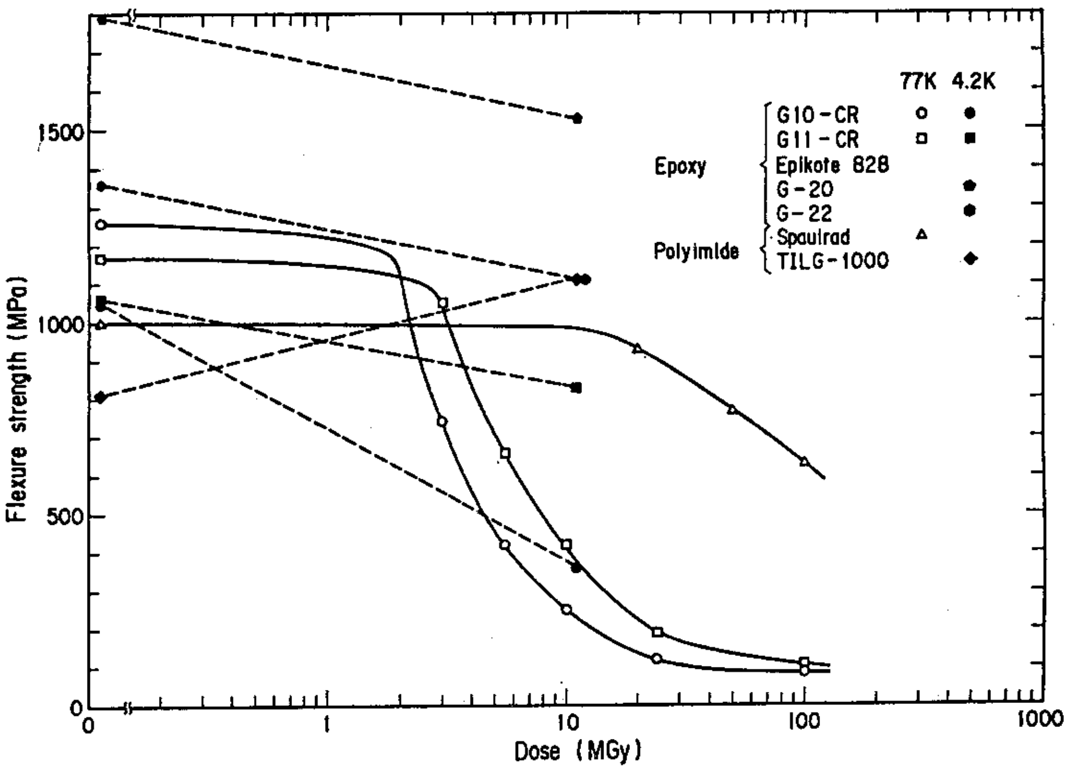

Fig. 3.7 Irradiation effect on flexure strength of epoxies and polyimides.

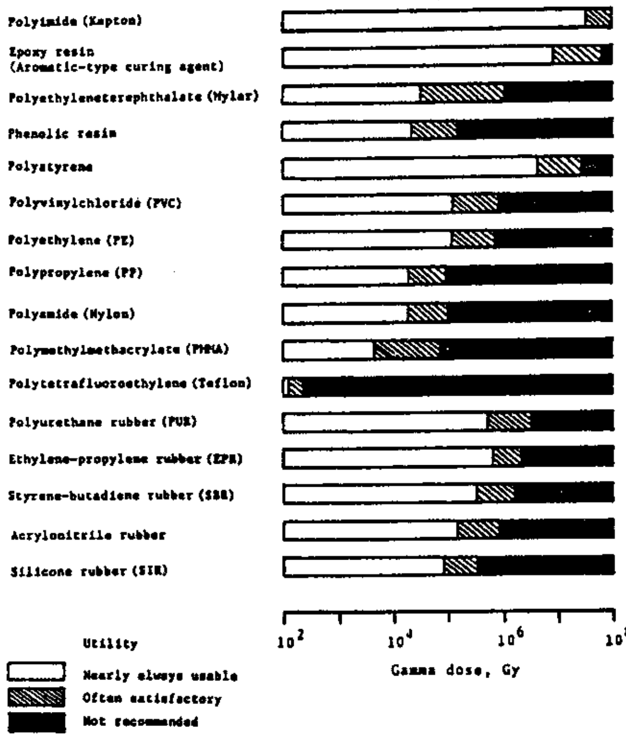

Fig.3.8 Radiation effects in several polymers at room temperature.

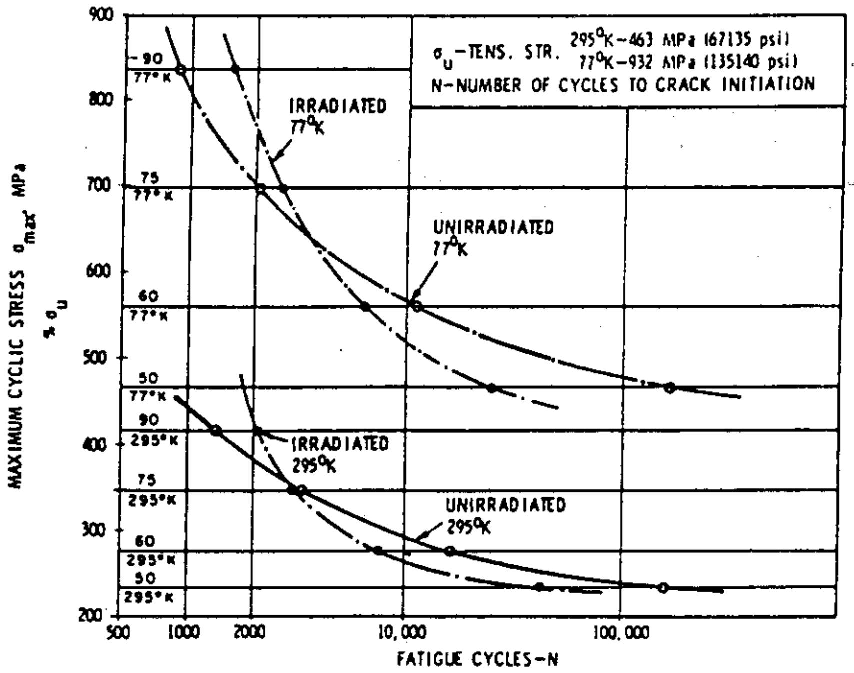

Fig.3.9 Tensile fatigue curves of unirradiaited and irradiated G-11CR.

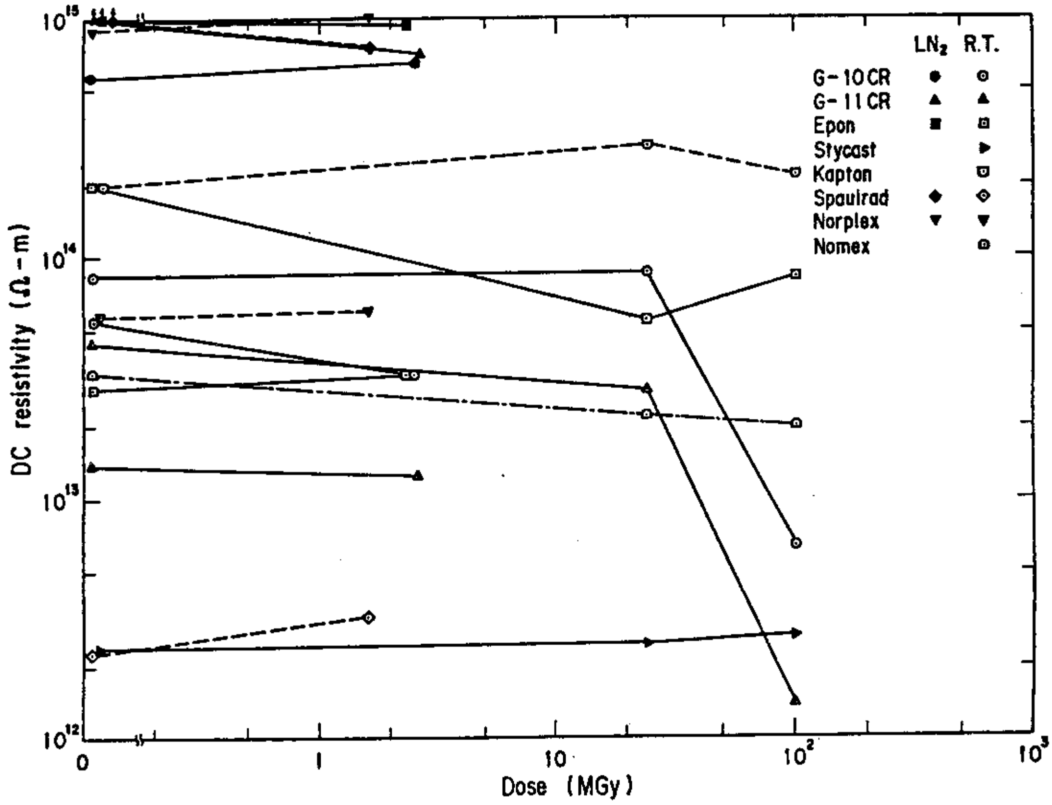

Fig.4.1 DC resistivity of various insulators after irradiation at liquid helium temperature.

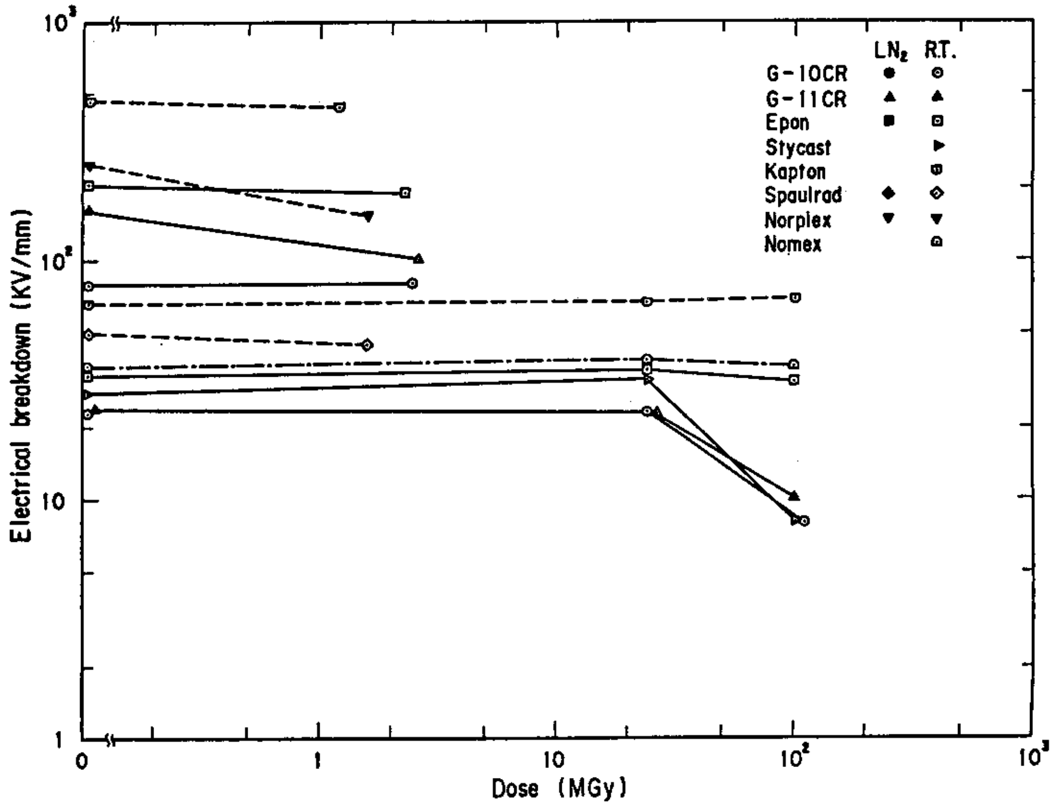

Fig.4.2 Electrical breakdown of various insulators after irradiation at liquid helium temperature.

Reference

[1] B.S.Brown, J.Nucl.Mater.97(1981)1.

[2] F.W.Clinard, Jr. and G.F.Hurley, J.Nucl.Mater.103&104(1981)705.

[3] R.D.Hay and E.J.Rapperport, ORNL/TM-2643(1976)

[4] D.C.Phillips, AERE-R8923(1978)

[5] M.A.Abdou, J.Nucl.Mater.72(1978)147.

[6] S.Nishijima and T.Okada, Teion Kogaku 14(1979)99 (In japanese).

[7] Van der Klein, RCN-240(1975)

[8] R.R.Coltman,Jr. and C.E.Klabunde, DOE/ER-0113/1(1982)101.

[9] T.Kato and S.Takamura, Teion Kogaku 18(1983)193 (In Japanese).

[10] S.Takamura and T.Kato, J.Nucl.Mater. 103&104(1981)729.

[11] R.R.Coltman, C.E.Klabunde, R.H.Kermohan, and C.J.Long, ORNL/TM-7077 (1979)

[12] G.F.Hurley and J.D.Fowler,Jr., DOE/ER-0113/2(1983)61.

[13] R.R.Coltman,Jr., C.E.Klabude, and C.J.Long, SDD No.81-10(1981).

[14] JAERI,"Kakuyugo kenkyu kaihatsu no genjo",(1983) (In Japanese).

[15] R.R.Coltman,Jr. and C.E.Klabunde, J.Nucl.Mater.113(1983)268.

[16] S.Takamura and T.Kato, Cryogenics (1980)441.

[17] R.R.Coltman,Jr. and C.E.Klabunde, J.Nucl.Mater. 103&104(1981)717.

[18] H.Yamaoka and S.Tagawa, Nippon Genshiryoku Gakkai Shi 26(1984) 739 (In Japanese)

[19] H.Schombacher and A.Stolarz-lzycka, CERN 79-04(1979),79-08(1979).

[20] B.Korukanda, J.C.Conway,Jr. and R.A.Queeney, J.Nucle.Mater.115 (1983)197.

[21] F.W.Clinard,Jr. and G.F.Hurley, J.Nucl.Mater. 103&104(1981)705.

7.1.3 Radiation Effects on Passive Shell Materials

S. Tsujimura*, H. Iida and T. Tone

Japan Atomic Energy Research Institute
801-1 Naka-machi, Naka-gun, Ibaraki, Japan

* On leave from Mitsubishi Heavy Industries, Ltd.,
Tokyo, Japan

The elongated plasma has a vertical positional instability. In order to stabilize it active and passive coils are required. Active coils are provided out of blankets or shields to control the vertical instability. However it can not cope with rapid movements of plasma. Consequently, it is necessary to place conducting passive shell as near plasma as possible. Since electric resistance of shell determines electric time constant of shell, when shape is fixed the smaller resistance is preferable for the shell material.

Candidate passive shell materials are copper, aluminum, beryllium, and lead. The resistivity of copper and aluminum are small. Other candidates which have small resistivity are silver and gold. But they are too expensive. The resistivities of beryllium and lead are larger than those of copper and aluminum, but beryllium and lead can serve as neutron multipliers as well, and then the larger allowable thickness for shell can compensate to some extent for their larger resistivities.

We will report the materials' data such as electrical resistivities, ductilities, swelling, neutron absorption. And we will evaluate their applicabilities for the passive shell.

The operating temperatures expected for these materials are assumed to be 20 through 200°C. Copper data are for OFHC grade copper. Aluminum data are for 1100 aluminum.

1. Copper

1.1 Electrical resistivity

The resistivities of copper and copper alloys are shown in Fig. 1.1.1 [1] and Fig. 1.1.2 [2]. The temperature coefficents of electrical resistivities for the copper elloys are little different from that of OFHC copper as shown in Fig. 1.1.1. The resistivity of the alloy doped 1 atom % Co at room temperature is sensitive to the heat treatments [2].

According to Matthiessen's rule the electrical resistivity $\rho(T)$ of metal is expressed at any temperature as follows:

$$\rho(T) = \rho_o + \rho_{Ph}(T) \quad , \qquad (1.1.1)$$

where ρ_o is the residual resistivity, and $\rho_{Ph}(T)$ is the resistivity at temperature T due to electron scattering by thermal vibration of lattices. The residual resistivity ρ_o can be divided further as follows:

$$\rho_o = \rho_D + \rho_{imp} \quad , \qquad (1.1.2)$$

where ρ_D is the resistivity due to the defects (e.g. point defects, dislocation, and voids), and ρ_{imp} is the resistivity due to the impurities. The electrical resistivity increases with defects and impurities by neutron irradiation. The impurity resistivity increases due to transmutations. ($\rho_T \approx \Delta\rho_{imp}$)

1.2 Ductility

Elongation of OFHC copper is shown in Fig. 1.2.1[1]. Large elongation can be obtained by thermal treatment.

Effect of neutron irradiation on room temperature elongation of copper is shown in Fig. 1.2.2[7,8,9,10]. Although the total elongations of copper irradiated at 60~100°C are very scattered, it can be seen that the elongation is reduced by irradiation. The total elongation falls rapidly at the fluence of 10^{18}~10^{20}n/cm^2. However is seens to decrease slowly for higher fluences. The same tendency is usually seen for other materials that is face-centered cubic metal such as aluminum. The elongation of copper irradiated at 327° does not change by neutron irradiation.

The temperature dependence of the elongation for copper irradiated with 7.9×10^{19} n/cm^2 (epithermal) of fluence at temperature below 100°C is shown in Fig.1.2.3[8]. Although the data are very scattered, there does not appear any change of the elongation for room temperature to 200°C.

It is difficult to estimate the elongation at the fluence of 1.0×10^{22} n/cm^2 (E>1 MeV). If the loss of elongation obeys the dushed curves, the elongation of 5% is expected at the fluence of 6 MWyr/m^2 (≃2~3×10^{22}n/cm^2).

1.3 Swelling

The dependence of the swelling of copper on neutron fluence is shown in Fig. 1.3.1[9,11,12,13,14]. The range of irradiation temperature is 250°C to 450°C. The maximum swelling for the fluence of 10^{22}n/cm^2 (E<1 MeV) is estimated to be 20~30% extrapolating from this figure.

The temperature dependence of the swelling of copper is shown in Fig. 1.3.2[13,14]. As the fluence increases the peak of swelling appears to shift to the lower side. The swelling at 200°C is a half or a third of the maximum swelling, and there is placticaliy no swelling at temperatures lower than 130°C for the fluence up to 5×10^{20} n/cm^2. It is necessary to study the swelling at temperatures between 100°C and 200°C and the swelling for fluences above 10^{21} n/cm^2.

The swellings of copper doped some elements are shown in Table 1.3.1[3]. The irradiation fluences is 5×10^{20} n/cm^2 and the irradiation temperature is 250°C. These elements are effective for the reduction of the swelling of copper.

The swelling of copper on irradiation with 200 keV Cu^+ ion to 60 dpa is shown in Fig. 1.3.3[15]. The maximum swelling of copper alloys on the same irradiation is shown in Fig. 1.3.4[15]. The measurements show a strong dependence on the concentration of solute. Alloys of a 1 atom% solute show more swelling than pure copper, and alloys of 1 atom% show less swelling. Especially, alloy of 1 atom% Au or Be shows no void swelling.

The maximum of swelling in Fig. 1.3.3 occurs about 470°C. Damage rate in the ion irradiation is for more large than that in the neutron irradiation. It is thought that the higher damage rate in ion irradiation causes the higher temperature for maximum swelling and lower swelling rate in comparison with neutron irradiation.

The resistivity measured at 4.2 K after exposure at 60°C in the fission reactor is shown in Fig. 1.I.3 [3]. The increase rate of the defect resistivity ρ_D reduces as fluence increases. Contrastingly, the increase rate of the impurity resistivity is almost constant against fluence.

The annealing effects on the resistivity of copper at room temperature after neutron irradiation at 40 ∿ 45°C is shown in Fig. 1.1.4 [4]. The significant recovery of irradiation-induced defects occurs at room temperature in a rather long period.

The short period annealing characteristics of electrical resistivity in copper irradiated at 60°C is shown in Fig. 1.1.5 [5]. The recovery of defects up to 200°C is not so large.

Neutrons produce Ni, Zn and Co in copper by transmutations. The electrical resistivity increases due to these impurities are shown in Fig. 1.1.6 [6]. The specific resistivities of these element addition by small amount are 125 μΩcm/unit fraction for Ni, 53 μΩcm/unit fraction for Zn and 630 μΩcm/unit fraction for Co respectively. The resistivity increase due to impurities approximately follows the simple addition rule.

We will estimate the resistivity increase of copper irradiated by the neutron with spectrum at first wall. The resistivity increase due to neutron induced defects satulate 0.08 μΩcm at room temperature. Amount of transmutations is approximately proportional to fluence. Ni, Zn, and Co produced by the neutron fluence of 3 MWyr/m^2 are 1.2 atom%, 0.723 atom%, and 0.022 atom% respectively. The resistivity increase due to transmutations is calculated to be 2.064 μΩcm for a fluence of 3 MWyr/m^2. The total resistivity increase due to neutron irradiation for 3 MWyr/m^2 is estimated at 2.14 μΩcm. The resistivity change by neutron irradiation with first wall neutron spectrum is shown in Fig. 1.1.7. The resistivity of copper irradiated for a fluence of 3 MWyr/m^2 at 150°C is estimated to be 4.7 μΩcm and that of 6 MWyr/m^2 at 150°C is estimated to be 7.0 μΩcm.

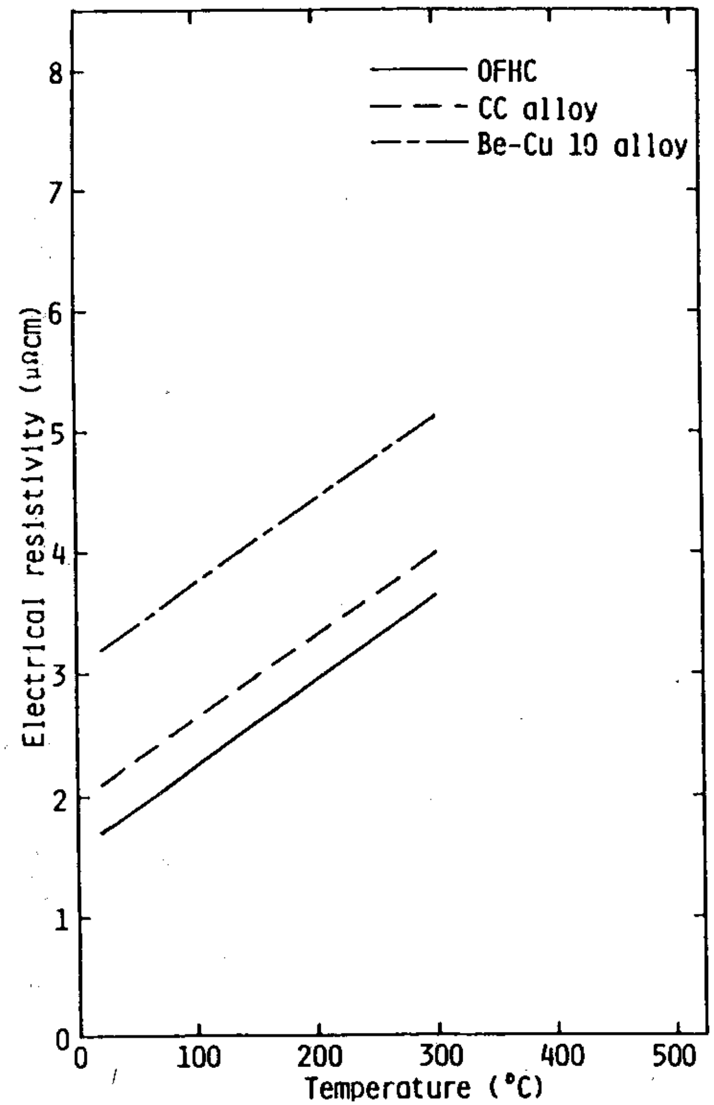

Fig.1.1.1. Temperature Dependence of Electrical Resistivities of Copper and Copper Alloys.

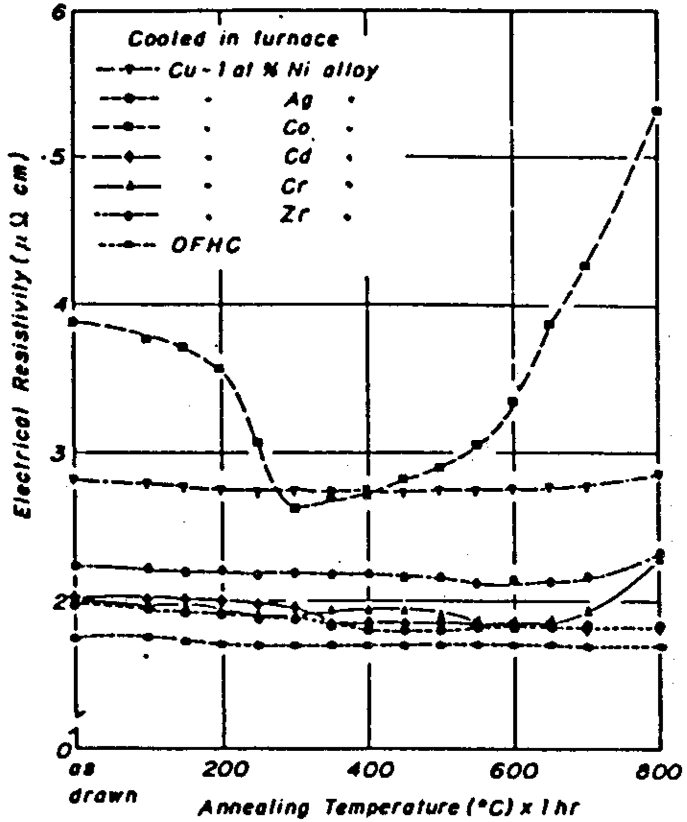

Fig.1.1.2. Changes in Electrical Resistivity of the Copper Alloys Annealed for 1hr at Various Temperatures after Furnance Cooling and Drawing.

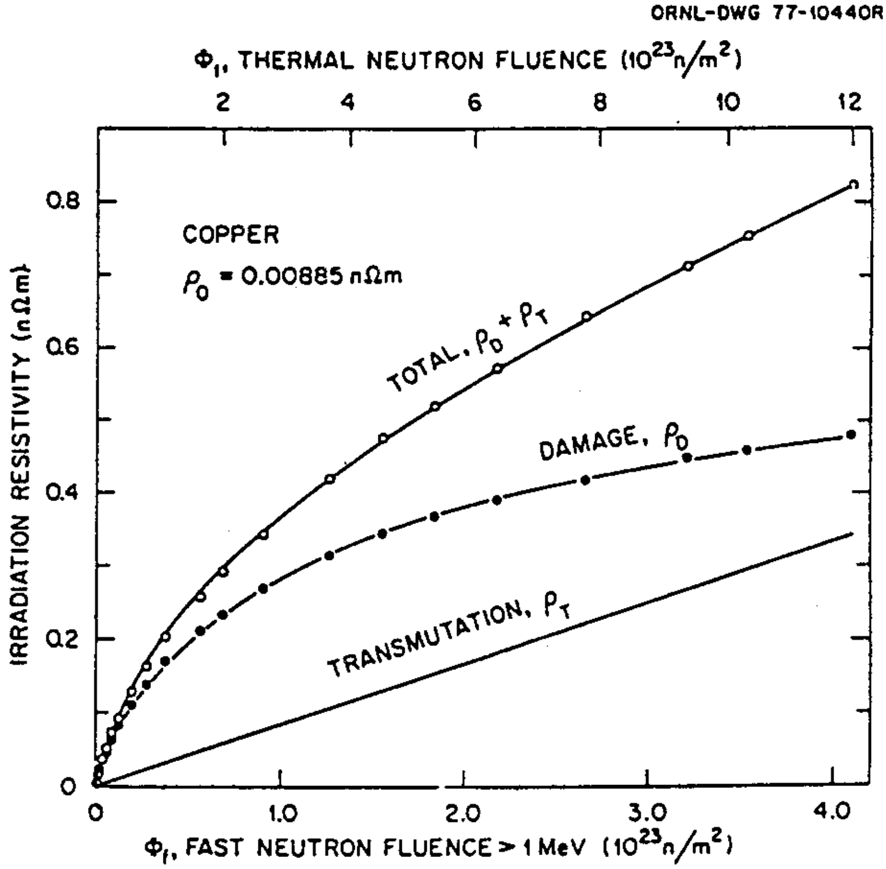

Fig.1.1.3. The total Residual-Resistivity Increase versus Thermal and Fast-Neutron Fluence for Sample Pair No.1. The Resolved Contributions due to Damage and Transmutation Resistivity are Shown for Comparison.

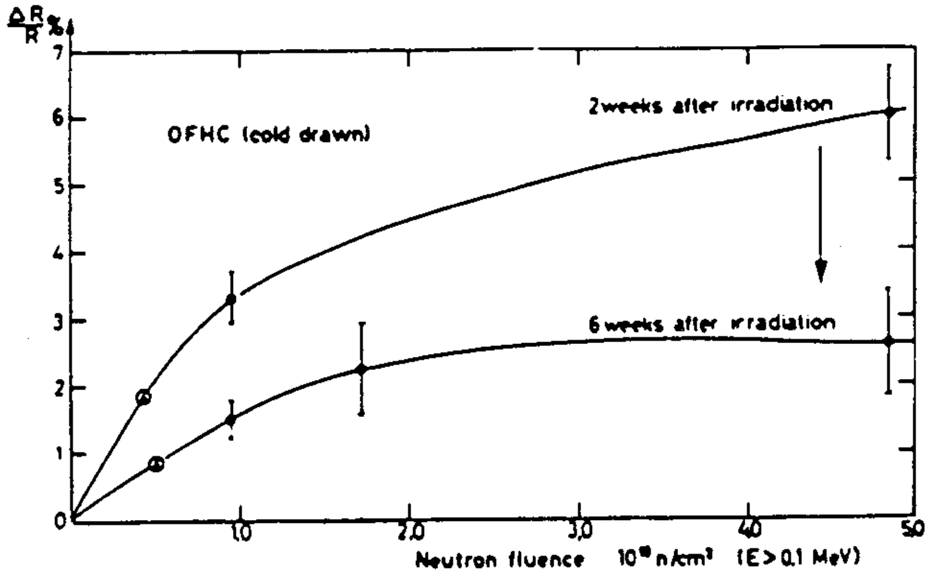

Fig.1.1.4. Annealing Effects in Irradiated OFHC Cold-Drawn Copper Wire at Room Temperature.

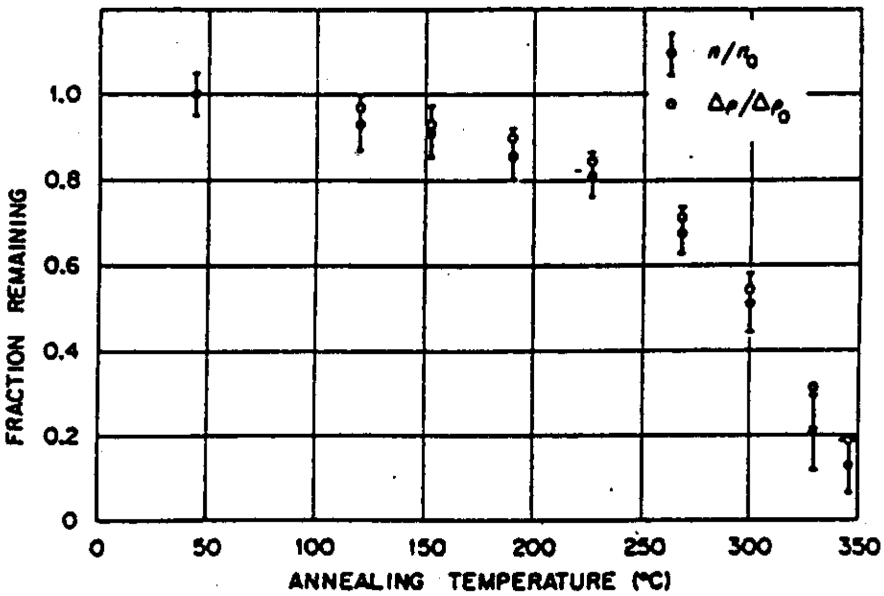

Fig.1.1.5. **Annealing characteristics of the number of point defects in loops as determined by integral diffuse scattering and the annealing characteristics of electrical resistivity in ambient-temperature neutron-irradiated copper.**

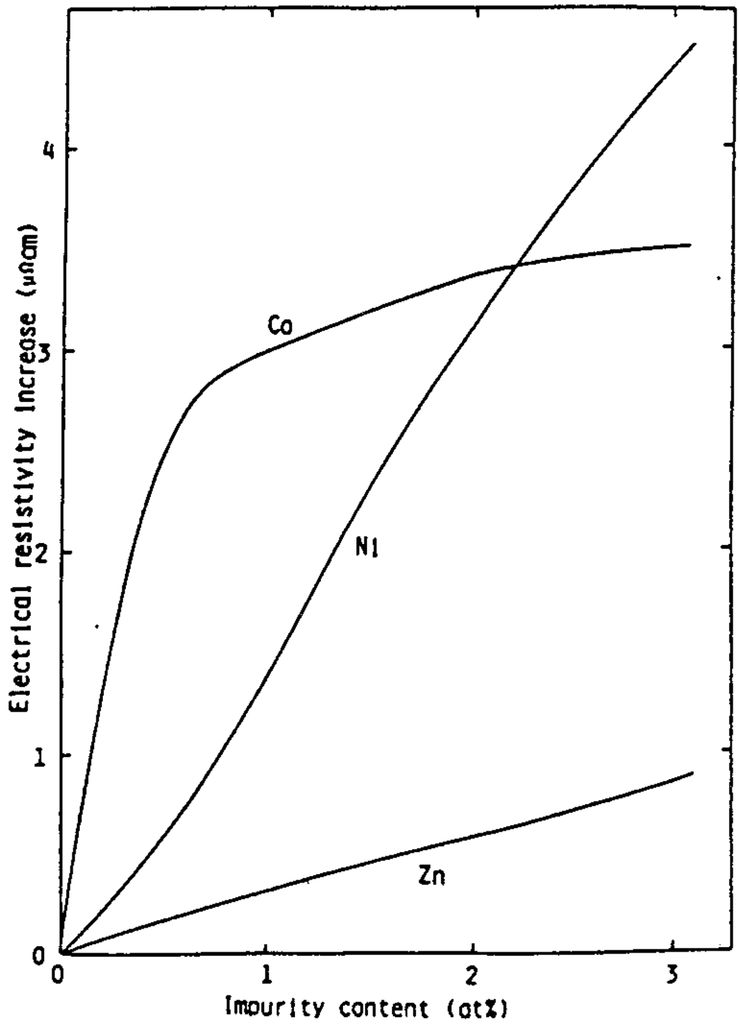

Fig.1.1.6. Electrical Resistivity Increase of Copper by Impurities.

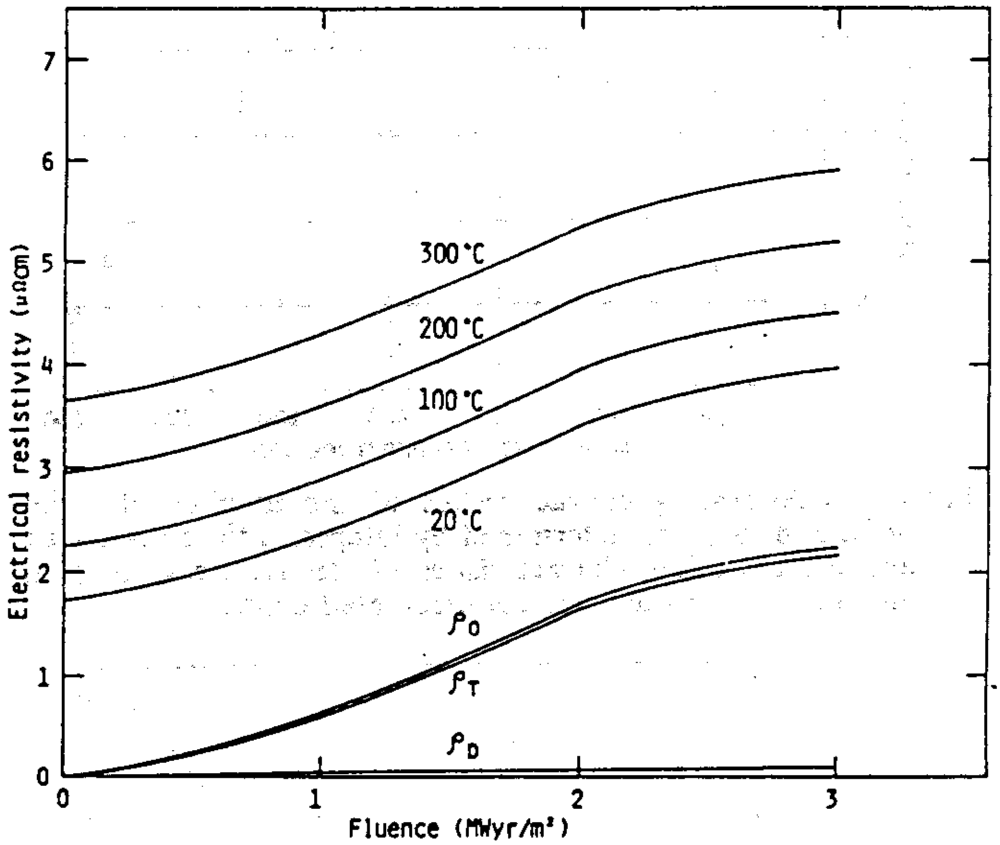

Fig.1.1.7 Effect of Neutron Irradiation on Electrical Resistivity of Copper.

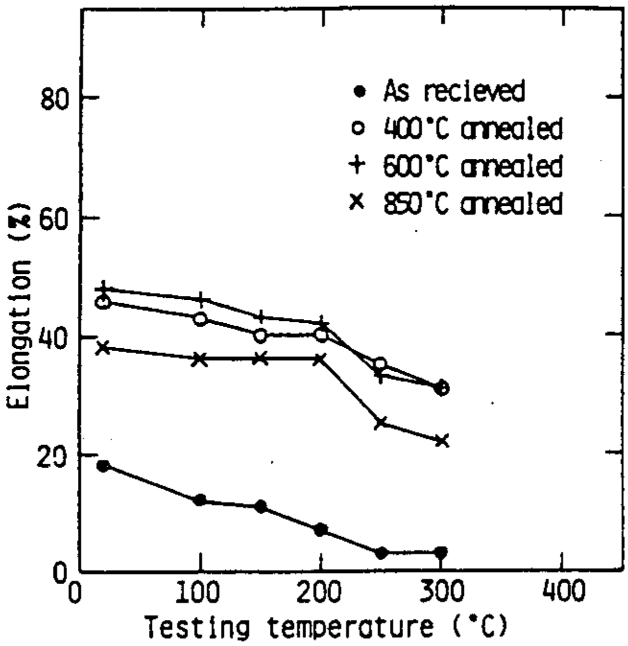

Fig.1.2.1. Effect of Heat Treatment on Elongation of OFHC Copper.

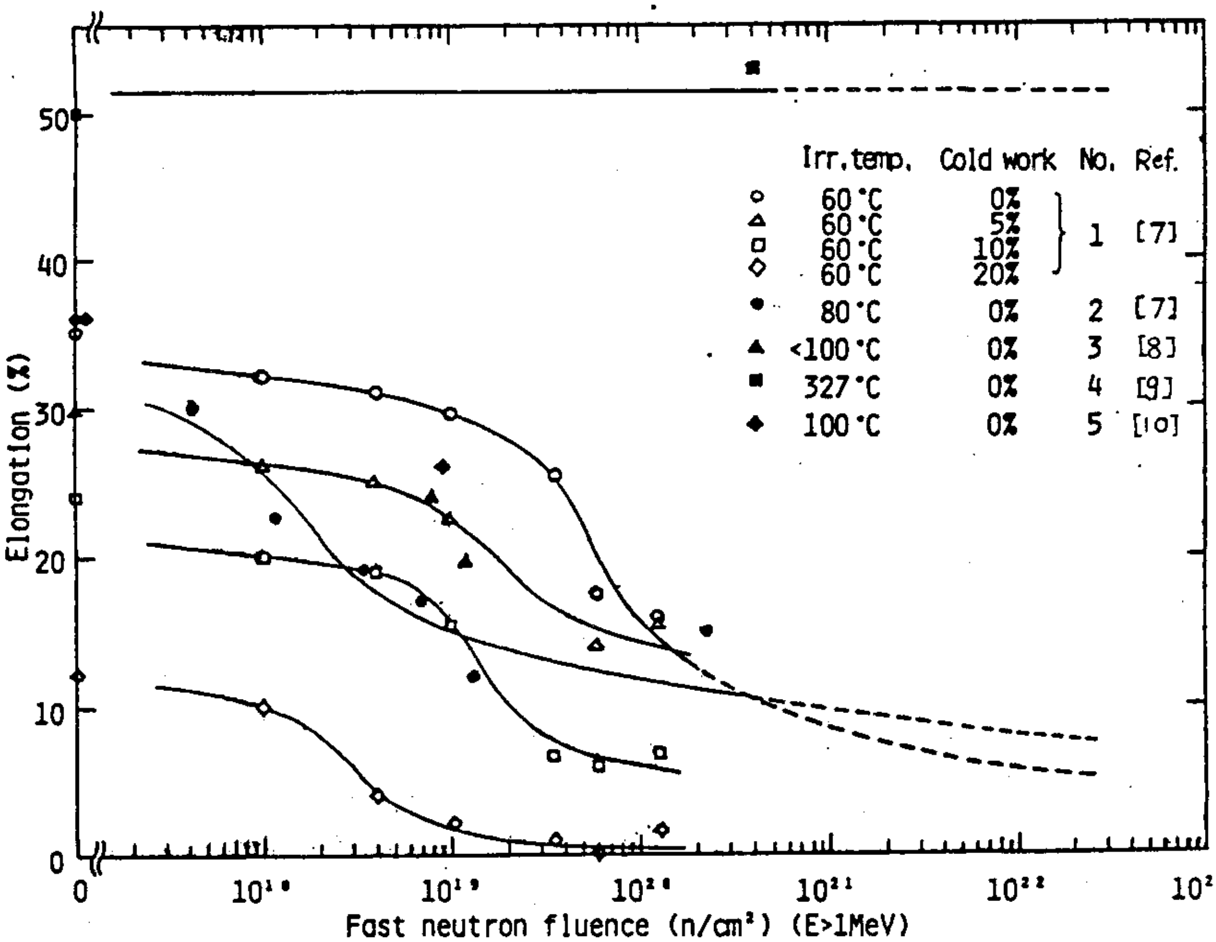

Fig.1.2.2. Effect of Neutron Irradiation on Room Temperature Elongation of Copper.

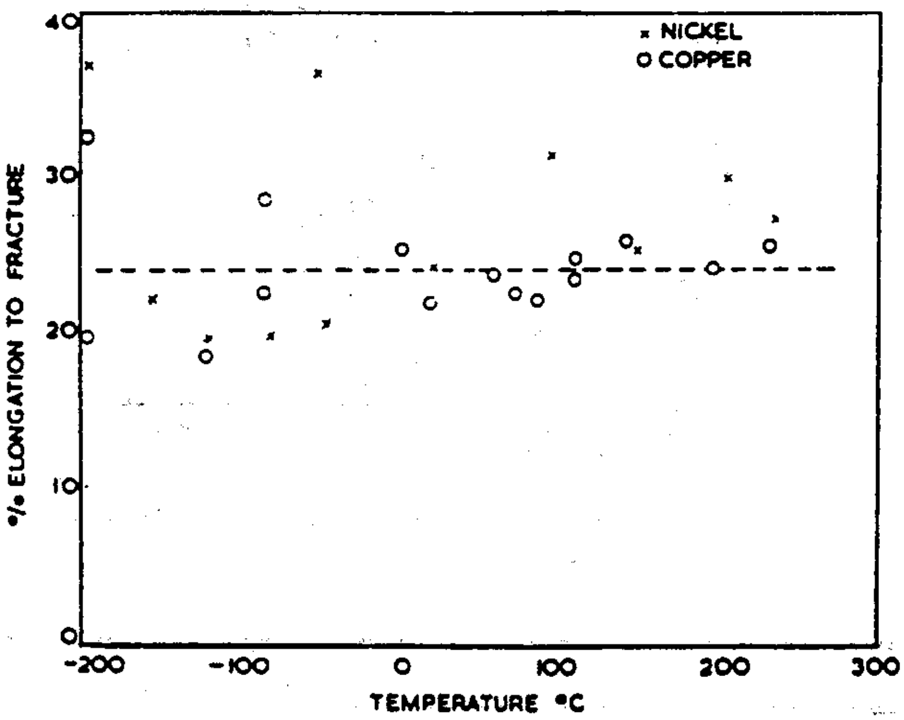

Fig.1.2.3. Elongation to fracture of irradiated copper and nickel.

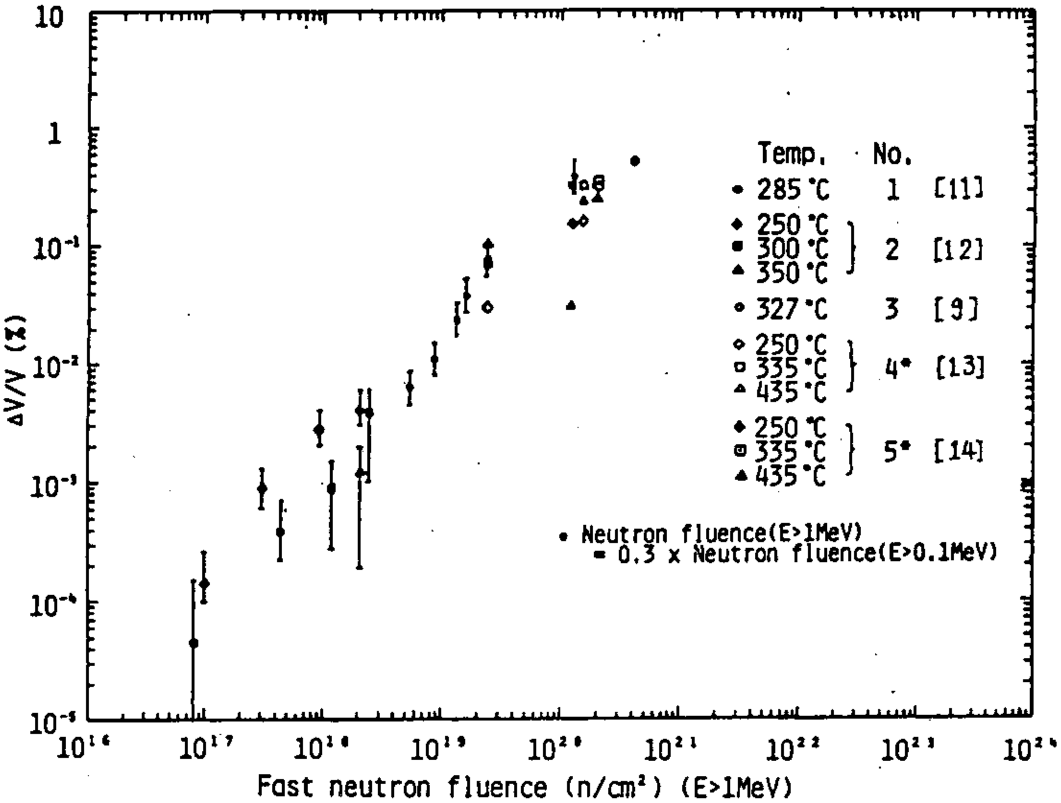

Fig.1.3.1. Neutron Irradiation Induced Swelling in Copper.

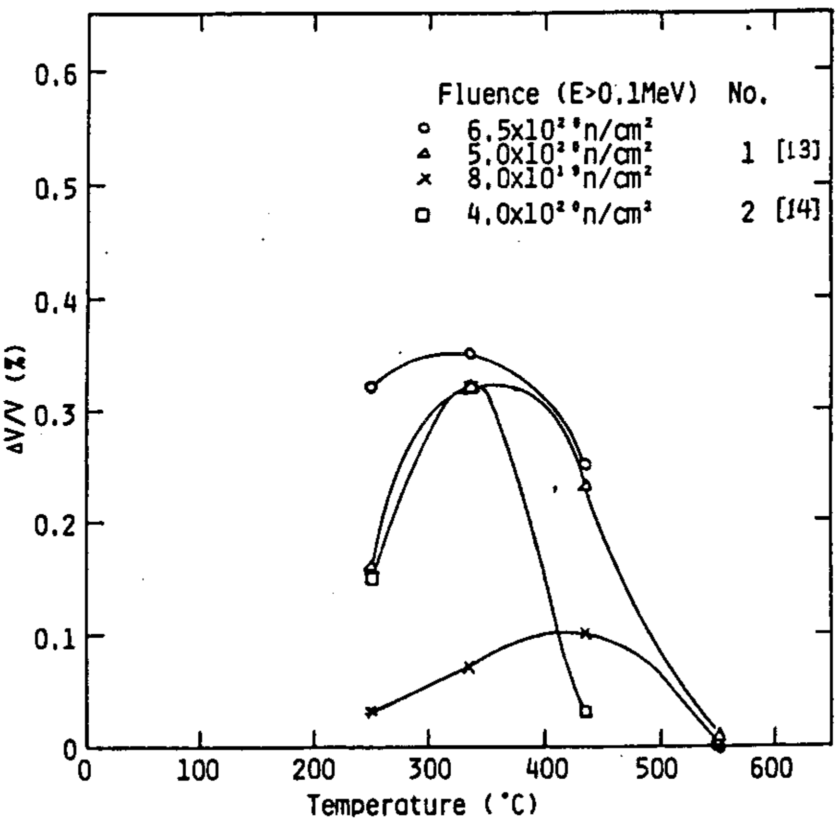

Fig.1.3.2. Temperature Dependence of Neutron Irradiation Induced Swelling of Copper.

Table 1.3.1.

Valeurs du gonflement de la densité moyenne et du diamètre moyen des cavités pour les alliages de cuivre d'énergie de faute différente (irradiation L 15–$T = 250$ °C)

Alliage	* γ_F (erg/cm²)	$\Delta V/V$ (%)	$\bar{n}$ (cav/cm³)	$\bar{d}$ (Å)
**Cu	55	0,16	$2{,}2 \times 10^{14}$	275
Cu-Ge 1%	50	0,10	$2{,}5 \times 10^{12}$	480
Cu-Ge 3%	~ 45	~ 0	quelques cavités	600
Cu-Si 1%	~ 45	~ 0	quelques cavités	120
Cu-Al 1%	~ 45	~ 0	quelques cavités	-
Cu-Al 3%	~ 30	0	quelques cavités	-
Cu-Al 5%	~ 5	0	0	-

* Les valeurs des énergies de faute d'empilement ont été tirées de ref. [10]).

** L'échantillon témoin de cuivre pur irradié dans L 15 n'ayant pu être observé on a donné ici les valeurs de l'irradiation MP 1, effectuée dans les mêmes conditions nominales.

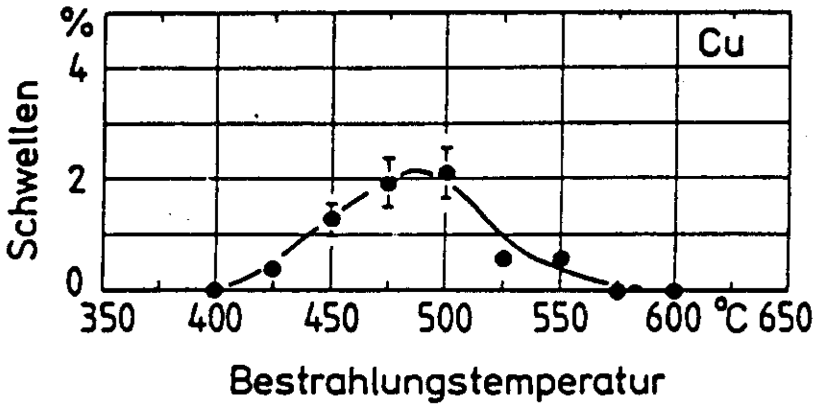

Fig.1.3.3. Schwellen von reinem Kupfer

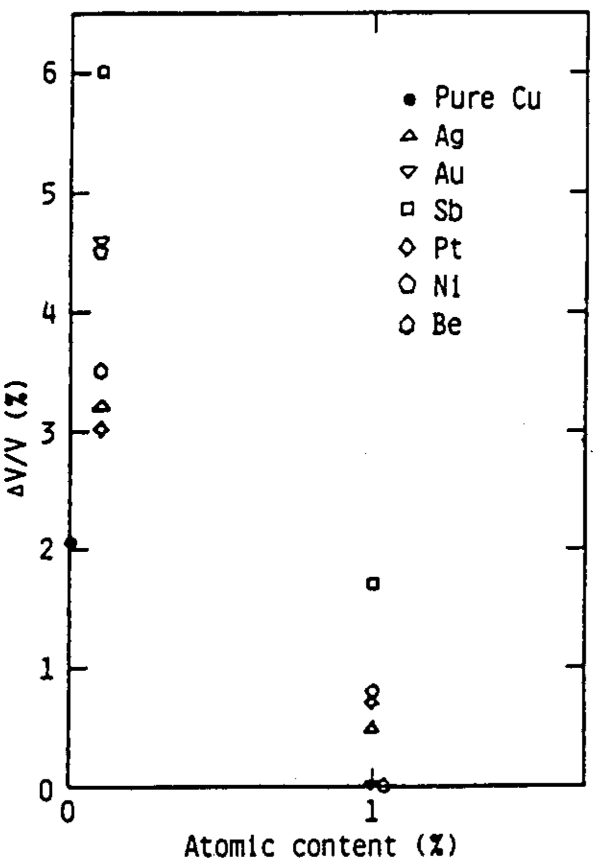

Fig.1.3.4. Effect of Solute on Swelling of Copper.

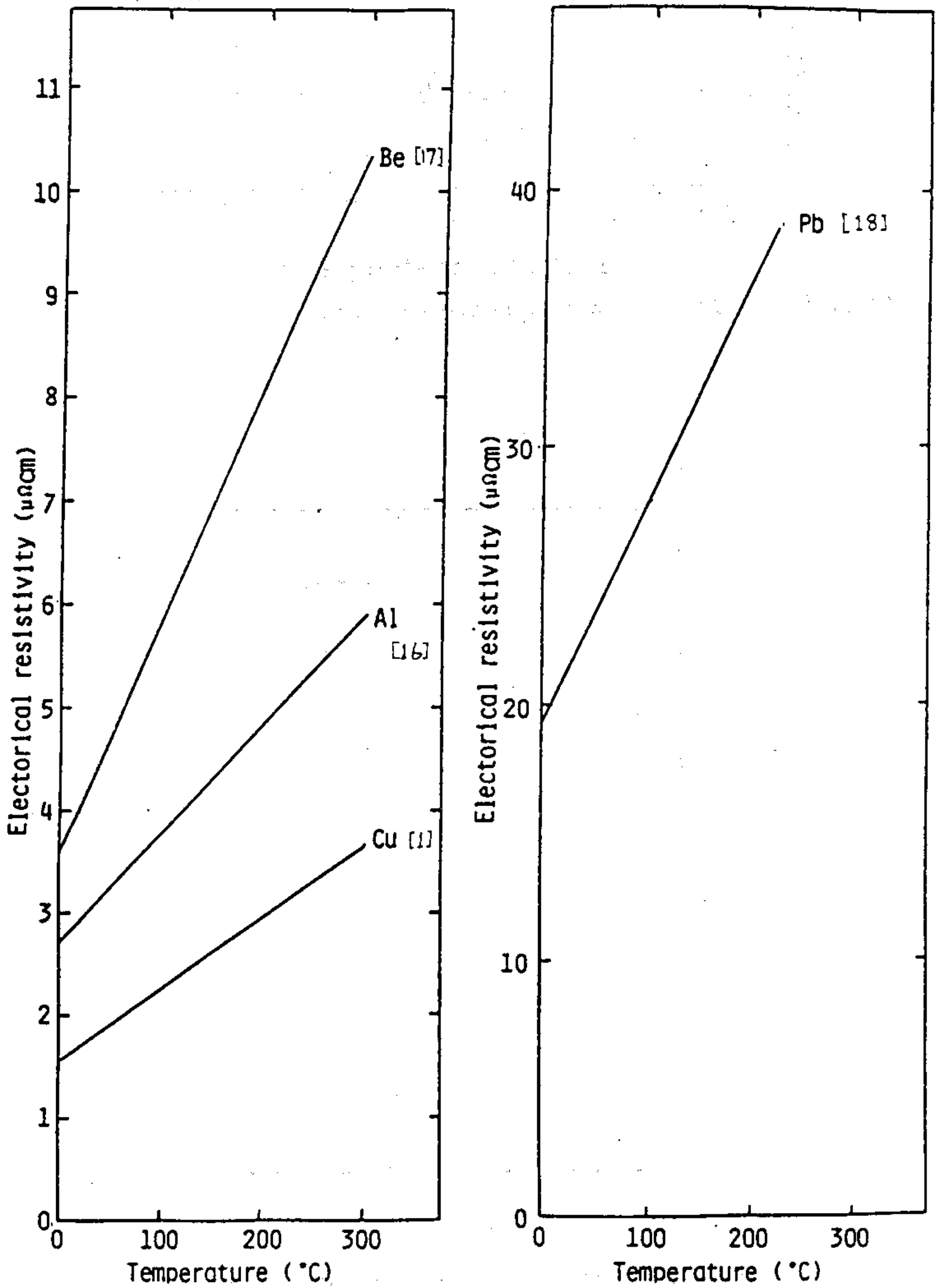

Fig.1.2.1. Temperature Dependence of Electrical Resistivities of Candidated Passive Shell Materials.

2. Aluminum

2.1 Electrical resistivity

The temperature dependence of electrical resistivity for aluminum in comparison with those for copper, beryllium and lead is shown in Fig. 2.1.1 [1,16,17,18].

The isochronal recovery of aluminum after the neutron irradiation of 2×10^{18} n/cm^2 (E>0.1 MeV) at 4.5 K is shown in Fig. 2.1.2[19]. The irradiation-induced resistivity of aluminum is recovered completely at 260 K. It can be expected that all of defect resistivity induced by neutron irradiation at temperatures above room temperature is recovered.

Neutron produces Mg, Si and Na in aluminum by transmutations. Amount of Na is very little. The electrical resistivity increase du to the impurities of Mg and Si is shown in Fig. 2.1.3[20].

The resistivity increase of aluminum irradiated by the neutron spectrum at first wall is estimated. Concentration of Mg, Si and Na transmutated by 3 MWyr/m^2 neutron irradiation are 0.214 atom%, 0.0295 atom% and 0.0001 atom%, respectively. The resistivity increase due to transmutation is calculated to be 0.2 $\mu\Omega$cm for 3 MWyr/m^2 neutron irradiation. The resistivity increase due to irradiated-induced defect is zero. The resistivity change by neutron irradiation with the first wall neutron spectrum is shown in Fig. 2.1.4.

2.2 Ductility

The effect of neutron irradiation on the temperature dependence of elongation of 1100 aluminum is shown in Fig. 2.2.1[21,22]. The elongation of aluminum irradiated to 1×10^{22} n/cm^2 (E>1 MeV) exhibits a minimum at about 250°C.

The effect of neutron irradiation on the elongation of 1100 aluminum is shown in Fig. 2.2.2[21,22]. The loss of elongation at 200°C is larger than that at room temperature. The significant loss of elongation occurs under the fluence of 10^{22} n/cm^2 and then the loss saturates.

2.3 Swelling

The swellings of aluminum and aluminum alloys are shown in Fig. 2.3.1 [22,23]. The swelling of 1100 aluminum at the fluence of 3×10^{22} n/cm^2 (E>0.1 MeV) is about 1%~5%.

The effect of isochronal annealing on swelling of 1100 aluminum irradiated to about 3×10^{22} n/cm^2 is shown in Fig. 2.3.2[24]. The swelling exhabits a minimum at about 300°C.

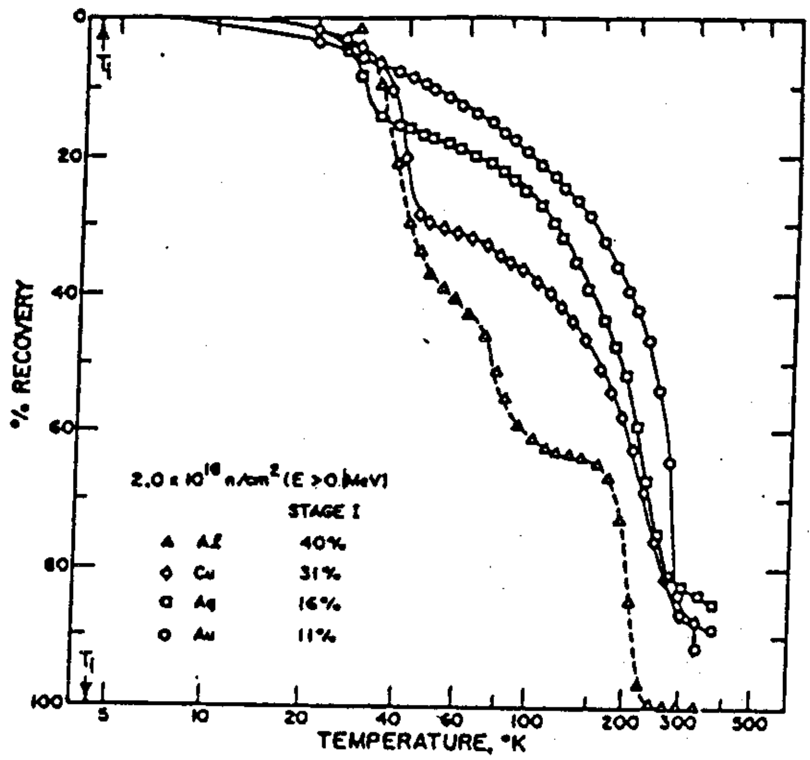

Fig.2.1.2. Recovery versus logarithm of absolute temperature showing decreased stage I and entire recovery spectra with increasing atomic mass for fcc metals.

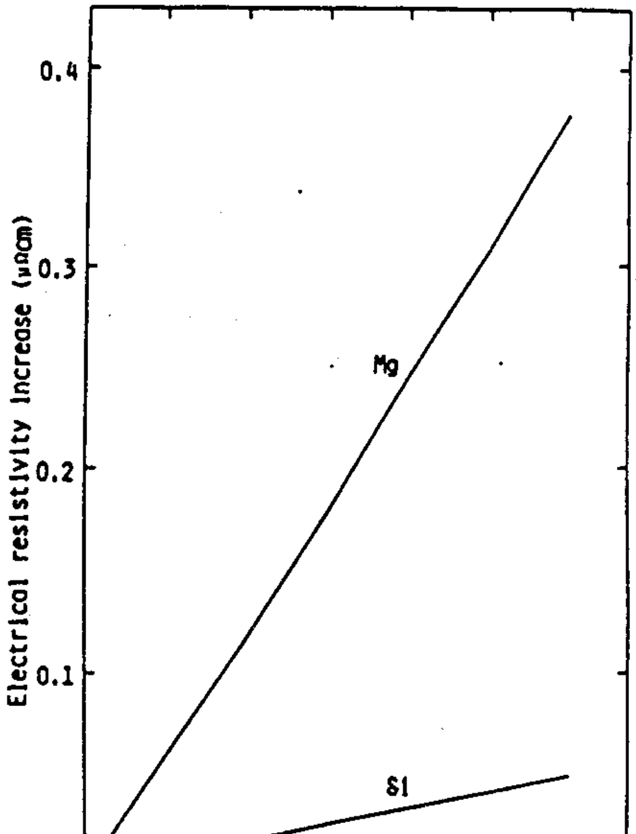

Fig.2.1.3. Electrical Resistivity Increase of Aluminum by Impurities.

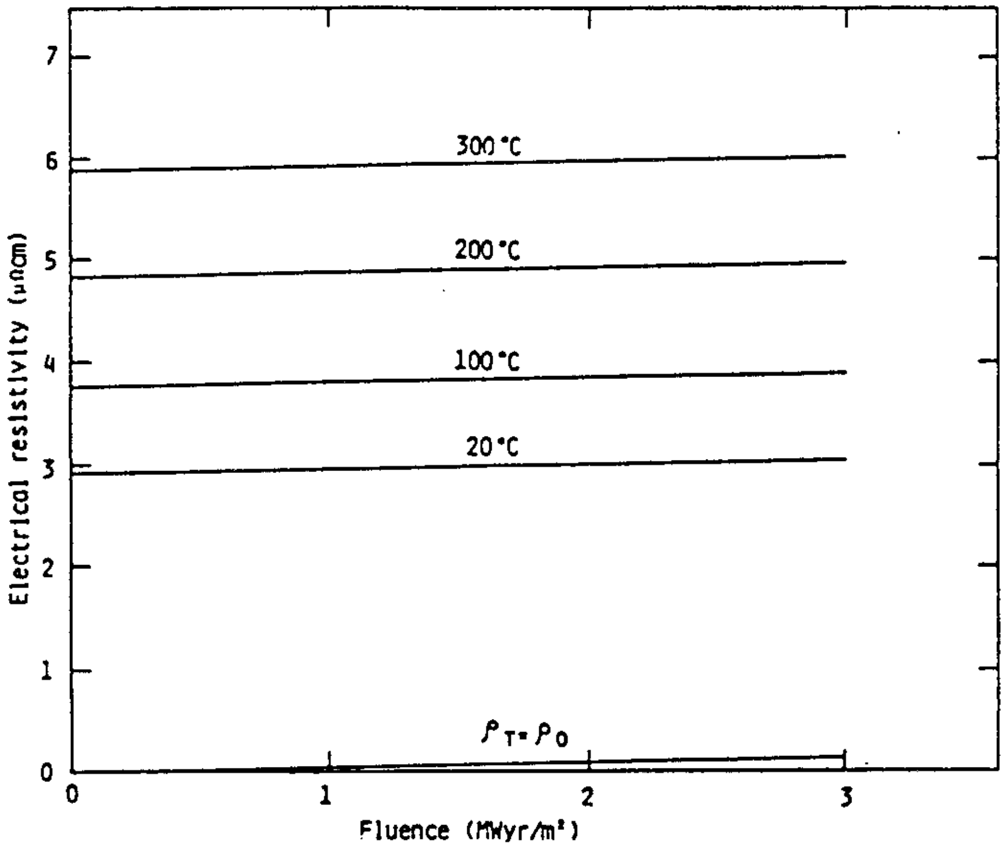

Fig.2.1.4. Effect of Neutron Irradiation on Electrical Resistivity of Aluminum.

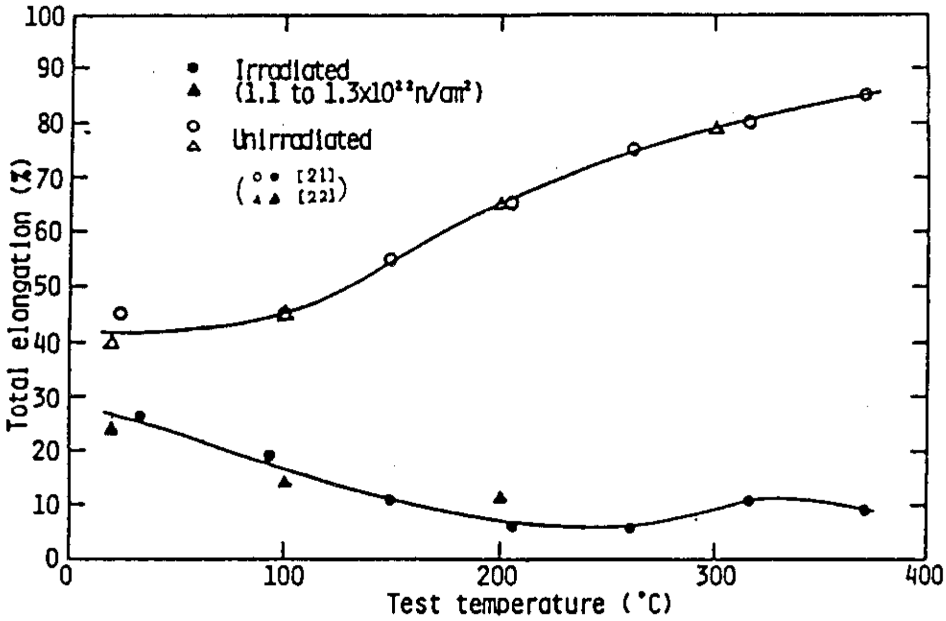

Fig.2.2.1. Effect of Neutron Irradiation on Temperature Dependence of Elongation of 1100 Aluminum.

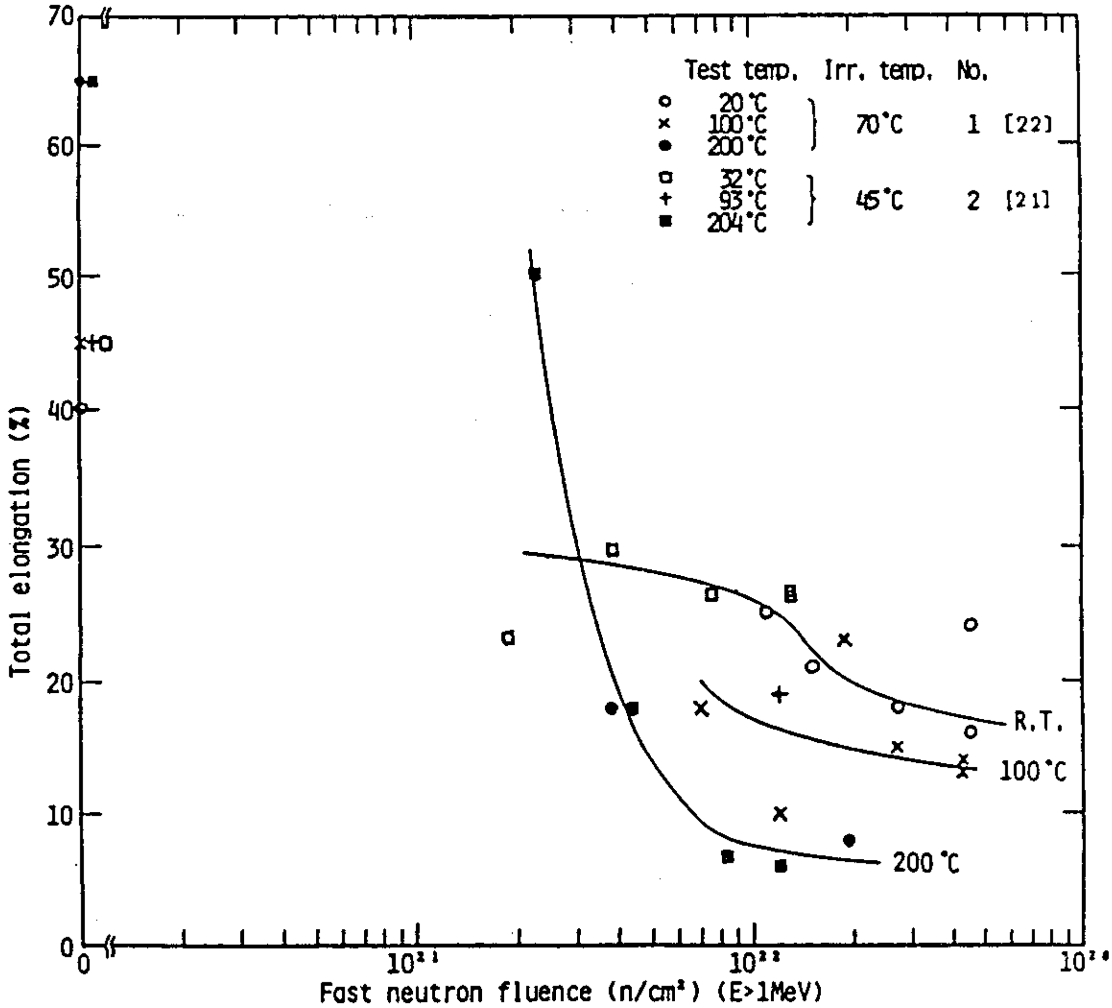

Fig.2.2.2. Effect of Neutron Irradiation on Elongation of 1100 Aluminum.

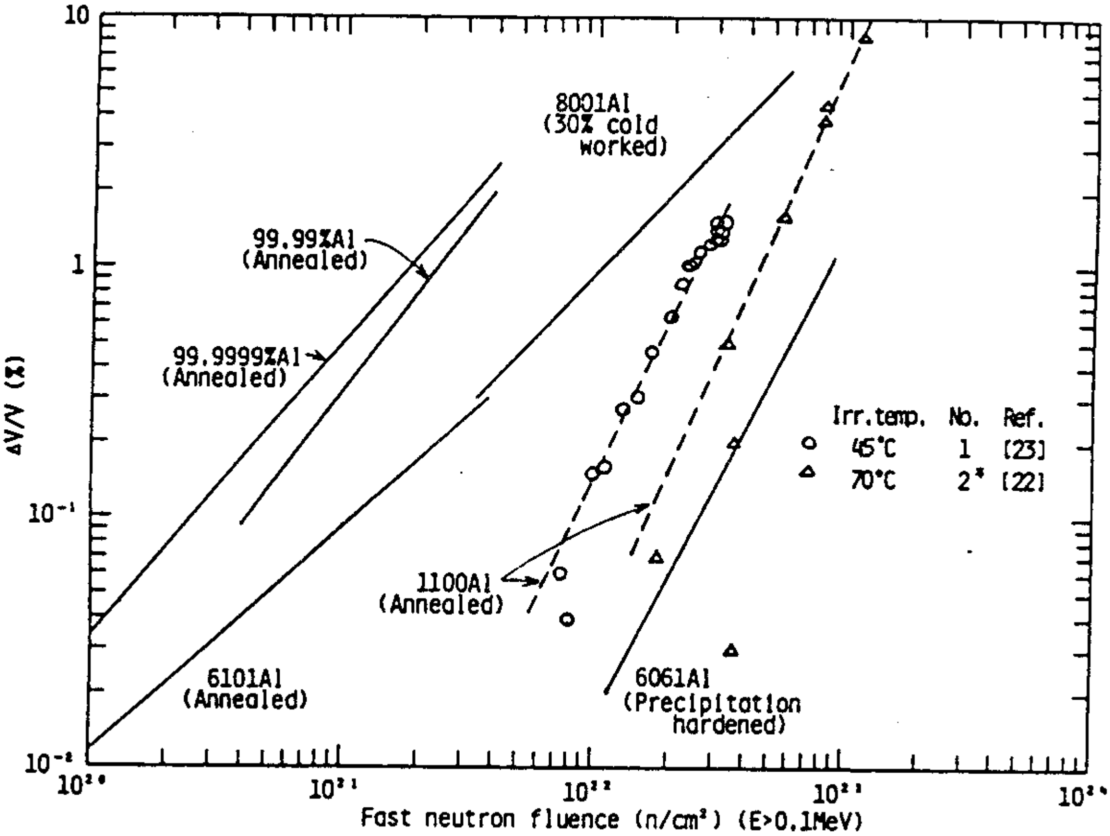

Fig.2.3.1 Irradiation-Induced Swelling in Aluminum and its Alloys.
* Neutron fluence(E>0.1MeV) = 2 x Neutron fluence(E>1MeV)

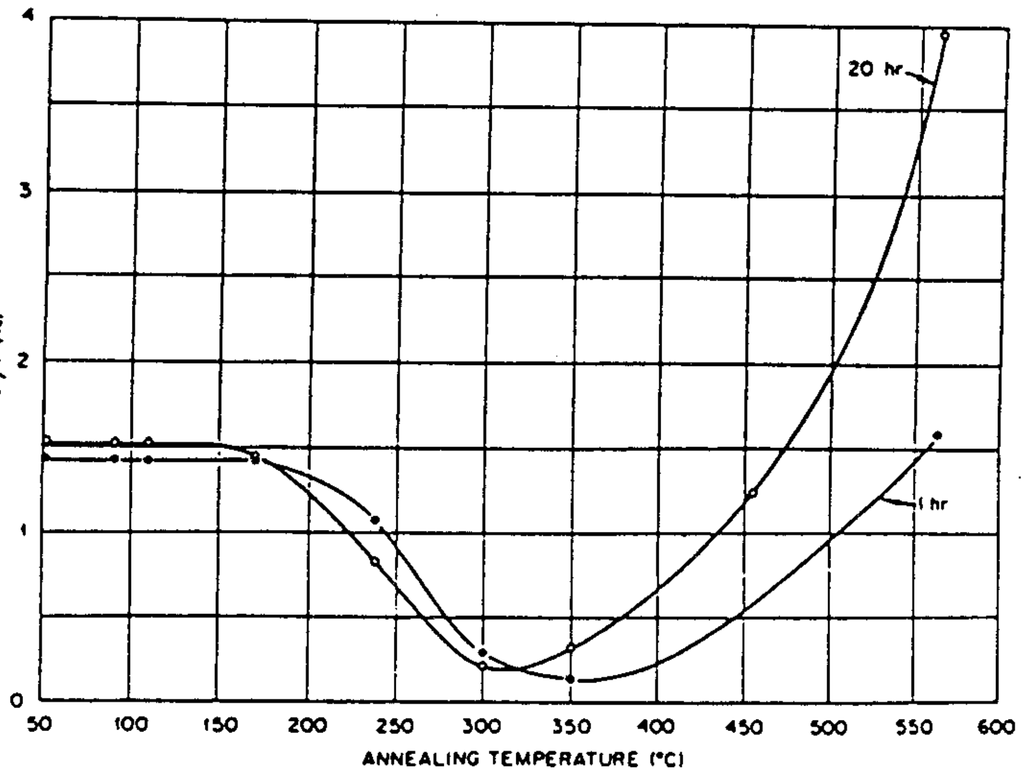

Fig.2.3.2. Effect of isochronal annealing on swelling of 1100 aluminum irradiated to about 3×10^{22} n/cm².

3. Beryllium

3.1 Electrical Resistivity

The electrical resistivity of beryllium is shown in Fig. 2.1.2[17].

The resistivity increase of beryllium irradiated at 90 K is shown in Fig. 3.1.1[25]. The isochronal reconery of resistivity of beryllium irradiated at 90 K to the fluence of 1.05×10^{19} n/cm^2 n/cm^2 (E>1.0 MeV) is shown in Fig. 3.1.2[25]. Almost all of the irradiation-induced resistivity is recovered at 330 K. But it should be noted the fluence of these data is very low.

3.2 Ductility

The elongation of beryllium is influenced by manufacturing process, distribution of impurities, and grain size. Beryllium has close packed hexagonal structure and the elongation of beryllium sheet exhabits anisotropy.

The effect of working on the elongation of beryllium is shown in Fig. 3.2.1[26]. The elongations of various form materials are shown in Table 3.2.1[17]. The maximum elongation of block material is about 4%. One of the sheet-type beryllium exhabits the elongation of 16% at room temperature. The temperature dependence of the elongation of hot-pressed beryllium is shown in Fig. 3.2.2[27]. The elongation of hot-pressed berryllium exhabits a minimum at room temperature. The elongation of other type beryllium exhabits a minimum between room temperature and 200°C.

The effect of irradiation on the elongations of sheet-type and block-type beryllium is shown in Fig. 3.2.3[28,29,30,31]. Neutron irradiation between room temperature to 350°C causes the striking loss of the longitudial elongation of sheet-type beryllium. The longitudinal elongations of sheet-type beryllium irradiated to the fluence higher than 10^{21} n/cm^2 (E>1 MeV) are estimated to be zero. The transverse elongation of unirradiated sheet-type beryllium is only about 0.2% at room temperature, and irradiation almost does not change it. The elongation of block-type beryllium irradiated to the fluence higher than 3×10^{21} n/cm^2 (E>1 MeV) is estimated to be almost zero.

Beryllium has been used as a reflector in some fission reactors, its life time fluence is about 10^{22} n/cm^2 (E>1 MeV) and in limited by thermal and swelling stress.

3.3 Swelling

The swelling of beryllium irradiated at room temperature and up to about 120°C is shown in Fig. 3.3.1[29,32,33,34,35].

The effect of postirradiation annealing on swelling of beryllium irradiated at 70°C to a fluence of about 7.6×10^{21} n/cm^2 (E>1 MeV) is shown in Fig. 3.3.2[35]. The large swelling occurs at higher temperature than 700°C.

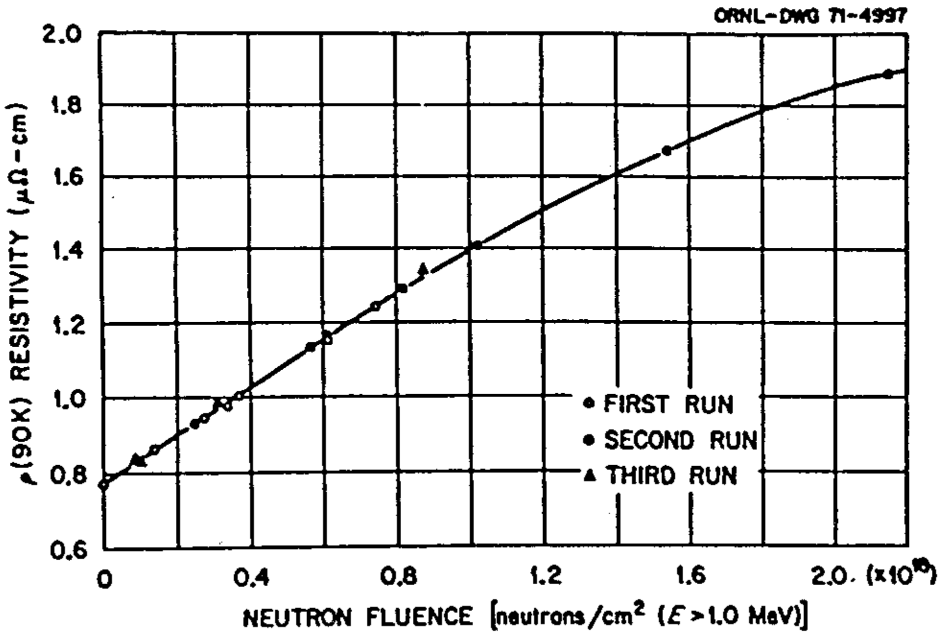

Fig.3.1.1. Electrical resistivity at 90K versus fluence.

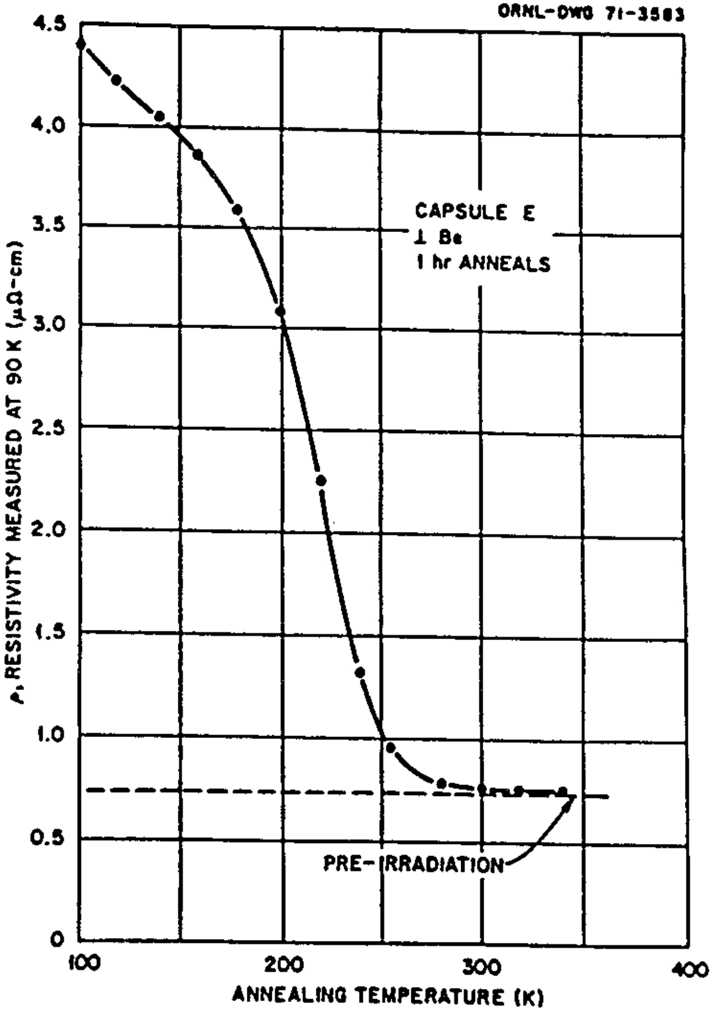

Fig.3.1.2. Isochronal recovery of electrical resistivity.

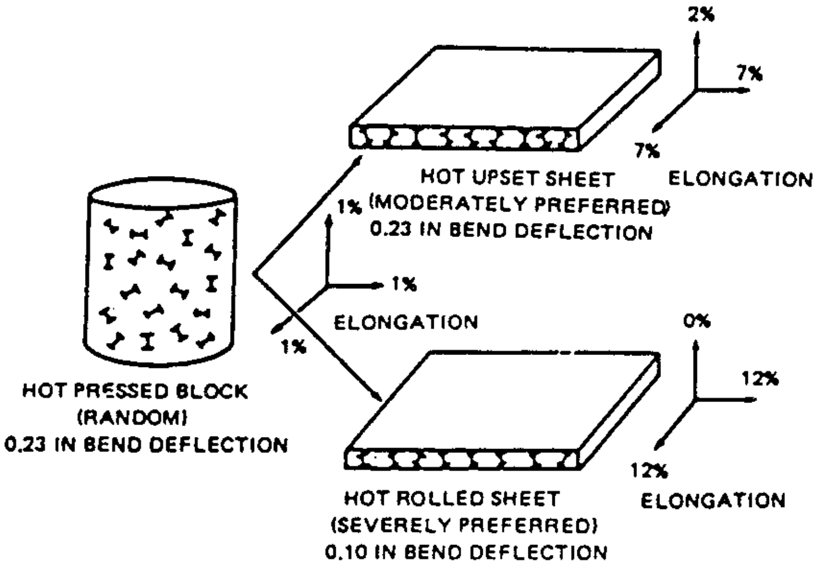

Fig.3.2.1. Effect of working and degree of preferred orientation on tensile ductility of beryllium hot-pressed block and sheet.

Table 3.2.1. Typical tensile properties of commercially avairable forms.

Material	Test direction	Ultimate tensile strength, F_{tu} [ksi (N/mm²)]	Yield strength 0.2% offset, F_{ty} [ksi (N/mm²)]	Elongation, e (%)[a]
Block				
normal-purity (hot-pressed)[b]				
structural grade	L[c]	53(370)	38(266)	2.3
	T	56(390)	39(273)	3.6
thermal or brake grade	L[c]	42(294)	28(196)	2.7
	T	46(322)	28(196)	4.6
high-purity (isopressed)	L	65(455)	41(287)	3.9
	T	65(455)	41(287)	4.4
high-oxide instrument grade				
(hot pressed)	L	68(476)	58(406)	1.5
	T	73(511)	59(413)	2.7
fine grain size (isopressed)	L	84(580)	59(407)	3.7
	T	85(587)	59(407)	4.2
Sheet (0.040–0.250 in. thick)				
normal-purity powder		77(531)	54(372)	16
normal-purity ingot[78]		51(352)	25(172)	7
Extrusions				
normal-purity powder		95–100(655–690)	50–75(345–518)	8–13
high-purity powder		95–120(655–828)	50–75(345–518)	8–13
Forgings				
normal-purity[a,71]		70–87(483–600)	63–87(435–600)	0–4.5
Wire (0.002–0.025 in. diameter)				
high-purity ingot[78]		140(966)	115(793)	3

[a]Elongation in 2 in., except 10 in. for wire.
[b]Structural grade contains about 1.8% BeO and thermal or brake grade about 0.9%.
[c]L and T refer to longitudinal and transverse test directions.

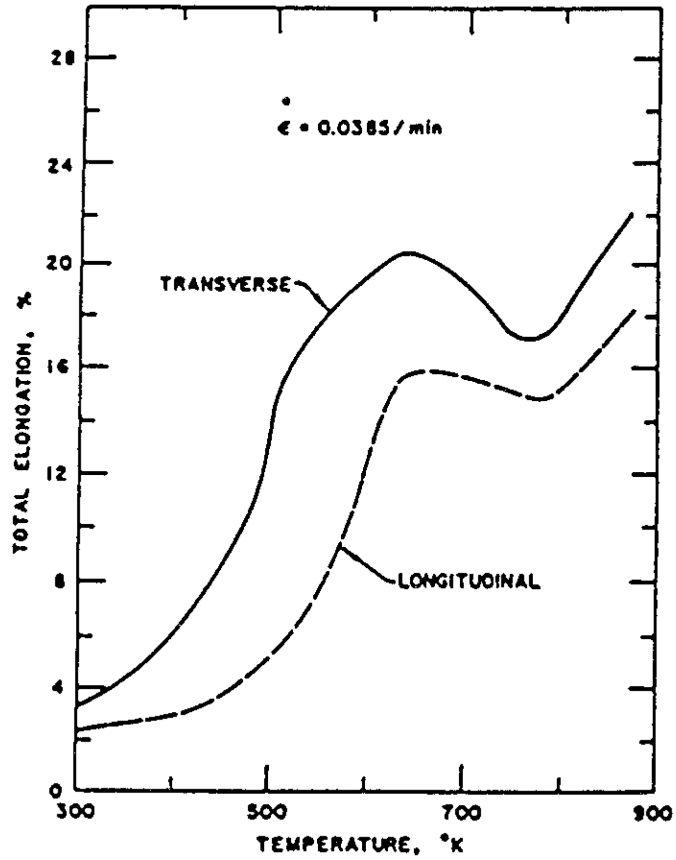

Fig.3.2.2. Temperature dependence of total elongation of HP21 beryllium.

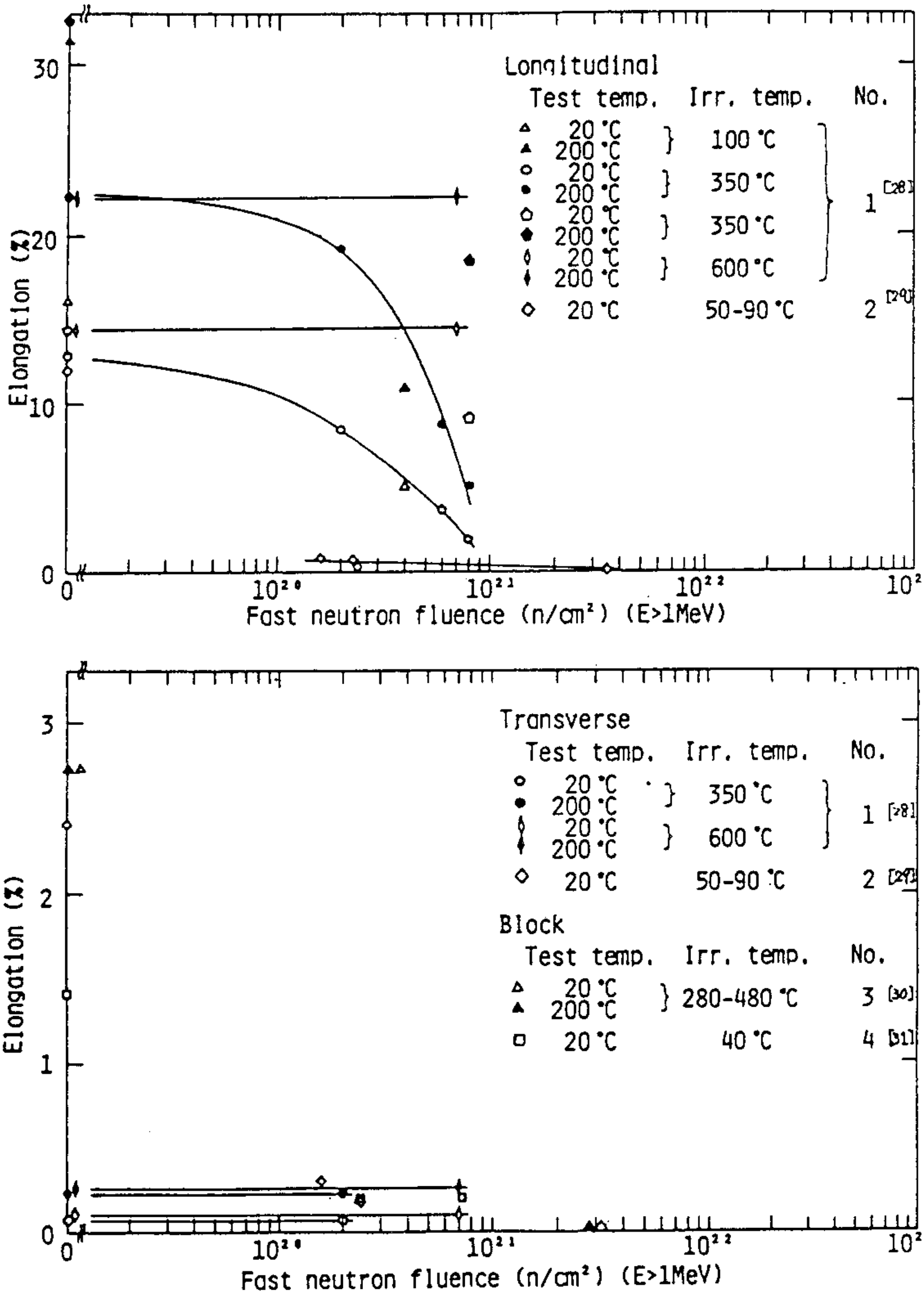

Fig.3.2.3. Effect of Neutron Irradiation on Elongation of Beryllium.

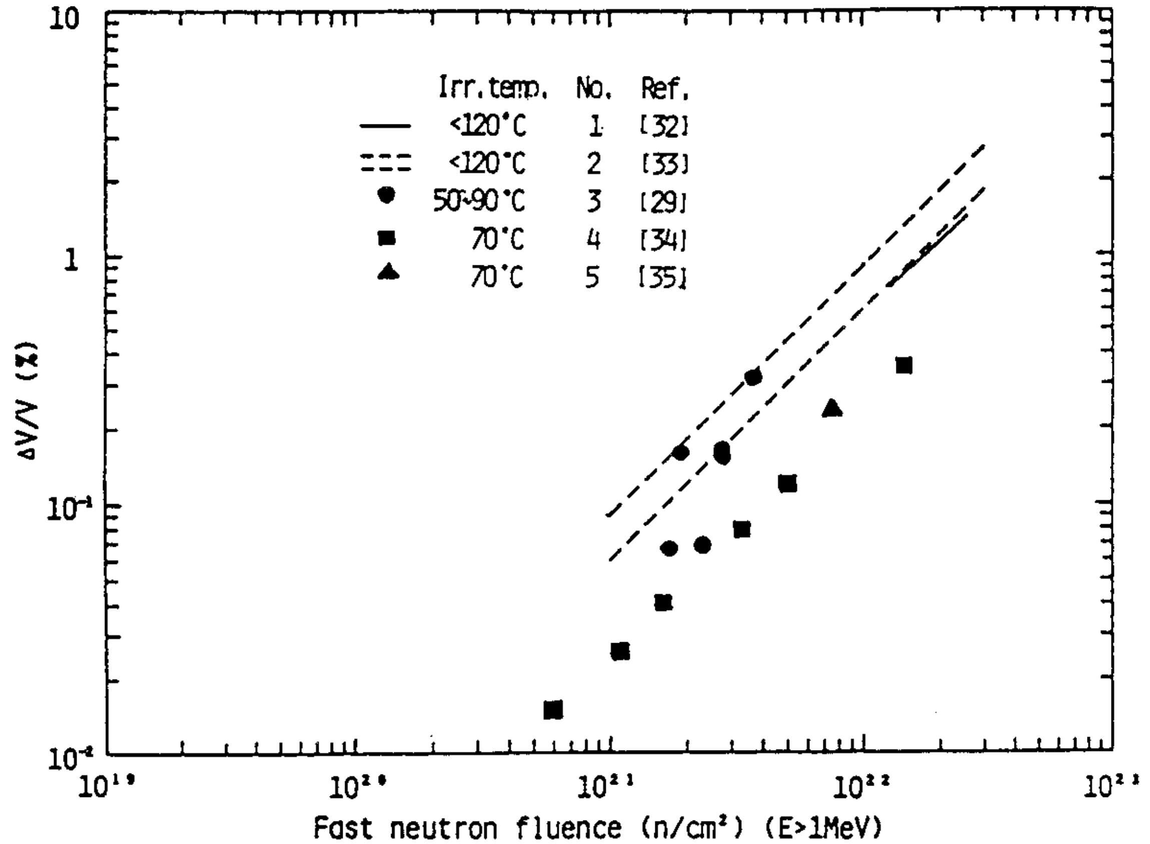

Fig.3.3.1. Neutron Irradiation Induced Swelling of Beryllium.

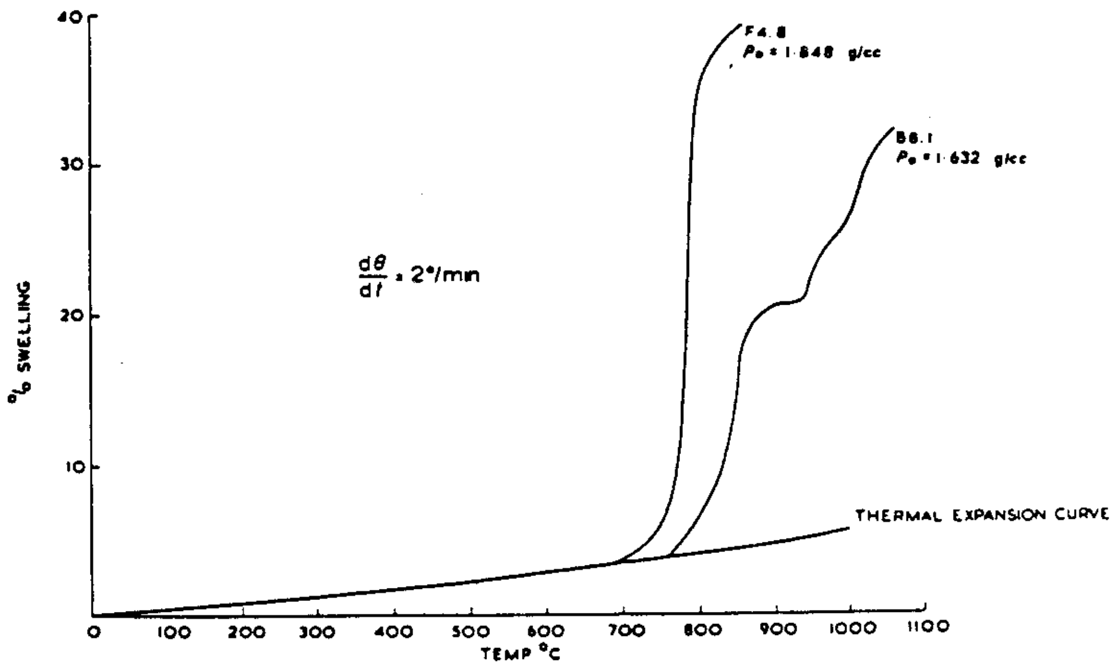

Fig.3.3.2. Linear temperature rise dilatometer curves.

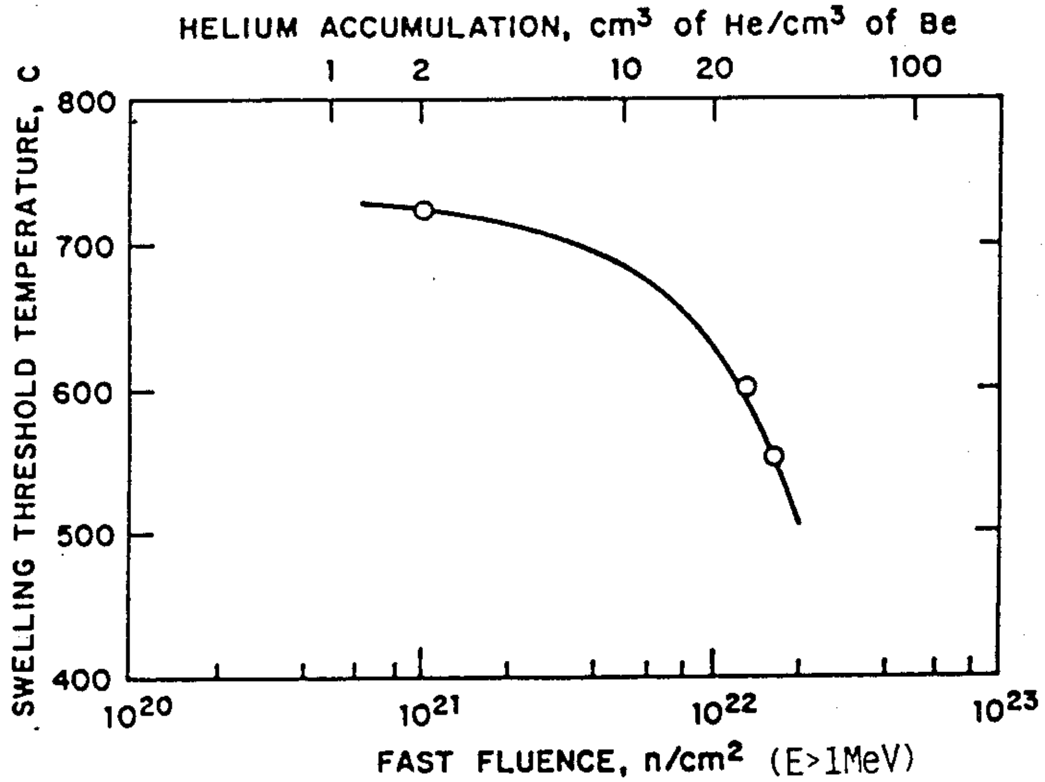

Fig.3.3.3. **Swelling threshold of beryllium as a function of gas content and fluence.**

At low temperatures, the helium atoms remain in solution in the matrix. However, at higher temperatures, the diffusion of helium atoms becomes significant and they agglomerate into bubbles and consequently the swelling grows larger.

The swelling threshold in irradiated beryllium is shown in Fig. 3.3.3 [27]. The swelling threshold temperature falls as irradiation fluence increases.

The swelling threshold temperature is estimated to be about 400°C for a fluence of 3.0×10^{22} n/cm^2 (~6 MWyr/m^2). When beryllium is used between room temperature and 200°C, the swelling reaches to 1~3% for a fluence of 3.0×10^{22} n/cm^2.

4. Lead

The electrical resistivity of lead is shown in Fig. 2.1.2[18].

The elongation of lead at room temperature is about 55%.

There are no data of irradiation effect on the electrical resistivity and the elongation of lead and no data of neutron-irradiated swelling. Lead has large atomic mass and low melting point. Neutrons produce little transmutations in lead. As a result, it seems that the material properties of lead change little.

At low temperatures, the helium atoms remain in solution in the matrix. However, at higher temperatures, the diffusion of helium atoms becomes significant and they agglomerate into bubbles and consequently the swelling grows larger.

The swelling threshold in irradiated beryllium is shown in Fig. 3.3.3 [27]. The swelling threshold temperature falls as irradiation fluence increases.

The swelling threshold temperature is estimated to be about 400°C for a fluence of 3.0×10^{22} n/cm^2 (~6 MWyr/m^2). When beryllium is used between room temperature and 200°C, the swelling reaches to 1~3% for a fluence of 3.0×10^{22} n/cm^2.

4. Lead

The electrical resistivity of lead is shown in Fig. 2.1.2[18].

The elongation of lead at room temperature is about 55%.

There are no data of irradiation effect on the electrical resistivity and the elongation of lead and no data of neutron-irradiated swelling. Lead has large atomic mass and low melting point. Neutrons produce little transmutations in lead. As a result, it seems that the material properties of lead change little.

5. Neutron absorption

We calculated the tritium breeding ratios by ANISN code in order to compare the effects of passive shell materials.

The calculation model is shown in Fig. 5.1 for the copper shell case. In case of aluminum, the composition of shell is 0.932 Al, 0.033 Cu and 0.035 SUS. In case of lead, the sixth zone is removed. In case of beryllium, the sixth zone is removed and lead in neutron multiplier is replaced by beryllium.

The results is shown in Fig. 5.2. The neutron absorption of copper is much larger than that of aluminum. The tritium breeding ratio in case of 3 cm aluminum shell is as large as that in case of 1 cm copper shell.

Zone No.	Radial distance (cm)	Volume fraction	Component
	0.		
1		He	Plasma
	110.		
2		He	Vacuum
	125.		
3		SUS	
	125.5		
4		SUS(0.3295), H_2O(0.6705)	First wall
	126.		
5		SUS	
	127.		
6		Al or Cu(0.932), Cu(0.033), SUS(0.035)	Shell
	127. +X		
7		Pb(0.612425), SUS(0.2317), H_2O(0.1279), Cu(0.03289)	
	127.9 +X		
8		Pb(0.9301), SUS(0.03714), Cu(0.03277)	Neutron multiplier
	132.1 +X		
9		Pb(0.61043), SUS(0.22997), H_2O(0.12695), Cu(0.03265)	
	133. +X		
10		SUS(0.96740), Cu(0.0326)	Second wall
	134. +X		
11		Li_2O(0.15018), Be(0.41227), SUS(0.0472), H_2O(0.02377), Cu(0.03242), Macor(0.05524)	
	140.605+X		
12		Li_2O(0.14815), Be(0.4067), SUS(0.04616), H_2O(0.02215), Cu(0.03212), Macor(0.06955)	
	146.49 +X		
13		Li_2O(0.15272), Be(0.41924), SUS(0.04190), H_2O(0.01329), Cu(0.03181), Macor(0.0574)	Breeder
	154.325+X		
14		Li_2O(0.15748), Be(0.4323), SUS(0.038289), H_2O(6.214-3), Cu(0.031372), Macor(0.04188)	
	166.22 +X		
15		Li_2O(0.15262), Be(0.41894), SUS(0.03788), H_2O(6.45-3), Cu(0.03092), Macor(0.07108)	
	175.		
16		SUS(0.98474), H_2O(0.01526)	End wall
	185.		

Fig.5.1. Blanket model for nuclear analysis.

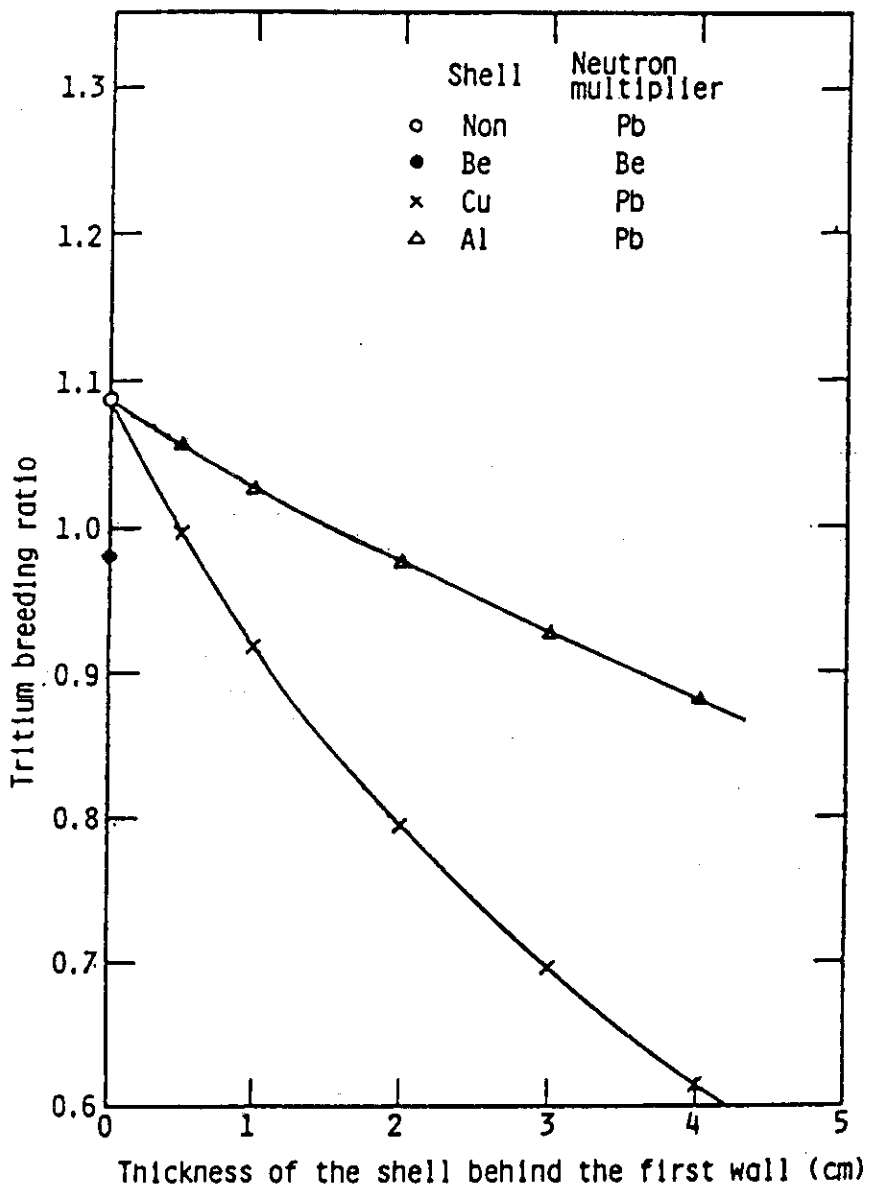

Fig.5.2. Effect of shell material and shell thickness on the tritium breeding ratio.

6. Summary

The summary of irradiated properties of candidate passive shell materials is shown in Table 6.1.

Copper has excellent electrical resistivity. However, the resistivity for a fluence of 6 $MWyr/m^2$ is 2.7 times as large as the initial value at 150°C. It seems that the elongation of copper irradiated up to fluence of 6 $MWyr/m^2$ at 200°C remains larger than 5%. The swelling of copper for a fluence of 6 $MWyr/m^2$ is estimated to be larger than 10% and this becomes a serious problem. Besides the neutron absorption of copper is large. It seems that the swelling of copper can be suppressed by alloying with appropriate elements. But it is necessary to pay special attention to the electrical resistivity increase due to alloying. It seems that copper is alloyed with Au, Ag, Cd or Zr from the standpoint of electrical resistivity and that about 1 atom% of solute is required.

The eleritical resistivity of aluminum at 150°C is 1.7 times as large as that of copper. The electrical resistivity increase due to neutron irradiation is very small. The elongation of aluminum remains larger than 5% at least up to a fluence of 6 $MWyr/m^2$. The swelling of aluminum to a fluence of 6 $MWyr/m^2$ is estimated to be about 1~ 5%. The neutron absorption of aluminum is smaller than that of copper and it has an advantage over copper from this point of view.

Beryllium is desirable from the standpoint of tritium breeding. The swelling of beryllium irradiated up to a fluence of 3 $MWyr/m^2$ is smaller than 1%. The electrical resistivity of beryllium are larger than those of copper or aluminum. However beryllium can serve as neutron multipliers as well, and than the bigger allowable thickness of shell can compensate sufficiency for these large resistivity. The problem of beryllium is its low ductility.

The electrical resistivity of lead is too large. And the low melting point is a porblem from the design standpoint.

As mentioned above copper and aluminum have advantage as possive shell material over beryllium and lead.

Admittedly, the data compiled in this report are gotten by fission neutron irradiation and are insufficient to make a final assessment on the behavior of passive shell materials under fusion operating condition. It is necessary to reappraise the effect of 14 MeV neutron irradiation on shell materials.

Table 6.1. Summary of Irradiated Properties of Passive Shell Materials

Service	Material	Electrical resistivity (μΩcm)		Ductility (%)		Swelling (%)	Neutron absorption	Problems
		Initial	6MWyr/m²	Initial	6MWyr/m²			
Passive shell	Cu (OFHC)	2.6	7.0	46	>5	20~30	Large	Neutron absorption & Swelling
	Al (1100)	4.5	4.9	45	5	1~5	Small	Neutron absorption
Passive shell & Neutron multiplier	Be	6.3	?	4	<0.1	1~3	-	Ductility
	Pb	32	?	55	?	?	-	No irradiation data & Electrical resistivity
Notice		150°C		Minimum at 20-200°C		Maximum at 20-200°C		

References

[1] KUROYANAGI, S., ISHIBASHI, K., YAMADO, K., ISHII, S., HOSHINO, S., and TAKANO, T., Hurukawa Denko Jihou, 59, 113 (1976).

[2] NAGAI, T., HENMI, Z., YAMAMOTO, R., and KODA, N., Nippon Kinzoku Gakkaishi, 39, 477 (1975).

[3] CHAPLIN, R.L., and COLTMAN, Jr.R.R., J. Nucl. Mater. 108 & 109, 175 (1982).

[4] McGRATH, B., SCHÖNBACHER, H., and VAN de VOORDE, M., Nuclear Instruments and Methods, 136, 575 (1976).

[5] EHRHART, P., SCHLAGHECK, U., and SCHILLING, W., J. Appl. Cryst., 8, 150 (1975).

[6] OTORI, S., et al., ed., "Denki Zairyo", Denki Gakkai, Tokyo (1980).

[7] MAKIN, M.J., Radiation Effects, SHEELY, W.F., Editor, Metallurgical Society Conferences, Vol.37, 627 (1965).

[8] MAKIN, M.J., and MINTER, F.J., Acta Met. 8, 691 (1960).

[9] ADAMSON, R.B., BELL, W.L., and KELLY, P.C., J. Nucl. Mater., 92, 149 (1980).

[10] HASEGAWA, M., KOIWA, M., and HIRABAYASHI, M., Trans. JIM, 12, 39 (1971).

[11] BRIMHALL, J.L. and KISSINGER, H.E., Radiation Effects, 15, 259 (1972).

[12] ENGLISH, C.A., J. Nucl. Mater., 108 & 109, 104 (1982).

[13] LABBE, M., and POIRIER, J.P., J. Nucl. Mater., 46, 86 (1973).

[14] COMOLINSKI, M., and BREBEC, G., J. Nucl. Mater., 43, 59 (1972).

[15] LEISTER, K.H., "Simulationsbestrahlungen binärer Kupferlegierungen zur Untersuchung des Einflusses von Fremdelementen auf das Schwellen", KfK 3499 (May 1983).

[16] MISHIMA, R., et al., ed. "Aluminum Handbook", Keikinzoku Kyokai, Asakura Shyoten, Tokyo.

[17] PINTO, N.P., "Properties", Chap. 16 in Beryllium Science and Technology, Vol.2, Eds., FLOYD, D.R. and LOWE, J.N., Plenum Press, New York, (1979).

[18] SOODAK, H. and BLIZARD, E.P. et al., ed., "Lead", in Reactor Handbook, Vol.1 (Materials).

[19] HORAK, J.A., and BLEWITT, T.H., J. Nucl. Mater., 49, 161 (1973/74).

[20] NAGASAKI, S., et al., ed., "Kinzoku Data Book", Nippon Kinzoku Gakkai, Maruzen Co., Tokyo (1979).

[21] CUNNIGAHAM, J.E., "Serer Radiation Damage to Aluminum Alloys", ORNL-IM-2138, (March 1968).

[22] KORTH, G.E., BEESTON, J.M., MARTIN, M.R. and BRINKMAN, C.R., "Damage in Highly Irradiated 1100 Aluminum"", Symp. Materials Performance in Operating Nuclear Systems, August 28-30, 1973, CONF-730801, p.88.

[23] FARRELL, K., KING, R.T., and JOSTSONS, A., "Examination of the Irradiated 6061 Aluminum HFIR Target Holder", ORNL-TM-4139 (May 1973).

[24) JOSTSTON, A., and LONG, Jr.E.L., Radiation Effects, 16, 83 (1972).

[25] WILLIAMS, J.M., HINKLE, N.E. and EATHERLY, W.P., "Final Report: The Effect of Neutron Irradiation at Cryogenic Temperatures and Subsequent Annealing on the Thermal Conductivity and Electrical Resistivity of Beryllium", ORNL-TM-3914 (August 1972).

[26] WEBSTER, D. and GILBERT, J., Beryllium Science and Technology, Vol.1, Eds., FLOYD, D.R. and LOWE, J.N., Plenum Press, New York (1979).

[27] ABDOU, M.A. et al., "Impurity Control and First Wall Engineering", Chap.VII in U.S. FED-INTOR, Phase 2A, Vol.1, USA FED-INTOR/82-1 (Oct. 1982).

[28] WALTERS, G.P., J. Less-Common Metals, 11, 77 (1966).

[29] TAKEDA, T., et al., JAERI-internal report

[30] RICH, J.B., WALTERS, G.P. and BARNES, R.S., J. Nucl. Mater. 4, 287 (1961).

[31] BARTZ, M.H., "Performance of Metals during Six Years Service in the Materials Testing Reactor", Proc. Second United Nations International Conference on the Peaceful Uses of Atomic Energy held in Geneva September 1-13, 1958 in Volume 5, Properties of Reactor Materials, p.466 (1958).

[32] BEESTON, J.M., MARTIN, M.R., BRINKMAN, C.R., KORTH, G.E. and FRANCIS, W.C., "Surveillance Testing and Property Evaluation of Beryllium in Test Reactors", Symp. Materials Performance in Operating Nuclear Systems, August 28-30, 1973, CONF-730801, p.59.

[33] KORTH, G.E. and BEESTON, J.M., "Surveillance of Test Reactor Beryllium and Hafnium", in Metallurgy and Materials Science Branch Annual Report Fiscal Year 1970, IN-1437, p.5 (Nov. 1970).

[34] BEESTON, J.M., "Gas Formation and Compression Fractures in Irradiated Beryllium", in Flow and Fracture of Metals in Nuclear Environments, ASTM-STP-380, p.395 (1965).

[35] RICH, J.B., REDDING, G.B. and BARNES, R.S., J. Nucl. Mater. 1, 96 (1959).

7.2 Benchmark Tests of the Model for Transient Electromagnetics

Benchmark Tests of the Model for Transient Electromagnetics

K. UEDA, K. MIYAMOTO and M. KASAI

Mitsubishi Fusion center
2-3, MARUNOUCHI 2-CHOME, CHIYODA-KU, TOKYO, JAPAN

H. IIDA*, N. FUJISAWA* and T. TONE*

*Japan Atomic Energy Research Institute
801-1 NAKA-MACHI, NAKA-GUN, IBARAKI-KEN, JAPAN

1. Introduction

Models of transient electromagnetics provide eddy current analyses, dynamic analyses of the horizontal and vertical position, analyses of electromagnetic forces caused by interaction between the eddy current and the toroidal mangetic field, etc. In general, the models are composed of three sub-models of an eddy current evaluation model, a suppression and control model of the positional instability, and an electromagnetic force evaluation model.

Therefore, benchmark tests should include some checks for each sub-model duscribed on the above.

In the previous workshop (January, 1984), [1] the benchmark models were set in consideration of the following points:

(1) The benchmark models need to provide the way to check if the models of transient electromagnetics can be endurable for analyses required on the design of a tokamak reactor.

(2) The structure of the benchmark models should not be so complex that the results obtained from the model of transient electromagnetics developed in each country can not be compared with each other and the differences among countries can not be analyzed.

Finally, three models were set: i.e. Models, 1, 2 and 3. The larger the model number is, the more complex the structure of model gets, as follows.

The Model-1 consists of a pair of ring shells, a plasma column (with the INTOR parameters... Major Radius: 5.3 m, Minor Radius: 1.2 m, Current: 6.4 MA) and a pair of control coils. In Model-2, the ring shells in Model-1 are replaced by 24 rectangular shells (shown in Figure X-26 in the green book[6]). In Model-3, radiation shields toroidally divided into 24 divisions are added to the structure of Model-2.

In this report, the following items are set on analyses of three Benchmark Models.

(1) The plasma column is treated as a filamentary current loop located along the major radius.

(2) As for the differential coefficient, M'_{ps} (with respect to the axial coordinate) of the mutual inductance between the plasma column and the structure (shell, control coils and radiation shield), the results obtained by three kinds of methods are used. Their methods are composed of the method using a filament current loop in place of the plasma column, the dipole approximation for a circular plasma, and the method using a distributed current plasma from plasma equilibrium calculations.

(3) In the case which the shell effect can be expected, the plasma inertial term can be neglected on the equation of plasma column motion.[7]

(4) The thin plate approximation method [8] is used on estimating the eddy currents flowing in the structure.

In the case of high-β INTOR plasma, it has been found that the magnetic axis lies considerably outside the major radius, and the above mentioned differential coefficient, M'_{ps} can be expected to have larger value than one obtained from setting the radial coordinate of the filament or the dipole on the major radius. On this meaning, the dependence of the shell effects upon their radial coordinates is estimated in this report.

2. Requirements and Constraints

2.1 Initial conditions

The structures of three benchmark models, which were set in the workshop held in January 1984, are shown in Figures 2.1(a),(b) and (c), respectively. Model-1 consists of a pair of ring shells, the plasma column and a pair of coils. In Model-2, the ring shells in Model-1 is replaced by 24 rectangular shells. In Model-3, radiation shields toroidally divided into 24 divisions are added to the structure of Model-2.

Among the constants used in Models, 1, 2 and 3, those which have been already determined are shown in Table 2.1. Additionally others than figures in the table are used for some constants.

For analyses of the vertical position instability, it is necessary to determine initial conditions since obtained results are anticipated to be dependent upon those conditions.

They can be determined in three ways as follows:

(A) $Z_p|_{t=0} \neq 0,\ \dot{Z}_p|_{t=0} = 0$ (1)

(B) $B_d = B_o \cdot [1-\exp(-t/\tau_d)]$ (2)

(C) $Z_p|_{t=0} \neq 0,\ \dot{Z}_p|_{t=0} = \gamma \cdot Z_p|_{t=0}$ (3)

where Z_p is the displacement in the plasma vertical direction, and denotes the time derivative. B_d is the horizontal magnetic field due to an external disturbance, and B_o and τ_d are the value of B_d at $t\to\infty$ and the time constant of the external disturbance, respectively. γ is the instability growth time.

In the initial condition (A), the plasma is instantaneously balanced at the position of $Z_p|_{t=0}\neq 0$ at t=0, and then the plasma position begins to diverge, because the eddy current balancing the plasma position attenuates according to its time constant. In the case there is a single eddy current mode in the object to be analyzed, the condition (A) are meaningful because the initial values for the eddy current can be definitely determined. In the case there are a number of eddy current modes, however, the condition (A) cannot be used.

In the condition (B), the initial values can be determined even if there are a number of eddy current modes. Moreover, if a value of τ_d is chosen properly, the condition $\dot{Z}_p \approx 0$ can be obtained at a certain point of time t>0, which is similar to the condition in (A), thus providing a way to compare the results with those obtained from the condition (A) for a single mode.

As seen from Table 2-1, Z_p at $\dot{Z}_p \approx 0$ is taken to be an initial displacement of 1 cm or a maximum displacement of 5 cm. In the case the condition (B) is taken, a position control is set to start at 1 ms after occurrence of the external disturbance. If a stable control can be obtained, the maximum displacement lies in the neighborhood of the displacement at the start of control. Consequently, in this case the initial displacement is found to be equal to the maximum displacement.

The condition (C) can be obtained from the initial condition (B), because the plasma displacement without active control, in the case which the shell effect can be expected, can be represented by the form of $Ae^{\gamma t}$ after an influence of the disturbance of type (B) will become negligibly small. In this report, very small B_d ($\approx 10^{-3}$ Gauss) is selected and the origin of new time is set at $(t-t')=0$ so that $Ae^{\gamma t'}$ is equal to Z_o (for example, 1 cm).

2.2 Resistance of control coils

As seen from Table 2-1, the control coils are made of copper. Taking its size into consideration, the self-inductance and the resistance are known to be approximately 54.4 μH and 5.6 μΩ, respectively. Since the resistance value of 5.6 μΩ is too small to be realistic, it is important to study if variation of this value largely affects the results given in this report.

In Figure 2.2, variations of the vertical displacement without active control are shown for two cases of 5.6 μΩ and 0.56 mΩ. Although slight difference can be observed between two cases, the small value of 5.6 μΩ is not supposed to largely affect the results.

In Figure 2.3, the maximum control current and maximum power required for the vertical position control are given. Moderate decrease on both parameters is observed in a range of more value of control coil resistance than 0.5 mΩ. On the other hand, time to return to 0.1 Z_o is found to abruptly increase in the corresponding range and have ∞ on about 1 mΩ in its resistance under a control condition: Gain = 1×10^4 V/m, Derivative time = 10 msec. In conclusion, active control characteristics for Model-1 are found to change whatever the coil resistance is more than 0.5 mΩ or not.

2.3 Plasma conductor models for evaluating M'_{ps}

Three kinds of methods have been proposed on evaluating the differential coeffcient, M'_{ps} (': derivative with respect to the axial coordinate) of the mutual inductance between the plasma column and the structure (shell, control coils, radiation shield, etc).

One of them is the method using a filamentary current loop in place of the plasma column (Here, this method is called the filamentary model), and being under an obligation to use on the benchmark calculation as shown in Table 2.1.

One of the rest methods in the dipole approximation method on which the plasma is assumed to have a circular cross-section with a constant current density, and additionally approximated as a dipole current. Redently, a new dipole method has been proposed.(10) In the method both of the dipole position and current are adjusted so as to have a flux function almost equal to the flux function from a plasma equilibrium calculation. This method is call the modified dipole model.

The final method, which is called the distributed current model, evaluates M'_{ps} using the distributed current distribution obtained by a plasma equilibrium calculation.

Others than the first method using a filamentary current loop are shown in Figure 2.4 where used parameters are defined for each method.

Figure 2.5 shows n_s ($\equiv \Sigma n_i$)[3] which is one of the measures for the shell effects, on comparing some results obtained by each method. In Fig. 2.5 the abscissa is selected so as to be equal to the radial coordinate of the location of the filament in case of the filamentary model, the dipole in case of the dipole and modified dipole approximation or the magnetic axis in case of the distributed current model.

In case of 5.3 m in the radial coordinate, comparison between the filamentary and dipole models is given on Table 2.2. The results from the filamentary model are found to be larger than them in case of the dipole model by 0.2∿0.23 in n_s and by about 53 ms (Model-1), 16 ms (Model-2) and 12 ms (Model-3) in the growth time.

In conclusion, difference between the filamentary and dipole model is considerably large in the growth time, but selection of the radial position, at which the filament, the dipole or the magnetic axis is located, is found to be important, too.

2.4 Comparison between circular coil and finite element models

In case of the eddy current calculation of the Benchmark Model-1, there are proposed three methods.[2]∿[5] Here, both of the circular and finite element models are examined and compared. Used circular coil models are shown in Figure 2.6. Figs. 2.6(a), (b) and (c) show the Benchmark Model-1, a circular coil which the Model-1 is represented by one coil, and two circular coils into which it is divided, respectively. Table 2.3 shows some results obtained by both methods of the circular coil and finite element models. Numerical difference between both methods is within several per cent in n_s, but is found to attain to a few tens per cent in the growth time, γ^{-1}.

Others than the first method using a filamentary current loop are shown in Figure 2.4 where used parameters are defined for each method.

Figure 2.5 shows n_s ($\equiv \Sigma n_i$)[3] which is one of the measures for the shell effects, on comparing some results obtained by each method. In Fig. 2.5 the abscissa is selected so as to be equal to the radial coordinate of the location of the filament in case of the filamentary model, the dipole in case of the dipole and modified dipole approximation or the magnetic axis in case of the distributed current model.

In case of 5.3 m in the radial coordinate, comparison between the filamentary and dipole models is given on Table 2.2. The results from the filamentary model are found to be larger than them in case of the dipole model by 0.2∿0.23 in n_s and by about 53 ms (Model-1), 16 ms (Model-2) and 12 ms (Model-3) in the growth time.

In conclusion, difference between the filamentary and dipole model is considerably large in the growth time, but selection of the radial position, at which the filament, the dipole or the magnetic axis is located, is found to be important, too.

2.4 Comparison between circular coil and finite element models

In case of the eddy current calculation of the Benchmark Model-1, there are proposed three methods.[(2)∿(5)] Here, both of the circular coil and finite element models are examined and compared. Used circular coil models are shown in Figure 2.6. Figs. 2.6(a), (b) and (c) show the Benchmark Model-1, a circular coil which the Model-1 is represented by one coil, and two circular coils into which it is divided, respectively. Table 2.3 shows some results obtained by both methods of the circular coil and finite element models. Numerical difference between both methods is within several per cent in n_s, but is found to attain to a few tens per cent in the growth time, γ^{-1}.

3. Structure of the Benchmark Models

In Figures 3.1 and 3.2, the structure of conductor and a typical eddy current flow (1/48 of a torus) in the Benchmark Model-1 are shown, respectively. In Figures 3.3 and 3.4 are shown the corresponding figures in the Benchmark Model-2. In Figures 3.5 and 3.6 the structure of the upper half of a 1/24 sector (a portion of 7.5 degrees in the torus direction) and its typical eddy current flow are shown, respectively.

Although the thickness of side walls in Models, 2 and 3 is selected to be 2 cm as shown in Table 2.1, the case of 1 cm in its thickness is calculated in this report, too. The gap between adjacent side walls is taken to be 1 cm, as the distance between the currents is set to be 3 cm, and then they are supposed to flow along the center of side wall thickness.

4. Results

4-1 Model-1

4.1.1 Initial condition of type (B)*

In Figure 4.1 is shown time evolution of the vertical displacement of plasma column, Z_p, which is obtained when external disturbance of the form of Equation (2) is applied to the Benchmark Model-1. Time evolutions of the horizontal magnetic field due to the external disturbance, the magnetic field due to the eddy currents, and the current in the control coils which are regarded as passive conductors, are also shown in the figure. The time constant of the control coils, τ_c, is taken to be approximately 9.73 s (= 54.5 μ H/5.6 μΩ). The magnetic field due to the external disturbance at $t \to \infty$, B_o, is taken to be 3.29 Gauss, which is determined so that Z_p is equal to 1 cm at t=1 ms. τ_d is selected to be equal to 0.1 ms.

The initial condition for position control is given at t=1 ms, and are used in the following discussion for the Benchmark Model-1. This initial condition will be found to be approximately equivalent to the initial condition of type (A) as known in Figure 4.1.

In Figure 4.2, time evolutions of Z_p are shown for the cases with and without control. In case with control, the gain is fixed at 10^4 V/m, and the derivative action time, T_d, is taken at 1 ms or 10 ms. In the case without control, the instability growth time is approximately 72 ms, and at $s \to \infty$, n_s is approximately 1.72.

In case of the control with T_d = 10 ms, Z_p tends to slightly fluctuate after external disturbance is applied. In Figure 4.3 is shown Bode diagram with T_d as a parameter. Since less frequency than 10^3 is used, there is no unatable factors in phases. Consequently, it is seen that instability occurs when T_d = 10 ms, because the gain is set to be too large.

In Figure 4.4, the control characteristics of Z_p are shown for T_d = 1 ms, and Z_p can be seen to stabilize by about 60 ms. Time evolution of the magnetic field due to the eddy current, the magnetic field produced by a pair of control coils, and the current and voltage of the control coils are also shown in the figure. The time in which Z_p is stabilized is almost the same as the time by which the voltage of control coils reaches a stationary value. The magnetic field due to the eddy current tends to decrease after Z_p is stabilized. Since the time dependence of the current of control coils is similar to that of the eddy current, it can be seen that the field by the control coils after Z_p is stabilized plays a role of cancelling the magnetic field due to the eddy current.

In Figure 4.5, time evolutions of the same parameters as in Figure 4.4 are shown for the case of T_d = 10 ms. Although both figures give similar curves, the time in which Z_p is stabilized is longer, and the time, at which the eddy current and the current of control coils turn to decrease, is different from then in case of T_d = 1 ms. This is caused by the fluctuation of Z_p on the initial stage of control and shows that selection of a suitable gain is important.

* When the initial condition of this type is used, the dipole model is used for evaluation of M'_{ps} all over this report.

4.1.2 Initial condition of type (C)**

Here, some characteristics of the vertical position control under the initial conditions of type (C) are studied. These initial conditions are set on the INTOR Workshop, May, 1984 and ought to be used on the benchmark tests.

Figure 4.6 shows time evolutions of the vertical position, Z_p, the control current, I_c and the required power, P_c under the initial condition of type (C). Figs. 4.6 (a) and (b) correspond to 1 ms and 10 ms in derivative time, T_d with a fixed gain, 10^4 V/m, respectively. The time evolution of each parameter is found to show the almost same feature as one in Figure 4.4 or Figure 4.5.

4.2 Model-2

4.2.1 Initial condition of type (B)

In Figure 4.7, time evolutions of Z_p in the Benchmark Model-2 are shown for both cases with and without active control. The gain with active control is fixed at 10^4 V/m, and the derivative action time, T_d, is set at 1 ms or 10 ms as used in Figure 4.2. The instability growth time is approximately 20 ms, and n_s at $s \to \infty$ is approximately 1.62 in this case. Although there is not significant difference in the values of n_s in Models, 1 and 2, both values of instability growth time differ largely.

The control characteristics vary largely as the value of T_d changes. Z_p at $T_d = 1$ ms is controlled so as to be stable, but diverging oscillation occurs at $T_d = 10$ ms. In Figure 4.8, Bode diagram corresponding to Figure 4.7 is shown. Figure 4.8 suggests that instability occurs when $T_d = 10$ ms, because the gain is set to be too larger.

Figure 4.9 shows time evolutions of the same parameters of Model-2 as in Figure 4.4. It can be seen that the time in which Z_p is stablized is approximately 40 ms, and is a little less than that for Model-1, as shown in Figure 4.4. Although time evolution of the magnetic field due to the eddy current is seen to be similar to that of the magnetic field due to the control coil current in Figure 4.4, the curves for these quantities show some differences in the starting part in this figure. The current of control coils rises rapidly because it is necessary for them to play a rule of the eddy current, and moreover to produce larger magnetic field than one produced by the eddy current.

The time in which Z_p is stabilized gets shorter because the time constant of shell itself, or the shell effect, is decreased on comparison with one of Model-1.

4.2.2 Initial condition of type (C)

Figure 4.10 shows time evolution of Z_p, I_c and P_c under the condition (C). Fig. 4.10 (a) corresponds to 1 ms in T_d and the time evolution of each parameters shows the almost same feature as one in Fig. 4.9. Fig. 4.10 (b) corresponds to 10 ms in T_d. Some signs of the unstable tendency, which the case of 10 ms in T_d in case of the condition of type (B) has

** When this conditon is used, the filamentary model is used for evaluation of M'_{ps} all over this report.

shown, are observed from Fig. 4.10(b), but the disturbance is stabilized little by little.

4.3 Model-3

4.3.1 Initial condition of type (B)

In Figure 4.11, Bode diagram is shown for the Benchmark Model-3. It can be expected that a stable control may be obtained when the derivative action time is 10 ms.

Figure 4.12 shows time evolutions of the same parameters of Model-3 as them in Fig. 4.4. Z_p is seen to fluctuate slightly on the initial stage, but the fluctuation attenuates in a short period.

For this model, the instability growth time is about 26 ms, and n_s is aporoximately 1.85. Additionally the instability growth time in case of the side walls with 1 cm in thickness decreases about 18 ms.

4.3.2 Initial condition of type (C)

Figure 4.13 shows time evolution of Z_p, I_c and P_c under the condition (C). Figs 4.13 (a) and (b) correspond to 1 ms and 10 ms in T_d, respectively.

4.4 Required Capacity of Power Supply

4.4.1 Initial condition of type (B)

The required capacity of power supply was evaluated for the Benchmark Models, 1, 2 and 3 and the results are given on Table 4.1. There are shown the required maximum voltage and current together.

As for Model-1, calculations are made for three values of B_o. These values of B_o give the maximum vertical displacements of 1, 3 and 5 cm (at 1 ms after imposition of each external disturbance), respectively. Using the calculated results, the requred capacity of power supply ($V_{max} \cdot I_{max}$, V_{max}: maximum voltage, I_{max}: maximum current) is given as follows:

$$P = 0.2072 \cdot B_o^{\,2} \text{ (MVA, } B_o\text{: Gauss)} \qquad (3)$$

$$= 2.248 \cdot Z_{max}^{\,2} \text{ (MVA, } Z_{max}\text{: cm)} \qquad (4)$$

where Z_{max} is the maximum vertical displacement. These equations can be used under the conditions that $G = 10^4$ V/m, $T_d = 1$ ms and $\tau_d = 0.1$ ms.

In case of Model-1, τ_c is calculated for a case set at 0.0973 s, too. (taking the resistance of control coils up two orders) and the required capacity of power supply is evaluated about 5% smaller than one in the case of 9.73 s in τ_c.

In cases of Models, 2 and 3, a value of B_o is set so that an initial displacement of about 1 cm can be given. There is only a little difference with respect to the shell effect between Models, 2 and 3. On Table 4.2, the major parameters are shown. It can be seen that the figures for two models are nearly equal. However, the required capacity for Models, 2 and 3 is about 2.0 and 6.4 MVA, respectively. This is caused by the structural difference of two models, that is, with and without radiation shield and also means that the magnetic shield effect of the radiation shield is significant.

Table 4.2 shows number of the modes, taken into consideration in the analysis, whose contribution to n_s is greater than 5×10^{-3}. Whether the radiation shield exists or not is very different in the number of the modes taken for Models, 2 and 3.

4.4.2 Initial condition of type (C)

On Table 4.3, main results for three benchmark models in case of the initial condition of type (C) are listed.

It is found from the table that the required capacity of power supply is only a little dependent on the instability growth time, except Model-1b. Such a result seems to mean that, in case of the initial condition of type (C), only the vertical displacement, Z_o influences mainly one the required capacity of power supply.

4.5 Disruption Analysis

The eddy current and the electromagnetic force on a plasma disruption are analyzed using Model-2.

The disruption condition to be assumed is that the plasma current decreases linearly at the stationary position and at 20 ms in time constant.

Figure 4.14 shows variations of the eddy current on the rectangular shell for the case which the plasma disappears in the way described above. (a), (b), (c) and (d) show the results of observation at the time of 5, 10, 20 and 30 ms, respectively. The direction of the eddy current in the upper and lower parts of the toroidal bar is reversed, and a loop current is formed so as to flow through the side boards. The loop current reaches the maximum of about 260 KA at the time of 20 ms. The toroidal field (4.6T at R = 6.34 m) is coupled with the current flowing through the side walls.

The triangle, which will have the maximum line current density (A/m), is found to be the dark one of the side wall in Fig. 4.14. The electromagnetic force due to coupling between the toroidal magnetic field and the eddy current on the disruption has the maximum value all over the period of disruption on the above triangle of side wall, too, and the maximum is found to attain to about 50 in kgf/cm^2 at 20 ms after the disruption. Fig. 4.15 shows time evolutions of the plasma current, the looped eddy current on the toroidal bar, and the electromagnetic force on the dark triangle of side wall.

Neighboring side walls have an equal value but mutually inverse direction with the induced eddy currents at every time of the disruption, and therefore their currents result in a repulsive force between them. On evaluating this repulsive force under an assumption of infinitely extended parallel-planes for the neighbouring side walls, the force becomes about 7.2 in kgf/cm^2 at 20 ms and is found to be negligibly small compared with the above electromagnetic force between the toroidal magnetic field and the eddy current.

4.6 Current Flow on the Radiation Shield

Figures 4.16 and 4.17 show variations of current integral ($\equiv \int_a^s J_\theta \cdot t\, ds$)[9] on the radiation shield in cases of T_d = 1 mas and 10 ms for a fixed gain, 10^4 V/m, respectively. The current flow between a and c is found to have the largest one for both cases of Figs. 4.16 and 4.17.

The minimum current on time evolution is at t = 0 ms and the maximum occurs at about several tens ms on both cases, but decreasing speed (for example, KA/ms) from the maximum is found to be faster in the case of T_d = 1 ms than one of T_d = 10 ms.

5. Conclusions

From some studies with three kinds of benchmark models, which were proposed on the INTOR Workshop, January ('84) and modified partially on the Workshop, May ('84), are obtained the following results.

(1) Instability growth time, γ^{-1}

The results (about 125, 36 and 38 ms for Models, 1, 2 and 3, respectively) from the filamentary model are larger than them in case of the dipole model by 0.20∿0.23 in n_s and by about 53 ms (Benchmark Model-1), 16 ms (Model-2) and 12 ms (Model-3) in the growth time, respectively. Moreover, the selection of the radial position, at which the filament (of the filamentary model), the dipole (of the dipole approximation) or the magnetic axis (of the distributed current model) is located, is found to be important, too.

(2) Required capacity of power supply

Required capacity of power supply was studied under two kinds of initial conditions shown in the following conditions.

(1) $Z_p|_{t=0} \neq 0,\ \dot{Z}_p|_{t=0} \doteq 0$

(2) $Z_p|_{t=0} = 1$ cm, $\dot{Z}_p|_{t=0} = \gamma \cdot Z_p|_{t=0}$

Under the initial condition, (1), based on a disturbance field (B_o = 4.18 Gauss and τ_d = 0.1 ms), the required capacities for Models, 1, 2 and 3 are about 3.6, 6.5 and 6.4 in MVA, respectively, and difference between Model-1 and the others on the required capacity is found to be smaller than one in the instability growth time. The maximum vertical displacement under this disturbance filed for each of Models, 1, 2 and 3 is not kept constant and is about 1.27 cm, 1.8 cm and 1 cm (standard), respectively.

On the other hand, under the initial condition (2), the required capacity is only a little dependent on the instability growth time. Such a result seems to mean that, in case of this initial condition, only the initial vertical displacement, Z_o influence mainly on the required capacity of power supply. The capacity for each Model-1, 2 or 3 in case of T_d = 1 ms is about 3.22, 2.82 or 3.55 MVA.

(3) Electromagnetic force

The maximum electromagnetic force by the toroidal magnetic field and the induced eddy current on the disruption is produced on the top and bottom of side walls, directs normal to and out of the toroidal bar and parallel to the side wall, and attains to about 50 in kgf/cm^2 at 20 ms.

Table 2.1 - 1 Parameter Values for Benchmark Models

Model	1	1 bis	2	3
Shell Geometry				
no. of sectors	0	0	24	24
shell shape	toroidal	toroidal	saddle	saddle
toroidal shell thickness, t_1, m	0.01	0.01	0.01	0.01
sidewall thickness, m	0	0	0.02	0.02
sidewall width, m	0	0	0.5	0.5
gap between adjacent sectors, m	-	-	0.03	0.03
Radiation Sheild				
no. of sectors	-	-	-	24
thickness, t_2, m	-	-	-	0.1
resistivity, Ωm	-	-	-	10^{-6}
gap between adjacent sectors, m	-	-	-	0.01
Plasma Current, MA	6.4	6.4	6.4	6.4
Plasma Radius, m	5.3	-	5.3	5.3
Plasma Model	1 filament	distributed	1 filament	1 filament
Plasma Mass, kg	0	0	0	0
Vertical Field, T	-0.5	-0.5	-0.5	-0.5
Field Index	-1.3	-1.5517	-1.3	-1.3

Table 2.1 - 2 Additional Parameters for Model 1 bis only

Between plasma and;	M (10^{-6}H)	dM/dz (10^{-6}H/m)
passive upper loop	13.4	2.91
passive lower loop	8.77	-2.83
active upper loop	3.09	0.747
active lower loop	2.25	-0.505

Table 2.1 - 3 <u>Control Parameters for All Models</u>

control coil location:	6.5 m $\pm$ 6.5 m
cross-section per coil:	0.5 x 0.5 m
resistivity (solid Cu):	1.72 x 10^{-8} Ωm
control law:	$V_c = -G(Z_p + T_d Z_p)$

V_c = voltage across two coils connected series opposing

$G = 10^4$ V/m

T_d = 1 ms

Table 2.1 - 4 <u>Additional Parameters for Model 2 Only</u>

For Model 2 Plasma Disruption:

1) Plasma stationary at (5.3, 0)
2) Time scale: 20 ms linear decay to 0 current
3) Plasma initial current = 6.4 MA
4) Toroidal field = 5.5 x 5.3/R, T.

Table 2.2 Comparison between Filamentary and Dipole Models

Plasma Models / Benchmark Models / Parameters	Filamentary Model			Dipole Model		
	1*	2	3	1*	2	3
n_s	1.88	1.82	2.08	1.72	1.62	1.85
γ^{-1} (ms)	125	36	38	72	20	26

* This is in case of Ne = 12 [Ne: Number of the triangle elements (per 7.5 degrees in the toroidal angle) of which the Benchmark Model 1 is composed].

Table 2.3 Comparison between Cricular Coil and Finite Element Models***

Shell Models / Parameters	Circular Coil Model			Finite Element Model	
	$N*_c=1$	$N*_c=2$	$N*_c=10$	$N**_e=12$	$N**_e=24$
n_s	2.11	-	-	1.88	2.00
γ^{-1} (ms)	163	139	111	·125	141

* N_c: Number of the circular coils of which the Benchmark Model 1 is composed.

** N_e: Number of the triangle elements (per 7.5 degrees in the toroidal angle) of which the Benchmark Model 1 is composed.

*** These results were obtained from the filamentary model.

Table 4.1 Required maximum voltage and current for Model-1, 2 and 3

Model No.	B_o (Gauss)	τ_c (sec.)	T_d (ms)	V_{max} (Volt)	I_{max} (10 KA)	$V_{max} \times I_{max}$ (MVA)
1**	3.29	9.73	10	116.7	2.225	2.597
		9.73	1	102.4	2.196	2.248
		0.0973	10	117.1	2.121	2.484
	9.88	9.73	1	307.4	6.592	20.26
		9.73	10	350.4	6.681	23.41
	16.47	9.73	1	512.3	10.986	56.28
2	2.32	9.73	1	109.0	1.848	2.014
		9.73	10	V_{max}>5kV required	-	-
3	4.18	9.73	10	180.6	3.522	6.361

* (1) Gain, G is fixed at 10^4 V/m.

(2) Dipole current model for a circular cross-sectional plasma is used.

** $P(\equiv V_{max} \cdot I_{max})$ can be approximated by the following equation,

$$P = 0.2072 \cdot B_o^2 = 2.248 \times Z_{max}^2, \text{ (MVA, } B_o\text{: Gauss, } Z_{max}\text{: cm)}$$

where Z_{max} is the vertical displacement in cm.

Table 4.2 Major parameters for evaluating shell effects

Contents \ Model No.	1	2	3
· Number of total eddy current modes	3	6	32
· Σn_i	1.72 (1.65)	1.62 (1.56)	1.85 (1.78)
· The maximum time constant of modes (s)	0.283	0.097	0.101
· Instability growth time (ms)	72 (59)	20 (16)	26 (22)

Note: Numerical values with ( ) are in case of τ_c = 97.3 ms.

Table 4.3 Main Results for Three Benchmark Models (1)

Model / T_d (ms) / Parameters	1			2 (2)		3 (2)	
	1a (2)		1b				
	1	10	1	1	10	1	10
I_c^{MAX} (KA)	-32.2	-31.0	13.5	-27.1	-25.8	-34.5	-31.3
V_c^{MAX} (Volt)	-100.0	-108.0	-107.0	-104.0	-128.0	-103.0	-125.0
P_c^{MAX} (MW)	1.1	0.72	0.40	1.0	0.75	1.5	1.1
T_R (ms) (3)	40	57	11	28	44	32	46
T_I (ms) (3)	48	60	23	31	38	35	38
T_p (ms) (3)	16	16	5	12	12	14	14
n_s	1.88	1.88	1.80	1.82	1.82	2.08	2.08
γ^{-1} (ms)	125	125	39	36	36	38	38

(1) Grain, G is fixed at 10^4 V/m. (2) The filamentary model is used.
(3) T_R: Time to 0.1 Z_o, T_I: Time to Max. current, T_p: Time to Max. Power.

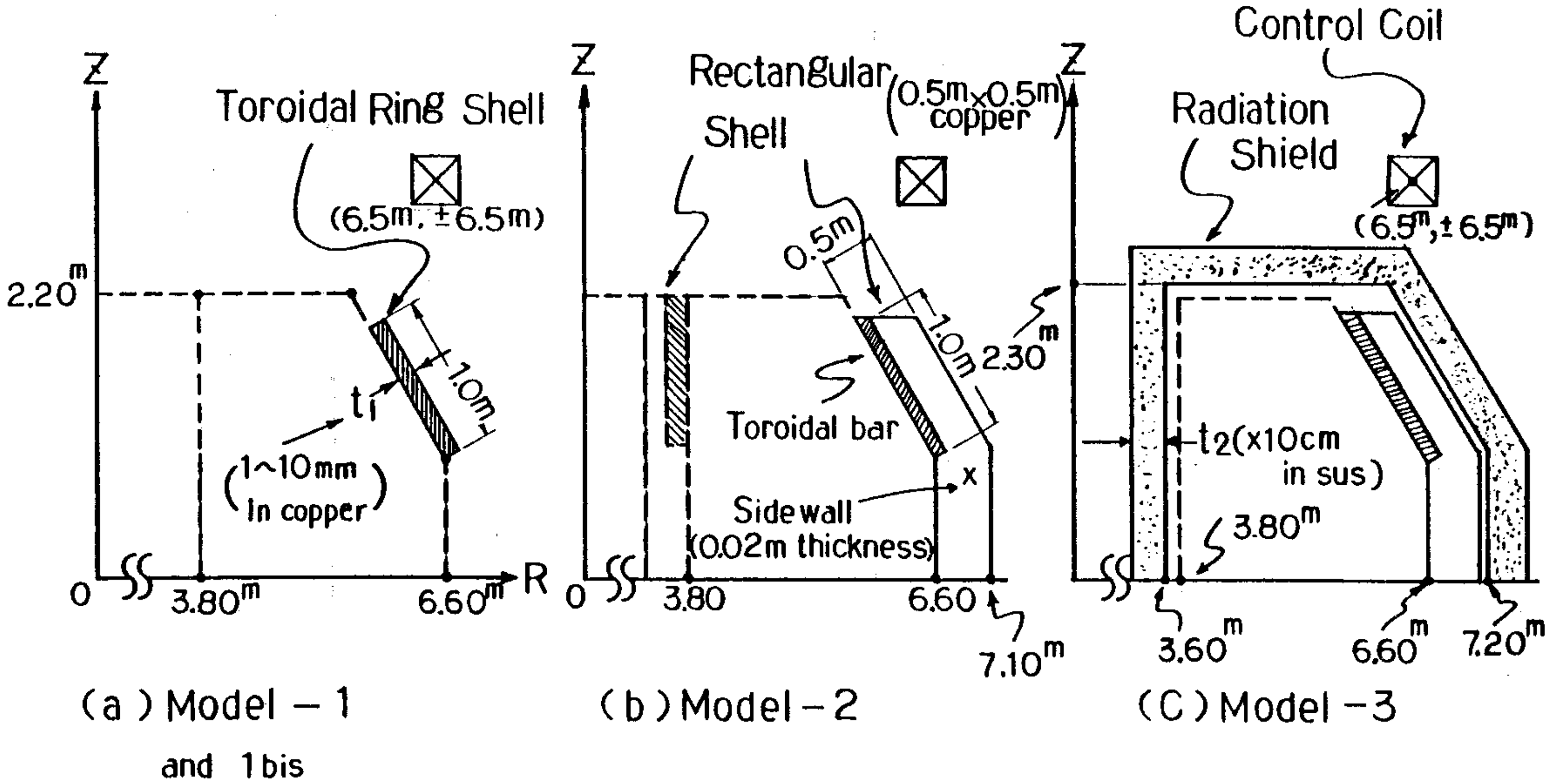

Fig. 2.1 Three benchmark models

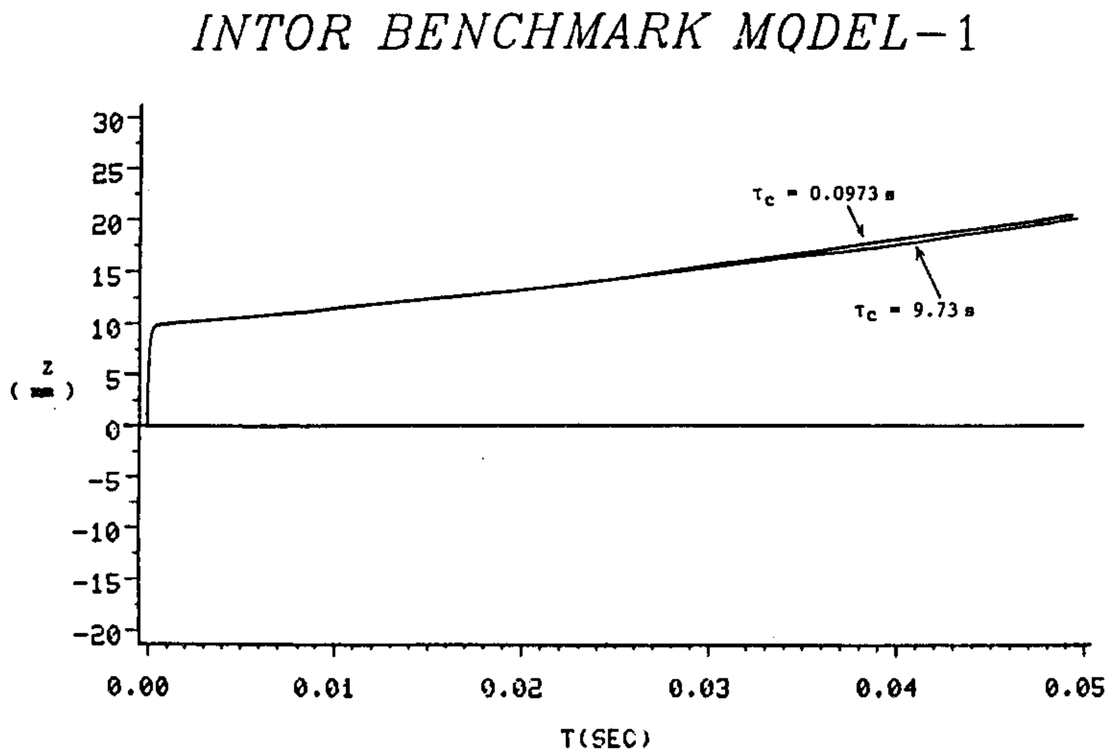

Fig. 2.2 Time evolution of the vertical displacement without PD controller for two cases of 5.6 and 560 μΩ in the resistance of control coil

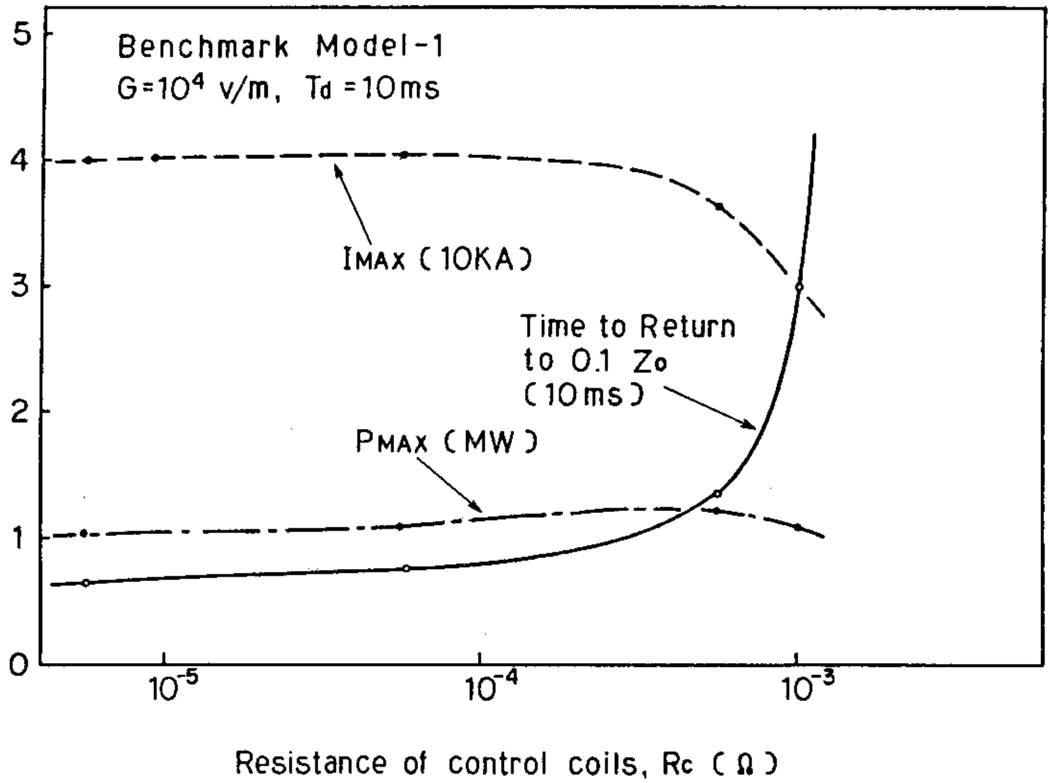

Fig. 2.3 Dependence of time to return to 0.1 Z_0 upon control coil resistance, R_c.

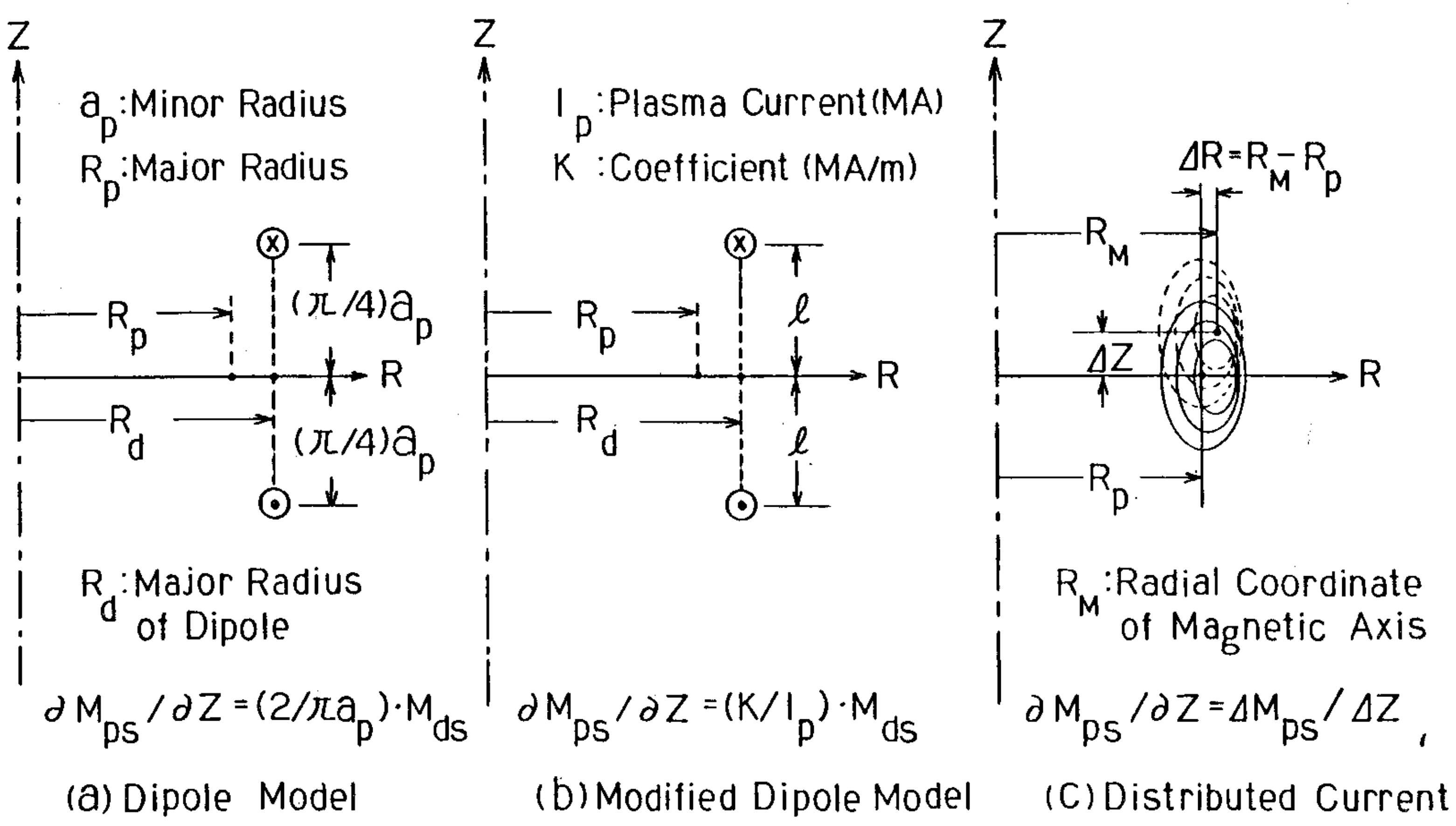

Fig 2.4 Plasma model for $(\partial M_{ps}/\partial Z)$ evaluation

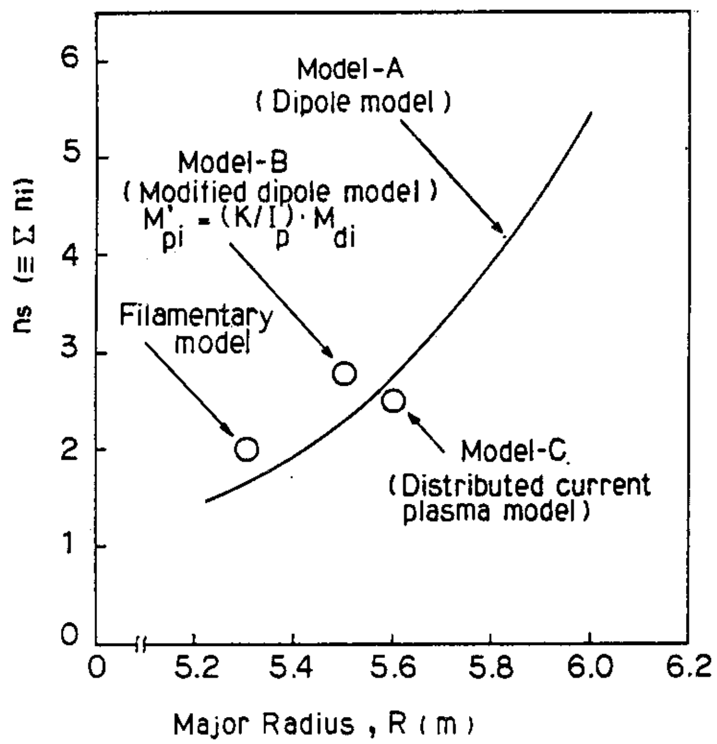

Fig. 2.5 Results of Σn_i evaluation obtained by the filamentary, dipole and distributed current models.

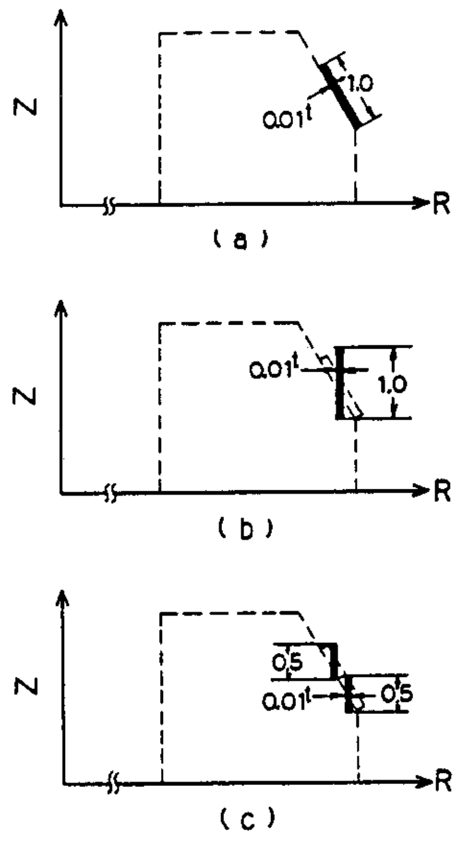

Fig. 2.6 Shell cross-sections used for test calculations.

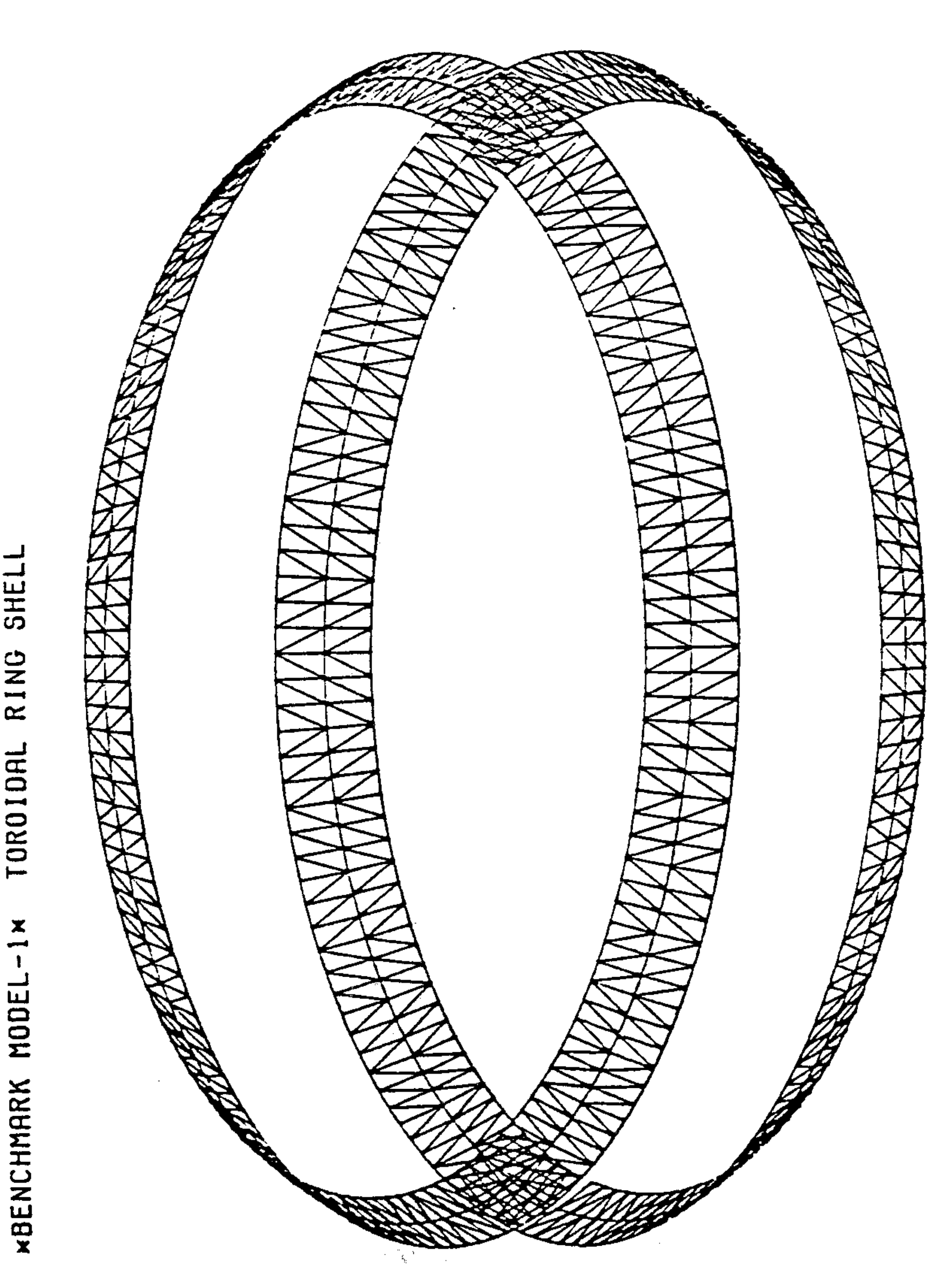

Fig. 3.1 A structure of finite elements for Benchmark Model-1

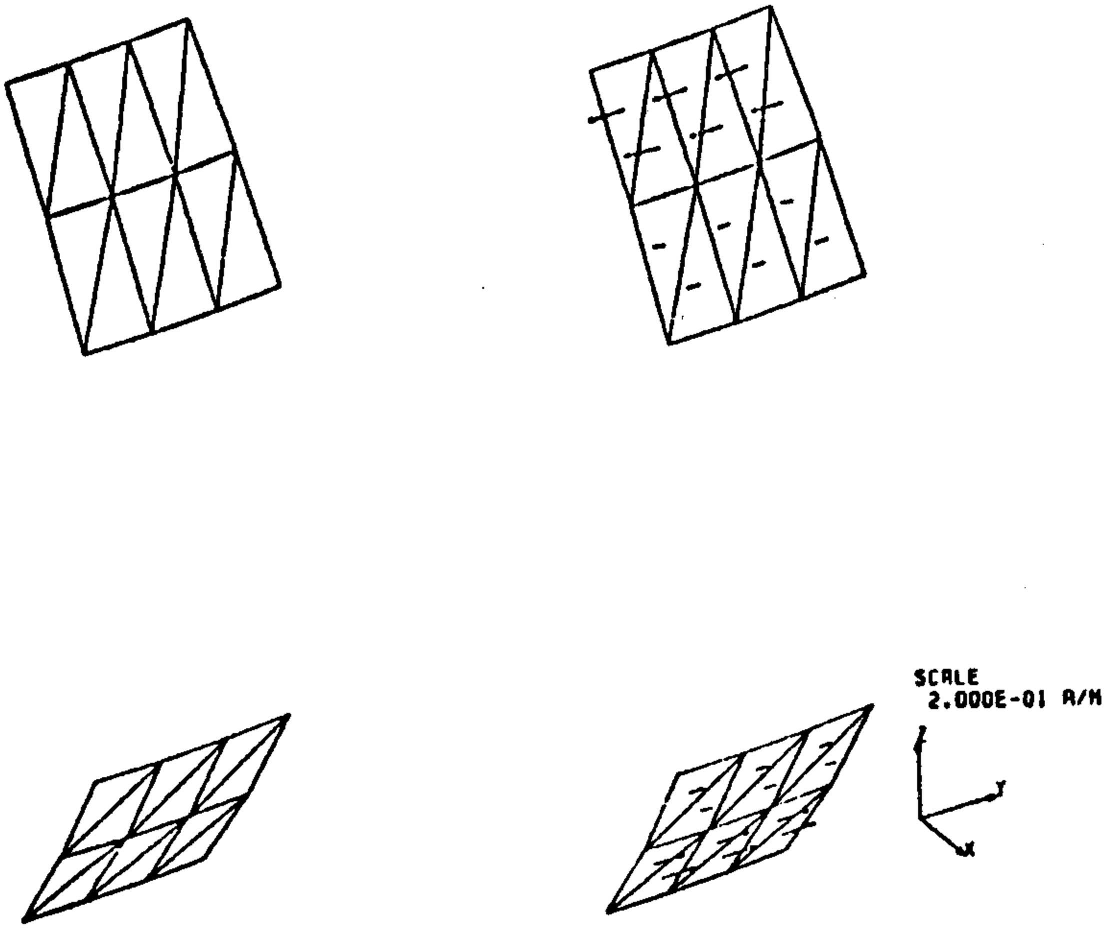

Fig. 3.2 An example of eddy current distributions for Model-1

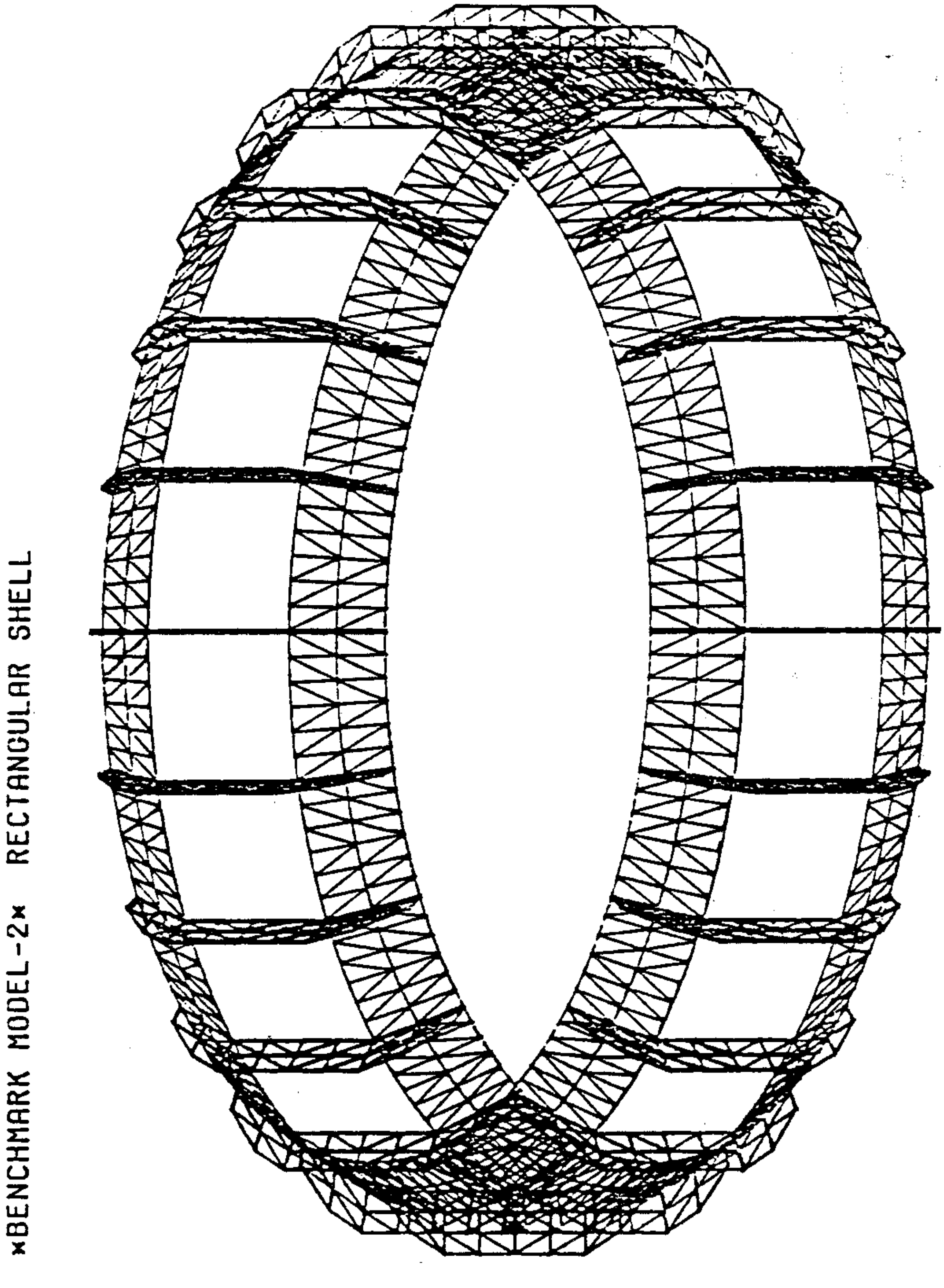

Fig. 3.3 A structure of finite elements for Benchmark Model-2

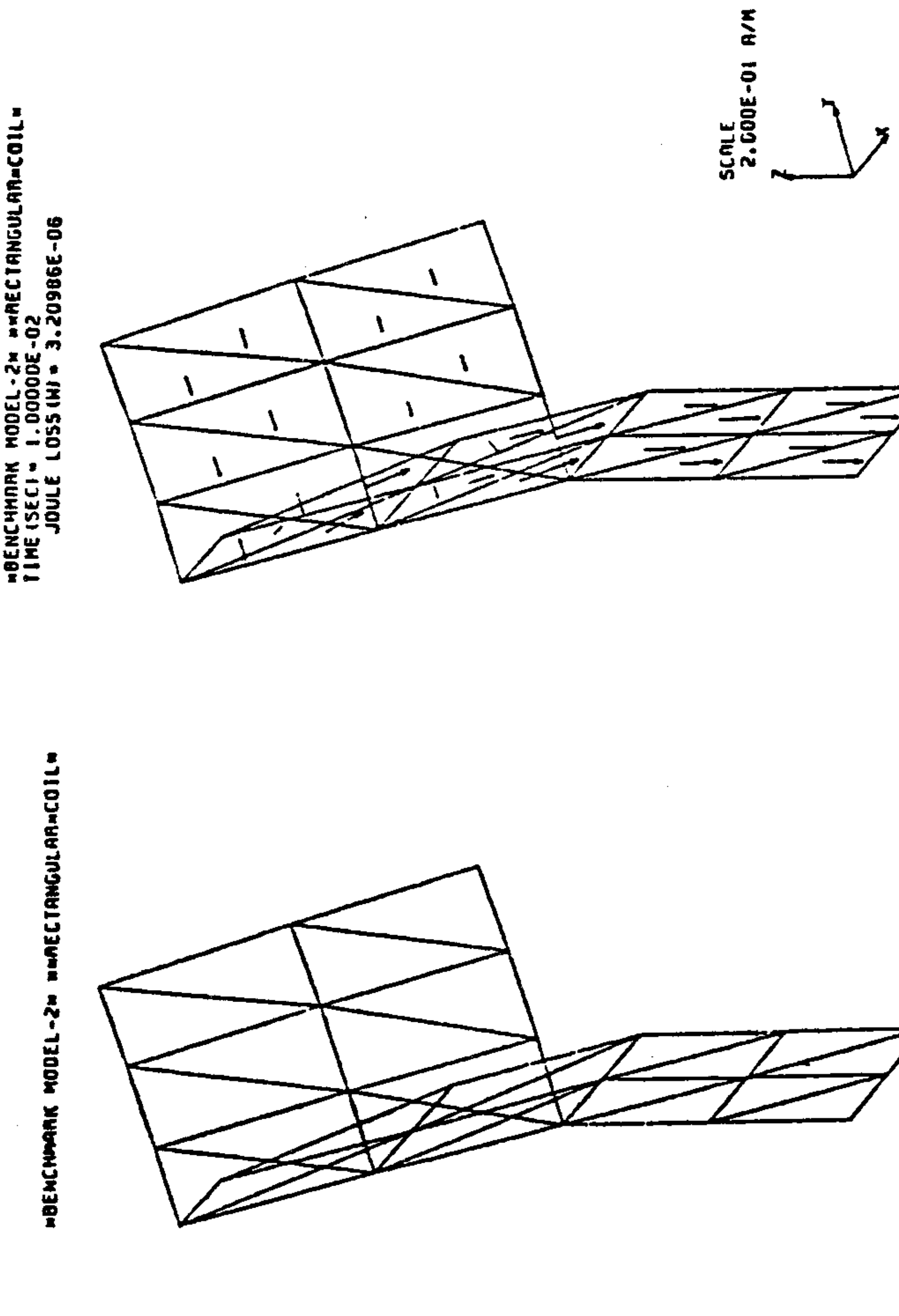

Fig. 3.4 An example of eddy current distributions for Model-2

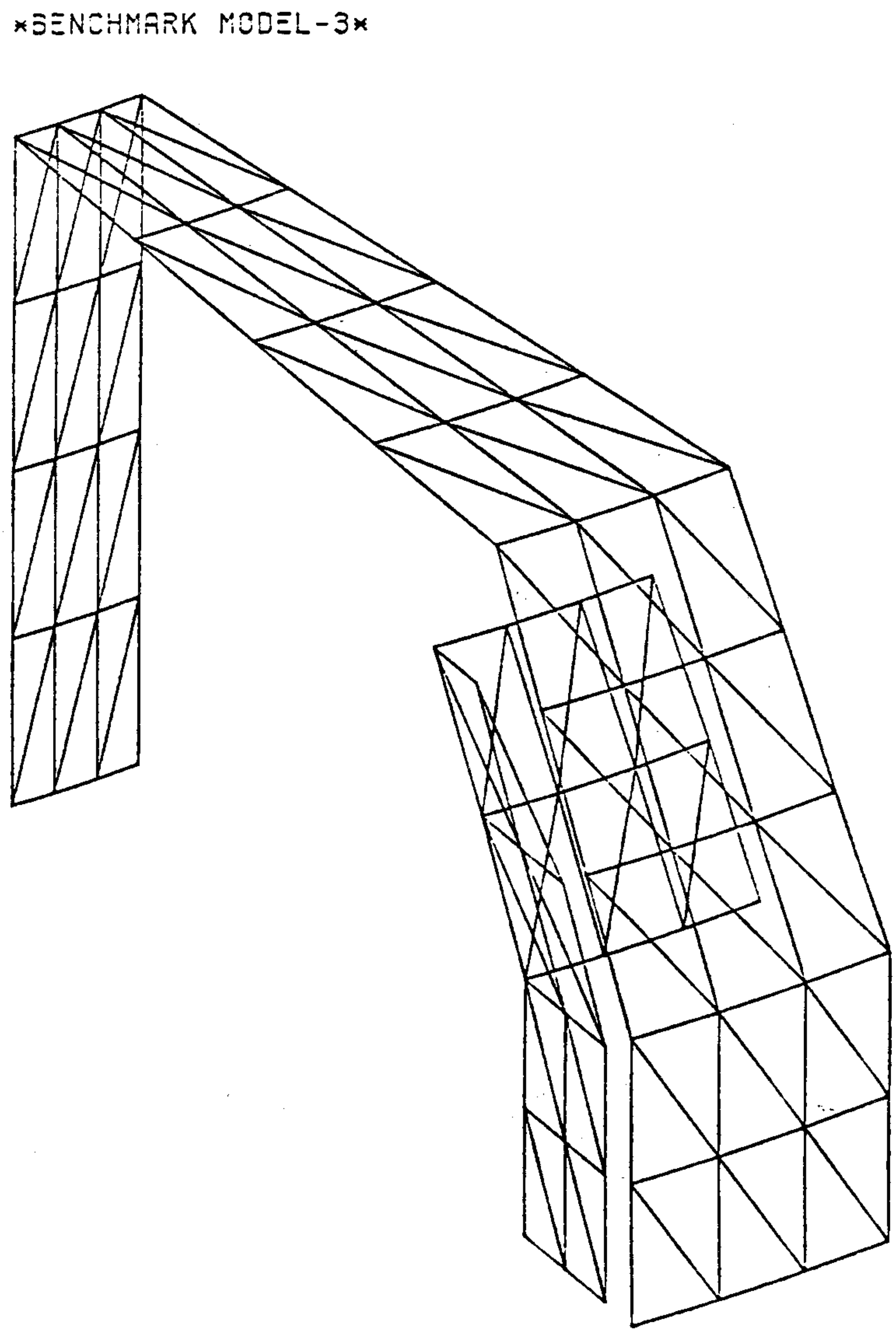

Fig. 3.5 A structure of finite elements for Benchmark Model-3

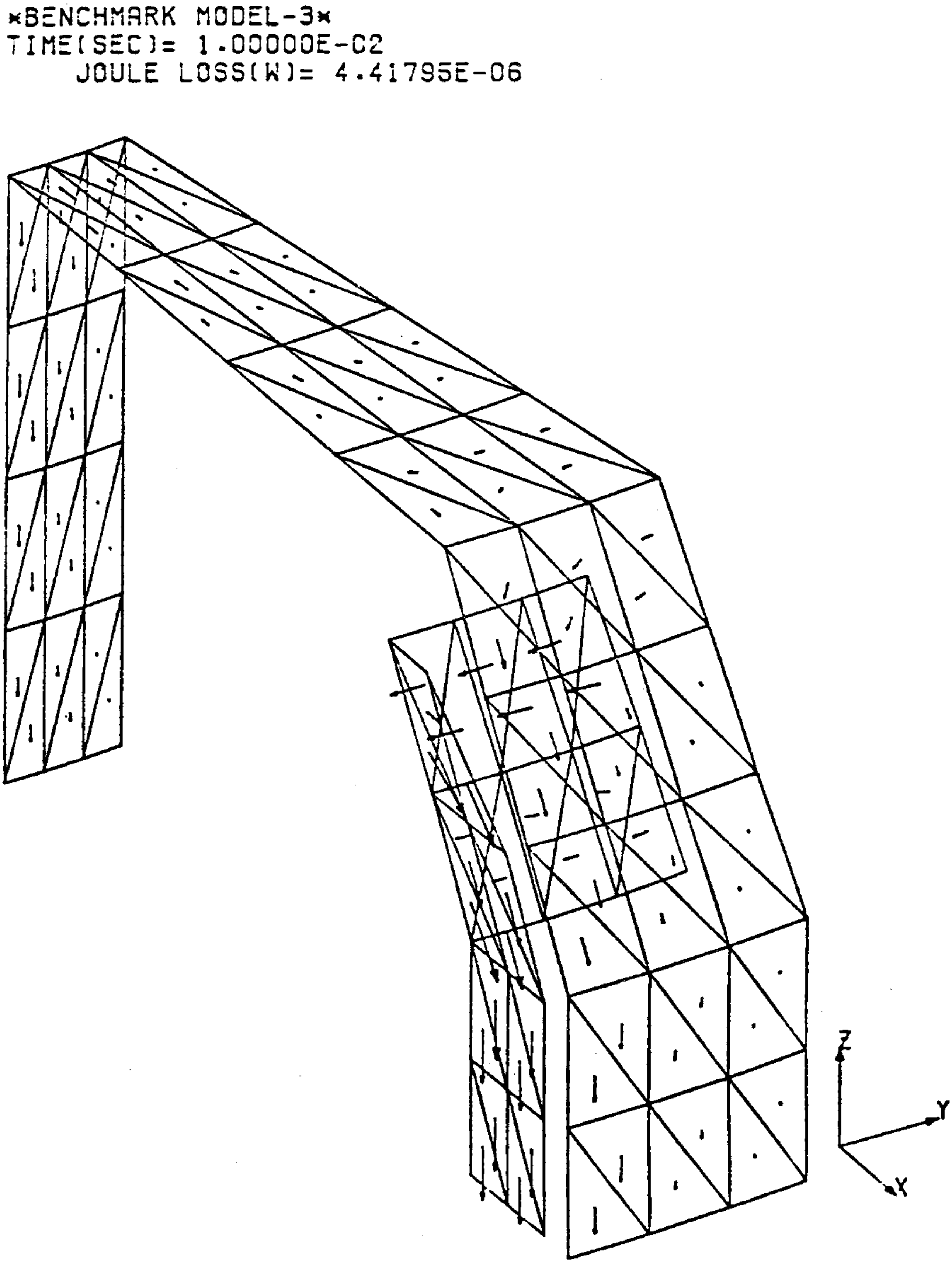

Fig. 3.6 An example of eddy current distributions for Model-3

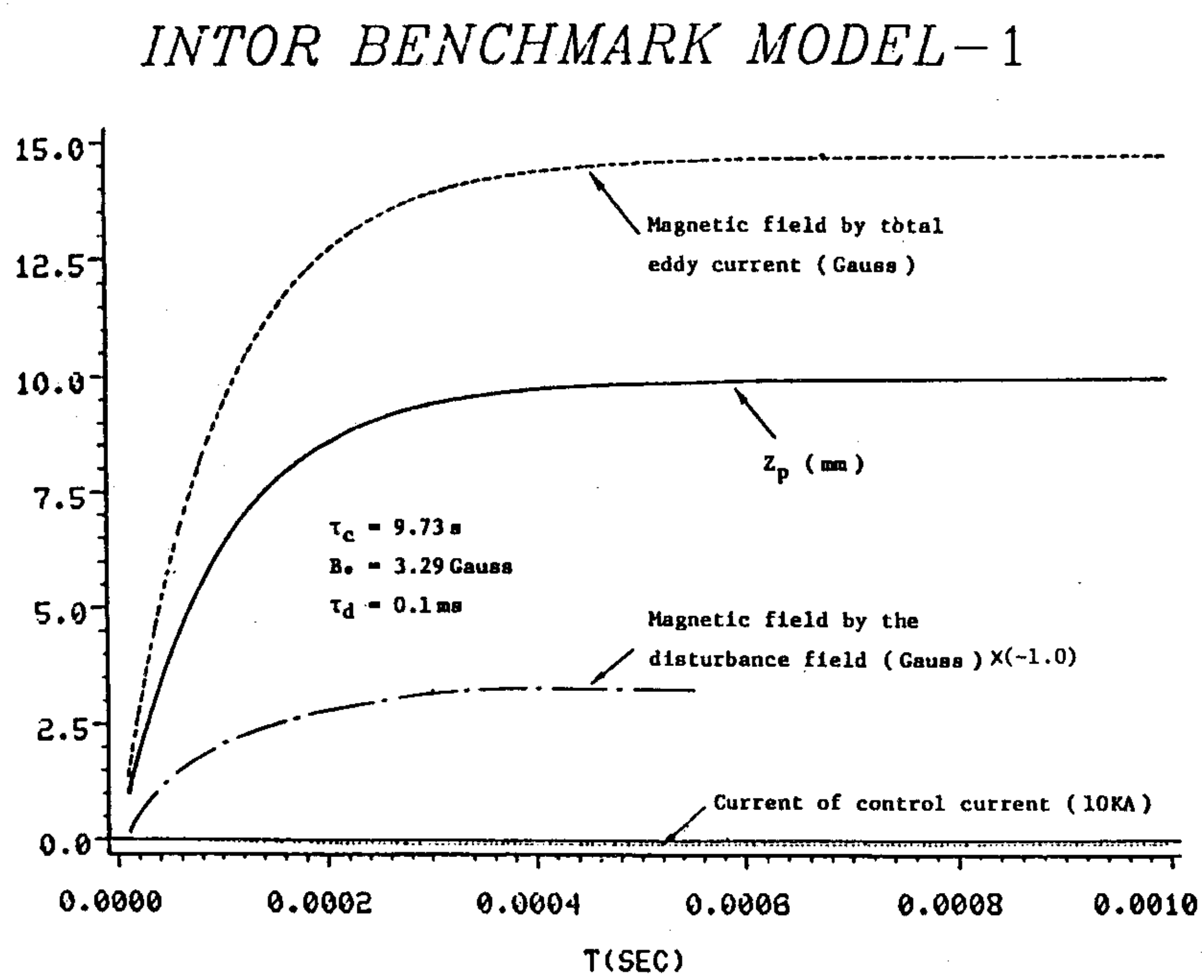

Fig. 4.1 Time evolution of the vertical displacement of plasma column, Z_p, under an external disturbance field, $B_d=B_o\cdot[1-\exp(-t/\tau_d)]$ for Benchmark Model-1, and time evolution of the horizontal magnetic field due to the external disturbance, the magnetic field due to the eddy currents, and the current in the control coils when being regarded as passive conductors.

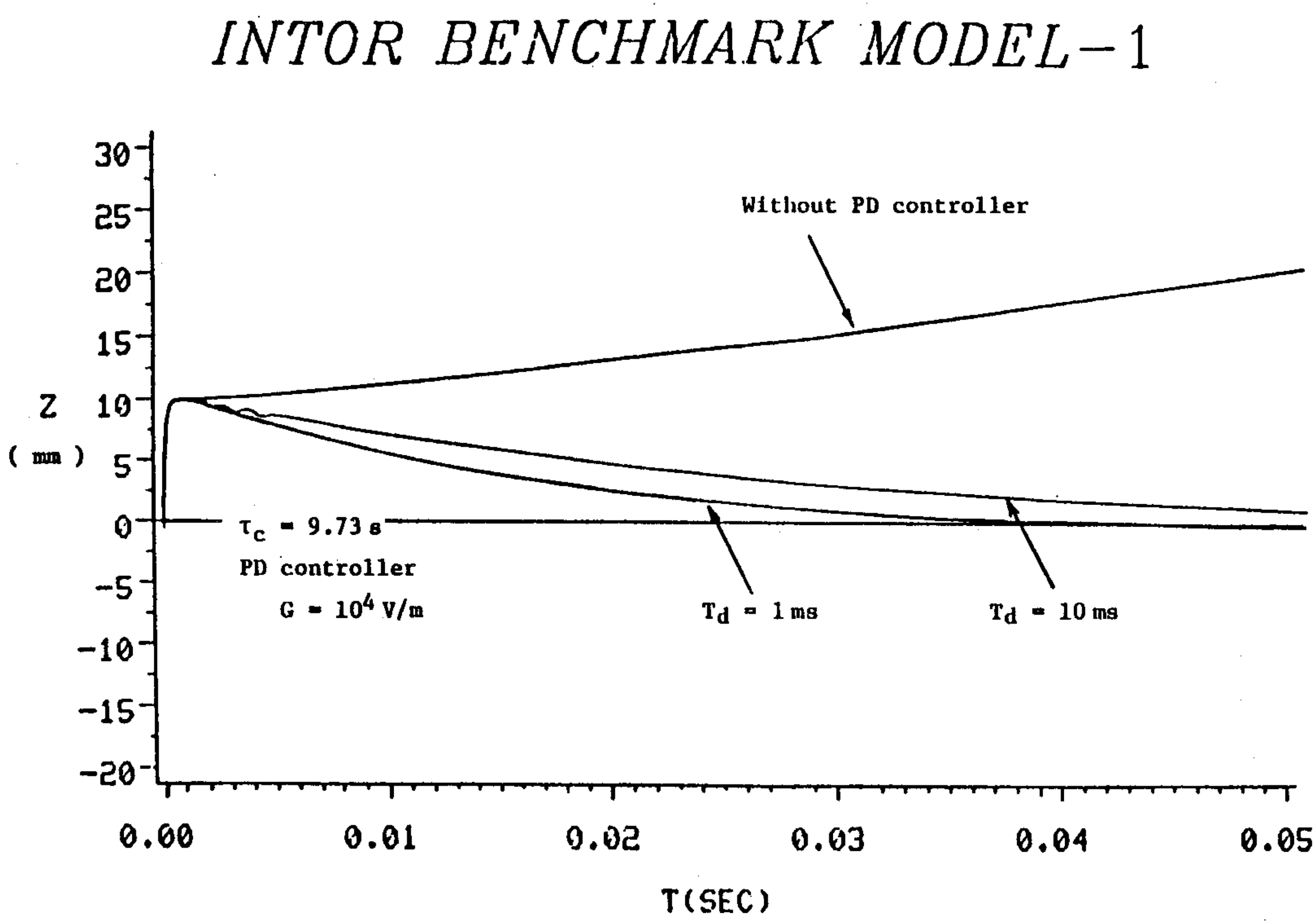

Fig. 4.2 Time evolutions of Z_p with and without active control for Benchmark Model-1

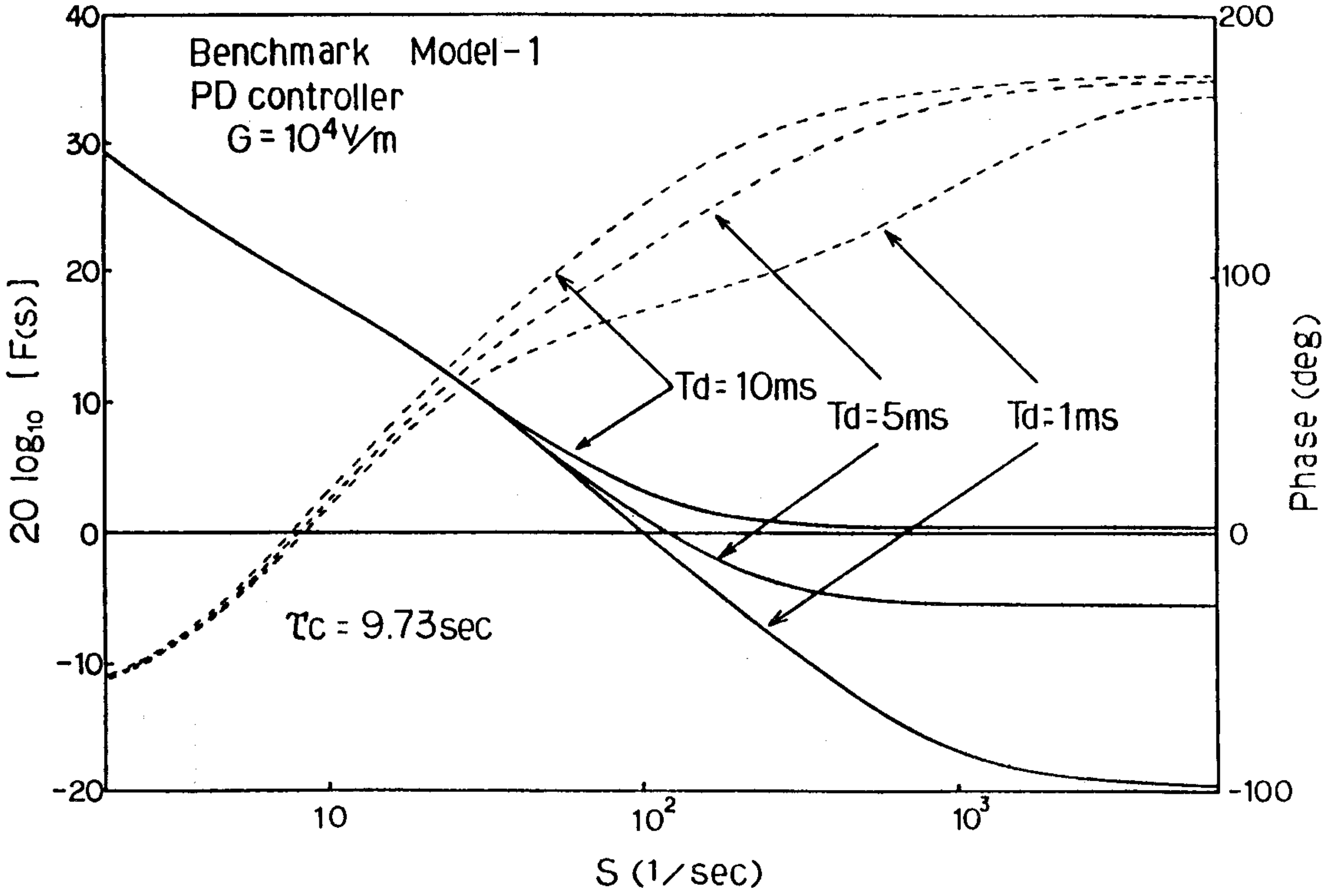

Fig. 4.3 Bode diagram with the derivative action time, T_d as a parameter for Benchmark Model-1

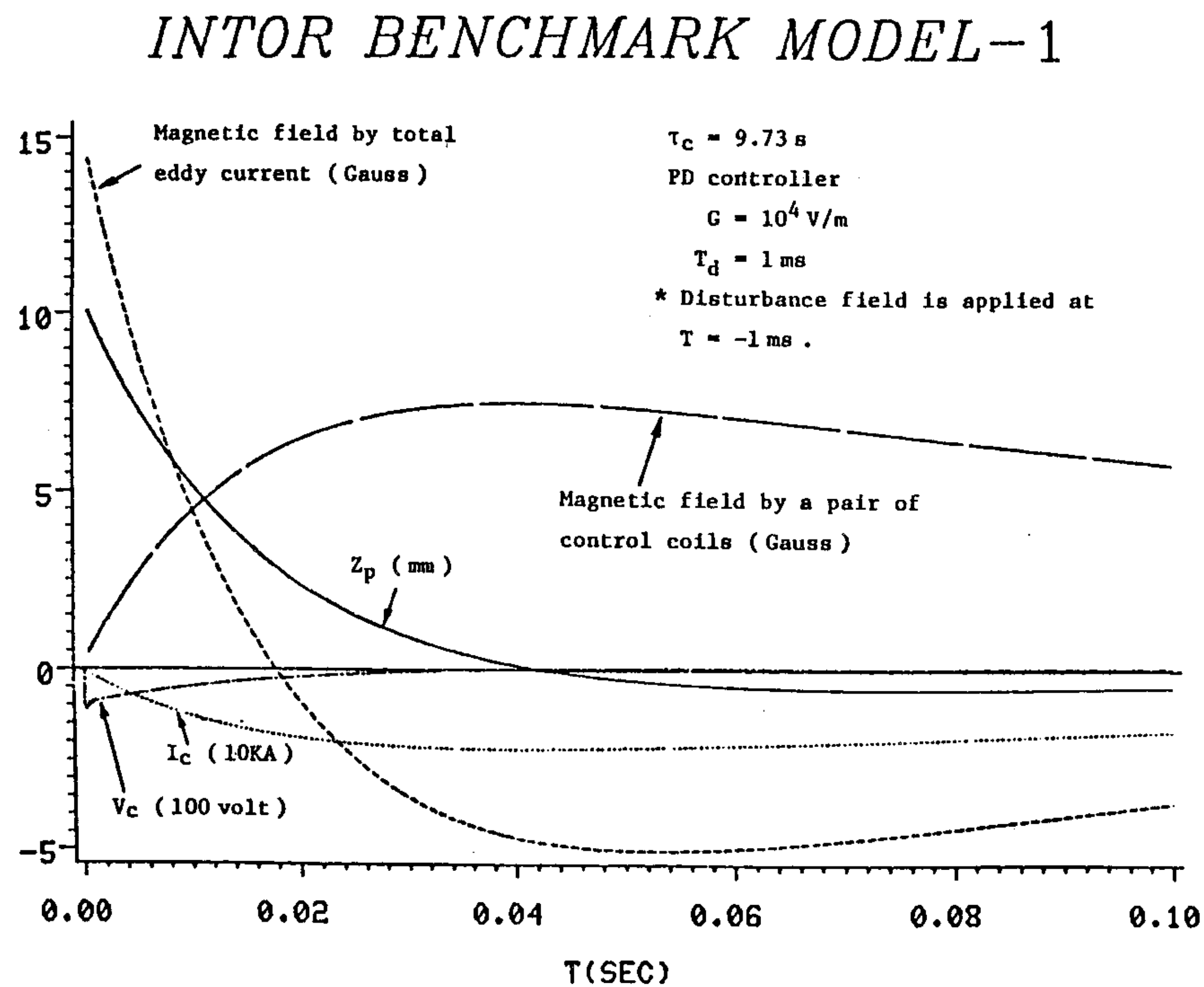

Fig. 4.4 Position control characteristics for Benchmark Model-1 on the derivative action time, T_d=1 ms, and time evolution of the magnetic field due to the eddy current, the magnetic field produced by a pair of control coils, the magnetic field composed from these two fields and the current and voltage of the control coils.

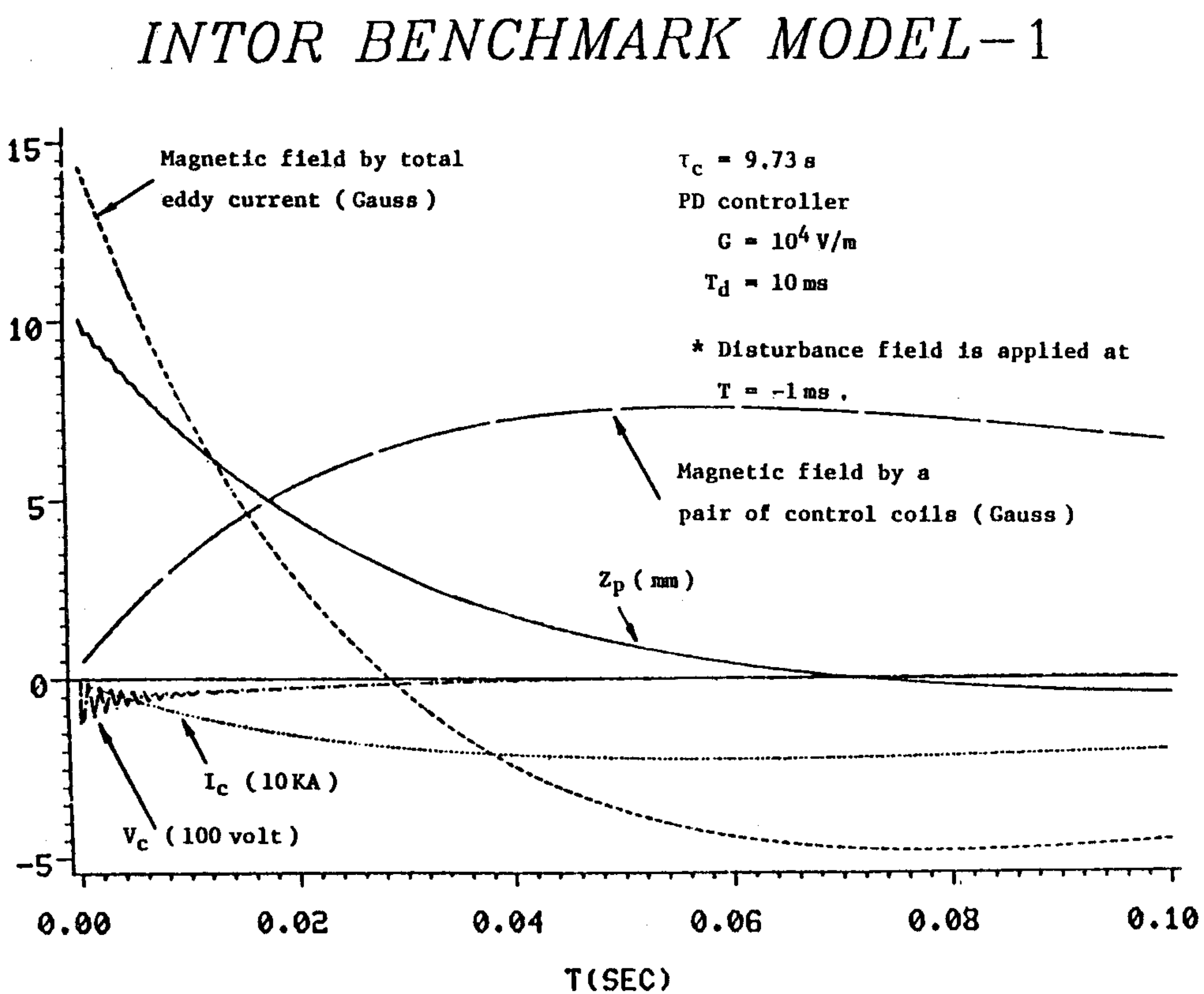

Fig. 4.5 Position control characteristics for Benchmark Model-1 on the derivative action time, T_d=10 ms, and time evolutions of the same parameters as in Fig. 4.4.

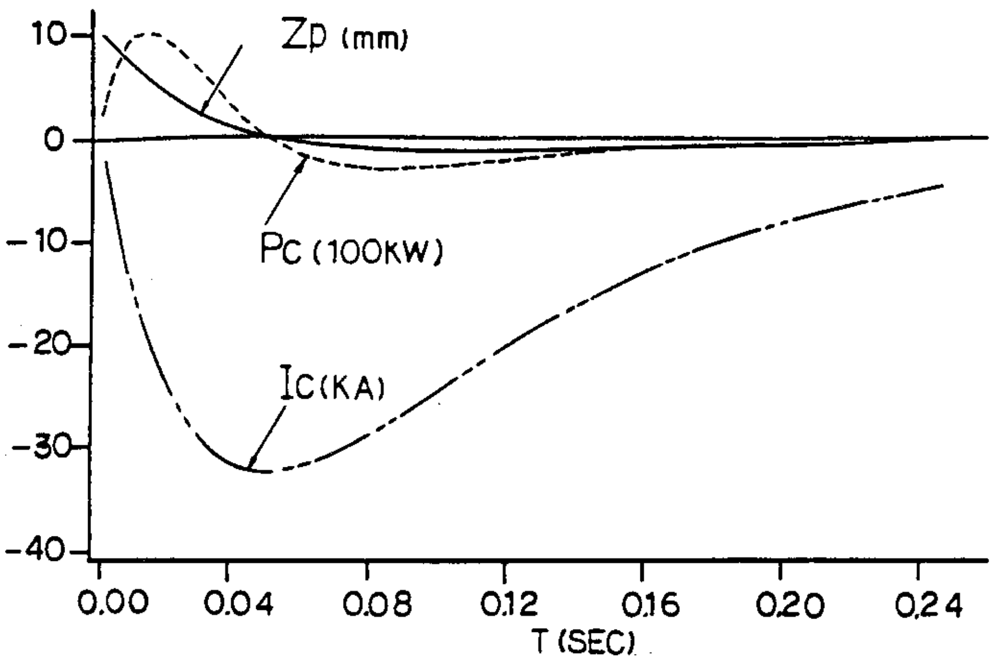

(a) Td = 1ms and G = 10^4 V/m

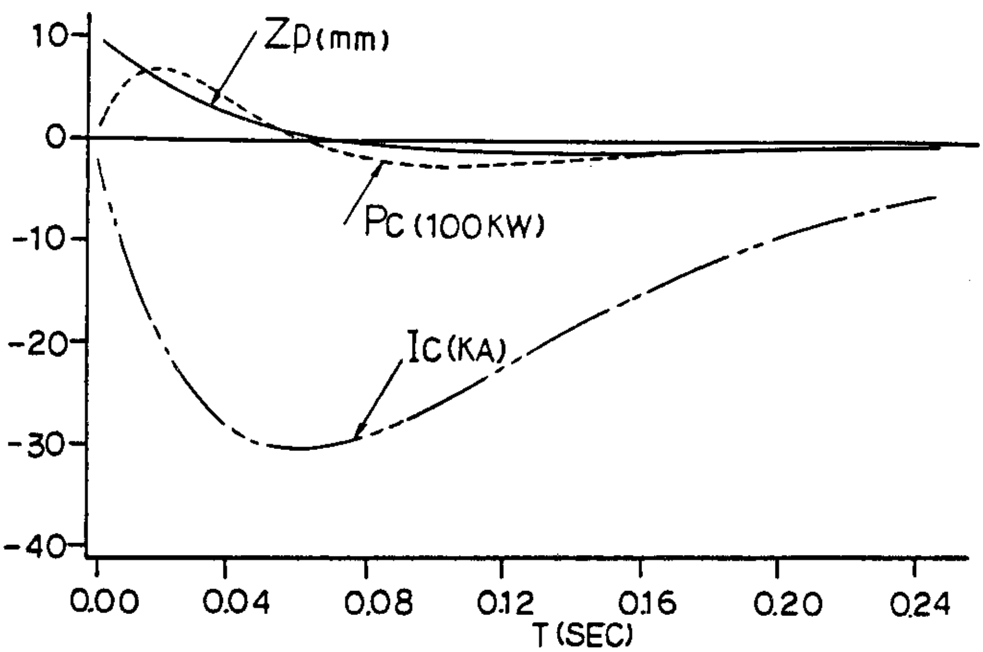

(b) Td = 10ms and G = 10^4 V/m

Fig. 4.6 Time evolution of Z_p, control coil current, I_c and required power, P_c in case of Benchmark Model-1 (The filamentary model is used for evaluation of ($\partial M_{ps}/\partial Z$) ($\equiv M_{ps}'$)

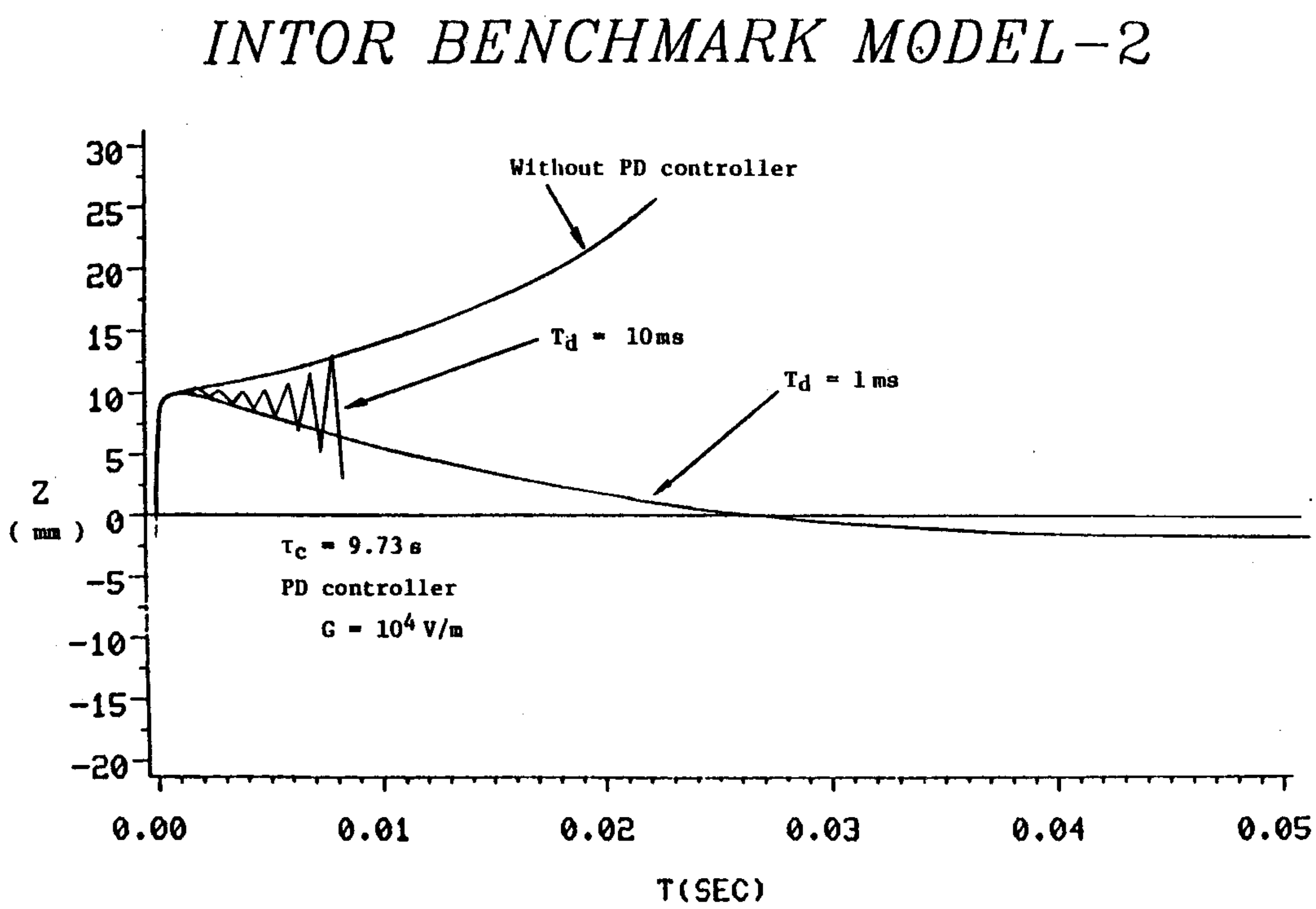

Fig. 4.7 Time evolutions of Z_p in Benchmark Model-2 with and without active control (T_d=1 or 10 ms)

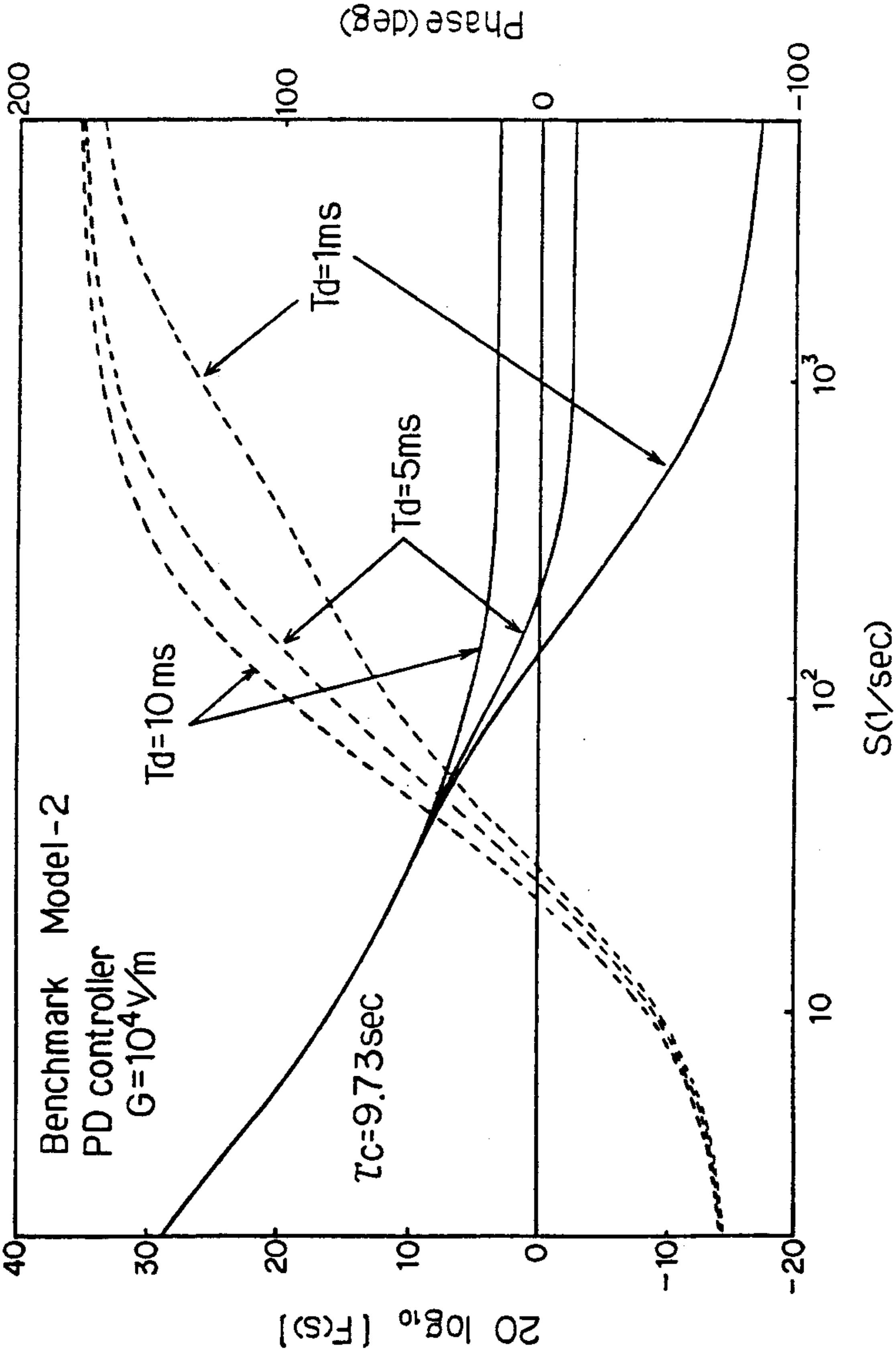

Fig. 4.8 Bode diagram with the derivative action time, T_d as a parameter

INTOR BENCHMARK MODEL−2

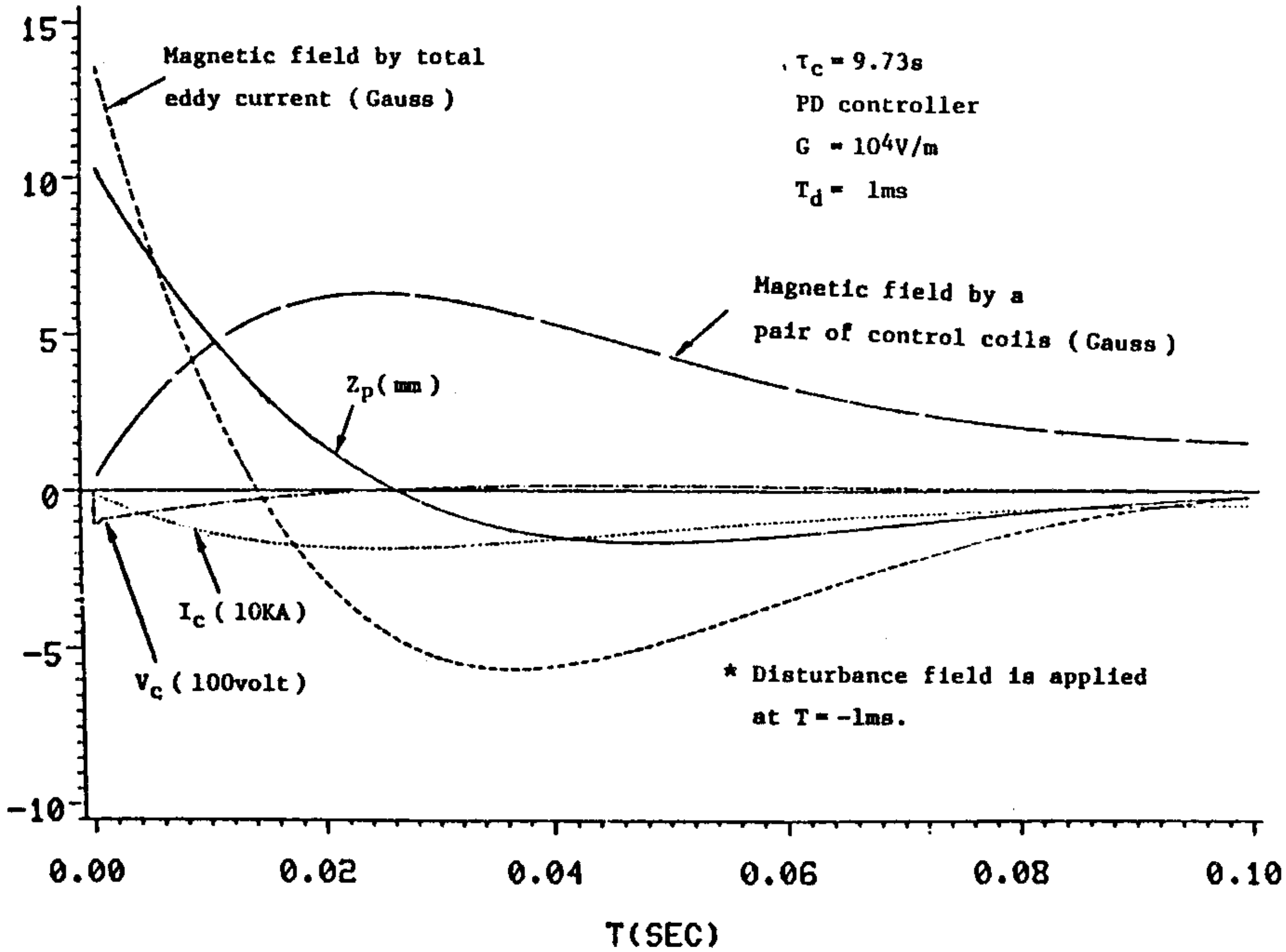

Fig. 4.9 Position control characteristics for Benchmark Model-2 on the derivative action time, T_d=1 ms, and time evolutions of the same parameters as in Fig. 4.4.

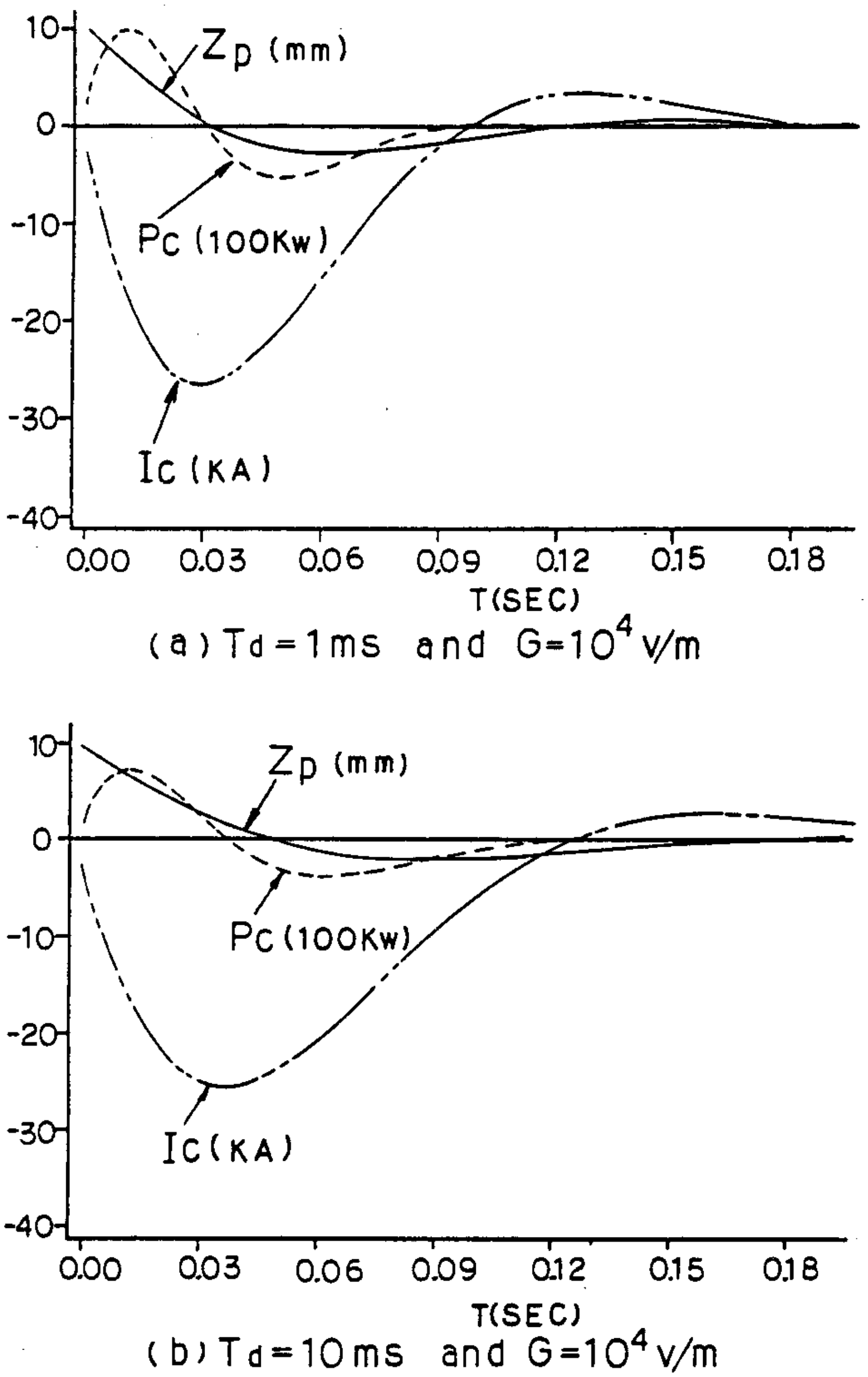

Fig. 4.10 Time evolution of Z_p, I_c, and P_c in case of Benchmark Model-2. (The filamentary model is used for evaluatin of M'_{ps})

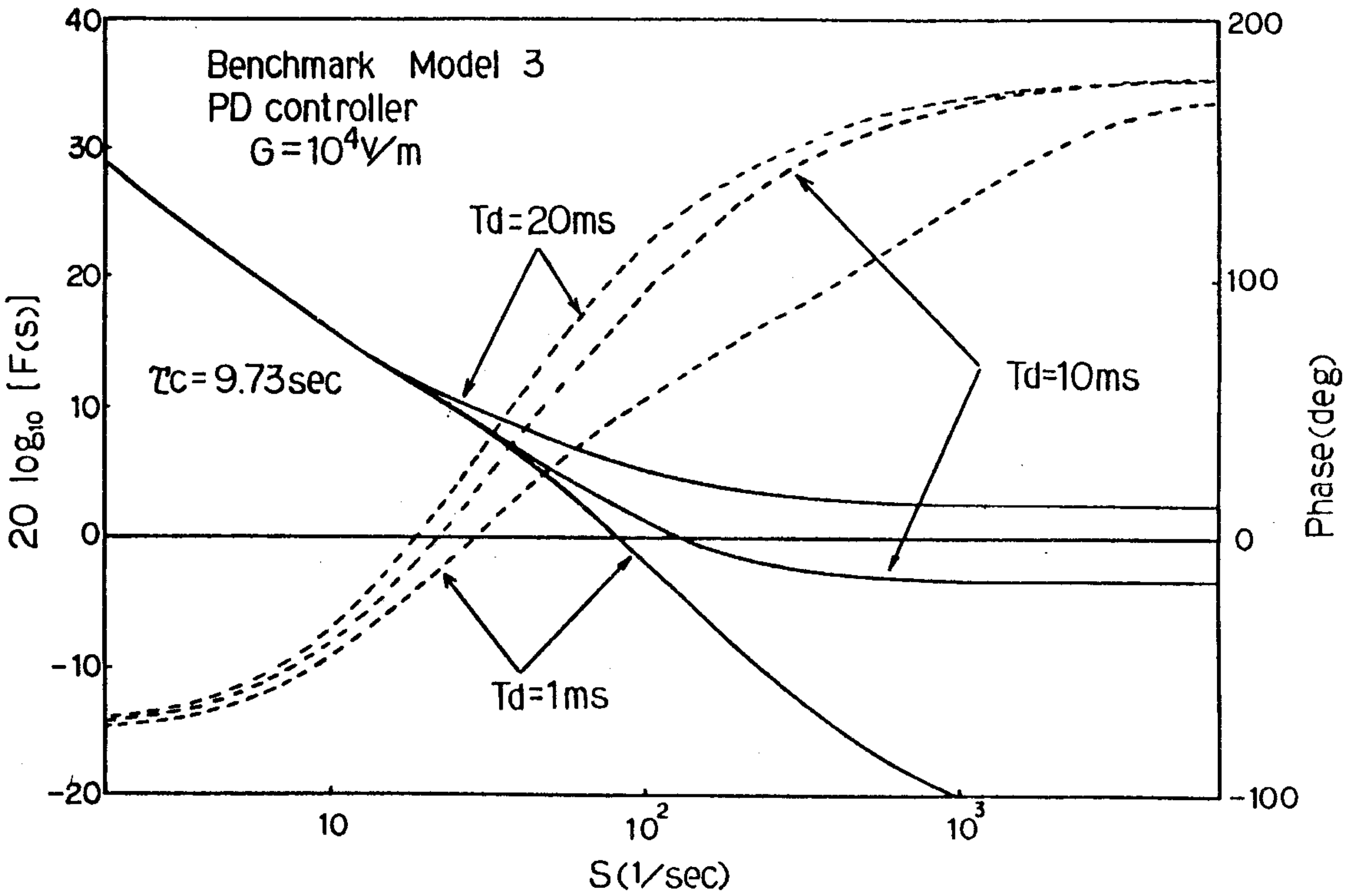

Fig. 4.11 Bode diagram with the derivative action time, T_d as a parameter

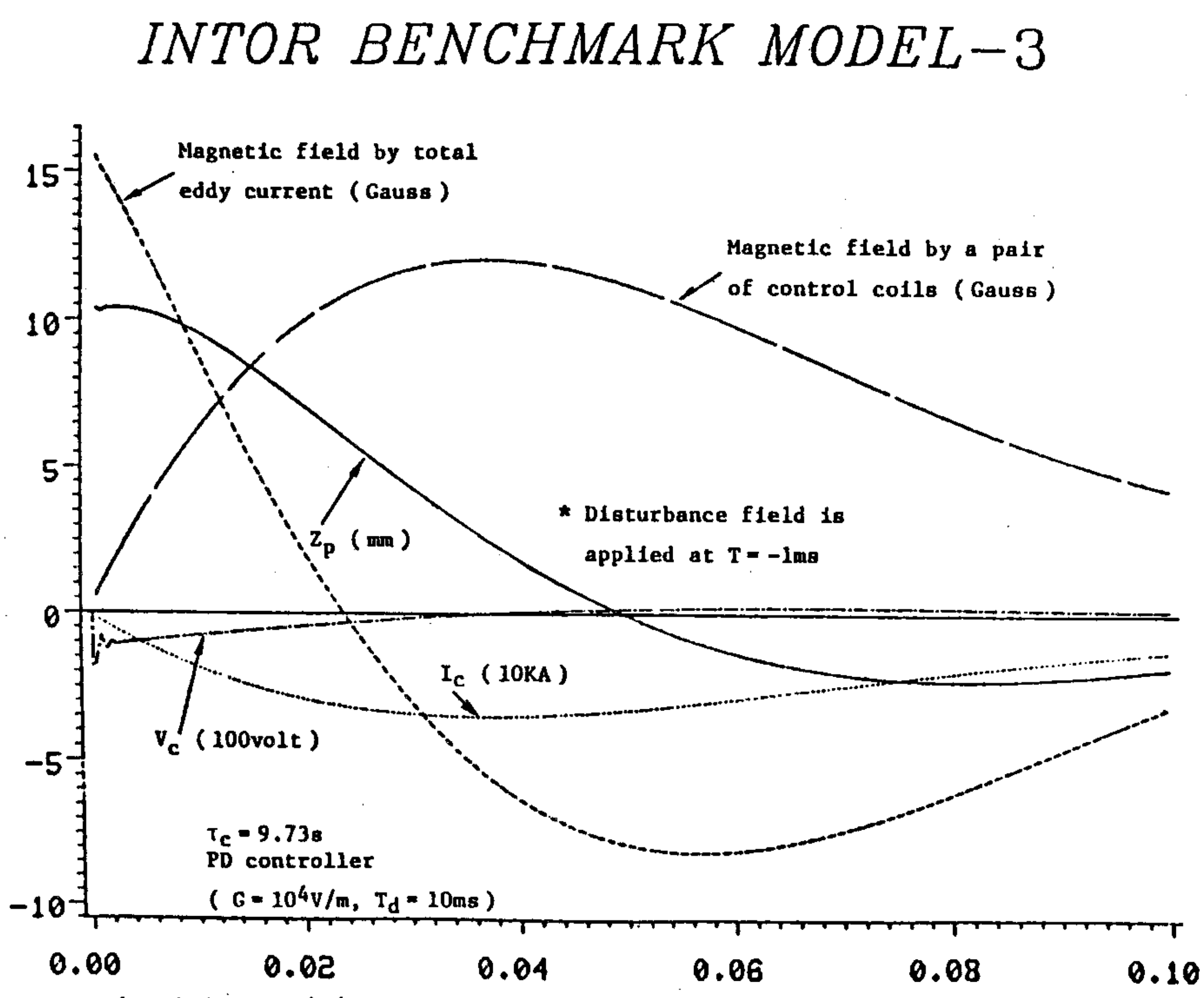

Fig. 4.12 Position control characteristics for Benchmark Model-3 on the derivative action time, T_d=10 ms, and time evolutions of the same parameters as in Fig. 4.4.

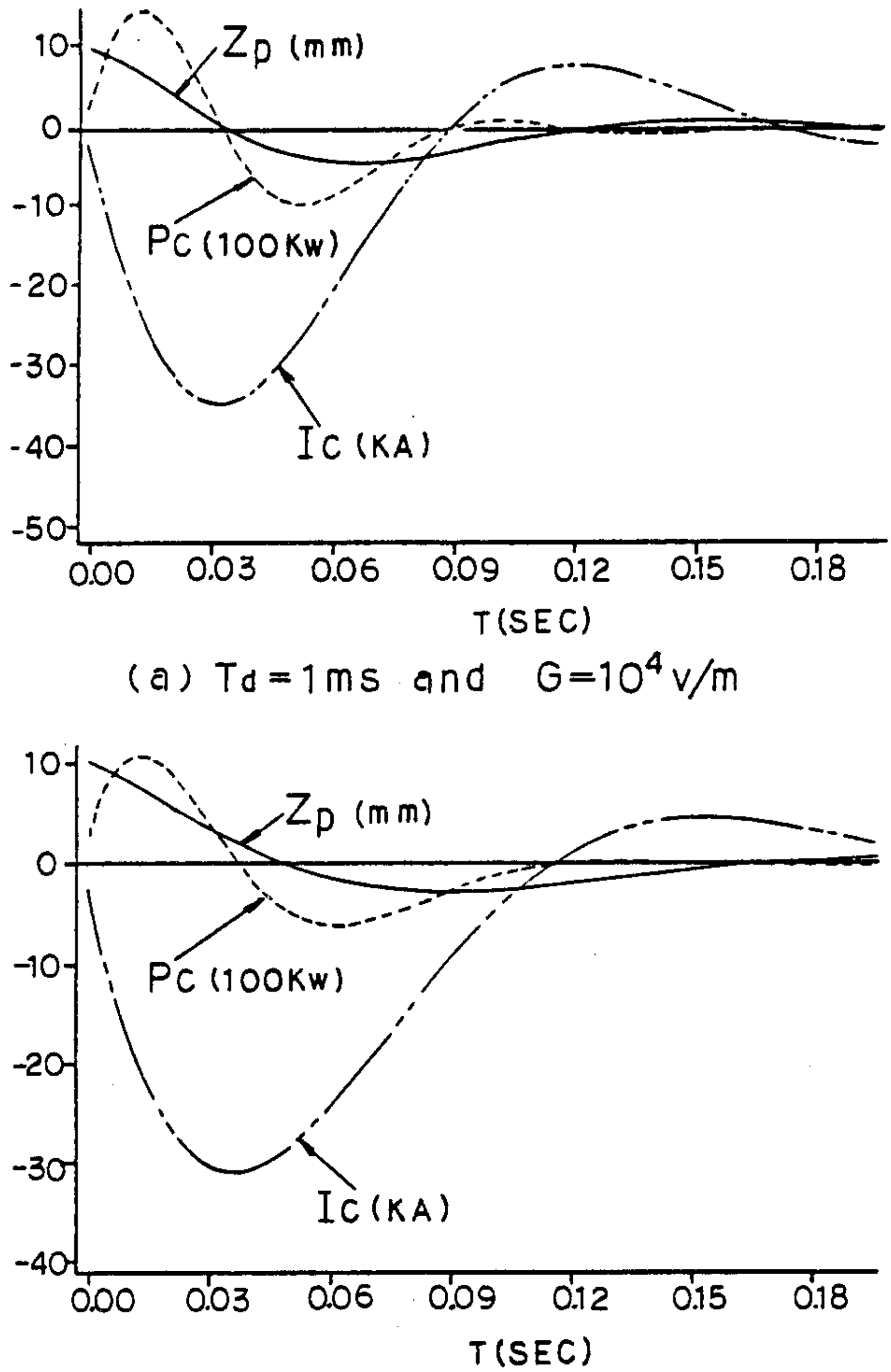

Fig. 4.13 Time evolution of Z_p, I_c, and P_c in case of Benchmark Model-3. (The filamentary model is used for evaluation of M'_{ps})

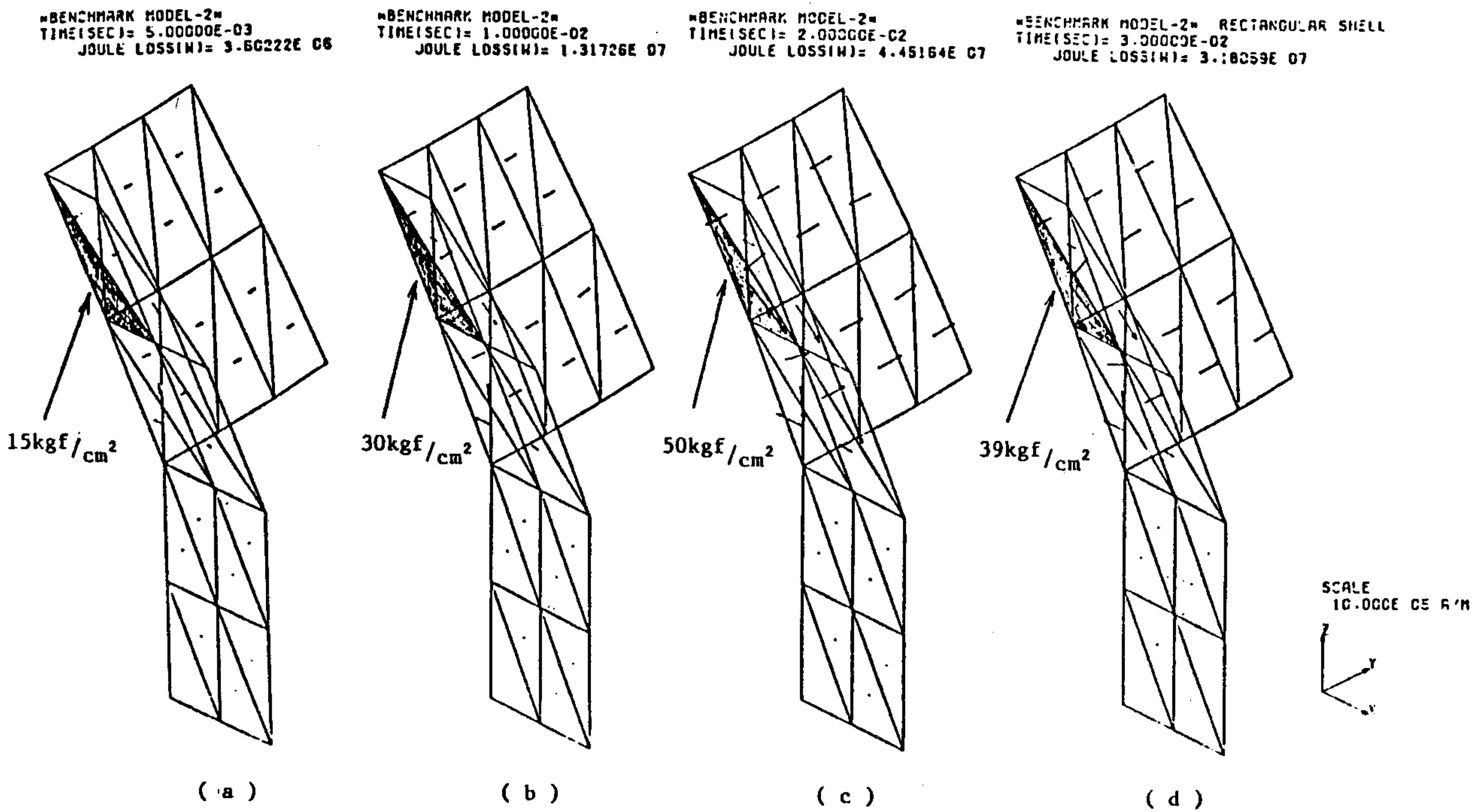

Fig. 4.14 Variation of the eddy current with the rectangular shell on plasma disruption in case of Benchmark Model-2.

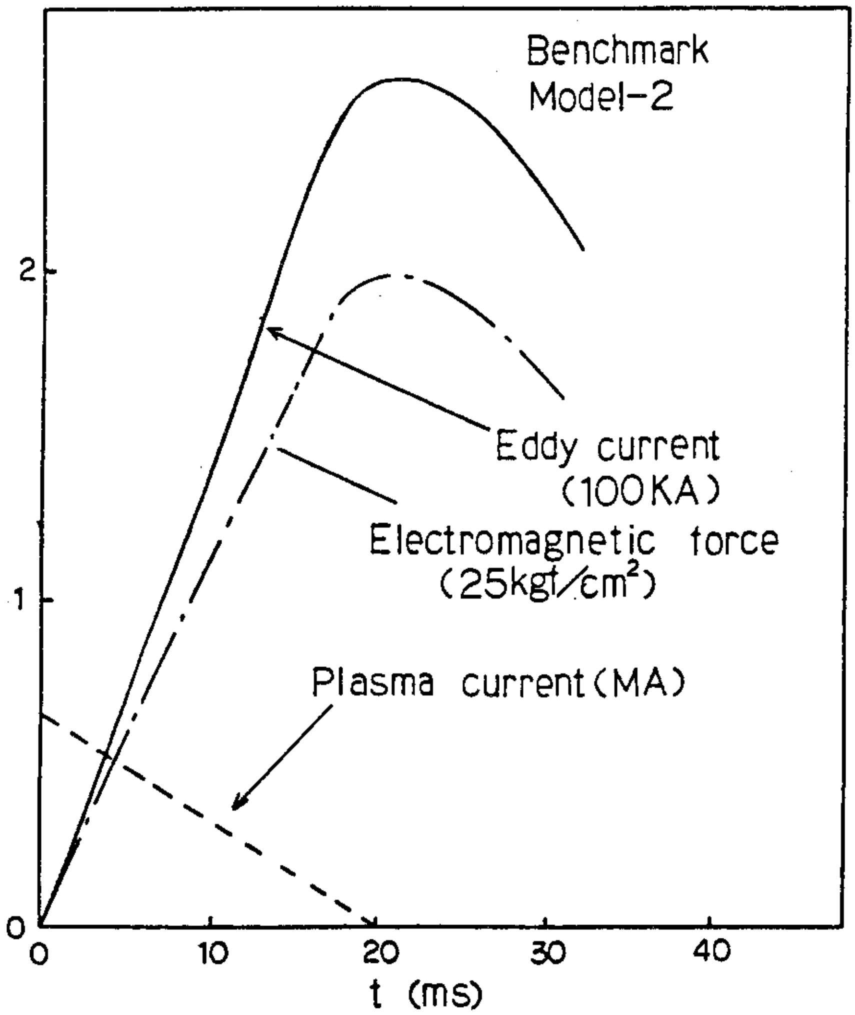

Fig. 4.15 Time evolutions of the plasma current, the eddy current and the electromagnetic force on plasma disruption in case of Benchmark Model-2.

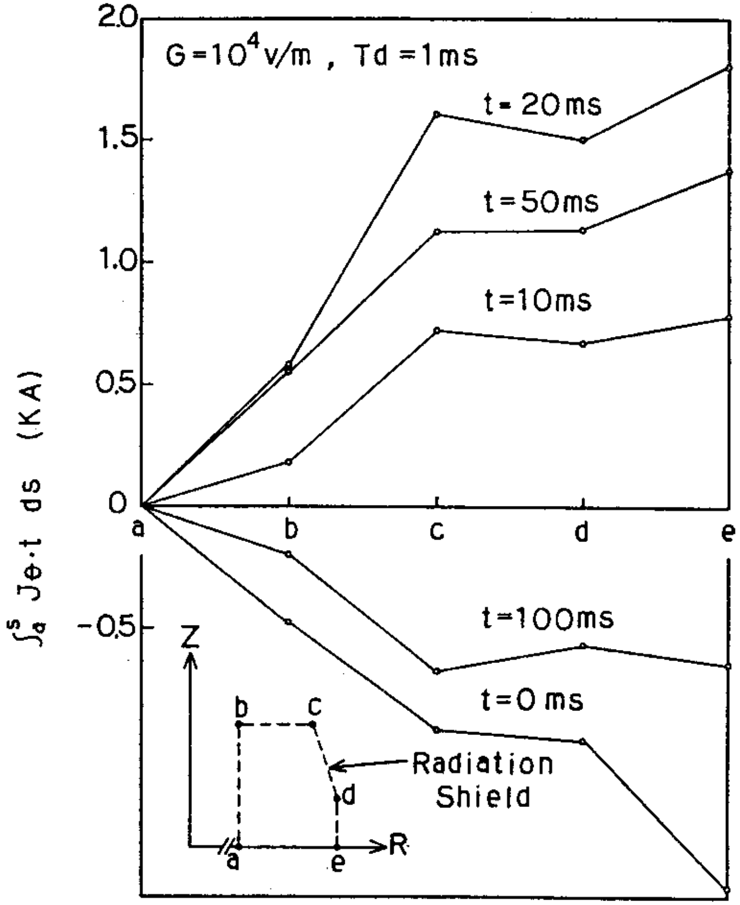

Fig. 4.16 Variations of current intergral on the radiation shield in case of T_d = 1 ms and G = 10^4 V/m.
[This figure corresponds to Fig. 4.13 (a)]

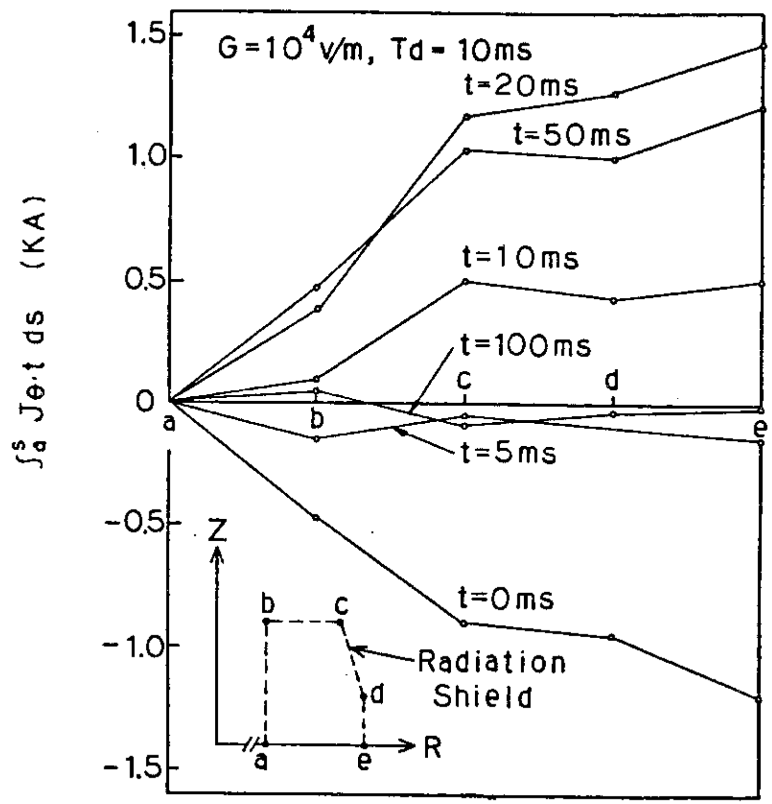

Fig. 4.17 Variations of current intergral on the radiation shield in case of T_d = 10 ms and G = 10^4 V/m.
[This figure corresponds to Fig. 4.13 (b)]

Acknowledgements

The authors would like to express their sincere thanks to Drs K. TOMABECHI, M. YOSHIKAWA and T. YAMAMOTO for their continuing encouragement. They also wish to thank Mr. S. NARIKAWA, Dr. M. NISHIKAWA, Mrs. H. TOMITA and Y. IMAMURA of Mitsubishi Fusion Center for their helpful discussions.

Reference

(1) Summary Document Critical Issue Group C, Transient Electromagnetic for the INTOR WORKSHOP PHASE IIA, PART 2, 27 January (1984).

(2) INTOR Phase IIA European Contributions to the INTOR Workshop Meeting (Group C) January 1984 and May 1984, Vienna.

(3) INTOR Workshop 2A, Part 2, January 16 and May 21, 1984, Japanese Contributions to Critical Issues Group C (Transient Electromagnetics).

(4) Transient Electromagnetic - USA Contributions, INTOR Critical Issue C, January 16, 1984, and May 21, 1984, Vienna.

(5) USSR Contributions to the IX Session of INTOR Workshop, Phase 2A, Part 2, January 16 and May 21, 1984 (Group C, Transient Electromagnetics).

(6) INTERNATIONAL TOKAMAK REACTOR Phase Two A, Part I, IAEA, VIENNA, 1983.

(7) K. UEDA, S. NISHIO, N. FUJISAWA, M. SUGIHARA, S. SAITO and K. MIYAMOTO: JAERI-M-82-213 (1983).

(8) A. KAMEARI: J. Computational Phys. 42, 124 (1981)

(9) Summary Report Critical Issue Group C Transient Electromagnetics for the INTOR Workshop Phase IIA, Part 2, 1 June, 1984.

(10) T. YAMAMOTO: Private Communication, February (1984)